



University of Kentucky
UKnowledge

Theses and Dissertations--Chemical and
Materials Engineering

Chemical and Materials Engineering

2016

THREE-DIMENSIONAL MICROSTRUCTURAL EFFECTS ON MULTI-SITE FATIGUE CRACK NUCLEATION BEHAVIORS OF HIGH STRENGTH ALUMINUM ALLOYS

Yan Jin

University of Kentucky, kingrauljin@gmail.com

Digital Object Identifier: <http://dx.doi.org/10.13023/ETD.2016.238>

[Right click to open a feedback form in a new tab to let us know how this document benefits you.](#)

Recommended Citation

Jin, Yan, "THREE-DIMENSIONAL MICROSTRUCTURAL EFFECTS ON MULTI-SITE FATIGUE CRACK NUCLEATION BEHAVIORS OF HIGH STRENGTH ALUMINUM ALLOYS" (2016). *Theses and Dissertations--Chemical and Materials Engineering*. 63.

https://uknowledge.uky.edu/cme_etds/63

This Doctoral Dissertation is brought to you for free and open access by the Chemical and Materials Engineering at UKnowledge. It has been accepted for inclusion in Theses and Dissertations--Chemical and Materials Engineering by an authorized administrator of UKnowledge. For more information, please contact UKnowledge@lsv.uky.edu.

STUDENT AGREEMENT:

I represent that my thesis or dissertation and abstract are my original work. Proper attribution has been given to all outside sources. I understand that I am solely responsible for obtaining any needed copyright permissions. I have obtained needed written permission statement(s) from the owner(s) of each third-party copyrighted matter to be included in my work, allowing electronic distribution (if such use is not permitted by the fair use doctrine) which will be submitted to UKnowledge as Additional File.

I hereby grant to The University of Kentucky and its agents the irrevocable, non-exclusive, and royalty-free license to archive and make accessible my work in whole or in part in all forms of media, now or hereafter known. I agree that the document mentioned above may be made available immediately for worldwide access unless an embargo applies.

I retain all other ownership rights to the copyright of my work. I also retain the right to use in future works (such as articles or books) all or part of my work. I understand that I am free to register the copyright to my work.

REVIEW, APPROVAL AND ACCEPTANCE

The document mentioned above has been reviewed and accepted by the student's advisor, on behalf of the advisory committee, and by the Director of Graduate Studies (DGS), on behalf of the program; we verify that this is the final, approved version of the student's thesis including all changes required by the advisory committee. The undersigned agree to abide by the statements above.

Yan Jin, Student

Dr. Tongguang Zhai, Major Professor

Dr. T. D. Dziubla, Director of Graduate Studies

THREE-DIMENSIONAL MICROSTRUCTURAL EFFECTS ON MULTI-SITE FATIGUE
CRACK NUCLEATION BEHAVIORS OF HIGH STRENGTH ALUMINUM ALLOYS

DISSERTATION

A dissertation submitted in partial fulfillment of the requirements for the degree of
Doctor of Philosophy in the College of Engineering at the University of Kentucky

By

Yan Jin

Lexington, Kentucky

Director: Dr. Tongguang Zhai, Associate Professor of Materials Engineering

Lexington, Kentucky

2016

Copyright © Yan Jin 2016

ABSTRACT OF DISSERTATION

THREE-DIMENSIONAL MICROSTRUCTURAL EFFECTS ON MULTI-SITE FATIGUE CRACK NUCLEATION BEHAVIORS OF HIGH STRENGTH ALUMINUM ALLOYS

An experimental method was further developed to quantify the anisotropy of multi-site fatigue crack initiation behaviors in high strength Al alloys by four-point bend fatigue testing under stress control. In this method, fatigue crack initiation sites (fatigue weak-links, FWLs) were measured on the sample surface at different cyclic stress levels. The FWL density in an alloy could be best described using a three-parameter Weibull function of stress, though other types of sigmoidal functions might also be used to quantify the relationship between FWL density and stress. The strength distribution of the FWLs was derived from the Weibull function determined by fitting the FWLs vs. stress curve experimentally obtained. As materials properties, the FWL density and strength distribution could be used to evaluate the fatigue crack nucleation behaviors of engineering alloys quantitatively and the alloy quality in terms of FWL density and strength distribution. In this work, the effects of environment, types of microstructural heterogeneities and loading direction on FWLs were all studied in detail in AA7075-T651, AA2026-T3511, and A713 Al alloys, etc. It was also found that FWLs should be quantified as a Weibull-type function of strain instead of stress, when the applied maximum cyclic stress exceeded the yield strength of the tested alloys.

In this work, four-point bend fatigue tests were conducted on the L-T (Rolling-Transverse), L-S (Rolling-Short transverse) and T-S planes of an AA7075-T651 alloy plate, respectively, at room temperature, 20 Hz, R=0.1, in air. The FWL populations, measured on these surfaces, were a Weibull-type function of the applied maximum cyclic stress, from which FWL density and strength distribution could be determined. The alloy showed a significant anisotropy of FWLs with the weak-link density being 11 mm^{-2} , 15 mm^{-2} and 4 mm^{-2} on the L-T, L-S and T-S planes, respectively. Fatigue cracks were predominantly initiated at Fe-containing particles on the L-T and L-S planes, but only at Si-bearing particles on the T-S plane, profoundly demonstrating that the pre-fractured Fe-containing particles were responsible for crack initiation on the L-T and L-S planes, since the pre-fracture of these particles due to extensive deformation in the L direction during the prior rolling operation could only promote crack initiation when the sample was cyclically stressed in the L direction on both the L-T and L-S planes. The fatigue strengths of the L-T, L-S and T-S planes of the AA7075 alloy were measured to be 243.6, 273.0 and 280.6 MPa, respectively. The differences in grain and particle structures

between these planes were responsible for the anisotropy of fatigue strength and FWLs on these planes.

Three types of fatigue cracks from particles, type-I: the micro-cracks in the particles could not propagate into the matrix, i.e., type-II: the micro-cracks were fully arrested soon after they propagated into the matrix, and type-III: the micro-cracks became long cracks, were observed in the AA7075-T651 alloy after fatigue testing. By cross-sectioning these three-types of particles using Focused Ion Beam (FIB), it was found that the thickness of the particles was the dominant factor controlling fatigue crack initiation at the particles, namely, the thicker a pre-fractured Fe-containing particle, the easier it became a type-III crack on the L-T and L-S planes. On the T-S plane, there were only types-I and III Si-bearing particles at which crack were initiated. The type-I particles were less than 6.5 μm in thickness and type-III particles were thicker than 8.3 μm . Cross-sectioning of these particles using FIB revealed that these particles all contained gas pores which promoted crack initiation at the particles because of higher stress concentration at the pores in connection with the particles. It was also found that fatigue cracks did not always follow the any specific crystallographic planes within each grain, based on the Electron Backscatter Diffraction (EBSD) measurement. Also, the grain orientation did not show a strong influence on crack initiation at particles which were located within the grains. The topography measurements with an Atomic Force Microscope (AFM) revealed that Fe-containing particles were protruded on the mechanically polished surface, while the Si-bearing particles were intruded on the surface, which was consistent with hardness measurements showing that Si-bearing particles were softer (4.03 ± 0.92 GPa) than Fe-containing ones (8.9 ± 0.87 GPa) in the alloy.

To verify the 3-D effects of the pre-fractured particles on fatigue crack initiation in high strength Al alloys, rectangular micro-notches of three different types of dimensions were fabricated using FIB in the selected grains on the T-S planes of both AA2024-T351 and AA7075-T651 Al alloys, to mimic the three types of pre-fractured particles found in these alloys. Fatigue testing on these samples with the micro-notches verified that the wider and deeper the micro-notches, the easier fatigue cracks could be initiated at the notches. In the AA2024-T351 samples, cracks preferred to propagate along the $\{111\}$ slip plane with the smallest twist angle and relatively large Schmid factor. These experimental data obtained in this work could pave a way to building a 3-D quantitative model for quantification of fatigue crack initiation behaviors by taking into account the driving force and resistance to short crack growth at the particles in the surface of these alloys.

KEYWORDS: High strength Al alloy, Fatigue Weak-link (FWL) density and Strength distribution, Multi-site fatigue crack nucleation, Focused Ion Beam (FIB), Constituent particle

Yan Jin

06/12/2016

THREE-DIMENSIONAL MICROSTRUCTURAL EFFECTS ON MULTI-SITE FATIGUE
CRACK NUCLEATION BEHAVIORS OF HIGH STRENGTH ALUMINUM ALLOYS

By

Yan Jin

Dr. Tongguang Zhai
Director of Dissertation

Dr. T. D. Dziubla
Director of Graduate Studies

06/12/2016

ACKNOWLEDGEMENTS

First of all, I would like to gratefully and sincerely thank my advisor Dr. Tongguang Zhai, without whose patient and professional guidance, unconditional understanding and support in the past almost five years, I could not have achieved so much and learnt precious research experience and technical skills in the course of pursuing my Ph.D. degree at the University of Kentucky. His characteristic mentorship is paramount in cultivating my scientific thinking approach and developing my personal maturity, which is tremendously helpful for me in doing everything in the future.

I also would like to thank the Department of Chemical and Materials Engineering (CME) at UK, especially my committee members, Dr. Yang-Tse Cheng, Dr. T. John Balk, and Dr. I. S. Jawahir for their time and professional suggestions on each committee meeting. Meanwhile, many thanks for the technical support from Electron Microscope Center (EMC) researchers Dr. Dali Qian and Dr. Nicolas Briot, AFM operation by Dr. Wei Sun, Nano-indentation operation by Jiagang Xu, and CME Lab staff, Jerry Rougeux and Nancy Miller. Moreover, I would appreciate the support and help from each of Dr. Zhai's current and former group members, including Dr. Wei Wen, Lin Yang, Gongwang Zhang, Pei Cai, Liang Chen, Zeren Xu, Rami A Almatani and Faez H Qahtani Sr.

I would furthermore like to express my gratitude to Dr. Alfonso H. W. Ngan at the University of Hong Kong (HKU) for giving me the opportunity to be a visiting researcher at HKU, Dr. Chad Parish and Dorothy for their time of training me on operating different types of electron microscopes at Oak Ridge National Laboratory, and Dr. Xiyu Wen at Secat Inc. for his suggestions in developing many of my experimental skills.

Finally but not the least, great appreciation to my girlfriend, Q. Lu, whose love and encouragement promoted the accomplishment of this dissertation. In the meantime, I want to thank my parents for their continuous support and great love for me throughout my life from the first moment I came to the world.

TABLE OF CONTENTS

ACKNOWLEDGEMENTS	iii
TABLE OF CONTENTS	iv
LIST OF TABLES	viii
LIST OF FIGURES	ix
Chapter 1 Introduction	1
1.1 Background introduction to high cycle fatigue of high strength Al alloys	1
1.1.1 History of the research on fatigue	1
1.1.2 Fatigue damage and crack initiation mechanism	3
1.1.3 Approaches to evaluate fatigue properties	5
1.2 Microstructural factors influencing fatigue crack initiation.....	6
1.2.1 Second-phase particle or inclusion	6
1.2.2 Grain boundary or interface	10
1.2.3 Porosity and void	13
1.2.4 Persistent slip bands	14
1.3 Other factors influencing fatigue crack initiation	15
1.3.1 Geometry of grain and crack.....	15
2.2.1 Effects of micro-texture on crack initiation	15
1.4 Rationale and purpose of the study	18
1.5 Key results obtained.....	19
Chapter 2 Experimental theory and technology	23
2.1 Mechanical Test.....	23
2.1.1 Tensile test	23
2.1.2 Four-point bend Fatigue test	23
2.1.3 Nano-indentation.....	24
2.2 Characterization methods.....	25
2.2.1 Scanning Electron Microscopy (SEM)	25

2.2.2 Focused Ion Beam (FIB).....	26
2.2.3 Atomic Force Microscope (AFM)	28
2.3 Crystallographic orientation.....	28
2.3.1 Orientation description.....	28
2.3.2 Texture measurement.....	31
Chapter 3 An experimental methodology to quantify multi-site fatigue crack nucleation behavior in high strength aluminum alloy	41
3.1 Introduction.....	41
3.2 Experiments	42
3.2.1 The alloys and samples	42
3.2.2 Four-point bend fatigue tests.....	43
3.2.3 Measurement of FWLs on surface.....	44
3.2.4 Quantification of FWL density and strength distribution	44
3.3 Results and Discussion	46
3.3.1 Environmental effects on FWLs in AA2026 T3511 Al alloy extruded bar	46
3.3.2 Effects of density of microstructural heterogeneities on FWLs in A713 cast Al alloy.	48
3.3.3 FWLs as a Weibull function of strain	49
3.3.4 FWLs-stress curve fitting by different sigmoidal-type functions	51
3.3.4 Evaluation of alloy quality in terms of FWL density.....	52
3.4 Conclusions.....	53
Chapter 4 The anisotropy of fatigue crack nucleation at constituent particles in AA7075-T651 Al alloy plane	67
4.1 Introduction.....	67
4.2 Experimental details.....	69
4.2.1 The Alloy and samples.....	69
4.2.2 Four-point bend fatigue tests.....	70
4.2.3 Examination of Fatigue Damage on Optical Microscope and SEM	71

4.3 Results and discussions.....	71
4.3.1 S-N curves.....	71
4.3.2 Crack Population vs. Stress.....	72
4.3.3 Strength Distribution of FWLs	74
4.3.4 Constituent particles before and after fatigue	76
4.4 Conclusions.....	82
Chapter 5 3-D microstructural effects on anisotropic behaviors of fatigue crack initiation at constituent particles in an AA7075 T651 aluminum alloy using focused ion beam combined with EBSD, AFM and Nano-indentation.....	91
5.1 Introduction.....	91
5.2 Experimental details.....	94
5.2.1 Materials and samples.....	94
5.2.2 Four-point bend fatigue testing	95
5.2.3 Characterization of 3-D geometries and microstructures of fractured Fe- and Si-bearing constituent particles using SEM/FIB	95
5.2.4 Measurements of micro-texture, hardness and topography of constituent particles using EBSD, Nano-indentation and AFM.....	96
5.3 Results and discussions.....	97
5.3.1 3-D characterization of fractured Fe- and Si-bearing constituent particles after fatigue loading using FIB.....	97
5.3.2 The effects of micro-texture on fatigue crack nucleation at constituent particles using EBSD	101
5.3.3 Examination of topography and mechanical properties of Fe- and Si-bearing constituent particles using AFM and Nano-indentation	104
5.4 Conclusions.....	106
Chapter 6 Simulation of multi-site fatigue crack nucleation behaviors at pre-crack in constituent particles by using micro-notches fabricated with FIB in AA2024-T351 and AA7075-T651 Al alloys rolled plate.....	122
6.1 Introduction.....	122

6.2 Experimental details.....	125
6.2.1 Materials and samples.....	125
6.2.2 Fabrication of micro-notches in selected grains using EBSD and FIB.....	125
6.2.3 Four-point bend fatigue testing for observation of fatigue crack nucleation behavior and FIB cross-sectioning.....	127
6.3 Results and discussions.....	128
6.3.1 Multi-site fatigue crack nucleation at micro-notches in AA2024-T351 and AA7075-T651 Al alloys.....	128
6.3.2 Comparison of fatigue crack nucleation behaviors at micro-notches to mimic fractured particles between AA2024 and AA7075.....	129
6.4 Conclusions.....	132
Chapter 7. Conclusions.....	142
References.....	145
VITA.....	154

LIST OF TABLES

Table 3.1 Chemical composition (wt %) of the AA7075, A713, AA2026 and AA2099.	55
Table 3.2 Mechanical properties of AA7075, A713, AA2026 Al alloys and AA2099.	55
Table 3.3 Parameters determined by fitting N vs σ curves using the Weibull function	58
Table 3.4 Adjusted R-squares and rankings of experimentally measured FWL data fitted using different types of sigmoidal functions in AA7075 T651, A713 and AA2026 Al alloys	64
Table 6.1 The designed and actual dimensions and fatigue crack initiation status of three batches of micro-notches fabricated by FIB in 2024.....	135
Table 6.2 The designed and actual dimensions and fatigue crack initiation status of three batches of micro-notches fabricated by FIB in 7075.....	136
Table 6.3 Twist angles α ($^{\circ}$) at notch root and maximum Schmid factor (SF) of the corresponding {111} of Type-2 crack initiated from #3-T3-4 and Type-3 crack initiated from #1-T3-1 in 2024.....	140

LIST OF FIGURES

Figure 1.1 Different phases of the fatigue life and relevant factors..... 21

Figure 1.2 Sketch diagram showing the geometry of slip at the materials surface according to Forsyth [24]..... 21

Figure 1.3 Schematic diagram showing a crystallographic mechanism for crack growth along slip 1 in grain 1 onto slip plane 2 in grain 2. The crack growth is controlled by α and β ... 22

Figure 1.4 Maps of the twist angle of crack deflection at the grain boundary between a Goss oriented grain and randomly oriented grain in Euler space [100]..... 22

Figure 2.1 The geometry of the dog bone shaped tensile test specimen of 7075..... 34

Figure 2.2 The Instron 8800 servo-hydraulic test machine used for the tensile testing..... 34

Figure 2.3 The actual four-point bend fatigue test rig during fatigue testing. 35

Figure 2.4 The drawing of loading condition and position of supporting and loading rollers on four-point bend samples..... 35

Figure 2.5 The equipment for measurement of modulus and hardness of constituent particles and matrix of AA7075, Nano Indenter G200 by Agilent Technologies..... 36

Figure 2.6 Schematic diagram of the LMIS and lens system of an FIB. 36

Figure 2.7 Main interaction of Ga⁺ with sample material in an FIB. 37

Figure 2.8 (a) spring depiction of cantilever (b) SEM image of triangular cantilever with probe (tip) (from from MikroMasch)[138]. 37

Figure 2.9 Relationship between sample coordinate system and crystal coordinate system in definition of Euler angles..... 38

Figure 2.10 Sketch diagram showing the relationship of two pole figure coordinate (α , β) and the spherical coordinate of n on the unit sphere. 38

Figure 2.11 Schematic diagram showing reflection geometry in X-ray diffraction experiments.. 39

Figure 2.12 Schematic diagram showing relation of rotation angles (α, β) in XRD geometry and angles (φ, χ) in pole figure.	39
Figure 2.13 Schematic diagram showing (a) the typical geometry for an EBSD system, (b) the formation of Kikuchi lines.	40
Figure 3.1 the overall operational procedure of this experimental methodology to quantify FWL density and strength distribution.....	55
Figure 3.2 A self-aligning four-point bend fatigue testing rig and, the geometry and dimensions of a four-point bend sample.	56
Figure 3.3 S-N curves of the samples in all metallic materials (L-T, L-S and T-S of AA7075-T651, A713, AA2026 and AA2099) by four-point bend fatigue.	56
Figure 3.4 Crack population vs. applied maximum cyclic stress curves in L-T, L-S and T-S samples of the AA7075-T651 Al alloy.....	57
Figure 3.5 $\ln(-\ln(1-(N/N_0)))$ vs $\ln((\sigma/\sigma_0)-1)$ plots fitted by a Weibull function in L-T, L-S and T-S samples of AA7075-T651 Al alloy.....	57
Figure 3.6 Strength distributions of fatigue weak-links in L-T, L-S and T-S samples of the AA7075-T651 Al alloy.	58
Figure 3.7 Plots of crack population vs applied maximum cyclic stress of AA2026 Al alloy samples in 0% and 50% RH environments respectively.	59
Figure 3.8 Plots of $\ln(-\ln(1-N/N_0))$ vs. $\ln(\sigma/\sigma_0-1)$ fitted by a Weibull function in 0% RH and 50% RH for AA2026 Al alloy.....	59
Figure 3.9 Strength distributions of fatigue weak-links in 0% RH and 50% RH experimental environments for AA2026 Al alloy.	60
Figure 3.10 Fatigue crack initiated at constituent particle (a) in AA2026 L-T samples at 0% RH and maximum cyclic stress of 483.6 MPa. (b) in AA2099 L-T samples in 0% RH environment.	60

Figure 3.11 the porosity morphology in as-received A713 cast Al alloys with (a) low pore density and (b) high pore density.	60
Figure 3.12 Crack population vs applied maximum stress in A713 samples and normalized crack population vs stress could be fitted by Weibull function (black square spots).	61
Figure 3.13 (a) multiple fatigue crack initiation at pores on the sample surface, and (b) pores without fatigue cracks initiation during cyclic loading.	61
Figure 3.14 Fracture surface of the fatigued A713 sample.	62
Figure 3.15 Plots of crack population vs calibrated strain measured using strain gage in L-T samples of the AA7075-T651 Al alloy.	62
Figure 3.16 Calibrated strain distribution of fatigue weak-links in L-T samples of the AA7075-T651 Al alloy.	63
Figure 3.17 Plots of crack population vs applied maximum cyclic stress fitted by a series of sigmoidal functions in AA7075 L-T samples.	63
Figure 3.18 Residual plots of fitting results using top 3 best sigmoidal functions matching experimental data (larger adj. R-squares) in (a) AA7075 L-T, (b) T-S, (c) A713 and (d) AA2026 50% RH, respectively.	64
Figure 3.19 Crack population vs. applied maximum stress in AA2026 and AA2099 Al alloys, respectively.	65
Figure 3.20 Strength distributions of FWLs in AA2026 and AA2099, respectively.	65
Figure 3.21 Comparison of constituent particles density between (a) AA2026 and (b) AA2099.	66
Figure 4.1 The Grain structure of the AA7075-T651 Al alloy.	83
Figure 4.2 The geometry and orientation of the samples for four-point bend fatigue.	83
Figure 4.3 S-N curves of the samples on L-T, L-S and T-S planes of the AA7075-T651 Al alloy by four-point bend fatigue.	84

Figure 4.4 Plots of crack population vs. applied maximum cyclic stress in L-T, L-S and T-S samples of the AA7075-T651 Al alloy.....	84
Figure 4.5 (a) Single fatigue crack initiation at a low stress level, the maximum cyclic stress = 70% σ_y ; and (b) multiple crack nucleation at a higher stress level, the maximum cyclic stress = 100% σ_y , in L-S samples.....	85
Figure 4.6 $\ln\left(-\ln\left(1-\frac{N}{N_0}\right)\right)$ vs $\ln\left(\frac{\sigma}{\sigma_0}-1\right)$ plots fitted by a Weibull function in L-T, L-S and T-S samples.....	85
Figure 4.7 EDS spectra of the particles where fatigue cracks are initiated: (a) a pre-fractured Fe-containing particle on the L-T plane, and (b) a Si-bearing particle on the T-S plane in the AA7075 T651 Al alloy.	86
Figure 4.8 Strength distributions of fatigue weak-links in L-T, L-S and T-S samples of the AA 7075-T651 Al alloy.....	87
Figure 4.9 Constituent particles in a L-T sample: (a) before and (b) after fatigue tests; a L-S sample: (e) before and (f) after fatigue tests; and a T-S sample: (g) before and (h) after fatigue tests. (c) Pre-fractured Fe-containing particle which does not lead to fatigue crack initiation in L-T samples; (d) a fatigue crack initiated from a pre-fractured Fe-containing particle in the L-T sample; (i) fatigue cracks initiated at Si-bearing particles in the T-S sample, the cracks not necessarily initiated from coarser particles.....	88
Figure 4.10 Number density (mm ⁻²) and fraction of all types of constituent particles in L-T, L-S and T-S samples before fatigue tests.....	89
Figure 4.11 Number density (mm ⁻²) and fraction of all types of the fractured constituent particles in L-T, L-S and T-S samples after fatigue failure.....	89
Figure 4.12 The area distribution of Fe-containing particle, Si-bearing particle and Fe-containing particle with fatigue cracks on L-T surface.	90

Figure 5.1 Three types of typical fractured Fe-bearing particles after fatigue loading and corresponding cross-sections using FIB in L-T or L-S planes: (a) a Type-1 particle, (b) a Type-2 particle, (c) a Type-3 particle, (d-f) Cross-sections of the Type-1, 2 and 3 particles, respectively.....	108
Figure 5.2 Two types of fractured Si-bearing particles after fatigue loading and corresponding cross-sections using FIB in T-S plane: (a) a Type-1 particle, (b) a Type-3 particle, (c) and (d) Cross-sections of the Type-1 and 3, respectively.	109
Figure 5.3 SEM observation of a fracture surface showing a main fatigue crack initiated at a single Type-3 Fe-bearing particle in a L-S sample.....	109
Figure 5.4 SEM observation of a fracture surface showing the coalescence of fatigue cracks initiated at Type-3 Fe-bearing particles in a L-T sample.	110
Figure 5.5 The plots of area vs. length of Fe-bearing particles on the L-T or L-S sample surface	110
Figure 5.6 The plots of aspect ratio (length/width) vs. width of Fe-bearing particles on the L-T or L-S sample surface.....	110
Figure 5.7 The plots of aspect ratio (length/thickness) vs. thickness of Fe-bearing particles on the L-T or L-S sample in 3-D	111
Figure 5.8 The plots of area vs. length of Si-bearing particles on the T-S sample surface.....	111
Figure 5.9 The plots of aspect ratio (length/width) vs. width of Si-bearing particles on the T-S sample surface.....	112
Figure 5.10 The plots of aspect ratio (length/thickness) vs. thickness of Si-bearing particles on the T-S sample in 3-D.....	112
Figure 5.11 (a) the exceptional thin type-3 Fe-bearing in L-T plane and (b) the corresponding cross-section using FIB	113
Figure 5.12 (a) the exceptional thin type-3 Si-bearing particle in T-S plane and (b) the cross-section of the corresponding particle using FIB.....	113

Figure 5.13 {111} pole figure of the grains where type-1, -2 and -3 fractured Fe-bearing particles were located in L-T or L-S samples in AA7075	114
Figure 5.14 {111} pole figure of the grains where type-3 fractured Si-bearing particles were located in T-S samples in AA7075.....	115
Figure 5.15 The typical textures in aluminum alloy rolled plate.	116
Figure 5.16 The distribution of parent grains of type-3 fractured Fe- and Si-bearing particles, respectively.	116
Figure 5.17 (a) a type-3 Fe-bearing particle with a crack normal to loading direction in L-T sample and {111} plane surface trace; (b) orientation map of surrounding grain in terms of IPF using EBSD. Euler angle: 234.5 34.9 68.7	117
Figure 5.18 (a) a type-3 Si-bearing particle with a crack normal to loading direction in T-S sample and crack surface trace; (b) orientation map of surrounding grain in terms of IPF using EBSD. Euler angle (o): 113.2 39.7 71.3; 55.5 27.4 22.4	117
Figure 5.19 Short fatigue crack propagation behavior in an AA7075 T651 rolled plate: (a) a type-3 fractured Fe-bearing particles in L-T sample; (b) orientation map of surrounding grain in terms of IPF using EBSD (c) the cross-section of fatigue crack plane on the crack growth path using FIB. Euler angle (o): 63.3 37 89.4; (d) low-angle grain boundaries in grain in EBSD mapping.....	118
Figure 5.20 Topography of Fe- and Si-bearing particle on the mechanically polished surface using AFM: (a) optical micrograph, (b) extruded topography using AFM (c) depth profile compared to surface between two crossings along the selected linear path in (b) of Fe-bearing, (d) optical micrograph, (e) intruded topography using AFM, (f) depth profile compared to surface between two crossings along the selected linear path in (e) of Si-bearing particle. (Unit: nm).....	119
Figure 5.21 Comparison of Young's moduli and hardness of matrix, Fe- and Si-bearing particles in AA7075 T651 aluminum alloy	119
Figure 5.22 SEM micrographs of indentations in (a) sample matrix, (b) Fe-bearing particle, and (c) Si-bearing particle on mechanically polished surface.....	120

Figure 5.23 Nano-indentation measurements using CSM technique on AA7075 T651 matrix, Fe- and Si-bearing particles: (a) Young’s modulus-displacement curve, and (b) hardness-displacement curve..... 121

Figure 6.1 The schematic working procedure of fabricating micro-notches in selected grains using EBSD and FIB on T-S plane of AA2024 and AA7075: (a) the geometry and dimension of T-S four-point bend samples and grain microstructure on the tensile surface; (b) EBSD mapping distributed uniformly on tensile surface of T-S sample; (c) selection of grain for fabrication of micro-notch using FIB in EBSD mapping; (d) a SEM micrograph of a micro-notch fabricated by FIB. (note: for only illustrating the working procedure, the arbitrary microstructure, EBSD mapping and scale were chosen from 2024 and 7075, respectively.) 133

Figure 6.2 The designed rectangular geometry and the definitions of width, depth and thickness of micro-notches fabricated by FIB in 3-D in T-S samples. 134

Figure 6.3 The detailed dimensions of three batches of micro-notches fabricated by FIB on S-L projection plane highlighted by light blue in Figure 6.2 in T-S samples..... 134

Figure 6.4 The schematic diagram to illustrate the designed and actual dimensions of three batches of micro-notches fabricated by FIB in AA2024 T351 Al alloy, fatigue crack nucleation status from notches after fatigue loading: notches pointed by red arrows nucleated type-3 fatigue cracks, and those pointed by blue arrows nucleated type-2 fatigue cracks, remaining notches did not nucleated any cracks representing type-1 situation (red highlighted area: type-3 cracks; blue highlighted area: type-2 cracks; other area might represent the type-1 crack.)..... 137

Figure 6.5 The schematic diagram to illustrate the designed and actual dimensions of three batches of micro-notches fabricated by FIB in AA7075 T651 Al alloy, fatigue crack nucleation status from notches after fatigue loading: notches pointed by red arrows nucleated type-3 fatigue cracks, and those pointed by blue arrows nucleated type-2 fatigue cracks, remaining notches did not nucleated any cracks representing type-1 situation (red highlighted area: type-3 cracks; blue highlighted area: type-2 cracks; other area might represent the type-1 crack.)..... 138

Figure 6.6 constituent particle width distribution on L-T plane of AA7075. 138

Figure 6.7 a Type-2 fatigue crack initiated at #3-T3-4 micro-notch in AA2024: (a) a short crack extended into matrix and crack path was parallel to (111) trace on the surface; (b) the EBSD mapping of surrounding grains and the Euler angles of parent grain;(c) the cross-section by using FIB on the crack path as shown in (a) and the intersection between crack plane and cross-section surface (L-T) parallel to (111) trace indicating the twist angle at notch root is equal to 10.50; (d) a 3-D schematic to illustrate the twist angle at notch root. 139

Figure 6.8 a Type-3 fatigue crack initiated at #1-T3-1 micro-notch in AA2024: (a) a relatively long crack extended into matrix and was propagating in the matrix leading to the final failure, and all traces of {111} planes on the surface; (b) the EBSD mapping of surrounding grains and the Euler angles of parent grain..... 139

Figure 6.9 (a) The slip bands locating along the relatively long fatigue crack in 2024; (b) no slip bands were observed along long crack in 7075, conversely large strain deformed topography could be observed on polarized light mode using optical microscope. . 140

Figure 6.10 The twist angles and Schmid factors of four {111} planes normalized by the corresponding the maximum values in (a) Type-2 and (b) Type-3 cases in 2024, respectively. 140

Figure 6.11 (a) a Type-2 fatigue crack initiated at #3-T2-1 micro-notch and {111} plane traces on the surface in 7075; (b) a Type-3 fatigue crack initiated at #1-T3-2 micro-notch and the {111} plane traces in 7075; (c) the EBSD mapping around #3-T2-1 and the Euler angles of parent grain where #3-T2-1 was located; (d) the EBSD mapping around #1-T3-2 and the Euler angles of parent grain where #1-T3-2 was located..... 141

Chapter 1 Introduction

1.1 Background introduction to high cycle fatigue of high strength Al alloys

1.1.1 History of the research on fatigue

The word fatigue originated from the Latin expression *fatigue* which means “to tire”. In reality, this word was initially associated with physical and mental weariness in people, however, it has become a widely accepted terminology in engineering vocabulary for the damage and failure of materials under cyclic loading in the following decades. In the report entitled *General Principles for Fatigue Testing of Metals* published in 1964 by the International Organization for Standardization in Geneva, a descriptive definition of fatigue could be found and referred to as a term which “applies to changes in properties which can occur in a metallic material due to the repeated application of stresses or strains, although usually this term applies specially to those changes which lead to cracking or failure”. Fatigue failures occur in a variety of forms: mechanical fatigue induced by mere fluctuations in external applied stresses or strains; creep-fatigue under cyclic loading associated with high temperatures, and even thermomechanical fatigue when thermal and mechanical fatigue were combined together; corrosion fatigue under recurring loading imposed in the presence of a chemically aggressive or embrittling environment; plus, sliding and rolling contact fatigue in different contact mode. The fatigue failure can be attributed to one of the above fatigue process in metal or nonmetallic materials, nevertheless the majority of fatigue failure merely take place in metallic materials in the mechanical fatigue mode[1].

Fatigue failures in metallic structures are a well-known phenomenon [2]. Approximately over 75% of the failure problems in the engineering systems are due to fatigue damage each year [3]. The failures were already observed in the 19th century and at that time the first investigations on fatigue were carried out. A research study on fatigue was conducted by August Wohler, who recognized that a single load application, far below the static strength of structure, did not do any damage to the structure. However, if the relatively low load was repeated many times it could induce a complete failure [2]. This domain of cyclic loading is that for which the strain cycles are largely confined to the elastic range, meanwhile it is associated with lower loads and long lives or cycles, and is commonly referred to as high-cycle failure (HCF) [4]. Fatigue was considered to be an engineering problem until 1903 when Ewing and Hunfrey [5] carried out a

microscopic investigation which showed that fatigue crack nuclei occurred at slip bands in metallic materials. Until then, fatigue damage began to be taken into consideration as a serious materials failure problem.

As mentioned above, the fatigue failure phenomenon was first found as high-cycle fatigue (HCF). Theoretically, there are two types of metal fatigue failure. One is low-cycle fatigue (LCF) which is associated with macro-plastic deformation imparted in every load cycle, due to the high stress amplitudes, typically with the maximum applied stress being over the yield strength. The other type is high-cycle fatigue (HCF) which is more related to elastic behavior of the material on a macro scale, in which the stresses applied are just above the fatigue limit [2, 6]. In most practical cases, the applied stress level which is much lower than yield strength is above the fatigue limit. After a while of cyclic loading, the fatigue crack nucleation occurs as invisible microcracks in slip bands. After observation at microscopic scale on the growth of microcrack, it turns out that the initiation of microcracks occurs very early in the fatigue life and cover over 90% of the fatigue life under high-cycle fatigue condition. Obviously, it takes very short time for microcrack to propagate into the matrix and induces final failure. Such a potential risk is supposed to cause sudden and catastrophic tragedy if it is not taken into account very seriously. Despite of extensive research work done by engineers and scientists in the past decades, we still have a very long distance from quantitatively understanding these mechanisms for fatigue damage. Accordingly, the current study is still mainly focused on high-cycle fatigue (HCF), especially on fatigue crack initiation and early growth in the research field of metal fatigue.

In the mid-20th century [7], the emergence of theory of Linear Elastic Fracture Mechanics (LEFM) prompted the advent of Paris law which can satisfactorily quantify the growth rate of long cracks, and subsequently led to a good understanding of long crack behavior in last several decades. However, short fatigue cracks behave differently from long cracks. Short fatigue cracks are defined as three various aspects: first, their length is small compared to relevant microstructural dimensions (a continuum mechanics limitation); Second, their length is small compared to the scale of local plasticity (a linear elastic fracture mechanics limitation); lastly, they are simply physically small (e.g. 0.5-1.0 mm). Since all three types of short crack are known to propagate faster due to their growth being microstructure-sensitive, thus are far from quantitatively understood.

Since the short crack initiation and propagation cover a large fraction of the fatigue life under high-cycle fatigue (HCF), accordingly, quantifying the short crack growth behavior becomes meaningful but challenging topic in the research field of fatigue of materials.

Since the 1920s, aluminum alloys have been used in aircraft structural applications, because they possess a lower density, and are reasonably strong, durable, damage tolerant, and economical to fabricate, compared with steels. Studies on the fuselage skin and wing materials indicated that the combination of fracture toughness and resistance to growth of fatigue cracks could reduce the frequency of required inspections and save weight by minimizing the need for supporting structures [8]. Therefore, it is of both academic and industrial interests to study the fatigue behaviors of aluminum alloys.

1.1.2 Fatigue damage and crack initiation mechanism

Fatigue is a process of damage accumulation starting at the scale of the crystal lattice and ending up to the scale of structural component. The entire damage evolution process consists of cyclic slip, crack initiation, short crack growth, long crack growth and final failure, as shown in Figure 1.1 [9]. Generally, the first three phases, i.e. cyclic slip, crack initiation and short crack growth, are referred to as crack initiation period, and the long crack growth is defined as crack growth period. The fatigue life was also decomposed into the following multistages: incubation, nucleation, microstructurally small fatigue crack (MSFC) growth and long crack growth as addressed by McDowell et al [10-12] in which the stages prior to and including MSFC phase was analogous to crack initiation period accounting for up to 90% of total fatigue life [1, 13-15]. Obviously, the fatigue crack initiation plays a much more important role in the fatigue life of materials under high-cycle fatigue loading, supporting the significance of studying physical mechanisms being responsible for initiation and early propagation of short fatigue crack. The crack initiation is moreover readily affected by the materials surface conditions, as crack nucleation commonly takes place along the slip bands induced by local stress concentration or plastic deformation on surface or subsurface defects due to less materials constraint. Those stress or strain concentration can be attributed to a variety of microstructural inhomogeneities [15, 16], such as persistent slip bands (PSB), nonmetallic inclusions, second phase particles, pores and grain boundary or interface, etc.

Basically, regardless of what types of microstructures nucleating fatigue crack, the localized plastic deformation commonly takes place on the surface or subsurface under cyclic fatigue loading even below yield strength because the dislocation slip is less constrained by the surrounding matrix of materials near the surface and facilitate the formation of slip bands in those “soft-oriented” grains near the surface [17]. Subsequently, the slip bands are extruded out of the sample surface and meanwhile the slip step forms leading to irreversible extruding features [18, 19]. The slip irreversibility could be illustrated by two main mechanisms [20, 21]. Firstly, a thin oxide layer is formed on the fresh surface of slip steps in a non-vacuum environment, and this oxide layer cannot be removed from the slip step surface during next the reversed cycle of fatigue loading, consequently prevents the reversible slip. The second mechanism is that the strain hardening taking place in slip bands makes it difficult to fully reverse cyclic slip. As a result, extrusions and intrusions (Figure 1.2) may remain on the surface, i.e. the permanent slip band (PSB) forms on the sample surface, acting as the precursor of micro-crack imitation [22, 23]. Forsyth [24] reported thin ribbons of the metal (0.1 μm thick and 10 μm long) ‘extruded’ on the specimen surface from the PSBs in an Al-Cu alloy and acted as a micro-crack initiation site. Likewise, fatigue crack was nucleated along a slip band in pure Cu [24]. Cheng and Laird revealed that crack nucleation occurred preferentially at PSBs with the highest slip offset or the largest strain localization [25]. Metallographic observation showed that fatigue-induced surface changes corresponded to a period of cyclic strain adjustment in which slip saturation and micro-cracking occurred [26, 27]. Boyce [28] revealed that thickening of the oxide on the freshly formed surface of the PSBs was the mechanism for crack initiation. It has been also reported that protrusion can be responsible for fatigue crack initiation in some materials [22, 29]. It is a macro-PSB with several micrometers in height and tens of micrometers in width. A protrusion may contain several intrusions and extrusions and extend all the way through the cross-section of the specimen. In overall, PSBs are the nucleation sites of the fatigue cracks on the surface in many ductile materials.

Based on the dislocation pile-ups model either at second-phase particle or any other microstructural heterogeneities, many parameters were proposed to quantify fatigue crack nucleation driving force so as to evaluate the fatigue life. The effective shear stress was assumed to be constant within each grain and incorporated into Monte carlo

simulation by Chang and Morris et al [30, 31]. Tanaka and Mura also assumed that fatigue nucleation occurs when a critical strain density is attained [32-35]. With the development of computational mechanics, the localized deformation in the vicinity of fatigue crack nucleation sites was modeled by many researchers [36-38]: the maximum plastic shear strain amplitude associated with a modified Coffin-Manson model was used to assess the number of cycles for different fatigue stages, including incubation, nucleation, and early growth of short fatigue crack [37]. Several other 'fatigue indicator parameters' [12, 39, 40] were also developed to calculate the driving force for microstructural small fatigue crack, such as cyclic plastic shear strain accumulation or the Fatemi-Socie metric [41, 42]. The critical local driving stress for fatigue crack nucleation has been present, which is strongly dependent on the local microstructure and accumulated slip based on a continuum crystal plasticity model [14, 43].

1.1.3 Approaches to evaluate fatigue properties

Traditionally, two major approaches have been involved to characterize fatigue properties and predict fatigue life of materials: total-life approach and defect-tolerant approach. The total-life approach is also referred to as the S-N curve approach in which the number of cycles or evolution time to final fatigue failure in an initially assumed flawless specimen is estimated under controlled stress or strain amplitude. Under this circumstance, the fatigue life at a specific stress or strain level and fatigue strength could be ultimately estimated [1]. However, due to inherent microstructural defects in real engineering metallic materials, the data measured from S-N curves are often obtained with a large scatter, let alone used to evaluate multiple crack nucleation phenomenon that are more complex. On the contrary, the defect-tolerant approach assumes that all engineering metallic materials are inherently flawed. The pre-existing flaw is usually examined by non-destructive detection techniques, which indicates that the size of flaw is relatively large. If no pre-cracks are detected by the non-destructive testing device, the largest initial crack size will be estimated from the resolution of detection device. Afterwards, the total fatigue life is regarded as the number of cycles or time starting from the initial size to critical length of a dominant crack which is determined based on the fracture toughness of materials. The crack propagation time is calculated based on empirical crack growth laws applicable in linear elastic fracture mechanics. Nevertheless, the propagation period of crack only cover 10 - 20% of total fatigue life, while the crack initiation period could consume up to 90% of total fatigue life in high cyclic fatigue and

is more microstructurally sensitive, which make the prediction of fatigue life inaccurately and challenging [1]. More importantly, according to the previous literature review on fatigue crack nucleation behavior at various weak-links, it has been found that fatigue cracks do not have to nucleate at large size defects, such as pores [44, 45] and constituent particles [46-48]. In addition, without considering crack coalescence and other factors in multiple crack nucleation to accelerate materials fracture, the approach of defect-tolerant is too conservative to evaluate fatigue life of metallic materials thoroughly and accurately.

In order to understand the multi-site crack nucleation thoroughly and quantitatively with reducing large scatter in measuring fatigue life at a specific stress or strain level and taking into account effects of microstructures characteristics of metallic materials, Zhai et al. have recently developed an experimental method to characterize the multiple fatigue crack nucleation phenomenon by measuring the number of fatigue cracks at fatigued sample surface at different stress levels in metallic alloys, such as Al-Li alloys and Al-Zn cast alloys [45, 49]. The crack population was found to be a Weibull-type function of the applied stress, which allowed quantification of the weak-links density and strength distribution. The weak-link concept was proposed by Weibull in 1939 and could be defined as any possible fatigue crack initiation sites in this work [50]. The defined density and strength distribution of weak-links could be regarded as materials fatigue properties which are very useful information for metallic materials metallurgists and users to either design new alloy or conduct materials reliability analysis.

1.2 Microstructural factors influencing fatigue crack initiation

1.2.1 Second-phase particle or inclusion

In high strength aluminum alloys (such as 2xxx and 7xxx series), there are generally two types of insoluble constituent particles, one is Fe-containing particles and the other Si-bearing particles [46, 47, 51, 52]. They are formed by eutectic reaction during solidification, and often the preferred fatigue crack initiation sites. The stoichiometric composition of the Fe-containing particles may vary slightly from one alloy to another due to change in alloying elements in Al alloys, such as $\text{Al}_7\text{Cu}_2\text{Fe}$ and $\text{Al}_{23}\text{CuFe}_4$, whereas Si-bearing particles are commonly assumed as Mg_2Si [47, 48, 52, 53]. Very often the Fe-containing phase may also contain some Si, possibly due to often the co-existence of the two types of phases. Since 1970s, it has been recognized that fatigue

crack nucleation prefers to occur at the brittle coarse Fe-containing particles in the surface region that are fractured during prior deformation processing, such as rolling, extrusion and forging, etc., in commercial high strength aluminum alloys, such as 2219, 2024, 2124 and 7075, etc. [30, 54-59]. Zabett observed that fatigue cracks were preferably initiated at the prior-fractured $\text{Al}_7\text{Cu}_2\text{Fe}$ second phase particles when loaded in the L direction (i.e., the rolling direction), whereas, in the T (long transverse) and S (short transverse) directions, cracks were formed at the localized slip bands within the largest available surface grains in the as-received AA2024 T351 plate [59]. The anisotropy of the fatigue crack nucleation behaviors was studied by Debartolo who found that cracks were formed primarily at single constituent particles or associated with pores on the L-S and S-T planes, and that the aligned particle clusters could contribute to the coalescence of cracks along the growth direction on the L-T plane, in 2024 T3 Al alloys [60]. The study of AA7010 aluminum alloys by Patton showed that cracks were preferentially initiated at the prior-fractured second phase particles located in grains with a r-cube orientation [52].

Intermetallic particles are the most common sites for initiation of short cracks [26, 56, 60-63] which could be due to either the cracking of the particle itself or fracture of the particle-matrix interface. According to the direct observation of particle cracking in a 7075 Al alloy, it appears that fracture occurs suddenly [64]. The failure showed as cleavage fracture with the river patterns on the fracture surface. Particle failure induced by cleavage is the result of an excessive critical tensile stress. Referring to research done by Goodier, it is indicated that the tensile stress across spherical particles might be twice as the principal stress σ_1 if the particle had infinite stiffness [65]. Patton and co-workers [52] found that a majority of cracks in 7010 Al alloys initiated at $\text{Al}_7\text{Cu}_2\text{Fe}$ and Mg_2Si intermetallic particles. The Young's modulus and hardness of these two kinds of particles were measured by using a nanoindentation technique [66]. The mean Young's modulus of $\text{Al}_7\text{Cu}_2\text{Fe}$ is 150 GPa, which is twice that of the matrix, and 97 GPa for Mg_2Si . This is consistent with the observation by Van [64] that the crack springs open widely through the particle after particle failure. Before fracture induced by stress concentration, due to elastic modulus discontinuity, the particles have undergone elastic deformation. By taking into account the effect of large particles on the fracture toughness, a model was developed by Van [64] to show the relation between K_{IC} and the particle population, $K_{IC} = C \lambda^{1/2} f^{-1/6m}$, where C and m are material constants, λ is taken

as the average particle distance and f is the particle volume fraction. K_{IC} is the critical stress intensity factor of mode I, in which the crack facets separate in a direction normal to the plane of crack. K_{IC} calculated by this equation is in a reasonably good agreement with the results measured experimentally in 7010 Al alloys. Similar investigations have been done on 7050 Al alloys by Gürbüz et al [67]. The shape-irregular particles of Al_7Cu_2Fe were found to be easily fractured with no evidence of plastic deformation. Spherical particles Mg_2Si are not fractured and can decelerate fatigue crack growth either by causing cracks branching or increasing the crack growth path as the crack propagates around these particles. Another type of less abundant particles, $CuAl_2Mg$, could also retard the fatigue crack growth in the same manner as Mg_2Si particles. There are some common features in fatigue crack initiation in 2024 Al alloys compared with 7xxx Al-alloys. Most of the cracks initiated at Al_7Cu_2Fe (also be termed as β -phase by Suresh [68] and Sigler [26]) particles [69] in the 2024 alloys. At a relatively high cyclic stress amplitude, such as 95% yield strength, a crack can also initiate at a $CuAl_2Mg$ (s -phase) particle [26]. No fatigue cracks emanating from broken particles were observed on the surface that is parallel to T and S directions [69]. In these two orientations, the longitudinal direction of the second phase particles is perpendicular to the loading axis, thus having the minimum stress concentration effect on the crack initiation process. Consequently, second phase particles may not be involved in fatigue crack initiation for cyclic loads perpendicular to the rolling direction, unlike the case where the applied stress is parallel to the rolling direction [70]. Fatigue damage started in the matrix itself have been observed by Haworth et al [26, 27]. In 2024 Aluminum alloy, it was found that matrix cracks are not generally associated with particularly intense area of slip. In these overaged materials, non-shearable precipitate particles were expected to cause cross-slip or dislocation tangling, leading to relatively homogeneous deformation without forming coarse slip bands. Concentrated slip is therefore unlikely to initiate cracks in slip bands. It is possible that the matrix cracks are associated with local stress raisers (such as constituent particles) that lie beneath the metal surface.

A comprehensive study of AA7075 T651 Al alloys has revealed that fractured particles under cyclic loading are almost all Fe-bearing particles, and that only about 3% of the particles could result in fatigue crack initiation, whereas Mg_2Si constituent particles are not effective crack initiation sites [47, 48]. The reason why Fe-containing particles become the preferred crack initiation sites is likely to be associated with their brittleness,

as revealed in hardness and modulus measurement using nano-indentation in the Al alloys [53, 71]. The sizes of the critical particles that lead to fatigue damage range from 2.3 μm to 200 μm in diameter, indicating that fatigue cracks are not necessarily nucleated at larger particles on the surface of the alloys [47, 48]. It has recently been demonstrated by the authors that the particle thickness is the key factor controlling the driving force of fatigue crack initiation at particles, as revealed by cross-sectioning the fractured particles using FIB (Focused Ion Beam) [72]. It has also been found that Fe-containing particles are responsible for fatigue crack initiation on L-T (L and T are the rolling and transverse directions, respectively) and L-S (S is the normal of the rolling plane) planes, but Si-bearing particles become the predominant crack nucleation sites on the T-S plane in AA7075 T651 Al alloys [46]. This is likely to be attributed to the Si-bearing particles being slightly tougher than the Fe-containing particles, thereby remain less damaged during the prior deformation processing. Fatigue crack nucleation at constituent particles is still not thoroughly understood, depending on materials microstructure (including grain size and orientation), loading condition, and particle size, geometry and properties, etc.

Meanwhile, inclusions inevitably exist in aluminum alloys, steels and other type alloys in form of oxides or sulphides of corresponding metal as defects initiating microcrack to reduce toughness and fatigue resistance of materials [73]. In case of other metallic alloys such as steel and nickel-base alloy, Al_2O_3 , MnS, SiO_2 and HfO_2 are the most frequent inclusion [15, 74], whereas the typical oxides in aluminum alloys are Al_2O_3 , MgO and sometimes MgAl_2O_4 [51]. For commercial aluminum alloys, aside from intermetallic or constituent particles regarded as weak-links for fatigue crack initiation, those types of inclusions mentioned above are also common fatigue crack initiation sites [75-78]. The same phenomenon was observed in steels: the non-metallic inclusions or small oxide particles are predominant crack initiation sites located at the surface or subsurface of specimens [79-84]. Base on observation of fracture surface, there was a dark area in the vicinity of an inclusion at the fracture origin that seemed like a fish-eye mark where a rough surface different from normal fracture surface and associated with martensite lath structure could be examined. Hydrogen embrittlement coupled with fatigue probably contributed to this phenomenon [79, 80]. The fatigue crack nucleation at inclusion perfectly bonded, partially debonded and cracked with matrix were studied by Prasannavenkatesan in martensitic gear steels, respectively. In nickel-base superalloy,

in low cyclic fatigue (LCF) cases, particularly at elevated temperature, the crack initiation was associated with a large pre-existing inclusion, such as hafnium oxide and ceramic inclusion due to use of crucibles [74, 85-87]. Besides, for ultra-fine grained Inconel 718 alloy, crack initiation also preferentially occurred at NbC and TiN particle in the low cyclic fatigue (LCF) [88]. In high cyclic fatigue (HCF) cases, the fatigue crack initiation usually occurred at large casting inclusion followed by non-crystallographic crack propagation in cast Ni-based superalloy. The fatigue crack nucleation behaviors were also influenced by R ratio: for $R = 0.8$, inclusions played a dominant role on crack nucleation; however the role of inclusions was hidden by the role of porosities when R ratio was equal to -1 or 0 [89, 90].

1.2.2 Grain boundary or interface

Grain boundaries (GBs) can be one of the factors influencing fatigue crack initiation in aluminum alloy. In general, crack initiation is associated with two types of GBs, one is the GBs normal to the loading axis and another is the GBs with precipitation free zone (PFZ). The normal GBs are barriers to the movement of dislocations and cyclic deformation in the engineering materials. Stress concentration and microvoid growth at large GB precipitates could cause crack initiation. Results by Sigler showed that crack initiation at grain boundaries was limited primarily to high stress amplitudes in 2024 Al alloy [26]. The grain boundary crack density is very low in the early stage of the fatigue life at a low stress level, but at a high stress level it increases dramatically with increasing the number of cycles. One inferred that, only at high applied stresses, the local strain caused by irreversible slip sufficiently could open up cracks along the grain boundaries. Srivatsan [63] indicated that the preferential plastic deformation throughout the favorably oriented grains resulted in a highly localized stress concentration at locations of grain boundary triple junctions, with concomitant early nucleation of microcracks. It is assumed that the grain boundaries are stress concentration sites compared with the matrix and promote preferential plastic deformation. A large number of studies showed that some of the GB fractures had relationship with precipitation free zone (PFZ) along GB [62, 63, 91-93]. In the age-hardenable aluminum alloys, the existence of a PFZ is due to the formation of equilibrium second phase at GBs, which consume supersaturated solute atoms in the vicinity of these GBs. As a result, there are no metastable hardening precipitates forming in the region which becomes a weak-link in fatigue damage. Vasudevan et al. [93] offered some ideas to explain the PFZ fracture

based on the published studies and their research on an Al-Li alloy. Their explanation included (1) strain localization in the soft precipitate free zones and (2) the influence of matrix precipitate shear giving rise to inhomogeneous planar slip that may apply large stress concentrations to the GB at the end of slip bands. This type of GB crack initiation can be prevented by inhibiting the formation of PFZ at GBs.

Occasionally, the interface between second phase particles or inclusions and matrix becomes a source for fatigue crack initiation, which has been observed in 2024-T4, 2219-T851, and 2524-T34, etc. [26, 70, 76, 77, 94], particularly in high-humidity which could weaken the bonding between particles and the matrix [70]. Grain boundaries (GBs) could also be regarded as weak-links for fatigue crack nucleation, due to: 1) micro-voids formed at large GB precipitates [95]; 2) strain/stress concentration in the precipitate free zone (PFZ) along GBs; and 3) stress/strain concentration due to inhomogeneous planar slip induced by precipitate shearing in the matrix in these precipitation hardened alloys. These explanations were supported by experimental results of fatigue test in Al-Li alloy, in which studies of surface slip lines suggested that slip was initiated at the large GB δ precipitates [93], meanwhile zhai also found that trace elements such as Na and K could also weaken GBs, leading to fatigue crack initiation at GBs, like in an Al-Li alloy where cracks are initiated predominantly along the planar grain boundaries of the pancake-shaped gains when cyclically loaded along S direction [49]. It was also found that in Ni-based alloys that fatigue crack initiation may occur at the grain boundaries of coarse grains and depended on the orientation of these coarse grains where intergranular crack nucleation would occur, when GB were 45 to 60 degree to the loading direction [96].

There is enough evidence showing that growth of microstructural fatigue small cracks is impeded by the presence of grain boundaries [97-99]. The majority of secondary cracks have been observed with their tips at grain boundary in Al-Li alloy. It is found that when the tips of these cracks reach the same grain boundary, some crack tips can cross one or two grains before arresting. This indicates that some grain boundaries offer much more resistance to the crack propagation than do others. The effect of GBs on crack propagation was also proved by Sarioglu et al [92]. The crack propagation rate was measured in the samples with different orientations, namely, L-T, T-L and 60° to the rolling direction in a 2024 Al alloy at different aging time. The lack of difference in fatigue crack propagation rates in these three orientations was explained by the change

of slip characteristics of the alloy after aging. For the under-aged condition, the slip length was determined by the grain size. The formation of large plastically deformed zone leads to crack arrest until a new crack is formed at slip steps in the nearest neighboring grain. After over-aging, slip length was determined by the inter-particle spacing. The grain boundary effect does not occur in the homogeneously deformed over-aged alloy. Based on micro-plasticity and crack closure effects, Taira et al. considered that the growth of microstructurally small cracks was impeded by grain boundaries in terms of the pinning slip bands emanating from the crack tip. The experimental results by Lankford [98] indicated that the minimum crack growth rate corresponded to a crack length roughly equal to the smallest grain dimension. When the misorientation between the grain containing the crack and the neighboring grain is relatively low, there will be a deceleration in the growth rates at the boundary [68]. In high-cycle fatigue many cracks never grow beyond the first grain, and any cracks that grow beyond the microstructural sizes may rapidly cause failure. The crack growth retardation at a GB triple junction was noticed by several investigators [93]. The continued growth of the retarded cracks takes place in a transgranular manner after an increase in stress range. Zhai et al. [99, 100] investigated the short crack growth in Al-Li alloys and Al-Cu alloys, and subsequently proposed a 3-D crystallographic model (Figure 1.3) to account for the variation of crack growth rate and crack deflection due to GB resistance. Since a short fatigue crack normally propagate along the favored slip plane within a grain in many metallic materials, crystallographic orientation changes across a GB can result in crack plane tilt and twist (Figure 1.3). The twist angle, $\alpha = |\psi_1 - \psi_2|$, being the angle between the two intersecting lines (ab and ac) of the two favored slip planes on the GB plane, represents the major resistance to crack propagation from one grain to another since the wedge shaped area (abc) described by α on the GB plane has to be fractured for the crack to pass through the GB. The tilt angle, $\beta = |\theta_2 - \theta_1|$, being the angle between the intersection lines of the two favored slip planes on the sample surface, can also contribute to the resistance to crack growth by reducing the driving force at the crack tip. For a short crack to pass across a GB from grain 1 into grain 2, the crack plane prefers to propagate onto the slip plane which offers the minimum α angle and relatively small β angle among four slip planes in grain 2.

1.2.3 Porosity and void

In cast aluminum alloys, porosities could become the predominant fatigue crack initiation sites [51]. Two types of pores are usually observed in the cast alloys: shrinkage pores, which are formed due to lack of interdendritic feeding during solidification, are more like microcracks often with sharp corners in their shapes to affect fatigue properties more adversely; whereas gas pores mainly formed due to hydrogen in the molten metal are usually spherical in shape, less detrimental to the fatigue properties than the shrinkage pores [51, 101]. In aluminum cast alloys, such as B319, A356 and E319, fatigue cracks are predominantly initiated at shrinkage pores with sharp radii regardless of the loading direction [102, 103]. Although fatigue cracks are generally initiated at large pores [104, 105], the size distribution of the pores could not be directly used to evaluate the fatigue crack initiation behaviors in the alloys [45]. Based on the calculation of stress field around a pore using finite element model, it was found that the pore depth beneath sample surface was the key factor to control the stress concentration, the maximum stress of which was increased sharply when the pore was just buried beneath the surface [44, 105-107]. Likewise, Fan and McDowell found that when large-scale shrinkage porosity was controlled, the initiation sites were often the larger Si particles within eutectic regions in A356 T6. Owing to local microstructure-induced plastic shear straining/slip intensification, fatigue cracks were nucleated at intersections of silicon particle clusters and debonded particles as well [105, 108]. In a super vacuum die cast Mg alloy, Wen et. al. observed that fatigue cracks were initiated at crack-like defects which were consisted of micro-pores formed in the surface [109]. In steels, porosities could lead to fatigue cracks in competition with inclusions, particularly when the R ratio is equal to zero or -1 [81, 82]. In comparison with steels, when R is equal to zero or -1 in high-cycle or gigacycle fatigue tests of cast nickel-based alloys, the porosity was dominant as a crack nucleation site [89, 90]. Pores in metals and alloys are as microcavities mostly a consequence of material shrinkage during the casting and solidification process, and can be basically considered as existing microcracks [110]. This is in particular the case when their size falls within the dimension of the most characteristic microstructural feature of the material, for example, the grain size or the phase distribution in two- or multi-phase materials. An example is the fatigue damage process of magnesium alloys, where cracks typically emanate from pores formed during dendritic solidification. In Stanzltschegg's study[111], the influence of microporosity on fatigue crack initiation in AlSi₇Mg cast alloy has been

investigated at very high numbers of cycles. The results showed that casting pores predominantly influence the number of cycles to crack initiation. For in-service loading conditions, the detrimental effect of microporosity on crack formation cannot be adequately predicted on the basis of linear damage calculation, because of premature crack initiation during high loads of the random sequence. Pang et al [112] proposed an assessment of the effects of microstructure on both crack initiation and propagation of short fatigue cracks in nickel-base turbine disc alloys. Comparisons of the performance of the different microstructures revealed that initiation occurred predominantly at pores at both temperatures. In Chan's research [73], fatigue crack initiation at defects such as pores, inclusions, and machined marks can lead to $S-N_f$ curves with no, one, or double fatigue limits, depending on the defect (pore, inclusion, or machine mark) size distribution.

Another type of potential crack initiation sites is void. The voids are not produced during fatigue but occur during prior processing when a large particle is broken into fragment [26]. The voids serve as initiators of internal penny-shaped fatigue cracks that grow to a visible size before they reach the surface or merge with a dominant crack [113]. The effect of particles and voids on crack growth might not be ignored. Debartolo et al. [60] found that the interaction between the crack tip and neighboring particles depended on the state of the constituent particles. When particles were well bonded with the matrix, the cracks tended to deviate from straight paths to avoid the particles, effectively slowing crack growth. When particles were cracked or debonded, fatigue cracks tended to grow through them, effectively speeding up crack growth. Srivatsan et al [63] considered the voids as being equivalent to second-phase particles having 'zero' stiffness. The local strain rate was greater for voids than for the matrix in the study of 2524 Al-alloy. This facilitated a gradual increase of both the size and relative volume fraction of voids during fatigue. The finer microscopic voids coalesced to form void sheets that were developed into the macroscopic voids randomly distributed through the alloy microstructure. The similar formation of void sheets was also found in the ductile fracture of 5754 Al-alloy [114].

1.2.4 Persistent slip bands

Persistent slip bands (PSBs) is generally recognized as a pre-requisite for the formation of fatigue cracks in pure crystals as well as alloys, especially those ductile alloys. The

detailed elucidation with regard to PSB has been introduced in previous fatigue crack nucleation mechanism. Here, some cases the crack initiated from PSB in aluminum alloys will be described. Studies on T and S directions of a 2024 Al-alloy by Zabett [69] showed that large surface grains were the potential sites for crack initiation because of the ease of the formation of PSB, extrusions and microcracks, when no pre-existing defects such as cracked particles were present. Reports from Polak and co-workers [115] indicated that in 1421 and 1450 Al-Li alloy extrusion, fatigue cracks also started from the slip bands and it was the size of grains that determined the size of the initiated crack. The cracks initiated from slip bands have the lowest growth rate.

1.3 Other factors influencing fatigue crack initiation

1.3.1 Geometry of grain and crack

It is not surprising that crack depth will affect short crack propagation. When crack depth is less than a critical value, crack growth behavior has been found to be highly dependent upon the microstructure [69]. Miller postulated an initially low nominal threshold strain range for microstructurally short cracks and that the stress range would increase due to the presence of microstructural barriers as crack depth increases. In the model for fatigue limit prediction given by Abdel-Raouf [116], the variation of the effective stress intensity parameter is the function of crack depth. The local stress intensity of a 2024 Al-alloy is a maximum at the crack depth approximately half a grain diameter and minimum at the depth slightly in excess of three grain diameters. In Wei's research[72], cross-section using FIB revealed that 3-D geometry of particle, especially the thickness of fractured particles, was the key factor controlling the driving force for short fatigue crack initiation.

1.3.2 Effects of micro-texture on crack initiation

Feng with his coworkers studied the effects of local grain orientations on crack initiation [117]. It was found that with the increasing of texture sharpness crack initiation might be promoted, because effective slip distances were increased beyond individual grain dimensions. Fatigue cracks preferred to be initiated in soft grains (i.e. with high Schmid factor) in polycrystalline materials. Mineur, M. et al. did work on the influence of the crystalline texture on the fatigue behavior of a 316L austenitic stainless steel [118]. Electron backscatter diffraction technique (EBSD) was utilized to measure the crystallographic texture of each selected damage zone. The analysis results indicated

that a strong effect of texture on the crack initiation. Additionally, hard grains with relatively small Schmid factor with crystalline direction close to $\langle 111 \rangle$ directions were observed to be associated with very small crack densities, while soft grains with direction close to $\langle 110 \rangle$ directions possessed high crack densities. Taylor et al. have studied the effect of grain orientations on the initiation of fatigue damage in an Al-Li 8090 alloy. [119]. It was found that the grains with a high Schmid factor were plastically softer and more likely to be the preferential sites for the initiation of fatigue cracks. Cracks initiation would mainly take place in grains with $\langle 100 \rangle$ parallel with the load axis. Fatigue cracking along $\{111\}$ was suggested for AA8090 Al-Li-based alloy in vacuum and moist air [119, 120]. The EBSD results showed that fatigue crack propagation (FCP) in vacuum progressed by micro cracking, approximately parallel to $\{111\}$, for over 80% of the facets analyzed in the recrystallized-coarse and unrecrystallized microstructure [120]. It is worth mentioning that small (0.5-1 μm height) steps were present on some facets. Fatigue facets parallel to $\{111\}$ were also reported in the study of an unrecrystallized Al alloy plate with the copper-type texture in vacuum test condition [121]. A similar result was observed for a Goss-oriented grain in recrystallized sheet, as well as in recrystallized grains with more random orientations. Patton et al. studied on fatigue damage in 7010 aluminum alloy [52], and the crystallographic orientations of grains around short cracks were measured using EBSD in 7010 Al alloys. The 12 Schmid factors from computing indicated that the crack propagated in the crystal plane with the highest Schmid factor. The test also showed that the crack induced by intermetallic rupture initiated at grains with twisted cube texture with respect to the tensile axis more possibly. It corresponded to the grain orientation for which the two highest Schmid factors were comparable and relatively large in the grains. Wu et al. studied on a 8090 Al-Li alloy plate [122]. The research result indicated that the directionality of the fatigue fracture behavior corresponded to the strong $\{110\}\langle 112 \rangle$ texture. A mechanistic model was developed for transgranular fatigue-crack growth in this highly textural material. The material texture was shown to strongly influence the crack growth rate. The effect of texture on fatigue crack growth rate (FCGR) was related via a geometric factor $\cos 2\phi$, where ϕ defined as the angle between the load axis and the normal of the favorable slip plane. The effect of specimen orientation on FCGR in this Al-Li alloy was shown to be related to a combination of its anisotropic mechanical properties and the variation of angle ϕ with specimen orientation. The model further predicts that fatigue-crack growth rates will be slower in many textural materials

than texture-free materials because $\varphi > 0$ and $\cos^2 \varphi < 1$. For a short crack, the low level of constraint on cyclic slip promoted crack growth in a predominantly crystallographic mode, leading to a straight path of the crack on the surface [62, 68]. When the crack tip reached a grain boundary, it tended to reorient itself in the adjacent grain to advance by the localized shear mechanism. The extent of deflection at the grain boundary was a function of the relative orientations of the most favorable slip systems in the adjacent crystals.

As for the propagation path of crack propagation at the point of reaching a grain boundary, A 3-D crystallographic model was proposed by Dr. Zhai, which introduced twist and tilt angles of crack plane deflection at grain boundary as the key variables controlling the path and growth rate of a short crack [99]. In this model, the twist and tilt of crack plane at a grain boundary were defined as the main resistance of crack propagation. A large twist angle can severely retard the crack growth and even arrest the short crack. It can be seen from Figure 1.3: the twist angle, $\alpha = |\psi_1 - \psi_2|$, being the angle between the two intersecting lines (ab and ac) of the two favored slip planes on the GB plane, represented the major resistance to crack propagation from one grain to another since the wedge shaped area (abc) described by α on the GB plane has to be fractured for the crack to pass through the GB. The tilt angle, $\beta = |\theta_2 - \theta_1|$, being the angle between the intersection lines of the two favored slip planes on the sample surface, can also contribute to the resistance to crack growth by reducing the driving force at the crack tip. What is more, through mapping of twist angle in Euler space (Figure 1.4) in grains around short crack an optimum twist angle in a certain texture could be determined [100]. In this 8090 Al-Li aluminum alloy studied, it showed that Goss grains (16.9% 5 degree) were more resistant to crack growth than brass grains (20.3% 5 degree).

In the study of a 2024 Al alloy in T351 temper, Zabett et al. [69] found that, compared with the transverse (T) and short-transverse (S) directions, specimens in the longitudinal (L) direction have the shortest fatigue life under the same normalized stress amplitude of $0.45 \sigma_{TS}$. Morris et al. [70] observed the same phenomenon in 2219 Al-alloy with T851 temper. Their observations led them to conclude that early particle cracking and coalescence of microcracks reduced the life of these specimens in the longitudinal direction. Gregory et al. have studied the crack propagation behavior in a highly textured 7475 material. They observed a marked enhancement in GB arresting crack in an L+45°

direction compared to the L direction [123]. The crack arrest was linked to the presence of two orientation variables in the underlying brass texture and the different Schmid factors experienced by each variable for the two testing orientations. Chen found that the effect of the specimen orientation on the cracking characteristics can also be associated with the presence of the texture and the relevant variation in strength [124]. The fatigue strength in the transverse direction was greater than that in the longitudinal direction because of the existence of texture in an Al-Li alloy.

1.4 Rationale and purpose of the study

Given that there has not been a desirable experimental method to evaluate multi-site fatigue crack nucleation behavior thoroughly and quantitatively in high strength aluminum alloys, a new experimental methodology need to be developed and improved to quantify the multi-site fatigue crack nucleation by characterizing new defined fatigue properties of materials, i.e., fatigue weak-link (FWL) density and strength distribution, which are applicable in a range of high strength aluminum alloys to study as many factors as possible influencing the nucleation behavior, particularly microstructural heterogeneities that are dominant contributors to multi-site fatigue crack nucleation behavior in high strength aluminum alloys. To fully understand the effects of those microstructural heterogeneities, especially constituent particles in wrought 2000 and 7000 series of aluminum alloys, on the fatigue crack nucleation behavior in 3-D, some essential advanced characterization methods need to be introduced to reveal all the relevant 3-D geometrical features and microstructure of those particles which are virtually detrimental to fatigue crack nucleation.

Since the ultimate purpose of the research is to develop a 3-D microstructural-based model for simulation of the fatigue crack nucleation behavior and quantification of FWL density and strength distribution in high strength aluminum alloys so as to assess and predict fatigue life of alloys more accurately and scientifically, a transition phase between experimental phenomena and numerical simulation is supposed to be filled to simplify the procedure of building model with more fundamental and reliable actual data. Consequently, designing a simplified and concrete method to verify actual nucleation behavior become essential. A series of rectangular micro-notches with different dimensions were thus fabricated using FIB to mimic fractured particles in these two representative alloys (2024 and 7075) aiming at providing our model with more concrete

and direct experimental information by considering driving force and resistance of fatigue crack nucleation.

1.5 Key results obtained

During the development and improvement of the experimental method to quantify multi-site fatigue crack nucleation, the three parameter Weibull-type function was firstly verified to be the more appropriate one to describe the relation of FWLs with the applied maximum cyclic stress or strain in high strength aluminum alloys among all the sigmoidal functions. In this method, the effects of environment, types of microstructural heterogeneities and loading direction on FWLs were all studied in detail in AA7075 T651, AA2026 T3511, A713 alloys, etc.

When applied in investigating the anisotropic multi-site fatigue crack nucleation in 7075, the experimental technique demonstrated advantages over the traditional S-N curve method to evaluate the fatigue crack initiation behavior. It could quantitatively characterize the FWL density and strength distribution, showing a strong anisotropy of FWLs in the alloy with the highest weak-link density (15 mm^{-2}) on the L-S plane and lowest (4 mm^{-2}) on the T-S plane. The weak-link density on the L-T plane was 11 mm^{-2} . Fatigue cracks were predominantly initiated at Fe-containing particles on the L-T and L-S planes, but only at Si-bearing particles on the T-S plane in the AA 7075-T651 aluminum alloy. The pre-fractured or pre-damaged Fe-containing particles were responsible for fatigue crack initiation at Fe-containing particles on the L-T and L-S planes in the alloy.

Based on the investigation of effects of constituent particles on multi-site fatigue crack nucleation behavior in 3-D in 7075 using FIB combined with EBSD, AFM and Nano-indentation, it was found that in L-T and L-S planes, the thicker and pre-cracked Fe-containing particles were the predominant sites for fatigue crack nucleation; In T-S plane, the thicker and debonded Si-bearing particles associated with pores were more likely to nucleate propagating cracks, which was convinced by the Nano-indentation measurement. Fatigue cracks did not perfectly follow the primary slip planes, i.e. $\{111\}$ planes, and sometimes propagated approximately normal to loading direction; the more detrimental Fe- and Si-particles initiating Type-3 fatigue cracks were not preferentially located in a certain oriented grain.

Finally, three batches of micro-notches with different dimensions were fabricated in selected grains of T-S samples in AA2024-T351 and AA7075-T651 aluminum alloys using FIB to mimic fractured particles. After fatigue loading, the wider and deeper micro-notches became the fatigue cracks initiation sites more easily. In AA2024-T351 samples, cracks preferred to propagate in the $\{111\}$ slip planes with smallest twist angle and relatively large Schmid factor. In AA7075-T651 samples, cracks did not follow the crystallographic slip planes perfectly. Based on these experimental data, a 3-D quantitative model could be eventually developed to simulate fatigue crack initiation by taking into consideration driving force and resistance to short crack growth.

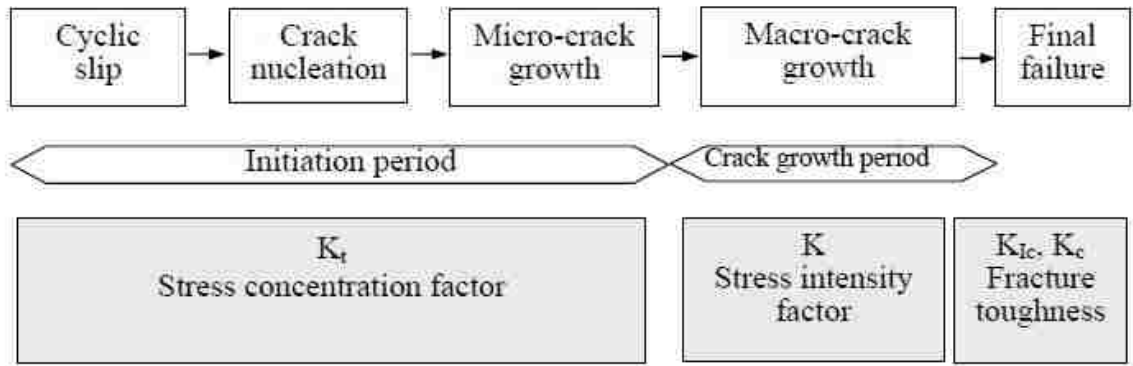


Figure 1.1 Different phases of the fatigue life and relevant factors.

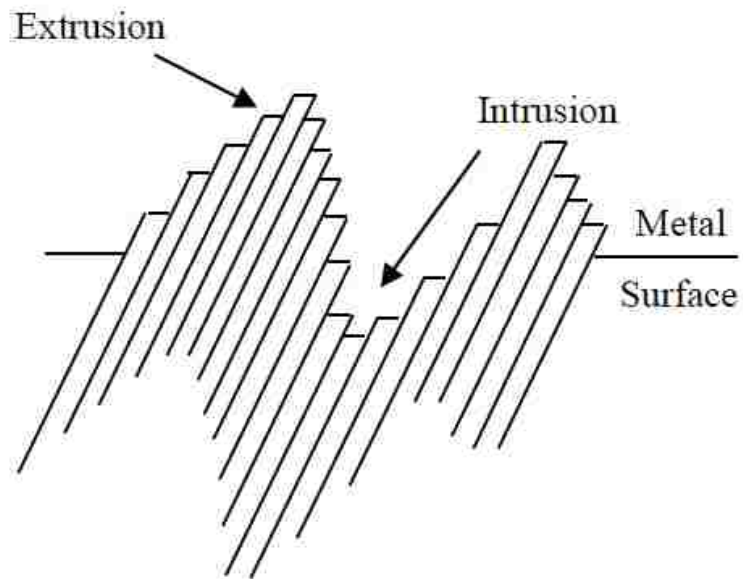


Figure 1.2 Sketch diagram showing the geometry of slip at the materials surface according to Forsyth [24]

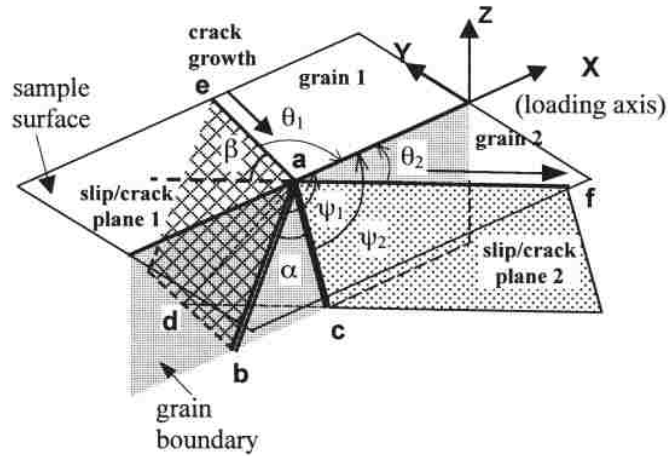


Figure 1.3 Schematic diagram showing a crystallographic mechanism for crack growth along slip 1 in grain 1 onto slip plane 2 in grain 2. The crack growth is controlled by α and β .

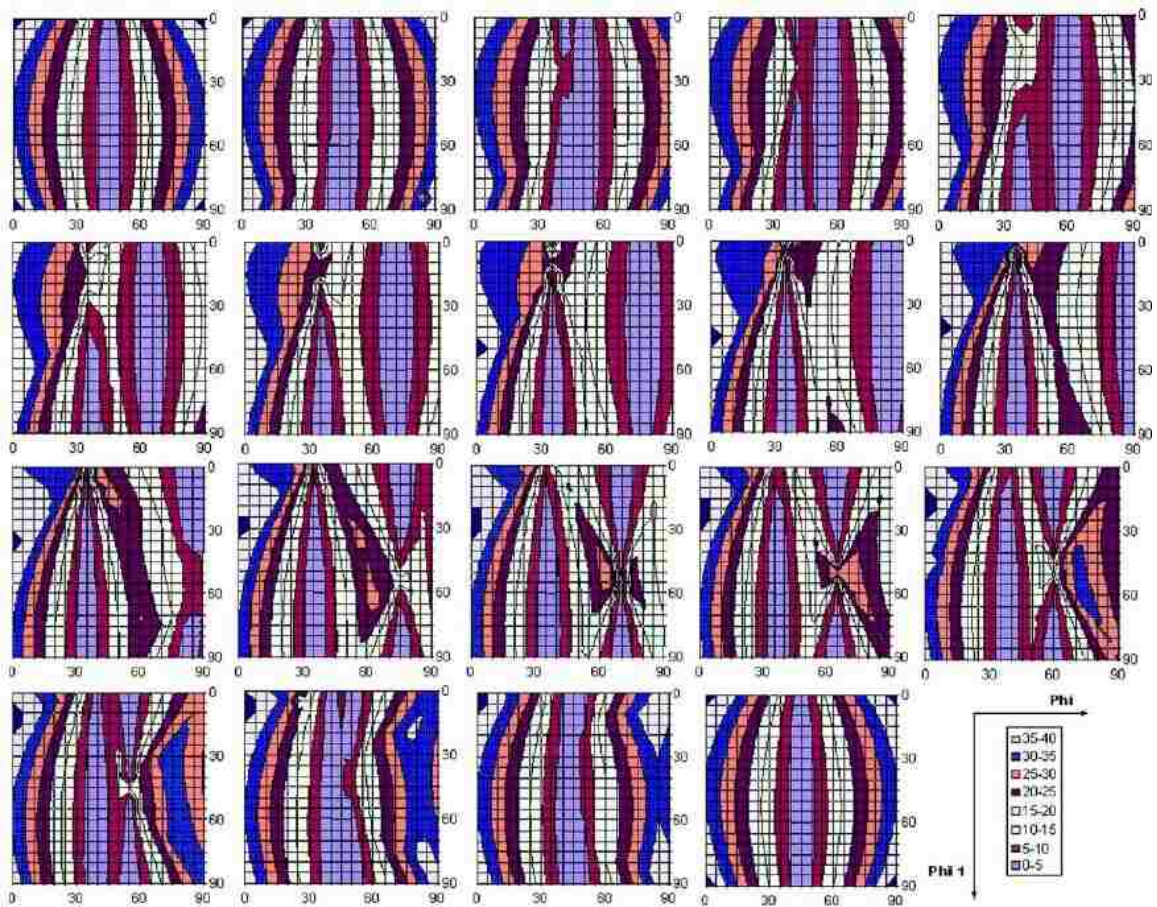


Figure 1.4 Maps of the twist angle of crack deflection at the grain boundary between a Goss oriented grain and randomly oriented grain in Euler space [100].

Chapter 2 Experimental theory and technology

In order to study the multi-site fatigue crack nucleation behavior in high strength aluminum alloys, a series of tests and characterizations were carried out on AA2024, AA7075, A713 and so forth. The traditional tensile tests and four-point bend fatigue tests were conducted to measure the mechanical properties of a variety of alloys, particularly to investigate the fatigue crack nucleation behavior at constituent particles and micro-notches fabricated using FIB to mimic those particles. Combined with optical microscope (OM), scanning electron microscope (SEM), electron backscattered diffraction (EBSD), focused ion beam (FIB), atomic force microscope (AFM) and Nano-indentation, the effects of microstructure and micro-texture on the multiple crack nucleation were studied in 3-D thoroughly.

2.1 Mechanical Test

2.1.1 Tensile test

The dog bone shaped tensile specimens were prepared according to ASTM [125], with a gage length of 25.4 mm and width of 6.35 mm, as shown in Figure 2.1. The specimens were cut along L direction (rolling direction) and T direction (long transverse direction) respectively. Tensile testing was performed on an Instron 8800 servo-hydraulic testing machine (Figure 2.2) at room temperature in air. Two samples were tested in each direction. Tensile properties are based on the average of two standard testing in each direction. The selection of the stress levels for the fatigue tests was determined according to their tensile properties, especially the tensile yield strength.

2.1.2 Four-point bend Fatigue test

The self-aligning four-point bend fatigue testing method was utilized to study the multi-site fatigue crack nucleation behavior of a series of high strength aluminum alloys as shown in Figure 2.3 and 3.2, primarily AA2024 and AA7075, also including A713, AA2026 and AA2099. High cycle fatigue tests were conducted in the L-T, L-S and T-S planes of AA7075 rolled plate, extrusion direction (L) on the L-T planes of extrusion bars of AA2026 and AA2099, and on the T-S plane of AA2024 and AA7075 in fatigue crack nucleation at micro-notches fabricated by FIB.

The dimensions and geometry of four-point bend samples as shown in Figure 2.4 and 3.2 have been found to influence the applied stress distribution on the tensile surface of four-point bend tests [126]. The loading condition, such as the support span/load span ratio (L/t), is commonly either three or two, which does not usually give rise to a uniform stress distribution on the sample surface under tension in four-point bend. The non-uniform stress distribution failed to provide the even probability of initiation at distinctive possible crack nucleation sites during cyclic fatigue loading. In order to obtain evenly distributed tensile stress on the top surface between the two inner rollers, the optimum test geometry (L/t of 4-5 and t/h of 1.2-1.5, where h is the sample thickness) for four-point bend fatigue has been established by both numerical and experimental work. This four-point bend technique introduced an optimum testing geometry, which gives rise to a uniform tensile stress on the sample surface between the two loading rollers. The nominal maximum stress σ_{nom} on the sample surface illustrated in Figure 2.4 can be calculated by the beam theory of engineering mechanics,

$$\sigma_{nom} = \frac{3F(L-t)}{wh^2} \quad (2.1)$$

Where w and h are the sample width and thickness respectively, while L and t represent the support span and load span, and F is the load applied by one of the two loading rollers. The schematic diagram of the four-point bend fatigue test was shown in Figure 3.2. The use of a hemisphere as the joint between the loading plate and the loading bar could minimize any of the misalignment during the test and produces consistent and reproducible results.

2.1.3 Nano-indentation

Indentation technique is an advanced method to characterize the mechanical properties of materials by contacting two materials under designed force conditions. The mechanical properties can be directly measured from the indentation load and displacement monitored by the high resolution testing facilitates [127]. Elastic modulus, hardness, and fracture toughness can be calculated from the load and displacement data [128]. Among these parameters, hardness and elastic modulus are the initial concern for the instrumented indentation, which was developed in 1992 [129, 130]. Due to its capabilities of characterizing the mechanical properties of thin films and small-scale materials, instrumented Nano-indentation has been used as one of the most important mechanical characterization techniques, especially on the micro- and nano-scale [129]. In this work, the Nano-indentation, Nano Indenter G200 by Agilent Technologies as

shown in Figure 2.5, was used to accurately measure the Young's modulus and hardness of the constituent particles as well as the matrix in the AA7075 aluminum alloy.

In the past, for Nano-indentation tests, many works have been done to improve the testing equipment and analysis methodology. The Oliver-Pharr model is the most extensively used method to evaluate the mechanical properties of materials. Oliver and Pharr [129, 131] approximated the unloading curves by a power law relation as

$$P = \alpha(h - h_f)^m \quad (2.2)$$

Where P is the indentation load and h is the indenter displacement, h_f is the final indentation depth, α and m are the power-law fitting constants. Here $m=1$ is for the flat-end indenter and $m=1.5$ for a parabolic indenter. The contact area of an indentation is calculated as a function of indentation depth, which is calibrated by independent measurements. The hardness is measured as

$$P = \frac{P_{max}}{A} \quad (2.3)$$

and the contact modulus can be calculated through the relation

$$E_{eff} = \frac{\sqrt{\pi}S}{2\beta\sqrt{A}} \quad (2.4)$$

$$S = \left. \frac{dP}{dh} \right|_{unloading} \quad (2.5)$$

The contact modulus is defined as

$$\frac{1}{E_{eff}} = \frac{1-\nu^2}{E} + \frac{1-\nu_i^2}{E_i} \quad (2.6)$$

Here P_{max} is the peak indentation load, A is the projected area of the hardness impression, S is the measured stiffness of the upper portion of the unloading curve, E and ν are Young's modulus and Poisson's ratio for the specimen and E_i and ν_i are the same parameters for the indenter.

2.2 Characterization methods

2.2.1 Scanning Electron Microscopy (SEM)

Scanning electron microscopy (SEM) is a type of electron microscopic techniques to produce high-resolution images of a sample surface by scanning it using a focused electron beam with an high energy of 0.5~30 keV. The high-energy electron beam is collimated by electromagnetic condenser lenses, focused by an objective lens, and

scanned across the surface of the sample by electromagnetic deflection coils [132]. When the accelerated incident electrons bombard on the sample surface, a variety of signals can be generated, including secondary electrons (SE), backscattered electrons (BSE), diffracted backscattered electrons (signal used to determine crystal structure and orientation by EBSD system, which will be intruded in more details in the next section), Auger electrons, X-rays, etc. The SEs, generated within a few nanometers from the sample surface, are very sensitive to the surface topography, thus is the most used signal. They are detected by a scintillator-photomultiplier device and the consequent signal is transformed into a 2-D intensity distribution that can be viewed as digital image. Being different SEs, the BSEs are generated because of the elastic scattering/reflection of the incident electron beam by the atomic nuclei in the sample surface. The larger the atoms (with a greater atomic number Z), the higher probability of producing an elastic collision due to greater cross-sectional area of the nuclei. Hence, the image in BSE mode qualitatively incorporates composition information of the scanned surface. By means of X-ray energy dispersive spectroscopy (EDS), the characteristic X-rays signal emitted from the sample can provide more quantitative elemental information [132]. In the present work, all the SE, BSE and EDS were used for the topography observation and chemical composition analysis on SEMs Hitachi S-4300 and S-3200.

2.2.2 Focused Ion Beam (FIB)

Focused ion beam (FIB) microscope has gained widespread use in fundamental materials studies and technological applications over the recent years because it offers both high-resolution imaging and flexible micromachining in a single platform. The FIB instrument is similar to an SEM, except that the beam that is rastered over the sample is an ion beam rather than an electron beam. By the means of adjusting the parameters, such as beam current and accelerating voltage, an FIB can be used to, but not limited to, obtain high-spatial-resolution images, precisely deposit and micro-machine the sample surface at a scale from submicron to hundreds of microns.

In most commercially available FIB systems, the liquid-metal ion type source (LMIS) is usually used [133]. Among various types of LMISs (such as In, Bi, Sn and Au based source), the Ga-based blunt needle source (Figure 2.6) has been widely used because of its decided advantages in terms of low melting temperature, low volatility, and low vapor pressure [134]. During operation, Ga flows from a reservoir to the needle tip (with an end radius of about 10 μm), where it is extracted by field emission. A large negative

potential between the needle and an extraction electrode generates an electric field of magnitude 10^{10} V/m at the needle tip. The balance between the electrostatic forces and the Ga surface tension results in the wetting of the tapered W needle geometry and the formation of a single Taylor cone at the needle tip. For typical emission currents used in FIB microscopes (~ 2 mA), a cusp forms at the tip of the Taylor cone with a tip radius of approximately 5 nm. Once the Ga^+ ions are extracted from the ion source, they immediately travel through a series of lens which can be simplified as a condenser lens and an objective lens, as shown in Figure 2.6.

When the Ga^+ ions bombard on the sample surface, the kinetic energy of the ions is transferred to other forms of energy or signals through interactions with the sample atoms. As shown in Figure 2.7, the ion-sample interaction generates a series of events, mainly including, but not limited to, ion reflection and backscattering, electron emission, electromagnetic radiation, atomic sputtering, ion emission and sample damage [135, 136]. Among these signals, the emitted electrons, especially the ion-induced secondary electrons (ISEs), are collected by the detector for imaging in FIB system. Since ion beams are not as finely focused as electron beams, thus they generally yield a relatively lower resolution. However, the FIB can offer complementary information about sample surface because ISE imaging can deliver stronger channeling contrast from the crystals than SE imaging [134]. Another major application of an FIB is ion beam sputtering which allows the precise local removal or milling of material. When an accelerated Ga^+ ion impinges the target sample, it enters the sample, resulting in the ejection of a sputtered particle (which may be an ion or a neutral atom). The effect zone depth of ion bombardment is controlled by the accelerating voltage. For example, the penetration depth is ~ 20 nm for 25 keV Ga^+ ions. The use of enhanced etching may increase the sputtering rate [135, 137]. Halogen gases, such as Cl_2 , I_2 , and XeF_2 , can be directed to the area of interest. These gases can form a volatile compound with the sputtered material, thus accelerate the sputtering process. In the sample preparation that is by the means of FIB milling, an ion beam assisted chemical vapor deposition is usually used. In this application, a hollow needle is brought to within ~ 100 - 200 μm of the target surface, then the suitable gas (e.g. $\text{W}(\text{CO})_6$) is injected from the needle tip and absorbed onto the target surface. When the Ga^+ beam is rastered over target region, the ion beam decomposes the gas, leaving a deposited layer of metal (e.g. W) while the by-product (e.g. CO) is extracted through the vacuum system [133, 136].

In this research work, the FIB was used to 1) reveal the 3-D geometry and dimensions of constituent particles and crack planes by cross-sectioning, 2) make micro-notches to mimic the fractured Fe-bearing particle as nucleation sites in the selected grains. Two dual-beam SEM/FIB systems, FEI Quanta 200-3D and Hitachi NB5000, were used to carry out the experiments above.

2.2.3 Atomic Force Microscope (AFM)

A 3-D topography of the surface on a nanoscale could be obtained by Atomic Force Microscope (AFM), by measuring forces between a sharp probe (<10 nm) and surface at very short distance (0.2-10 nm probe-sample separation). The probe is supported on a flexible cantilever (Figure 2.8). The AFM tip “gently” touches the surface and records the small force between the probe and the surface. The probe is placed on the end of a cantilever (which one can think of as a spring). The amount of force between the probe and the sample is dependent on the spring constant (stiffness) of the cantilever and the distance between the probe and the sample surface. This force can be described using Hooke’s Law:

$$F = -k \cdot x \quad (2.7)$$

Where F is Force, k is spring constant, x is representing cantilever deflection [138]. In this work, the topographies of the Fe- and Si-bearing particles in AA7075 on the mechanically polished surface were identified using AFM, Q-scope 250, to evaluate mechanical properties of the selected particles indirectly.

2.3 Crystallographic orientation

2.3.1 Orientation description

2.3.1.1 Miller indices

Miller indices is a common orientation description which is expressed in the form of $\{hkl\}\langle uvw \rangle$. The $\{hkl\}$ represents the crystal plane perpendicular to the sample normal direction (ND), while $\langle uvw \rangle$ denotes the crystal direction parallel to the certain processing (e.g. extrusion or rolling) direction of the sample (RD). For example, copper (Cu) orientation can be denoted by $\{112\}\langle 111 \rangle$, meaning $\{112\}$ plane being parallel to ND and $\langle 111 \rangle$ aligned along RD.

2.3.1.2 Euler angles and Euler Space

Compared to Miller indices, pole figure and rotation matrix, Euler angles are three numbers that can concisely express the crystal orientation. The Euler angles refer to three sequent rotations that transform the sample coordinate system onto the crystal coordinate system. Generally, there exist three major rotation conventions which were proposed and developed by Bunge, Roe and Kocks [139, 140], respectively. Among them, the most commonly used is Bunge's convention whose three sequent rotations are performed as following and Figure 2.9 [140-142]:

1. φ_1 - about the ND, transforming TD into TD' and RD into RD', rotation matrix = g_{φ_1}
2. Φ - about the axis RD' (new orientation), transforming TD' into TD'' and ND into ND'', rotation matrix = g_{Φ}
3. φ_2 - about the ND'' (new orientation), rotation matrix = g_{φ_2}

Here, φ_1 , Φ , φ_2 are the Euler angles. These three rotation results in a total rotation of

$$g = g_{\varphi_2} \cdot g_{\Phi} \cdot g_{\varphi_1} =$$

$$\begin{pmatrix} \cos\varphi_1\cos\varphi_2 - \sin\varphi_1\sin\varphi_2\cos\Phi & \sin\varphi_1\cos\varphi_2 + \cos\varphi_1\sin\varphi_2\cos\Phi & \sin\varphi_2\sin\Phi \\ -\cos\varphi_1\sin\varphi_2 - \sin\varphi_1\cos\varphi_2\cos\Phi & -\sin\varphi_1\sin\varphi_2 + \cos\varphi_1\cos\varphi_2\cos\Phi & \cos\varphi_2\sin\Phi \\ \cos\varphi_2\sin\Phi & -\cos\varphi_1\sin\Phi & \cos\Phi \end{pmatrix} \quad (2.8)$$

With the Euler angles, any crystal orientation can be represented unequivocally as a point in a 3-D coordinate system whose axes are spanned by the three Euler angles. Such a 3-D coordinate system (or space) is referred to as Euler space. To represent all possible crystal orientations, the maximum size of the Euler angle space varies with the symmetry of the crystal structure. It requires larger Euler space size for low-symmetry crystal structures while smaller for high-symmetry ones. For example, the range of $0^\circ \leq \varphi_1, \varphi_2 \leq 360^\circ$ and $0^\circ \leq \Phi \leq 180^\circ$ is required to define the triclinic crystal symmetry, which also define the maximum size of the Euler angle space; while the range of the Euler angles is reduced to $0^\circ \leq \varphi_1, \Phi, \varphi_2 \leq 90^\circ$ to fully represent $m\bar{3}m$ symmetry in cubic crystal system. If considering the symmetries of $6/mmm$, the space size can be further deducted to the range of $0^\circ \leq \Phi, \varphi_1 \leq 90^\circ$ and $0^\circ \leq \varphi_2 \leq 60^\circ$. Although the crystal orientation appears three times in the reduced Euler angle space due to high-symmetry of cubic structure, i.e. it only requires a further reduced Euler angle space to fully represent all crystal orientations, the range of $0^\circ \leq \varphi_1, \Phi, \varphi_2 \leq 90^\circ$ is commonly used for general description of the crystal orientation in a cubic system [140, 142].

2.3.1.3 Pole figure and inverse pole figure

The pole figure is a two-dimensional stereographic projection, with crystal orientation specified relative to the specimen geometry, which shows the variation of pole density with pole orientation for a selected set of crystal plane {hkl} [143]. For an individual crystal orientation (hkl)[uvw], its location on the pole figure is given by the stereographic projection of \bar{n} in the spatial equatorial plane, where \bar{n} is the unit vector normal to the (hkl) crystal plane and has spatial components in the (hkl)[uvw] orientation given by the column vector (Equation 2.9),

$$\begin{pmatrix} n_1 \\ n_2 \\ n_3 \end{pmatrix} = \frac{1}{\sqrt{h^2+k^2+l^2}} \begin{pmatrix} \frac{u}{n} & \frac{kw-lv}{mn} & \frac{h}{m} \\ \frac{v}{n} & \frac{lu-hw}{mn} & \frac{k}{m} \\ \frac{w}{n} & \frac{hv-ku}{mn} & \frac{l}{m} \end{pmatrix} \begin{pmatrix} h \\ k \\ l \end{pmatrix} \quad (2.9)$$

Where $m = \sqrt{h^2 + k^2 + l^2}$, $n = \sqrt{u^2 + v^2 + w^2}$.

To determine the position of a given pole on the sphere plane usually requires two angles: the angle α describing the azimuth of the pole, where $\alpha=0^\circ$ is the north pole of the unit sphere, and angle β characterizing the rotation of the pole around the polar axis. These two angles start from a set specified external reference directions, which are usually selected to coincide with sample coordinates or processing directions (such as ND and RD, respectively, for rolled/extruded symmetry, Figure 2.10). The two pole figure coordinates α and β are corresponding to the spherical coordinate of \bar{n} on the unit sphere through Equation 2.10 and is shown in Figure 2.10.

$$\begin{pmatrix} n_1 \\ n_2 \\ n_3 \end{pmatrix} = \begin{pmatrix} \sin\alpha\cos\beta \\ \sin\alpha\sin\beta \\ \cos\alpha \end{pmatrix} \quad (2.10)$$

In order to unambiguously represent an orientation, an individual pole is insufficient because the crystal can still rotate about this particular pole. The number of poles to unequivocally characterize a crystal orientation depends on the crystal symmetry or the pole symmetry, but generally three poles are necessary to determine an orientation completely. The more details regard measuring pole figures will be introduced later. In one word, the pole figure characterizes the pole positions on the equatorial plane in a stereographic projection, with respect to processing directions.

Rather than representing the orientation of the crystal coordinate system in the sample coordinate system, vice versa, the orientation of the specimen coordinate system can be

projected into the crystal coordinate system, which is referred to as inverse pole figure. In the reverse pole figure, the reference system is the crystal coordinate system, and the “orientation” is defined by the axes of the sample coordinate system, e.g. RD, TD and ND. Unlike the pole figure, the inverse pole figures have not to show the entire equatorial plane, but one unit triangle will suffice. For example, for the cubic crystal symmetry, the unit triangle $\langle 100 \rangle$, $\langle 110 \rangle$ and $\langle 111 \rangle$ is sufficient. However, for representation of macro-texture data, inverse pole figures are usually inferior to pole figures.

2.3.2 Texture measurement

2.3.2.1 Macro-texture measurement by X-ray diffraction

The macro-texture is usually measured by X-ray diffraction and expressed by pole figure. The principle of pole figure measurement by X-ray is based on Bragg’s law for reflection of radiation at the crystal lattice planes, i.e. $\lambda = 2d_{hkl}\sin\theta$. For most bulk materials, back reflection method is commonly used, and its geometry is demonstrated in Figure 2.11. During the measurement, the sample is first mounted on a sample stage driven by a goniometer, with its sample coordinates coinciding with three perpendicular rotation axes (φ , χ and ω/θ) of the goniometer, i.e. RD// ω , TD// χ and ND// φ [144]. To measure the intensity of pole (hkl), the X-ray source and detector/counter are then positioned to have an angle of $180 - 2\theta_{hkl}$, with the bisectrix between the incident and diffracted beams being normal to the sample surface. In this geometry, only the crystal planes (hkl) with normals parallel to the bisectrix can diffract the X-ray beam that can be received by the detector. In order to measure the orientation of all (hkl) planes in the sample surface, the sample has to be rotated around axis φ and axis χ , respectively. In most modern stepper-motor driven X-ray systems, the sample firstly rotates 360 about axis φ (i.e. $\varphi=0 \rightarrow 360^\circ$), then around χ for a certain degree that meets the requirement on resolution (typically 5°), followed by the rotation around axis φ for 360 and subsequently χ for 5° again. This cycle is repeated until χ spans to 90° for a complete pole figure. The rotations about axis φ and axis χ are related to the coordinates, α and β , in the texture analysis pole figure, by the relation of $\beta=\varphi$ and $\alpha=90^\circ-\chi$ (Figure 2.12). As the specimen rotates, the X-ray scans over the area on the equatorial plane. The intensity distribution of a particular crystallographic direction in the polycrystalline in the specimen can be recorded and analyzed. It is defined by the volume fraction dV/V of crystals having their crystallographic direction parallel the bisectrix (Equation 2.11)

$$\frac{dV}{V} = P_{hkl}(\alpha, \beta) \sin\alpha d\alpha d\beta \quad (2.11)$$

where $\sin\alpha d\alpha d\beta$ is the unit area on the sample direction. (α, β) is the pole density which represents the number of crystals whose direction is parallel to sample direction, i.e., the probabilities of crystal direction aligns in the normal direction to (hkl). It is necessary to note that the description of texture by pole figure is incomplete because it just provides a specific crystal direction without discerning the rotation of the crystals about this direction. There is no way to use pole figures to obtain an unequivocal and complete orientation of individual grains or volume elements.

2.3.2.2 Micro-texture measurement by EBSD

Electron backscatter diffraction (EBSD) has become a widely used microstructural crystallographic technique to examine the crystallographic orientation of many materials. An EBSD system is usually associated with an SEM and uses the diffraction pattern (Kikuchi pattern [145]) from the illuminated volume to determine the crystal orientation. The configuration of an EBSD system is schematically shown in Figure 2.13. In the EBSD measurement [146, 147], the sample is tilted towards to the EBSD detector (fluoresces screen) at a relatively high angle (usually 70° for most systems), allowing more electrons to be diffracted towards a fluorescent screen positioned at a certain distance to the tilted sample. When the incident electrons bombard the sample surface, they are diffusely scattered in all directions. This means that there must always be some electrons arriving at the Bragg angle at every set of lattice planes, and these electrons can then undergo elastic scattering to give a strong and reinforced beam that gives rise to Kikuchi pattern, which is schematically shown in Figure 2.13(b). The locus of the diffracted radiation is the surface of cone (called Kossel cone) that extends about the normal of the diffracting atomic plane (hkl). The source of electron scattering can be considered to be between the lattice planes, thus two cones of radiation result from each plane-family. Because of the high energy of the incident beam (20-30 keV), the electron wavelength is very small, which generally yield the Bragg angle to be $\sim 0.5^\circ$. Consequently, the apex angle of a diffraction cone is close to 180° , meaning the cones are almost flat. The diffracted electrons (cones) are intercepted by a phosphor screen positioned against the sample surface, so that the electrons (cone surfaces) can be recorded as almost straight lines and form Kikuchi pattern on the screen. Since the Kossel cones from a lattice plane are formed in pairs, thus the whole Kikuchi pattern

consists of pairs of parallel lines where each pair, or “band” has a distinct width and corresponds to a distinct crystal plane. The Kikuchi pattern contains a wealth of crystallographic information, such as angle between Kikuchi bands, band width, and distance between poles. In determining an individual pattern, the experimentally recorded pattern is processed, and compared with the theoretically one simulated based on the database, and then the software can calculate the crystallographic orientation.

In this study, EBSD work was carried out on a Field Emission Gun SEM (Hitachi S-4300), equipped with a CCD camera and a Channel EBSD system (HKL Technology, Demark). The crystal orientation of the surrounding target constituent particles or micro-notches in the sample was measured by scanning the area point by point in a step size of 0.3-1 μm , with the acceleration voltage of 20 KV and working distance of 21 mm. The measured crystal orientation was expressed in Euler angles (ϕ_1, ϕ, ϕ_2).

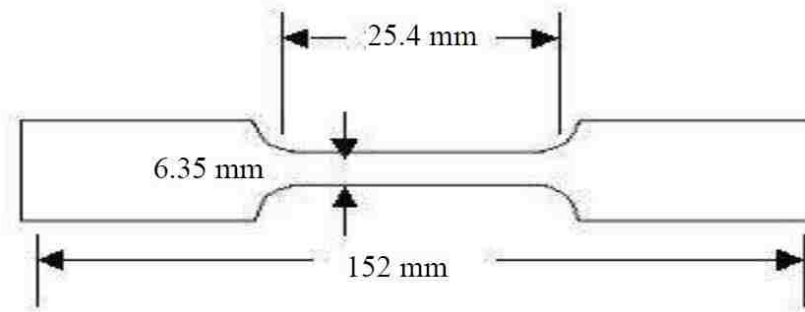


Figure 2.1 The geometry of the dog bone shaped tensile test specimen of 7075.



Figure 2.2 The Instron 8800 servo-hydraulic test machine used for the tensile testing.



Figure 2.3 The actual four-point bend fatigue test rig during fatigue testing.

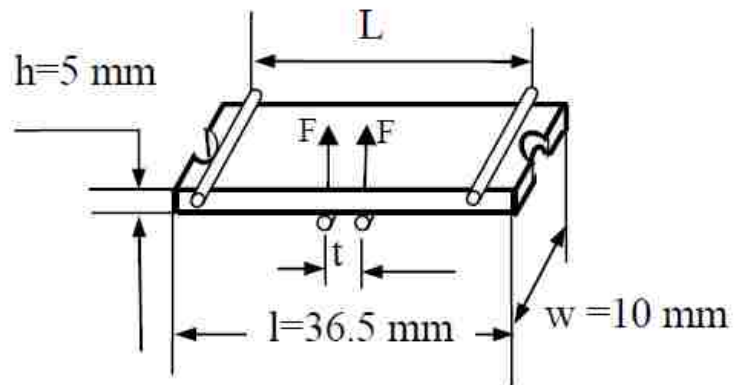


Figure 2.4 The drawing of loading condition and position of supporting and loading rollers on four-point bend samples.

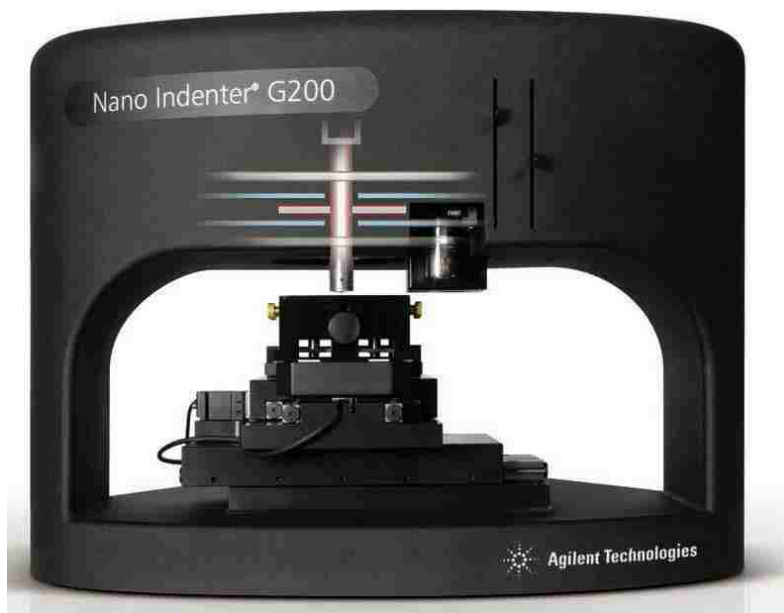


Figure 2.5 The equipment for measurement of modulus and hardness of constituent particles and matrix of AA7075, Nano Indenter G200 by Agilent Technologies.

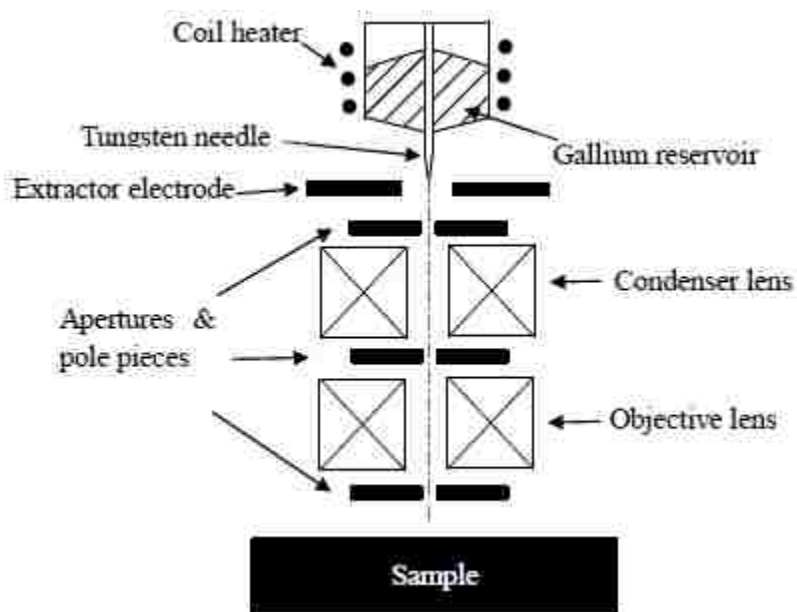


Figure 2.6 Schematic diagram of the LMIS and lens system of an FIB.

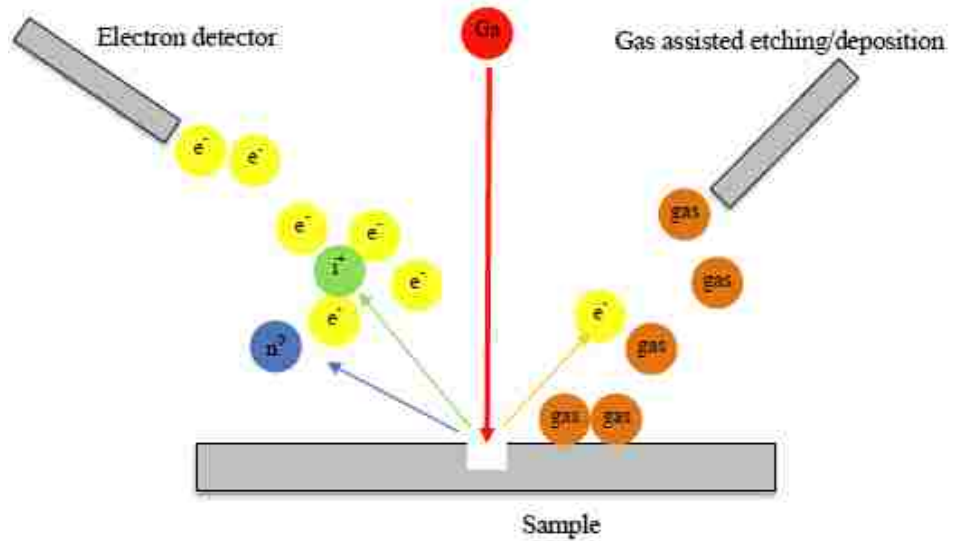


Figure 2.7 Main interaction of Ga^+ with sample material in an FIB.

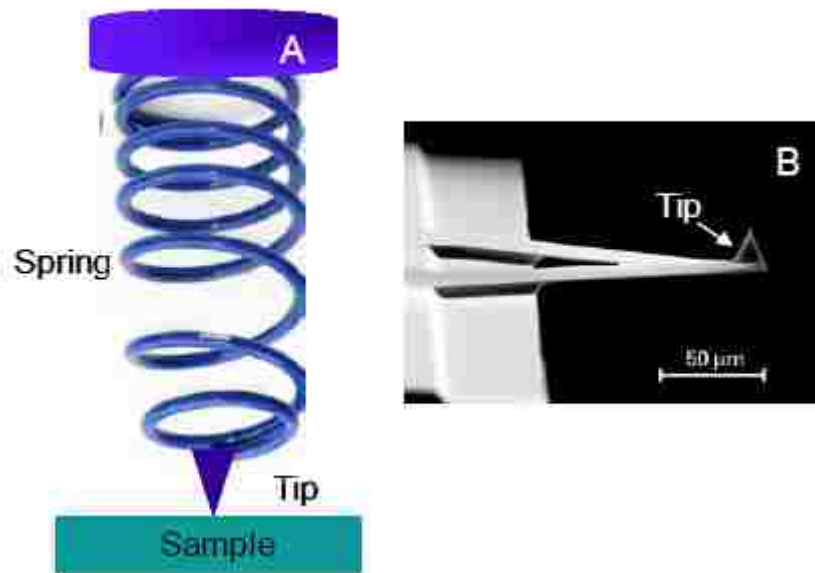


Figure 2.8 (a) spring depiction of cantilever (b) SEM image of triangular cantilever with probe (tip) (from from MikroMasch)[138].

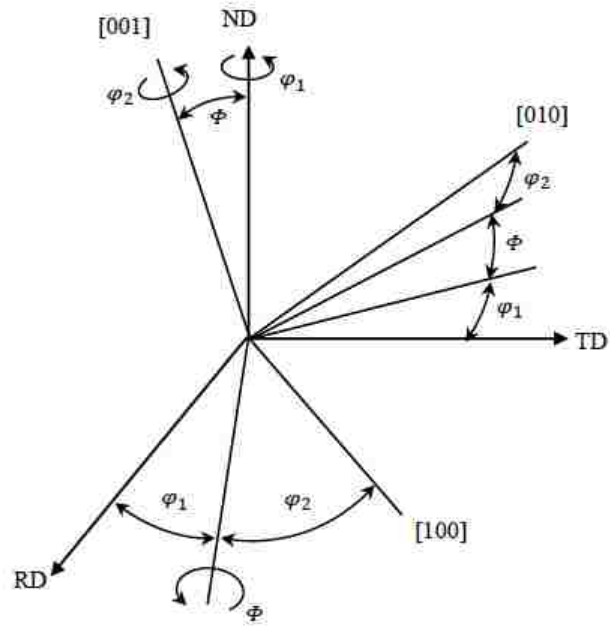


Figure 2.9 Relationship between sample coordinate system and crystal coordinate system in definition of Euler angles.

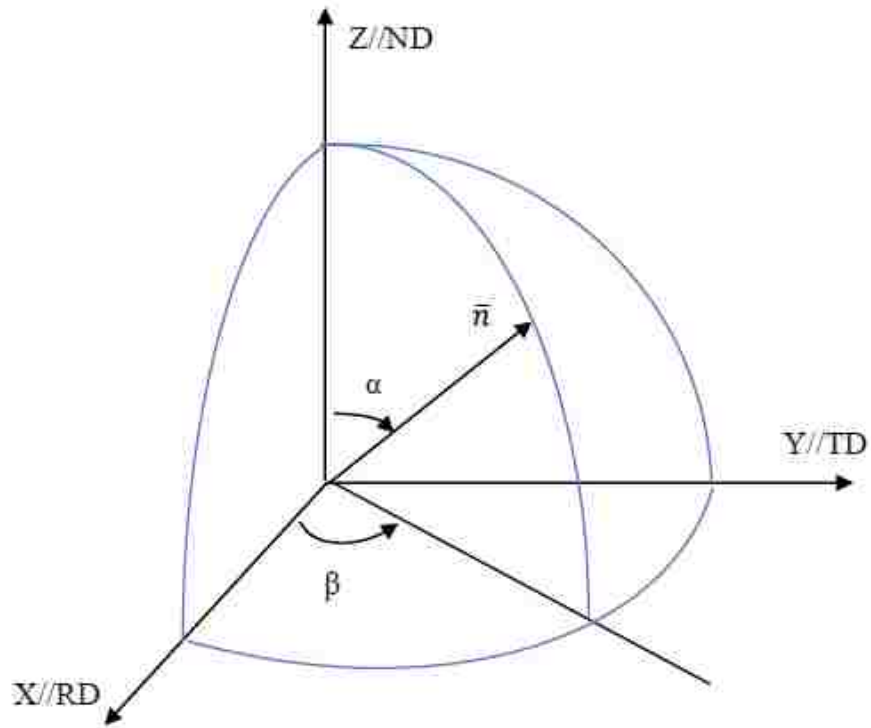


Figure 2.10 Sketch diagram showing the relationship of two pole figure coordinate (α , β) and the spherical coordinate of \bar{n} on the unit sphere.

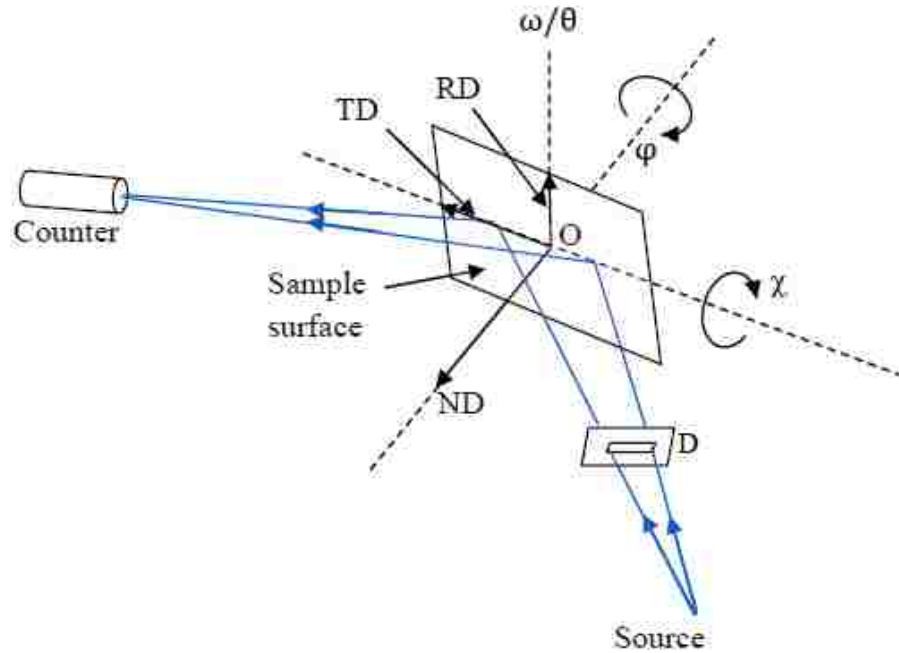


Figure 2.11 Schematic diagram showing reflection geometry in X-ray diffraction experiments.

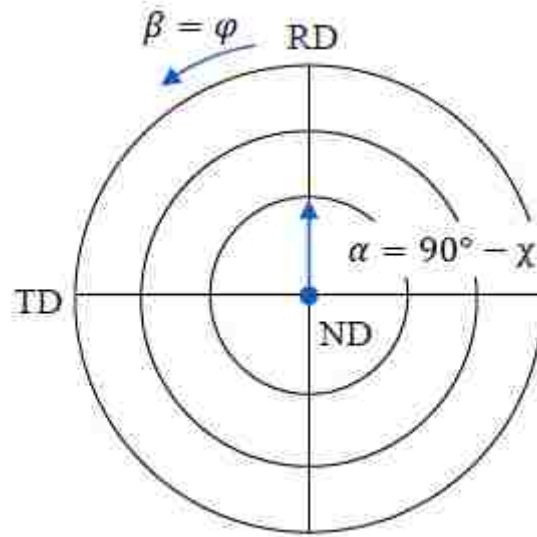


Figure 2.12 Schematic diagram showing relation of rotation angles (α, β) in XRD geometry and angles (ϕ, χ) in pole figure.

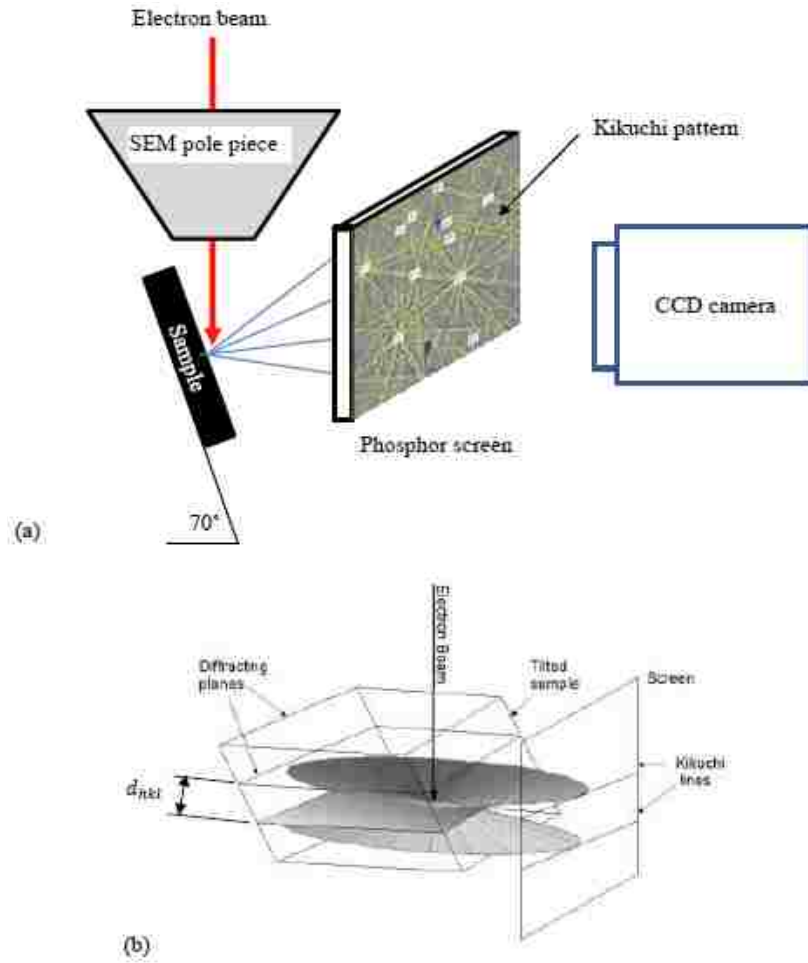


Figure 2.13 Schematic diagram showing (a) the typical geometry for an EBSD system, (b) the formation of Kikuchi lines.

Chapter 3 An experimental methodology to quantify multi-site fatigue crack nucleation behavior in high strength aluminum alloy

3.1 Introduction

It has been recognized that multi-site fatigue cracks are commonly nucleated at microstructural inhomogeneities in metallic materials, wherein most of the cracks become non-propagating, while only a few cracks propagate continuously, leading to the final fracture [52], in metallic materials, such as nickel-based superalloys [148], titanium alloys [149] and aluminum alloys [26, 46, 49, 52, 59]. Multi-site crack nucleation has not been thoroughly and quantitatively understood so far. Zhai et al. have recently developed an experimental method to characterize the multi-site fatigue crack nucleation phenomenon by measuring the number of fatigue cracks observed on the sample surface at different stress levels in engineering alloys, such as Al-Li alloys and Al-Zn cast alloys [45, 49]. The crack population is a Weibull-type function of the applied cyclic stress, which allows quantification of the weak-link density and strength distribution in the alloys. The weak-link concept was proposed by Weibull in 1939 [50], and is used to define the potential fatigue crack initiation sites in this work. The fatigue weak-link (FWL) density and strength distribution are materials properties which could be used to evaluate the fatigue crack initiation behavior and design alloys with the desired FWL density and strength distribution. In an Al-Li alloy thick plate, the crack nucleation behavior appears to be significantly anisotropic, due to the differences in grain structure and texture between the different planes of the plate. When the load axis is parallel to S direction, the FWL density is much higher than that when loaded along the L direction in the plate, since cracks are preferentially initiated along the major grain boundaries of the pancake-shaped grain structure which is perpendicular to S direction, whereas cracks initiation occurs only along the {111} plane perpendicular to the loading axis when fatigued in the L direction [53]. The microstructure and texture of an alloy could substantially influence the FWL density and strength distribution in the alloy. There are still many other factors that may influence these two characteristic parameters in quantifying multi-site fatigue crack nucleation, such as types of FWLs, mode of applied cyclic fatigue loads, experimental environments, and the applied fitting functions, etc. It is therefore essential to improve this experimental method effectively by conducting more attempts to make it applicable in a wider range of materials and in more actual circumstances.

In this chapter, an experimental method to quantify multi-site fatigue crack nucleation behavior in high strength Al alloys will be thoroughly introduced in detail. In this method, two key parameters, which are FWL density and strength distribution, were regarded as materials properties to be used to characterize multi-site fatigue crack nucleation phenomenon quantitatively in a range of high strength Al alloys, such as AA7075 T651, A713, AA2026 T3511, and AA2099 Al-Li alloys, etc. The effects of humidity, porosity density, the type of microstructural heterogeneities on FWLs, and the mechanisms for the formation of FWLs at particles or porosities were studied thoroughly. It was found that a three parameter Weibull-type function could better describe the relation of FWLs with the applied cyclic stress than any other sigmoidal-type functions, and that the applied cyclic strain should be used in describing FWLs when the maximum cyclic stress exceeded the yield stress of an alloy.

3.2 Experiments

The procedure to characterize FWLs experimentally is illustrated in Figure 3.1, consisting of four steps, sample preparation, four-point bend fatigue testing, measurement of FWLs, and quantification of FWL density and strength distribution as following:

3.2.1 The alloys and samples

The engineering alloys used in this study are: 1) an AA7075 T651 Al alloy plate 8 mm in thickness, 2) an AA2026 T3511 Al alloy extruded bar, 3) an AA2099 T8E67 Al-Li alloy extruded bar, and 4) an A713 sand cast Al alloy. Their chemical compositions and mechanical properties (ultimate and yield strengths) of these alloy are shown in Tables 3.1 and 3.2, respectively. Figure 3.2 shows the geometry and dimensions (36.5 x 10 x 4.6 mm³) of the samples used in four point bend fatigue tests. In order to compare anisotropic crack initiation behavior on different planes of the AA7075 T651 plate, the samples were cut parallel to three different planes, i.e., L-T, L-S and T-S planes, in the rolled plate. The alloy had a pancake-shaped grain structure with an average grain size of 4502.8×376.6×45.8 μm³ (L×T×S) [46]. The A713 samples were cut from the lower part of 12 mm thick cast plate, while the long axis of an AA2026 Al alloy sample was parallel to the extrusion direction, i.e. L-T type samples. Similarly, AA2099 samples were also made from an extruded rectangular bar along the L-T plane. The surfaces of

all these samples in tension under four-point bend were ground using waterproof abrasive papers gradually from grit 240 to 1200, followed by mechanical polishing using alumina powders of 1 micron, 0.3 micron and 0.05 micron in size, respectively, and final polishing using a silica colloidal suspension liquid.

3.2.2 Four-point bend fatigue tests

Four-point bend fatigue tests were carried out on the samples of different materials at a stress ratio $R=0.1$, frequency of 20 Hz, and room temperature, in a sinusoidal waveform, and ambient air or moist atmosphere (for AA2026 samples in 50% relative humidity environment). A self-aligning four-point bend rig, which was developed by Zhai, et al [126], was used on an Instron 8802 servo-hydraulic materials testing machine. As shown in Figure 3.2, the optimum testing geometry and dimensions for four-point bend testing were loading span of 6 mm (inner rollers) and supporting span of 30 mm (outer rollers), when the sample thickness is between 4.5 and 4.7 mm, in order to generate a uniform stress distribution on the sample surface in tension. For detail about the FEA calculation to determine the optimum testing geometry and dimensions, please see reference[126]. The main advantages of four-point bend fatigue testing over the more commonly used fatigue testing method, uniaxial fatigue, include: 1) convenience of studying fatigue damage on sample surface, 2) simple sample preparation, 3) easy sample mounting and dismounting for studying the evolution of surface fatigue damage by interrupting and resuming fatigue tests. In this study, four-point bend fatigue testing was particularly beneficial for studying fatigue damage (i.e., fatigue weak-links) prior to and after cyclic loading on the sample surfaces. The run-out number was set to be 5,500,000 cycles, at which if a sample did not fracture in a fatigue test, it was counted as unbroken. In the process of fatigue testing, a test was terminated automatically when the sample deflection exceeded the limit which was 15% larger than its maximum value before fracture. As such, the sample surface still remained sufficiently flat, making it possible to measure the crack population on an optical microscope after the fatigue test. Samples from different materials were tested at various maximum stress levels ranging from around the fatigue limit to the ultimate tensile strength. Two samples at each stress level were tested, and the measured crack population was averaged over those from the samples. More details about experiment for each type of alloy will be introduced in separate sections in the following chapters.

3.2.3 Measurement of FWLs on surface

Optical microscopy (OM) and scanning electron microscopy (SEM) were employed to study not only the evolution of fatigue damage but also weak-links initiated on the surface after fatigue tests. The constituent particles were characterized on the surface of the AA7075 T651 alloy before and after fatigue testing, to verify whether the micro-cracks in some of the particles before fatigue could lead to fatigue crack initiation. Optical micrographs were taken at 200× magnification before and after fatigue in the same areas (approximately 11 mm²) on the surface. The porosity in A713 and the second phase particles or inclusions in AA2099 Al-Li alloy were also found to be the potential fatigue nucleation sites. Furthermore, the crack initiation sites in these samples were examined on the fracture surfaces using SEM. The fatigued samples of AA2026 at 0% and 50% relative humidity (RH) environments were studied, respectively. The crack population, i.e. number of fatigue weak-links, found on each sample surface after the fatigue test was measured at 50× magnification using optical microscope, ignoring the effect of crack coalescence.

The four-point fatigue tests were conducted at different maximum cyclic stresses ranging from fatigue limit to ultimate tensile strength. When the applied maximum cyclic stress exceeded the yield strength of the tested alloy, strain gages, 4.7 x 3.4 mm² in dimensions, were used to measure the corresponding strain on sample surface, with regard to the applied stress, so that the FWLs could be described as a function of strain instead of stress.

3.2.4 Quantification of FWL density and strength distribution

The anisotropy of fatigue crack nucleation in the rolled plate of an AA7075 T651 Al alloy was taken as an example to demonstrate the procedure of quantifying FWL density and strength distributions in L-T, L-S, and T-S planes of the plate. Four-point bend fatigue tests were carried out to measure the S-N curve of each of these samples in this work, so that the population of fatigue cracks (i.e., FWLs) found on the surface at each cyclic stress or strain level could be measured using optical microscopy, after the sample failed. The S-N curves of all the alloys studied in this study are shown in Figure 3.3. The fatigue limits of L-T, L-S, and T-S samples could be determined to be approximately 243.6 MPa, 273.0 MPa and 280.6 MPa, respectively. As for anisotropy of fatigue crack

nucleation in the AA7075 T651 rolled plate, comprehensive discussion with regard to the experimental results will be made in the following chapters.

A 3-parameter Weibull function was used to fit the plots of crack population vs applied maximum stress, as shown in Figure 3.3.

$$N = N_0 \left(1 - \exp \left[-k \left(\frac{\sigma - \sigma_0}{\sigma_0} \right)^m \right] \right) \quad (3.1)$$

Where N_0 is the maximum possible number of cracks per mm^2 that can be formed on the surface, equivalent to the crack population observed on the surface between the two loading bars at the stress level close to the ultimate tensile strength (σ_s), $k = \text{constant}$; $m = \text{Weibull modulus}$; $\sigma_0 = \text{fatigue limit}$. σ_0 can be determined by S-N curve measurement, and N_0 also can be determined by counting the number of cracks formed at the stress level close to σ_s . k and m could subsequently be determined by fitting the crack population vs. stress level using the Weibull function (Eq. 3.1) which could be rewritten as,

$$\ln \left(-\ln \left(1 - \frac{N}{N_0} \right) \right) = m \ln \left(\frac{\sigma}{\sigma_0} - 1 \right) + \ln k \quad (3.2)$$

The measured crack population vs stress level curves in Figure 3.4 could then be fitted by the linear regression method in a $\ln(-\ln(1-N/N_0))$ vs $\ln(\sigma/\sigma_0-1)$ plot with m as the slope and $\ln k$ as the intercept values on the $\ln(-\ln(1-N/N_0))$ axis when $\ln(\sigma/\sigma_0-1)$ is zero, as shown in Figure 3.5. Only the data points of crack population at relatively higher stress levels were used in the curve fitting, since the data points just above the fatigue limit were relatively unreliable for the linear curve fitting. These data points might likely contain substantial measurement errors as they were small in value, i.e., only 1-2 cracks could be initiated on the entire sample surface tested at a stress level just above the fatigue limit, compared to hundreds of cracks observed at higher stress levels. A variation of one crack in the crack population measurement could lead to a measurement error over 50% at this stress level, but it could only cause an error less than 1% if the crack population was over one hundred at a higher stress level. The parameters (k and m) were obtained by linear fitting using Eq. (3.2) as well as the FWL densities (N_0), for L-T, L-S and T-S samples, respectively, as shown in Table 3.3.

By using these parameters, the strength distributions of FWLs on the L-T, L-S and T-S planes could be quantified as shown in Figure 3.6, respectively, by taking the derivative of Eq. (3.1)

$$n = CN_0 \left(\frac{km}{\sigma_0} \right) \left(\frac{\sigma - \sigma_0}{\sigma_0} \right)^{m-1} \exp \left[-k \left(\frac{\sigma - \sigma_0}{\sigma_0} \right)^m \right] \quad (3.3)$$

Where

$$N_0 = \int_0^{+\infty} n d\sigma \quad (3.4)$$

n is the characteristic strength distribution of FWLs in materials, representing the number of newly formed cracks at a specific stress level σ , and C is a scaling constant. N_0 was defined as the weak-link density which, together with FWL strength distribution, can be regarded as material fatigue properties.

3.3 Results and Discussion

3.3.1 Environmental effects on FWLs in AA2026 T3511 Al alloy extruded bar

As AA2026 aluminum alloys are a modified version of high purity AA2024 alloys, the preferred fatigue crack initiation sites in the alloys are same as those (i.e., Fe-containing particles Al_7Cu_2Fe) found in the AA2024 alloys, though the particle number density in AA2026 alloys is much lower than in the AA2024 alloys [72, 150]. It has been recognized that moisture in ambient air could compromise the high cyclic fatigue properties, especially crack initiation behavior from constituent particles, in the Al alloys, because of hydrogen embrittlement caused by water moisture reacting with Al [151, 152]. In this work, the effects of relative humidity on FWL density and strength distribution were studied in the AA2026 T3511 Al alloys.

As shown in Figure 3.7, the population of the fatigue cracks found on the L-T surface of the AA2026 T3511 alloy at failure was measured against stress level at relative humidity of 0% and 50%, respectively. Although the crack population was increased with the applied maximum cyclic stress at both tested relative humidities, 50% RH increased FWL density markedly from that at the dry condition in the alloy at all the stress levels tested. This appeared to be consistent with the S-N curve measurements of the alloy in both RH conditions, as shown in Figure 3.3 where the fatigue life at 50% RH is much shorter than at 0% RH for each stress level tested, in addition to the fatigue limit lowered by 14.1% at 50% RH, compared with that (390 MPa) at 0% RH. The

experimental data in Figure 3.7 could be fitted with a three-parameter Weibull function (Eq. (3-1)).

By fitting double log curves ($\ln(-\ln(1-N/N_0))$ vs. $\ln(\sigma/\sigma_0-1)$) of the experimental data, as shown in Figure 3.8, parameters, k and m , in Eq. (3.1) were determined, as listed in Table 3-3. The strength distributions of FWLs at both 0% and 50% RH could then be quantified using Eq. (3.3), as shown in Figure 3.9 which profoundly reveals the behaviors of fatigue crack initiation in the alloy at 0% and 50% RH. As shown in Figure 3.9, the peak in the FWL strength distribution curve at 50% RH is located at a lower stress (434.3 MPa) than that (487.4 MPa) of 0% RH, indicating that humidity significantly weakened FWLs, making it easier to initiate cracks at particles in the alloy. The measured FWL density (N_0) in Table 3.3 also revealed the moisture-sensitive behavior in fatigue crack initiation in alloy, as the FWL density was 1 mm^{-2} at 0% RH, as compared to 1.3 mm^{-2} at 50% RH. This indicated that moisture could facilitate fatigue crack initiation in the Al alloy, whereas the measured S-N curves in Figure 3.3 could only show that moisture shortened the life of the alloy, compared with that at 0% RH at the same stress level in the alloy. Using the FWL method developed in this work, the fatigue crack initiation behavior could be quantitatively characterized and studied explicitly.

The reason why moisture promoted fatigue crack initiation at particles in the AA2026 T3511 alloy was likely to be attributed to that water molecules might reduce the resistance to micro-crack growth at the tips of the micro-cracks in the prior-fractured particles at which cracks were predominantly initiated in the alloy (Figure 3.10(a)), similar as in AA2024 and AA7075 Al alloys [46, 72] As a result, those prior-fractured particles that could not lead to fatigue crack initiation at a cyclic stress in dry air could do so at a higher RH but the same stress level in the alloy, thereby more FWLs could occur at 50% RH than at 0% RH, as shown in Figure 3.7 and 3.9. It has been reported that hydrogen produced by water molecule reacting with Al could result in brittleness at a crack tip in Al alloys [151, 152], though further work still needs to be conducted to verify that moisture could reduce the resistance to micro-crack growth at prior fractured particles in high strength Al alloys. As shown in Figure 3.3, deterioration of fatigue life in AA2026 alloys due to 50% RH could be possibly attributed to the combination of early crack initiation and faster crack growth due to hydrogen embrittlement in the alloys.

3.3.2 Effects of density of microstructural heterogeneities on FWLs in A713 cast Al alloy

In this work, an A713 Al-Zn cast alloy plate, 12 mm thick, was used to study the effect of the porosity density on FWL density and strength distribution since pores were the predominant crack initiation sites in the alloy. As shown in Figure 3.11, it was found that the top surface of the plate had a much higher pore density (23.7 mm^{-2}) than that (9.1 mm^{-2}) of the bottom surface, since the alloy plate was sand cast horizontally. On the top surface, more gaseous pores could be formed in the plate. Consequently, fatigue samples with different densities of porosities could be made by cutting the samples from the top and bottom surfaces, respectively.

Before fatigue testing, the pore number density was measured on the surface of each sample using optical microscopy. Four-point bend fatigue tests at different cyclic stresses were conducted on the samples randomly selected from either the top or bottom surface of the plate, in other words, they could have different pore densities. The crack populations found on the surfaces of these samples after fatigue tests were measured, as shown by triangle marks in Figure 3.12. It is evident that the as-measured crack density data appeared to be scattering significantly from a Weibull function of stress. However, the data followed the Weibull function of stress nicely, after each data point was normalized by the pore density measured on the surface of the corresponding sample. The normalized FWL density became now crack initiation rate per area, i.e., FWL rate density, as marked by square marks in Figure 3.12. This demonstrated that the crack initiation rate density, i.e., FWL rate density, should be used to describe the fatigue initiation behavior as Weibull function of stress in engineering alloys which manifested multi-site crack nucleation. This is particularly important for those alloys that have substantially different densities of those microstructural heterogeneities which are potential crack initiation sites. This effect of non-uniform density of microstructural heterogeneities might be ignored in characterization of FWLs in those alloys, such as wrought form of high strength Al alloys, AA2024 and AA7075 alloys, etc., that possess relatively uniform distributions of microstructural heterogeneities that are potential FWLs. This was why the crack population vs. stress curves measured in AA7075 [46] and AA2026 Al alloys could be fitted nicely with Weibull functions, since the particles that are potential FWLs are relatively uniformly distributed in these alloys, i.e., the same

type of samples (e.g., all cut from the same plane of an alloy plate) from such an alloy possessed almost same particle density.

As for fatigue crack nucleation behavior in A713 cast aluminum alloys in this work, almost all the fatigue cracks were also initiated at pores, particularly at shrinkage porosities because of the stress/strain concentration around pores (Figure 3.13(a)). Moreover, the unpredictable feeding of melting metal during solidification commonly made geometry of pores remaining irregular. In some cases the pores were elongated like pre-microcrack in materials as shown in Figure 3.13(a), where fatigue cracks preferred to be initiated. At the same time, there were also many pores that did not nucleate fatigue cracks as shown in Figure 3.13(b). It could be observed in the both SEM micrographs that the angular tips of pores that cracks initiated from were much sharper than those not associated with fatigue cracks, which made stress concentration more easily occurred in the left picture. It was also noticed that the elongated axis of pores initiating cracks were almost perpendicular to cyclic loading direction. Such type of pores with angular tips were more analogous to Mode I crack situation, therefore these pores were more prone to form fatigue cracks than those pores whose long axis parallel or with an acute angle to the loading direction just as pores in Figure 3.13(b). More importantly, the depth of pores affected fatigue crack nucleation behaviors significantly, since the closer the pores located to sample surface, the larger the stress concentration was, especially when the pores were coincidentally tangent to the surface, the maximum stress soared up [44, 105-107]. It was illustrated that why fatigue cracks did not have to be initiated at large pores on the surface [94]. From the observation of fracture surface of A713 as shown in Figure 3.14, only very small part of the pore was exposed to the sample surface, therefore it seemed like a small-size defect on the surface. However, there was a huge pore located beneath the surface and right intercept with surface to induce the stress concentration to an extreme value. In this A713 cast alloy, only this type of pore (FWLs) was more likely to nucleate a detrimental fatigue crack.

3.3.3 FWLs as a Weibull function of strain

In four-point bend fatigue testing, the samples can still be kept flat after failure if the machine is set to be stopped by a critical sample deflection that is just over the value equivalent to the maximum cyclic stress. So that, the FWLs could still be measured on the sample surface with an optical microscope after the sample failed. The FWL density

and strength distribution can be used to quantify the multi-site crack nucleation behavior in a variety of engineering materials. In this work, the four-point bend fatigue tests were carried out under load control at frequency of 20 Hz with $R = 0.1$ and the applied maximum cyclic stress ranging from around the fatigue limit to the ultimate tensile strength of the alloy tested. However, stress was no longer valid to represent the strain produced on the top surface of a sample, if the applied stress exceeded the yield strength. In this work, the strain on the top surface in tension in the sample under four-point bend was measured using a small strain gage ($4.7 \times 3.4 \text{ mm}^2$) glued on the surface. The measured maximum value of the strain cycle was then used to describe FWLs found in AA7075 L-T samples, as shown in Figures 3.15 and 3.16. The corresponding Weibull functions used for curve fitting are as following:

$$N = N_0 \left(1 - \exp \left[-k \left(\frac{\varepsilon - \varepsilon_0}{\varepsilon_0} \right)^m \right] \right) \quad (3.5)$$

$$\ln \left(-\ln \left(1 - \frac{N}{N_0} \right) \right) = m \ln \left(\frac{\varepsilon}{\varepsilon_0} - 1 \right) + \ln k \quad (3.6)$$

$$n = CN_0 \left(\frac{km}{\varepsilon_0} \right) \left(\frac{\varepsilon - \varepsilon_0}{\varepsilon_0} \right)^{m-1} \exp \left[-k \left(\frac{\varepsilon - \varepsilon_0}{\varepsilon_0} \right)^m \right] \quad (3.7)$$

$$N_0 = \int_0^{+\infty} n d\varepsilon \quad (3.8)$$

where all the variables or parameters in Eqs. (3.5) - (3.8) represented the same physical meaning as those in Eqs. (3.1) - (3.4), except for ε and ε_0 which are the strain associated with the applied stress σ and the strain measured at stress of the fatigue limit σ_0 , respectively. It could be observed that the new plots in terms of strain were a little off from the original curves particularly at high stress levels after yielding (110% and 115% pointed by black arrows in Figure 3.15) and the experimental data could be more convincing and scientific. The new fitting results were shown in Table 3.3 and the adjusted R-square was still over 0.95 indicating the fitted regression curve matched the experimental data very well. Even if the multi-site crack nucleation behavior in a higher loading condition need to be quantified in the future, this experimental method would still work well by calibrating the strain using strain gage, i.e. strain control mode fatigue testing.

3.3.4 FWLs-stress curve fitting by different sigmoidal-type functions

As shown in Figures 3.4, 3.7 and 3.12, the crack population vs. applied maximum cyclic stress curves were all S-shape distributions in which the crack population increased slowly at low stress levels followed by rapid increase over medium stresses and finally reached a plateau at stresses close to the ultimate tensile strength. In this work, a three-parameter Weibull type of function (Eq. (3.1)) was used to fit these experimentally measured FWL-stress curves to quantify the FWL density and strength distribution in the alloys studied. The Weibull function was first proposed to quantify some statistical phenomena by W. Weibull in 1951 [153]. It was since used extensively in the evaluation of fatigue properties of materials statistically. For instance, the distribution of size of surface fatigue cracks or pores as crack nucleation sites could be established as a Weibull function in the welded pipe steel and Al-Si sand cast aluminum alloy, respectively [154, 155]. The Weibull function could also be used to characterize fatigue crack growth lives and reliability of turbine, and to predict the fatigue strength probabilities of the components of a series of engineering materials [156-158]. Although the experimental data of FWLs could be fitted well using the three-parameter Weibull function, there are still other types of sigmoidal functions which might show a better or worse goodness of fit in describing the experimentally measured FWL data.

In order to identify the most reliable and consistent function to quantify FWLs, aside from Weibull function, eleven other types of sigmoidal functions were utilized to fit the experimental FWL data obtained in AA7075 T651 L-T, T-S, A713 and AA2026 50% RH samples. As shown in Figure 3.17, all these functions were capable of fitting the data reasonably well. As listed in Table 3.4, the coefficient of determination (i.e., adjusted R-square) for each of these sigmoidal functions, which was a value to describe how close the experimental data were to a fitted function, was calculated in the corresponding set of experimental data. As shown in Table 3.4, these functions were ranked in fitting goodness by the adjusted R-square in each of the four sets of experimental data. It appeared that the Weibull function was the only one that was ranked in top 3 among all these experimental data. Although functions SRichards 1 and 2 were ranked at the first and second place in AA7075 L-T and T-S samples, separately, their rankings were at the bottom for the A713 sample data. It might indicate that SRichards functions were not as reliable as the Weibull function in describing the relationship between FWLs and stress/strain. The Weibull function was likely to be the more appropriate one to quantify

FWLs. For further verification of the fitting goodness of the Weibull function, the residual plots for the top 3 functions from each set of the experimental data were also calculated, as shown in Figure 3.18. It can be seen in Figure 3.18 that the residual patterns of all the selected functions (including the Weibull function) showed somehow unbiased distributions. Therefore, it was indeed more appropriate to use the Weibull function to fit the experimentally measured FWLs-stress/strain curves of engineering alloys.

3.3.4 Evaluation of alloy quality in terms of FWL density

An AA2099-T8E67 Al-Li extrusion bar, which has been developed by Alcoa to replace traditional high strength Al alloys (2xxx and 7xxx series) for use in aerospace requiring excellent damage tolerance, corrosion resistance, high stiffness and low density, was used in the study on the advantages of our experimental methodology evaluating the quality of new designed alloy quantitatively in this section [159]. In this work, the samples for four-point bend fatigue were made along the extrusion direction in the rectangular region of an extruded bar of the AA2099 alloy, i.e. L-T sample, similar as those AA2026 L-T samples. As shown in Table 3.1, Li was added to increase the strength (Table 3.2) and modulus of the alloy, while lowering its density. The AA2099 alloy possesses a strength (554 MPa) higher than that (510 MPa) of the AA2026 alloy along L direction (Table 2). However, it might not be sufficient to evaluate the mechanical properties of Al alloys under a dynamic load by their strengths, since the difference of the strengths between different alloys might not be significant enough to distinguish between the AA2099 alloy with the other high strength Al alloys, such as AA2026, as shown in Table 3.2. In order to better evaluate the quality of these alloys quantitatively under dynamic loading, their FWL density and strength distribution were measured in AA2099 L-T and AA2026 L-T samples in dry air.

In both AA2026 and AA2099 Al alloys, fatigue cracks were preferably initiated at second phase particles as shown in Figures 3.10(a) and (b). However, as shown in Figure 3.19, the population of fatigue cracks measured in both AA2026 and AA2099 Al alloys were increased with the applied cyclic stress, but fatigue cracks initiated in AA2026 were much more than those in AA2099 at the same stress level, and the FWL density for AA2026 was approximately 0.95 mm^{-2} that was almost eight times as 0.125 mm^{-2} in AA2099, which could not be previously recognized quantitatively with the traditional

experimental methods, such as S-N curve measurements. The population of fatigue cracks found in the AA2026 Al alloy was saturated around ultimate tensile strength (510 MPa), whereas only one fatigue crack could be observed on the entire sample surface (area of 60 mm²) under four-point bend fatigue up to around 525 MPa (1.1 σ_y), and the multi-site crack nucleation behavior did not appear until the applied stress reached 625 MPa (1.3 σ_y). This profoundly indicated that the AA2099 Al-Li alloy contained much less potential fatigue crack initiation sites, i.e. fewer constituent particles, which is also verified by optical micrographs (Figure 3.21) of the alloy, than those in the AA2026 alloy. Owing to the fewer potential fatigue crack initiation sites, the AA2099 Al-Li alloy showed a much better quality in terms of the resistance against fatigue crack nucleation, i.e., lower FWL density and better strength distribution, as shown in Figure 3.20. The peak in the FWL strength distribution curve of the AA2099 was located at a stress much higher than that of the AA2026 alloy, and the value (5.59×10^{-4} mm⁻²) of its FWL peak was much lower than that (0.0111 mm⁻²) of the AA2026 alloy. This could partially explain why the Al-Li alloy showed a fatigue strength of 450 MPa, much higher than that (390 MPa) of the AA2026 alloy. The experimental methodology developed in this work has also been used to characterize FWL densities and strength distributions in an austenitic stainless steel [160] and IN 718 Ni-based superalloy [161].

3.4 Conclusions

- Among all the sigmodal functions, the three parameter Weibull-type function was the more appropriate one to describe the relation of FWLs with the applied maximum cyclic stress or strain in engineering alloys.
- Non-uniform distribution of the porosities that were potential FWLs in an A713 alloy could affect the FWL density observed on the sample surface. The crack initiation rate density instead of FWL density should be used in the Weibull function to quantify the relation between FWLs and the applied stress more accurately and reliably.
- The applied maximum cyclic strain should be used in the Weibull function to describe the fatigue crack initiation behavior in an alloy, when the maximum cyclic stress exceeded the yield stress of an alloy.

- The experimental technique developed in this work to characterize FWLs possesses advantages over the traditional S-N curve method to evaluate the fatigue crack initiation behavior of engineering alloys. It could quantitatively characterize the FWL density and strength distribution of an alloy which shows multi-site fatigue crack nucleation, which allows quantitative evaluation of the crack nucleation sites in engineering alloys for alloy design, quality control and improvement.

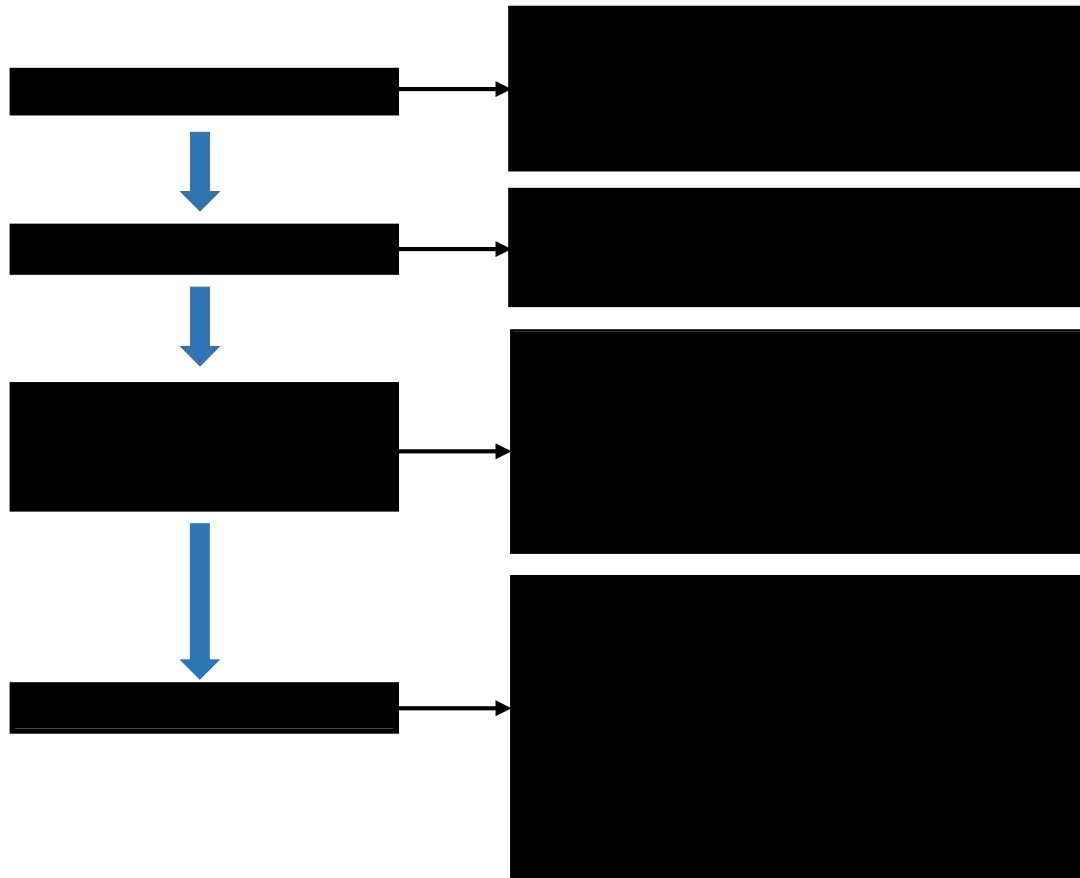


Figure 3.1 the overall operational procedure of this experimental methodology to quantify FWL density and strength distribution

Table 3.1 Chemical composition (wt %) of the AA7075, A713, AA2026 and AA2099.

Alloys	Al	Zn	Mg	Cu	Mn	Fe	Si	Cr	Ti	Li
AA7075	Balance	5.53	2.5	1.61	0.3	0.5	0.4	0.189	0.2	-
A713	Balance	7.0-8.0	0.2-0.5	0.1-1.0	-	-	-	-	-	-
AA2026	Balance	0.1	0.1-0.5	3.6-4.3	0.59	0.07	0.05	-	0.06	-
AA2099	Balance	0.4-1.0	0.1-0.5	2.4-3.0	0.1-0.5	0.07	0.05	-	0.10	1.6-2.0

Table 3.2 Mechanical properties of AA7075, A713, AA2026 Al alloys and AA2099.

Alloys	Ultimate tensile strength (MPa)	Yield strength (MPa)
AA7075	530 (L)/548 (T)	474 (L)/483 (T)
A713	-	171.9
AA2026	510	372
AA2099	554	474

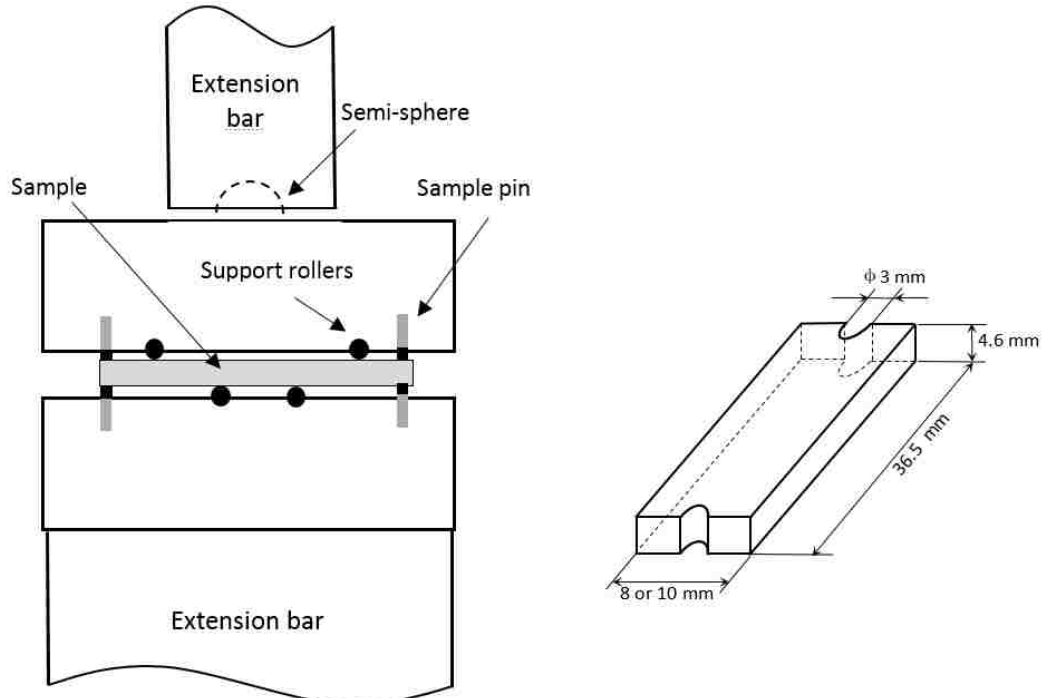


Figure 3.2 A self-aligning four-point bend fatigue testing rig and, the geometry and dimensions of a four-point bend sample.

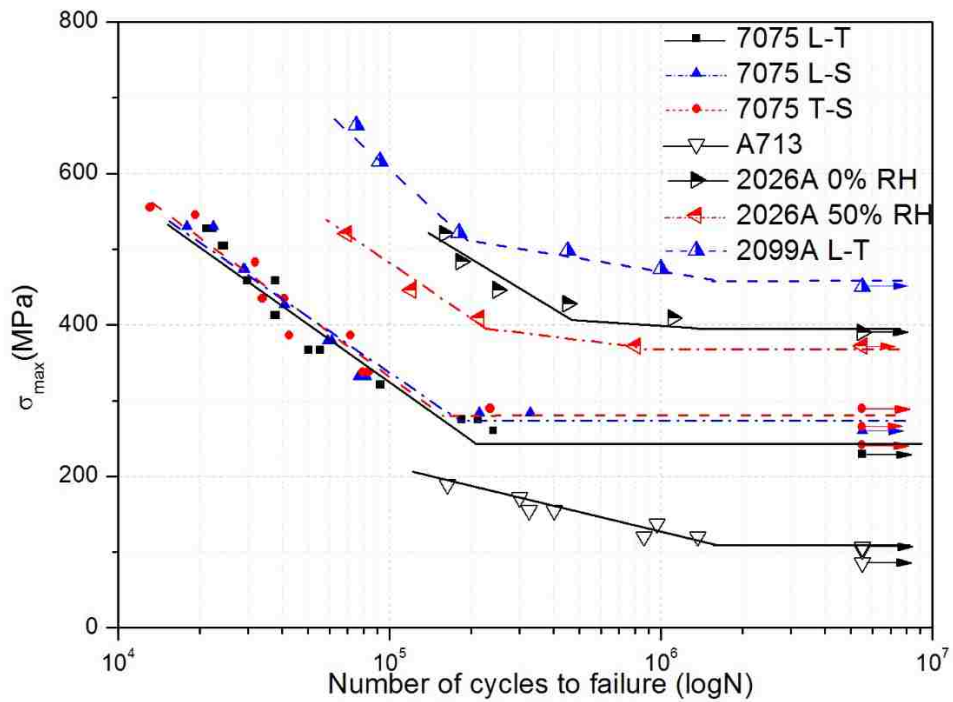


Figure 3.3 S-N curves of the samples in all metallic materials (L-T, L-S and T-S of AA7075-T651, A713, AA2026 and AA2099) by four-point bend fatigue.

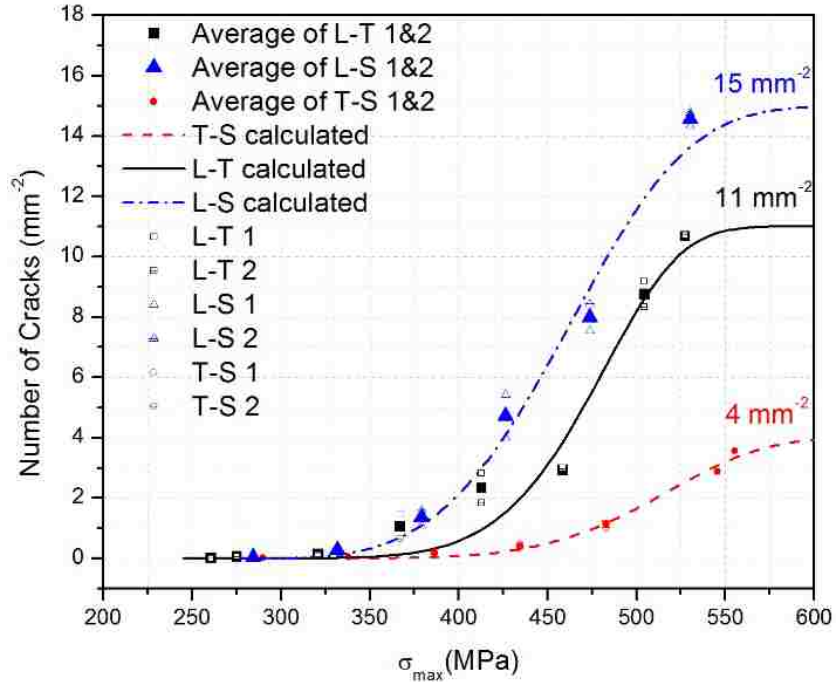


Figure 3.4 Crack population vs. applied maximum cyclic stress curves in L-T, L-S and T-S samples of the AA7075-T651 Al alloy.

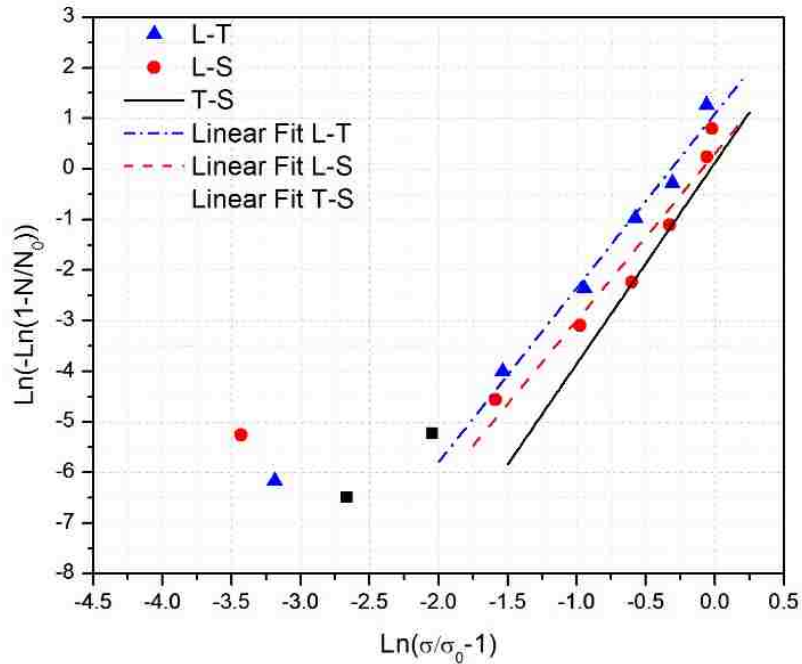


Figure 3.5 $\ln(-\ln(1-(N/N_0)))$ vs $\ln((\sigma/\sigma_0)-1)$ plots fitted by a Weibull function in L-T, L-S and T-S samples of AA7075-T651 Al alloy.

Table 3.3 Parameters determined by fitting N vs σ curves using the Weibull function

Samples	k	m	σ_0 (MPa)	N_0 (mm^{-2})	Adj. R^2
7075 L-T	0.9770	6.5248	243.6	11	0.96285
7075 L-S	3.0229	3.8989	273.0	15	0.98214
7075 T-S	1.9984	5.3632	280.6	4	0.98782
A713	5.5495	2.0631	110.0	0.048 (cracks/pores)	0.96886
2026 0%RH	65.897	3.2726	390	1.0	0.94838
2026 50%RH	10.454	2.4108	335	1.3	0.99956
7075 L-T calibrated	0.6356	4.9375	0.3096% (ϵ_0)	11	0.95815
2099 Al-Li	5.5338	2.0303	450	0.125	0.8727

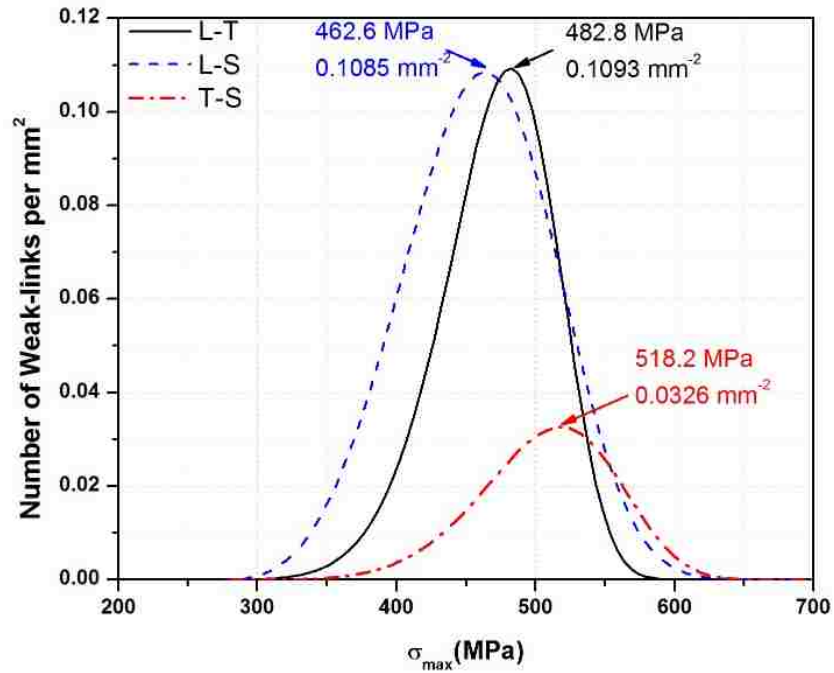


Figure 3.6 Strength distributions of fatigue weak-links in L-T, L-S and T-S samples of the AA7075-T651 Al alloy.

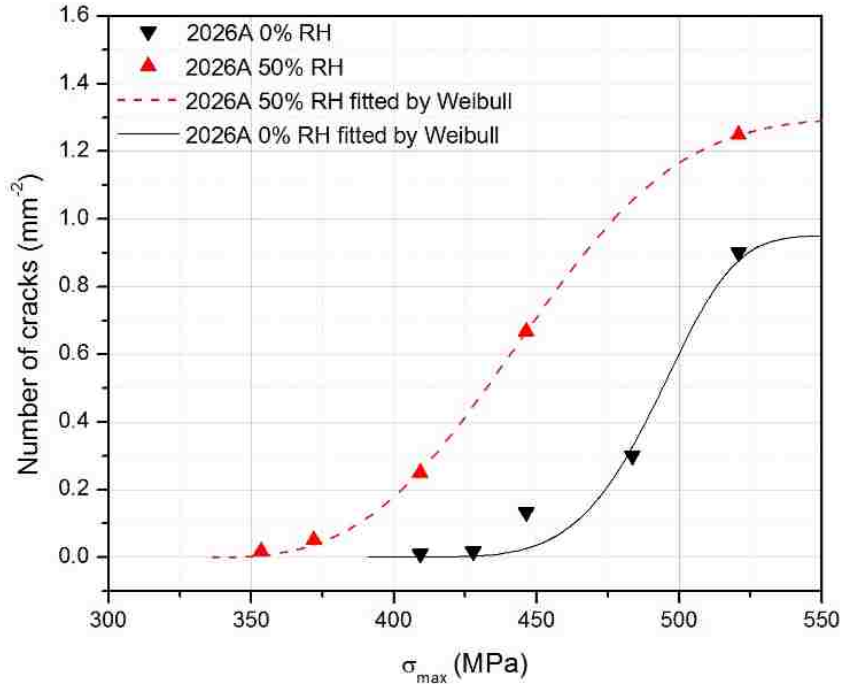


Figure 3.7 Plots of crack population vs applied maximum cyclic stress of AA2026 Al alloy samples in 0% and 50% RH environments respectively.

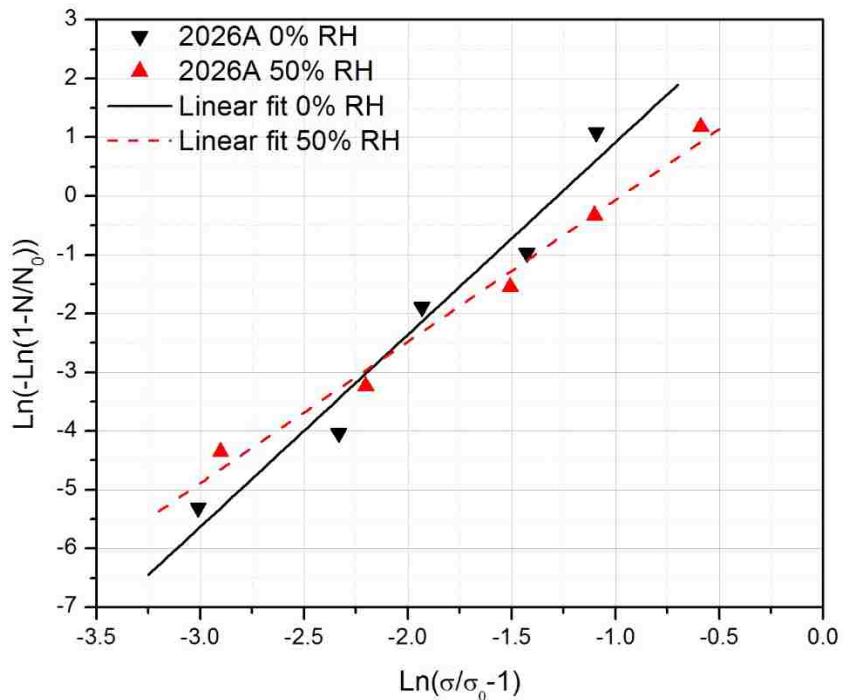


Figure 3.8 Plots of $\ln(-\ln(1-N/N_0))$ vs. $\ln(\sigma/\sigma_0-1)$ fitted by a Weibull function in 0% RH and 50% RH for AA2026 Al alloy

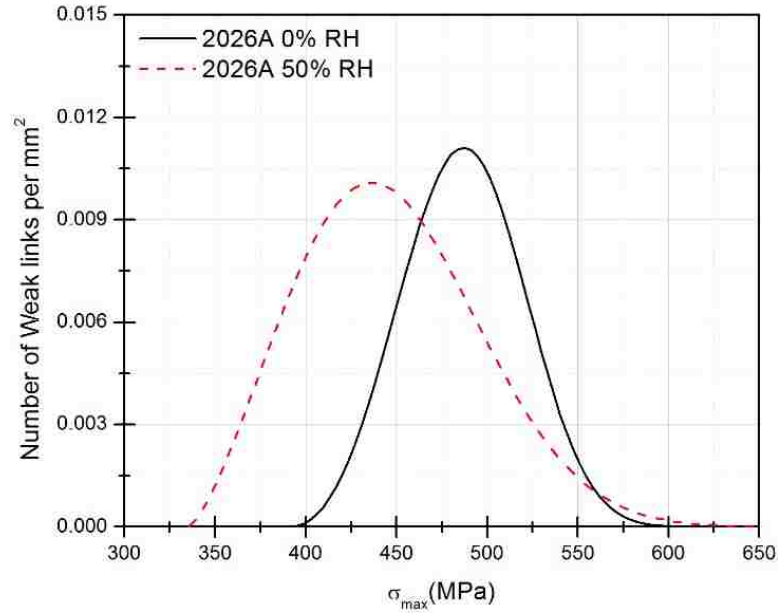


Figure 3.9 Strength distributions of fatigue weak-links in 0% RH and 50% RH experimental environments for AA2026 Al alloy.

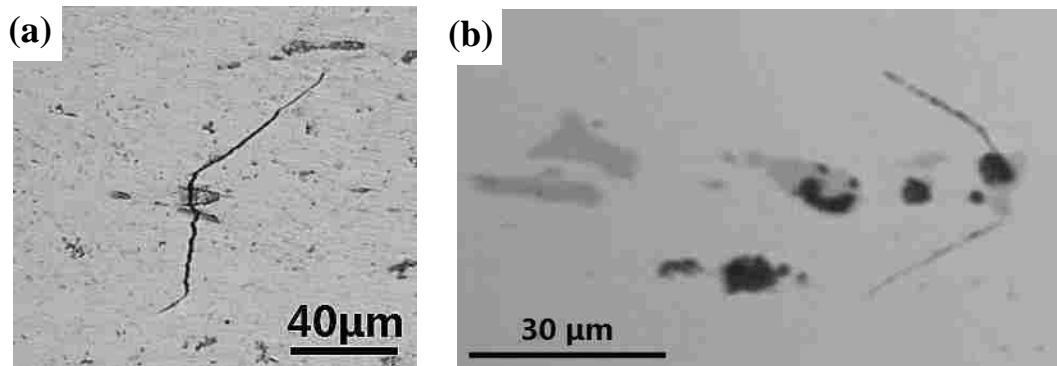


Figure 3.10 Fatigue crack initiated at constituent particle (a) in AA2026 L-T samples at 0% RH and maximum cyclic stress of 483.6 MPa. (b) in AA2099 L-T samples in 0% RH environment.

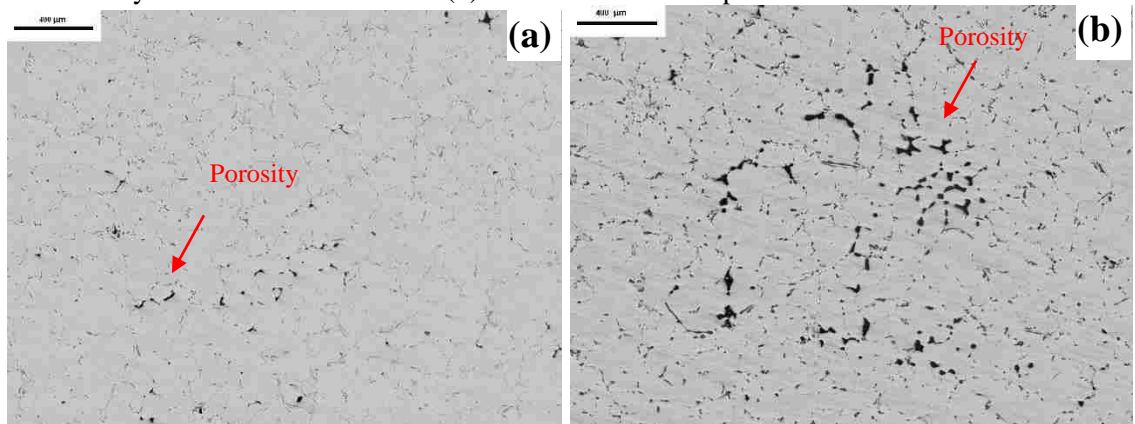


Figure 3.11 the porosity morphology in as-received A713 cast Al alloys with (a) low pore density and (b) high pore density.

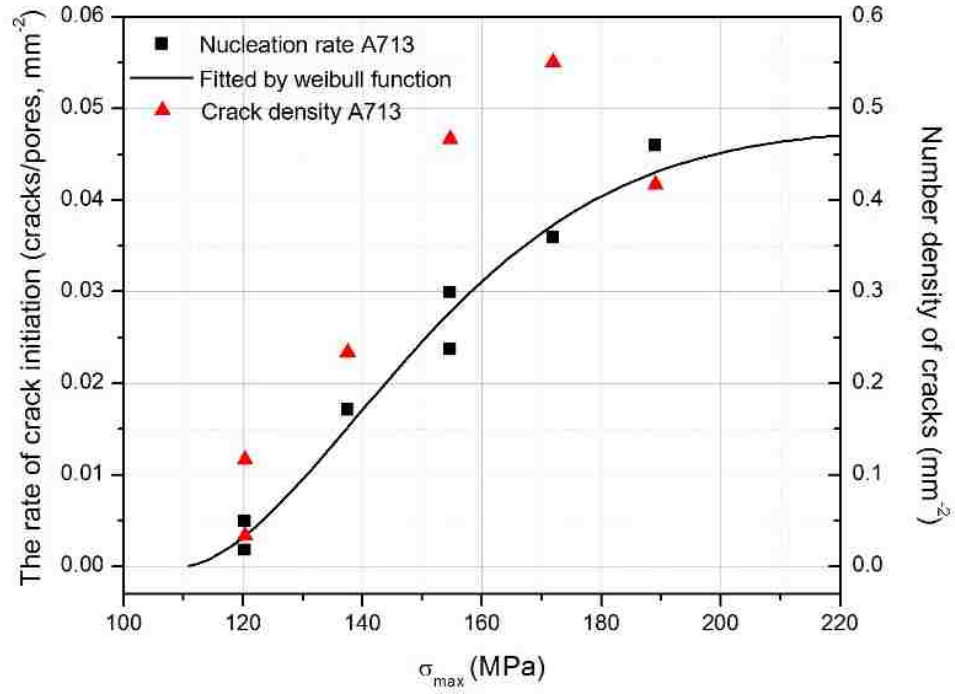


Figure 3.12 Crack population vs applied maximum stress in A713 samples and normalized crack population vs stress could be fitted by Weibull function (black square spots).

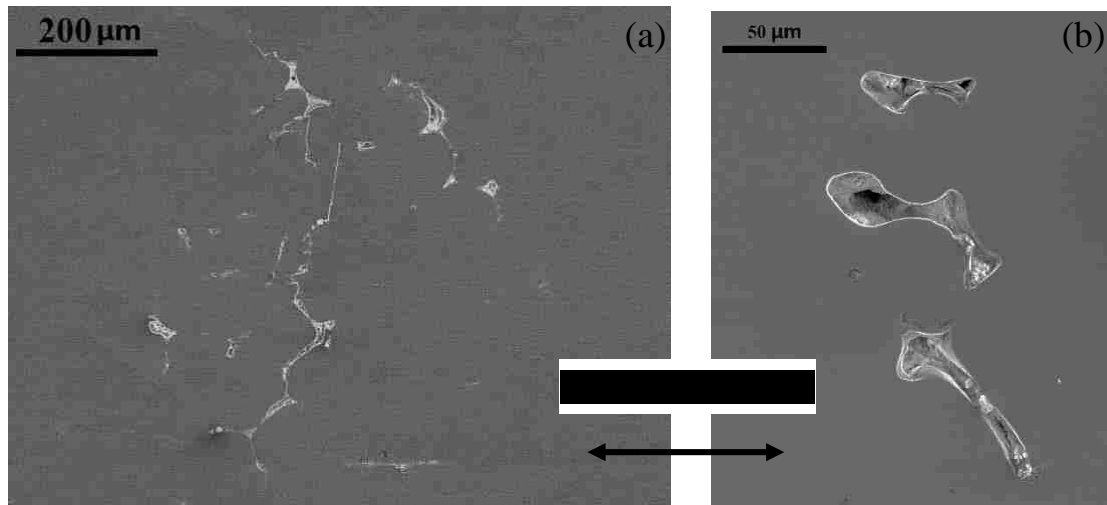


Figure 3.13 (a) multiple fatigue crack initiation at pores on the sample surface, and (b) pores without fatigue cracks initiation during cyclic loading.

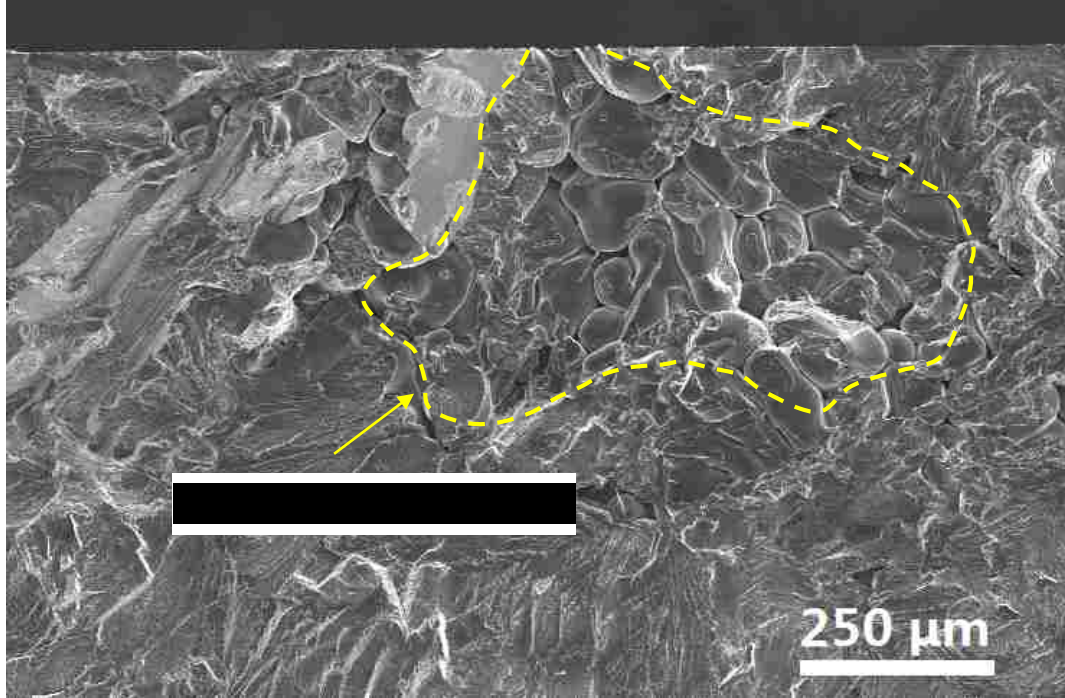


Figure 3.14 Fracture surface of the fatigued A713 sample.

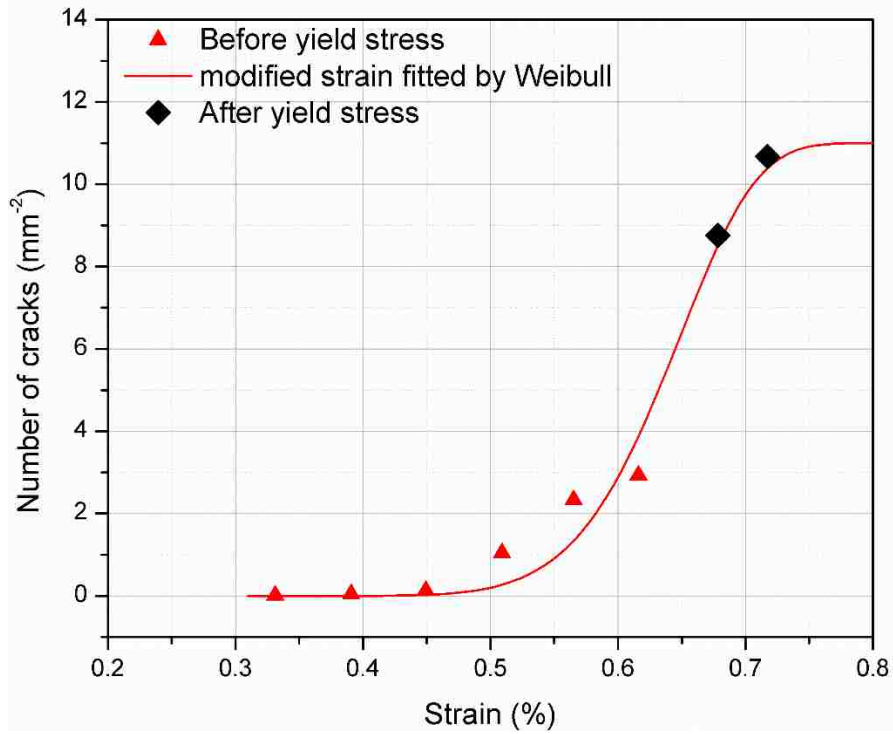


Figure 3.15 Plots of crack population vs calibrated strain measured using strain gage in L-T samples of the AA7075-T651 Al alloy.

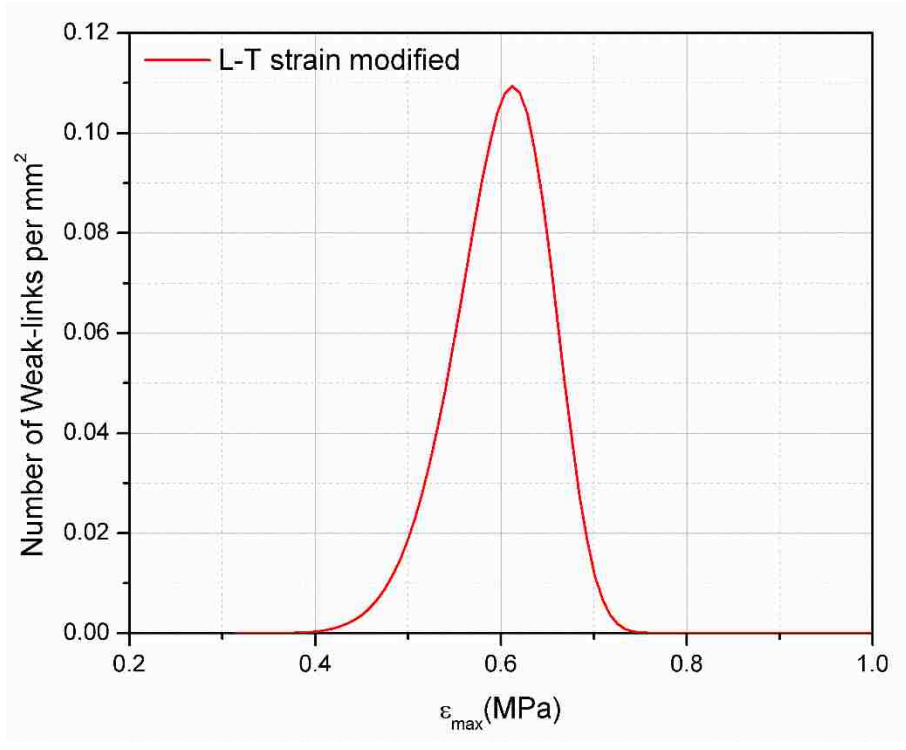


Figure 3.16 Calibrated strain distribution of fatigue weak-links in L-T samples of the AA7075-T651 Al alloy.

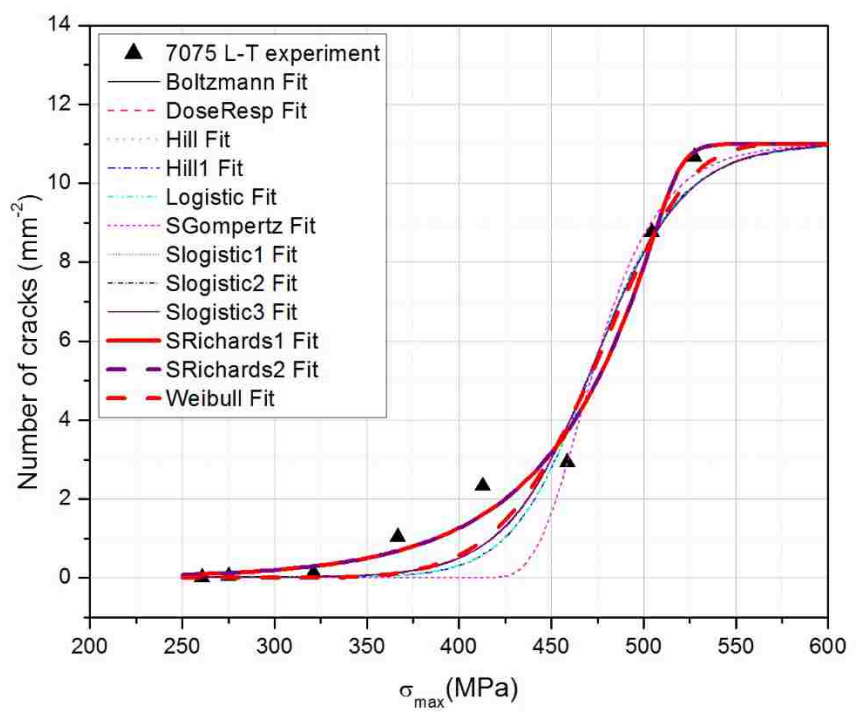


Figure 3.17 Plots of crack population vs applied maximum cyclic stress fitted by a series of sigmoidal functions in AA7075 L-T samples.

Table 3.4 Adjusted R-squares and rankings of experimentally measured FWL data fitted using different types of sigmoidal functions in AA7075 T651, A713 and AA2026 Al alloys

Functions	7075 L-T		7075 T-S		A713		AA2026 50% RH	
	Adj. R-square	Ranking	Adj. R-square	Ranking	Adj. R-square	Ranking	Adj. R-square	Ranking
Weibull	0.96285	3	0.98782	3	0.96886	1	0.99956	2
SRichards1	0.98413	1	0.99669	1	0.95701	11	0.99941	3
SRichards2	0.98413	2	0.99669	2	0.95701	12	0.99941	4
Boltzmann	0.95689	4	0.98659	4	0.96076	4	0.99641	10
DoseResp	0.95689	5	0.98659	5	0.96076	5	0.99974	1
Slogistic1	0.95626	6	0.98659	6	0.95948	6	0.99761	7
Slogistic2	0.95626	7	0.98659	7	0.95948	7	0.99761	8
Slogistic3	0.95626	8	0.98659	8	0.95948	8	0.99761	9
Hill1	0.95085	9	0.98323	10	0.95709	9	0.99885	5
Logistic	0.95085	10	0.98323	11	0.95709	10	0.99885	6
Hill	0.95008	11	0.98402	9	0.9626	3	0.9959	11
SGompertz	0.93412	12	0.97362	12	0.96555	2	0.9874	12

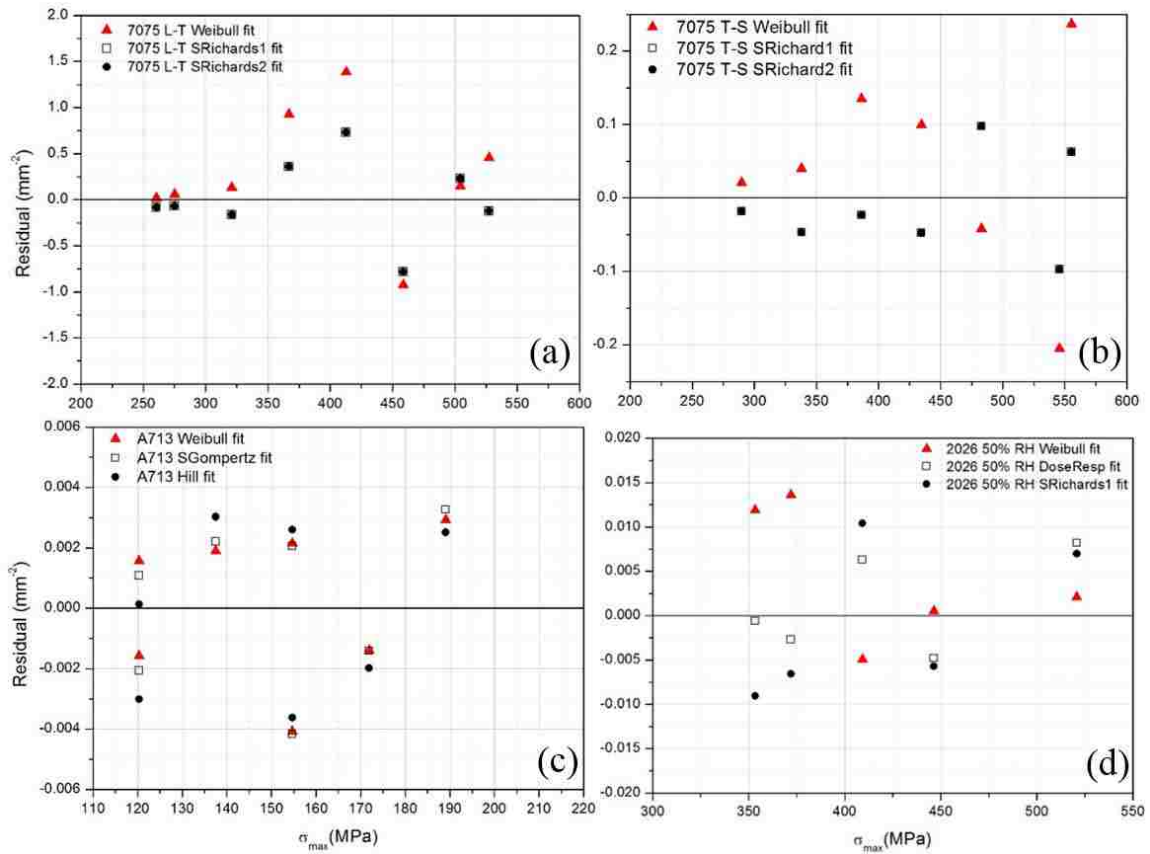


Figure 3.18 Residual plots of fitting results using top 3 best sigmoidal functions matching experimental data (larger adj. R-squares) in (a) AA7075 L-T, (b) T-S, (c) A713 and (d) AA2026 50% RH, respectively.

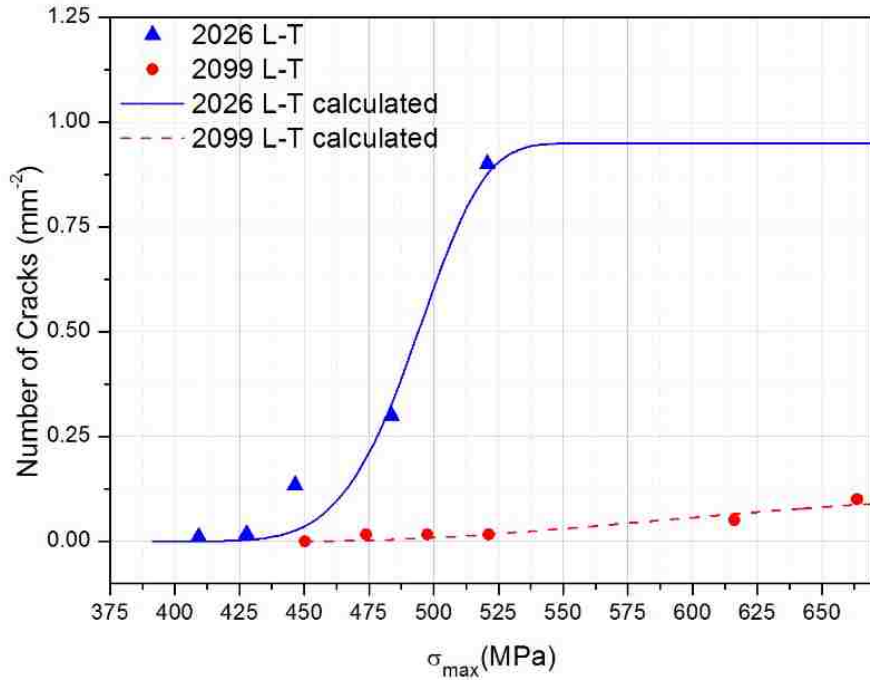


Figure 3.19 Crack population vs. applied maximum stress in AA2026 and AA2099 Al alloys, respectively.

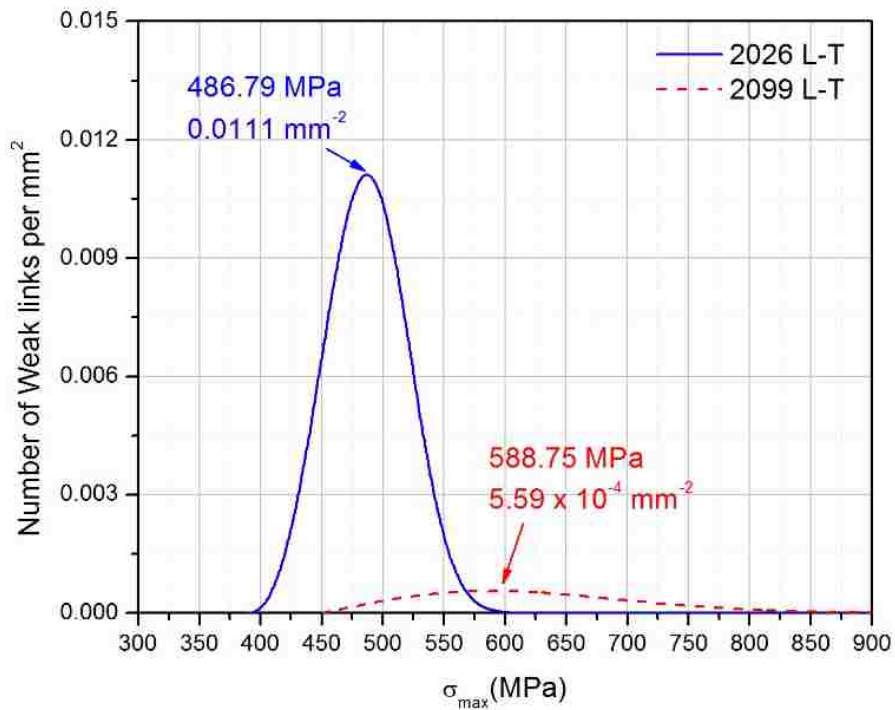


Figure 3.20 Strength distributions of FWLs in AA2026 and AA2099, respectively.

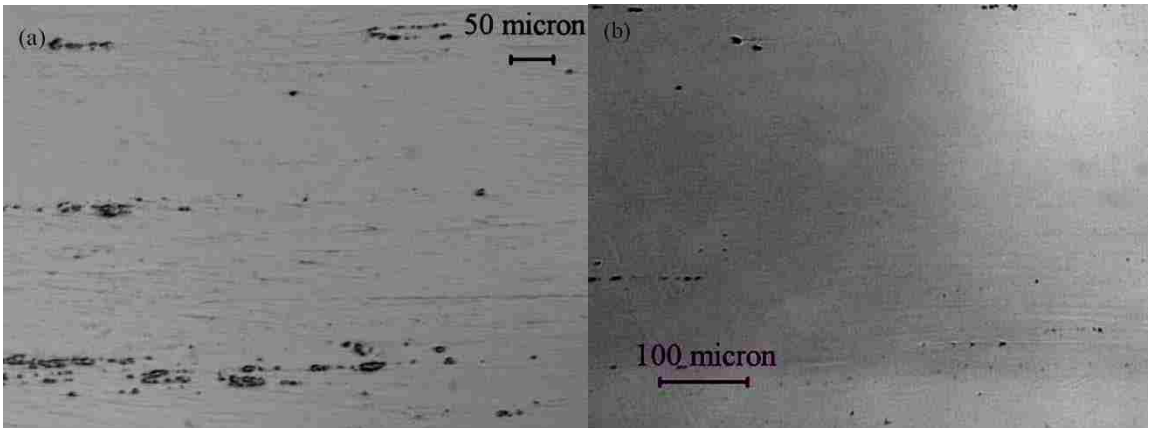


Figure 3.21 Comparison of constituent particles density between (a) AA2026 and (b) AA2099.

Chapter 4 The anisotropy of fatigue crack nucleation at constituent particles in AA7075-T651 Al alloy plate

In this chapter, the experimental method described in chapter 3 will be employed to better understand the anisotropy of fatigue crack nucleation at constituent particles in an AA7075 T651 alloy plate. In overall, Four-point bend fatigue tests were conducted on the L-T (Rolling-Transverse), L-S (Rolling-Short transverse) and T-S planes of an AA7075 T651 alloy plate, respectively, at room temperature, 20 Hz, R=0.1, in air. The populations of crack initiation sites (i.e., fatigue weak-links, FWLs), measured on these surfaces, were found to be a Weibull-type function of the applied maximum cyclic stress, from which fatigue weak-link density and strength distribution could be determined. The alloy showed a profound anisotropy of fatigue weak-links with the weak-link density being 11 mm^{-2} , 15 mm^{-2} and 4 mm^{-2} on the L-T, L-S and T-S planes, respectively. The fact that cracks were predominantly initiated at Fe-containing particles on the L-T and L-S planes, but only at Si-bearing particles on the T-S plane, profoundly demonstrated the pre-fractured Fe-containing particles were responsible for crack initiation on the L-T and L-S planes, since the pre-fracture of these particles due to extensive deformation in the L direction during the prior rolling operation could only promote crack initiation when the sample was cyclic stressed in the L direction on both the L-T and L-S planes. The fatigue strengths of the L-T, L-S and T-S planes were measured to be 243.6, 273.0 and 280.6 MPa, respectively. The difference in grain structure and particle between these planes were responsible for the anisotropy of fatigue strength on these planes.

4.1 Introduction

High strength aluminum alloys, especially 7xxx series, are extensively used in load frame applications, e.g., in aerospace and automotive industries, due to their excellent specific strength and fatigue resistance. In these applications, the lives of these aluminum alloy components are commonly dominated by fatigue crack initiation and early growth, as over 90% of the fatigue life of a metallic structural component is consumed in nucleation and early growth of a dominant fatigue crack [1, 162]. Thorough and quantitative understanding of the crack incubation and initiation behaviors is of paramount importance for determination of the fatigue lives of aluminum alloys. Multiple crack nucleation commonly takes place under cyclic loading, and has been studied in a range of alloys, such as nickel-base superalloys [148], ANSI 304 stainless steels [163] and Al alloys [69, 164], etc. In high strength aluminum alloys, e.g. 2000

and 7000 series Al alloys, it has been reported that multiple fatigue crack nucleation occurs preferably from coarse Fe-containing particles or pores on the surface due to stress/strain concentration at these particles [165-169]. However, it has also been recognized that fatigue cracks are not necessarily initiated at the coarse particles but often at relatively smaller ones [45, 47], and that the crack nucleation rate at particles is typically just about 3% in high strength Al alloys [47]. This indicates that the statistical size distribution of the particles cannot simply be used to describe the multiple fatigue crack initiation behaviors in the alloys, though stress/strain concentration should be one of the major factors controlling fatigue crack initiation at the particles. Zhai et al. [45, 49] have recently developed an experimental method to characterize the multiple fatigue crack initiation behaviors by measuring the fatigue crack populations found on the sample surface in an alloy at different stress levels. The crack population was found to be a Weibull-type function of the applied stress, which allowed quantification of the fatigue weak-link (FWL, i.e., crack initiation site) density and strength distribution in Al-Li alloys and Al-Zn cast alloys. The FWL density and strength distribution are materials fatigue properties which are particularly useful for describing the high cycle fatigue property of the material since fatigue crack initiation takes the majority of the total life of the material.

In high strength Al alloys, there are mainly two types of coarse constituent particles, i.e., Fe- and Si-containing particles which are grey and dark in contrast in an optical microscope, respectively. The Fe-containing particles are commonly believed to be $\text{Al}_7\text{Cu}_2\text{Fe}$, or $\text{Al}_{23}\text{CuFe}_4$ and $\text{Al}_6(\text{Fe},\text{Mn})$ phases [67, 170]. They may also contain Si, since they are sometimes mixed with the Mg_2Si phase [51, 67, 167]. It has been reported in literature that the Fe-containing particles are relatively brittle and could be fractured during forming operations, such as rolling and extrusion, in the Al alloys [26, 57, 71, 171]. The pre-fractured particles could therefore be believed to be the preferred fatigue crack initiation sites due to stress concentration at the micro-cracks in the particles [59, 78]. However, it has also been reported that not all the pre-fractured particles could lead to fatigue cracks and that cracks could also be initiated from non-prior fractured particles in high strength Al alloys [47]. It is still desirable to clarify if fatigue cracks could be initiated from those non-prior fractured Fe-containing particles in these alloys. There might be other factors that could affect fatigue crack initiation at these particles in Al alloys. Si-bearing coarse particles, on the other hand, are believed to be not as brittle as

those Fe-containing ones, and do not contribute to the process of fatigue crack initiation in high strength Al alloys [48, 71]. The question still remains unanswered regarding the effect of the Si-bearing particles on crack initiation if the Fe-containing particles are not pre-fractured in the Al alloys.

The anisotropy of the multiple fatigue crack initiation behavior, especially FWLs, in an Al-Li alloy thick plate was previously investigated by Zhai [49]. In this alloy, the crack initiation behavior varied significantly on different planes of the plate, due to the differences in grain structure and texture between these planes. When loaded in the S (short transverse) direction, the fatigue weak-link density was much higher than that in the L (rolling) direction in the plate, since cracks were preferably initiated along the major grain boundaries of the pancake-shaped grain structure which was perpendicular to the S direction, whereas they were formed along the {100} plane perpendicular to the load axis when loaded in the L direction. There is still a need to investigate the anisotropy of the crack initiation behaviors, in addition to the effect of the preceding fractured Fe- and Si-containing particles on fatigue crack initiation, in 7000 series Al alloys.

In this work, four-point bend fatigue tests were carried out on the L-T, L-S and T-S planes of an AA7075 T651 Al alloy plate, respectively, to study the effects of the preceding fractured particles and the anisotropy of fatigue crack initiation in the plate. The fatigue damage, such as cracks and particles at which crack were formed, were investigated on the fatigued surface. The results obtained demonstrated that the proceeding fractured particles showed a major effect on the fatigue crack initiation behavior, including FWL density and strength distribution, in the alloy.

4.2 Experimental details

4.2.1 The Alloy and samples

In this study, the material used was an AA 7075-T651 Aluminum alloy plate which had been hot rolled to 8 mm in thickness and its chemical composition was 0.4%Si, 0.5%Fe, 1.61%Cu, 0.3%Mn, 2.5%Mg, 5.53%Zn, 0.2%Ti, 0.189%Cr in weight percentage as shown in Table 3.1. The alloy had a pancake-shaped grain structure, average grain size of $4502.8 \times 376.6 \times 45.8 \mu\text{m}^3$ (L×T×S), as shown in Figure 4.1. Its yield and ultimate tensile strengths were measured to be 474 MPa and 530 MPa, 483 MPa and 548 MPa

along the L (rolling) and T (transverse) directions as shown in Table 3.2, respectively. As shown in Figure 4.2, samples of 36.5 x 10 x 4.6 mm³ for four point bend fatigue tests were cut parallel to three different planes, i.e., L-T (Rolling-Transverse), L-S (Rolling-Short transverse) and T-S planes, of the alloy plate. The sample surface in tension under four-point bend was ground using waterproof abrasive papers gradually from grit 240 to 1200, followed by mechanical polishing using alumina powders of 1 micron, 0.3 micron and 0.05 micron in size respectively, and final polishing using a silica colloidal suspension liquid.

4.2.2 Four-point bend fatigue tests

Four-point bend fatigue tests were conducted on the samples mentioned above at a stress ratio $R = 0.1$, frequency of 20Hz, and room temperature, in a sinusoidal waveform, and ambient air. A self-aligning four-point bend rig (for details see ref. [126]) was employed on an Instron 8802 servo-hydraulic materials testing machine. The run-out number was set to be 5,500,000 cycles in S-N curve measurement. As shown in Figure 3.2, the optimum testing geometry of the four-point bend for a uniform stress distribution on the sample surface in tension was loading span of 6 mm, supporting span of 30 mm and sample thickness of 4.5-4.7 mm. The main advantages of four-point bend fatigue testing over the more commonly used fatigue testing such as uniaxial fatigue are 1) convenience of studying fatigue damage on sample surface, 2) simple sample preparation, 3) easy sample mounting and dismounting for studying the evolution of surface fatigue damage by interrupting and resuming fatigue tests. In this work, four-point bend fatigue testing was particularly useful for studying fatigue damage (i.e., fatigue weak-links, FWLs) on surface in the alloy mentioned above.

In order to study the fatigue crack initiation behavior of the alloy, a fatigue test was terminated automatically when the sample deflection exceeded its maximum value, equivalent to the maximum cyclic stress, by 15%, to minimize growth of long cracks in the sample. As a result, the sample surface after the fatigue test could remain sufficiently flat for examining fatigue crack initiation sites on an optical microscope. Samples cut from different orientations in the alloy plate were tested at different maximum cyclic stresses ranging from 48.4% to 115% of yield strength (σ_y) for L-T samples, 48.5% to 111.3% σ_y (530 MPa) for L-S samples, and 55% to 113.5% σ_y (548 MPa) for T-S samples.

Two samples were tested at each stress level and their fatigue data, such as fatigue lives and weak links, were averaged.

4.2.3 Examination of Fatigue Damage on Optical Microscope and SEM

Both optical microscopy (OM) and scanning electron microscopy (SEM) were employed to study the constituent particles where fatigue cracks were initiated on the surface of the alloy. In each sample, optical micrographs were taken at 200× magnification before and after fatigue in the same areas (approximately 11 mm²) on the surface to study the effects of preceding fractured particles on fatigue crack initiation. The crack population, i.e. fatigue weak-links, found on the sample surface were measured at 50× magnification. Fe- and Si-bearing constituent particles, and their fracture rates under fatigue loading were all analyzed statistically with optical microscopy and SEM.

4.3 Results and discussions

4.3.1 S-N curves

As shown in Figure 4.3, the S-N curves of the L-T, L-S, and T-S samples were measured, and their fatigue limits could then be determined to be approximately 243.6 MPa, 273.0 MPa and 280.6 MPa, respectively. The fatigue limit of the T-S sample was the highest among these samples, though it was close in value to that of the L-S sample. The result that the T-S sample had a fatigue limit substantially higher than the L-T sample was consistent with their tensile properties that the yield and ultimate strengths (483 MPa and 548 MPa) in the T direction were slightly higher than those (474 MPa and 530 MPa) along the rolling direction (L direction) in the alloy. Although it is often true that the higher the yield strength is, the higher the fatigue limit of an alloy could be, there were also microstructural factors, such as grain and particle structures, and texture, etc., that could influence the fatigue limit of the alloy. These microstructural factors might have different effects on different stages of the fatigue process, i.e., crack initiation and early growth, and long crack growth, in the alloy. As discussed in details later in this chapter, the FWL density was measured to be much lower (4 mm⁻²) in the T-S sample than those of the L-T (11 mm⁻²) and L-S (15 mm⁻²) samples, which could partially contribute to the higher fatigue limit found in the T-S sample, since the lower FWL density should lead to a longer crack initiation life, thereby a higher fatigue limit. The detailed discussion about these Si- and Fe-bearing particles will be given later in the chapter.

As shown in Figure 4.3, the L-S sample showed a fatigue limit higher than that of the L-T sample, though both the L-T and L-S samples had the same yield strength and the L-S sample even had a FWL density higher than that in the L-T sample, as discussed later in the chapter. This could be largely attributed to the fact that the number density (21.8 mm^{-1}) of grain boundaries was much higher in the direction of fatigue crack growth (i.e., in the S direction) in the L-S sample than that (2.7 mm^{-1}) in the L-T sample, because the alloy had a pancake-shaped grain structure. In the L-S sample, the major grain boundaries were roughly perpendicular to the testing surface (i.e., the L-S plane) and aligned in the L direction, while they were parallel to the testing surface (i.e., the L-T plane) in the L-T sample. Since grain boundaries are a major resistance to short fatigue crack growth, the L-S sample should therefore have a much longer short crack life than the L-T sample. This could be the main reason for the L-S sample to have a fatigue limit higher than the L-T sample, though the L-S sample had a higher weak-link density on the surface.

4.3.2 Crack Population vs. Stress

As shown in Figure 4.4, the number of cracks formed on the surfaces of L-T, L-S and T-S samples at failure were measured against the applied maximum cyclic stress in the AA7075 Al alloy. The crack populations on these sample surfaces were generally increased with the applied stress and eventually reached a plateau at the stress level close to the ultimate tensile strength. At the same stress level, there were more cracks nucleated in the L-S sample than in the L-T sample, and the T-S sample had the fewest cracks. Figure 4.5 shows the typical crack morphologies on the sample surfaces at both low (the maximum cyclic stress is $70\% \sigma_y$) and high (the maximum cyclic stress is $100\% \sigma_y$) stress levels in the L-S samples. At a stress level just above the fatigue limit, there was commonly only one or two cracks initiated that led to the final failure (Figure 4.5(a)), whereas multiple cracks were nucleated at the stress level much higher than the fatigue limit (Figure 4.5(b)). Although most cracks counted on the sample surface in Figure 4.4 were initiated from single initiation sites, some cracks might be formed by coalescence of several cracks initiated separately. Such a coalesced crack was then counted as the number of the individually initiated cracks that formed the crack, since these cracks were predominantly initiated from particles in this alloy. These crack nucleation behaviors as shown in Figure 4.4 were also observed previously in AA8090 Al-Li [14] and 713 Al-Zn cast alloys [13].

Like in the AA8090 Al-Li alloys [14] and 713 Al-Zn cast alloy [49], A 3-parameter Weibull function was used to fit the plots of crack population vs applied maximum stress in Figure 4.4,

$$N = N_0 \left(1 - \exp \left[-k \left(\frac{\sigma - \sigma_0}{\sigma_0} \right)^m \right] \right) \quad (4.1)$$

Where N_0 is the maximum possible number of cracks per mm^2 that can be formed on the surface, equivalent to the crack population observed on the surface between the two loading bars at the stress level close to the ultimate tensile strength (σ_s), $k = \text{constant}$; $m = \text{Weibull modulus}$; $\sigma_0 = \text{fatigue limit}$. σ_0 can be measured by fatigue experiments, and N_0 also can be determined by counting the number of cracks formed at the stress level close to σ_s . k and m could subsequently be determined by fitting the crack population vs stress level curve using the Weibull function (Equation 4.1) which could be rewritten as,

$$\ln \left(-\ln \left(1 - \frac{N}{N_0} \right) \right) = m \ln \left(\frac{\sigma}{\sigma_0} - 1 \right) + \ln k \quad (4.2)$$

The measured crack population vs stress level curves in Figure 4.4 could then be fitted by the linear regression method in a $\ln(-\ln(1-N/N_0))$ vs. $\ln(\sigma/\sigma_0-1)$ plot with m as the slope and $\ln k$ as the intercept values on the $\ln(-\ln(1-N/N_0))$ axis when $\ln(\sigma/\sigma_0-1)$ is zero, as shown in Figure 4.6. Only the data points of crack population at relatively higher stress levels were used in the curve fitting, since the data points just above the fatigue limit were relatively unreliable for use in the linear curve fitting. These data points might likely contain substantial measurement errors as they were small in value, i.e., only 1-2 crack could be initiated on the entire sample surface tested at a stress level just above the fatigue limit, compared to hundreds of cracks observed at higher stress levels. A variation of one crack in the crack population measurement was a measurement error over 50% at the stress level just above the fatigue limit, but it could only cause an error less than 1% if the crack population was over one hundred at a higher stress level.

Table 3.3 shows the parameters (k and m) determined from the curve fitting using Equation 4.2, together with the weak-link densities (N_0), for L-T, L-S and T-S samples,

respectively. It is evident in Table 3.3 that the values of N_0 on the L-T (11 mm^{-2}) and L-S (15 mm^{-2}) surface are about 3-4 times that (4 mm^{-2}) on the T-S surface. As mentioned earlier in the chapter, this was attributed to the differences found in the preferred crack nucleation sites between these samples. In both the L-T and L-S samples, the Fe-containing particles were the preferred crack nucleation sites (Figure 4.7(a)), while it was mainly the Si-bearing particles that led to fatigue crack initiation in the T-S samples (Figure 4.7(b)). The Fe-containing particle densities measured on the L-T and L-S planes of the alloy were 535 and 1053 per mm^2 , respectively, much higher than that, 157 per mm^2 , of the Si-bearing particles on the T-S plane. As a result, the T-S sample showed a relatively lower FWL density (4 mm^{-2}) than those (11 mm^{-2} and 15 mm^{-2}) in the L-T and L-S samples, respectively. This explained why the L-S sample exhibited the largest crack population and the T-S had the lowest crack population at the same stress level in the alloy (Figure 4.4). Same is true for the FWL density being higher on the L-S plane than on the L-T plane, since the Fe-containing particles density (1053 per mm^{-2}) on the L-S plane was about twice that (535 per mm^{-2}) on the L-T plane. The more Fe-containing particles on the L-S plane, the more fatigue cracks could be initiated on the plane.

4.3.3 Strength Distribution of FWLs

As shown in Figure 4.8, the strength distributions of FWLs on the L-T, L-S and T-S planes could be quantified, respectively, by taking the derivative of Equation (4.1) [49]:

$$n = CN_0 \left(\frac{km}{\sigma_0} \right) \left(\frac{\sigma - \sigma_0}{\sigma_0} \right)^{m-1} \exp \left[-k \left(\frac{\sigma - \sigma_0}{\sigma_0} \right)^m \right] \quad (4.3)$$

Where
$$N_0 = \int_0^{+\infty} n d\sigma \quad (4.4)$$

n is the characteristic strength distribution of FWLs in materials, representing the number of newly formed cracks at a specific stress level σ , and C is a scaling constant. N_0 was defined as the FWL density which, together with FWL strength distribution, can be regarded as materials fatigue properties, since they could be used to evaluate the quality of an alloy in terms of fatigue crack initiation behaviors. For a material with a better fatigue performance, N_0 should be as small as possible, the peak in the weak-link strength distribution is as narrow and low as possible, and the peak is located at a stress as high as possible [49]. These properties are directly related to the microstructure and texture in the alloy, e.g., porosities, particles, and grain boundaries, etc. Evaluation of

these properties allows manufacturers to evaluate and optimize the fatigue resistance of alloys by controlling the microstructure and texture in the alloys.

As illustrated in Figure 4.8, there is a strong anisotropy in strength distribution of weak-links in the alloy, with the lowest FWL peak being in the T-S plane. This was consistent with the particle density measurements that the T-S plane possessed the lowest particle density and the L-S plane had the highest density, though the peak values (0.109 and 0.11 mm⁻²) of the FWL strength distribution curves for the L-S and L-T planes were close but several times higher than that (0.03 mm⁻²) of the T-S plane. This might be related to the difference in crack nucleation mechanism between the L-S/L-T and T-S planes, as the pre-fractured Fe-containing particles were the preferred crack initiation sites on the L-T and L-S planes, whereas cracks were predominantly formed from the Si-bearing particles on the T-S plane. Meanwhile, the corresponding strength of the FWLs peak of the T-S plane was the highest and that of the L-S plane was the lowest, which was also consistent with the particle density measurement on these planes, namely, the fewer particles on a sample surface, the higher the strength of the FWL peak will be on the surface.

Although constituent particles were the predominant crack initiation sites, only a very small percentage of them could lead to crack formation. The crack nucleation rates of the particles were found to be only 1.13%, 1.26%, and 0.15% on L-T, L-S, and T-S planes, respectively, in the AA7075-T651 Al alloy. It was reported that, in low cycle fatigue, the crack nucleation rate was about 3% in an AA7075 Al alloy [47]. The authors of relevant paper have recently revealed that the thickness of a particle in surface is a key factor controlling fatigue crack initiation at the particles in AA2024 Al alloys [72], in addition to the effects of particle size and shape, and texture, as investigated previously by Hochhalter, et al. [14, 72] in AA7075 Al alloys. Furthermore, some of the Fe-containing particles could sustain mechanical damage during the prior rolling deformation, which favored crack initiation from these particles when cyclic loaded in the L direction. Because of all the factors mentioned above, it is understandable that the particles in the surface of the alloy might have different strengths for fatigue crack nucleation. It is therefore desirable to characterize the strength distribution of all the potential FWLs and their anisotropy in the alloy.

4.3.4 Constituent particles before and after fatigue

In this work, thirty optical micrographs were consecutively taken at 200x magnification in each of the three sample surfaces (i.e., L-T, L-S and T-S planes) in the same locations before and after fatigue tests, in order to study fatigue crack initiation at particles on surface in the AA7075 Al alloy plate.

4.3.4.1 Before fatigue loading

In this work, constituent particles were statistically analyzed as different categories, such as Si-bearing, non-pre-fractured and pre-fractured Fe-containing particles, using Image-Pro Plus software on the surfaces of L-T, L-S and T-S samples before fatigue the tests conducted at the maximum cyclic stress of 100% σ_y . Because, at this stress level, a sufficiently large number of particles could generate fatigue cracks on the surface, which could lead to relatively smaller errors in the statistical measurement of the FWLs after fatigue tests. The same areas that were studied with optical microscopy on the L-T, L-S and T-S planes were also examined after fatigue tests, so that fatigue crack initiation behaviors could be studied with regard to the particle structures on the surfaces in these samples.

Figures 4.9(a,e,g) show the particle structures on the L-T, L-S and T-S planes before the fatigue tests. As shown in Figure 4.10, the densities of Fe-containing and Si-bearing particles were measured to be 535 and 83 mm^{-2} on the L-T plane, 1053 and 146 mm^{-2} on the L-S plane, and 712 and 157 mm^{-2} on the T-S plane in the alloy. In general, the Si-bearing particles were much less than the Fe-containing particles on all the three planes measured. This is consistent with the recent measurements on volume fractions of these two types of particles in an AA7075 Al alloys using X-ray tomography [53]. The Si-bearing particles, about 0.35% in volume fraction, is only less than one third of that (1.28%) of Fe-containing particles in the alloy. The lower volume fraction could lead to a smaller number density of Si-bearing particles in the AA7075 Al alloy studied in this work. The reason why the density of Si-bearing particles was highest on the T-S plane and the smallest on the L-T plane was attributed to that the alloy was rolled, i.e., extensively deformed in plane strain rolling. On the L-T plane, the alloy was stretched substantially in the L direction, while it remained almost unchanged in the T direction. Assuming the total number of particles was constant, the particle density should be substantially reduced after rolling deformation on the L-T plane, as compared to that

before rolling. On the L-S plane, the alloy experienced both compression in the S direction and stretching in the L direction, thereby the particle density was changed by a minimum amount in this plane, compared to that before rolling deformation. By the same token, the particle density on the T-S plane was significantly increased since the alloy was only compressed in the S direction after rolling. As a result, the Si-bearing particle density was the highest on the T-S plane, and lowest on the L-T plane.

With regard to the marked difference in density of Fe-containing particles among the L-T, L-S and T-S planes, the above arguments are still valid but the Fe-containing particles could be fragmented during the prior extensive forming operation. Such fragmentation was supported by the observation of pre-fractured Fe-containing particles in the alloy before fatigue tests, as shown in Figures 4.9(a,c). No pre-fractured Si-bearing particles were observed in the alloy. The particle fragmentation could increase the particle densities on the L-T and L-S planes by increasing the total number of the particles, but it had no effect on the particle density on the T-S plane. The reason why the number density of Fe-containing particles was much higher in the L-S plane than in the L-T plane was mainly due to the substantial difference in the area change between L-S and L-T planes during rolling, assuming the increase in the number of particles due to fragmentation should be same in both planes. In the L-T plane, the area change mainly resulted from the stretch in the L direction with the width being almost constant during rolling, while it was also contributed from the decrease in thickness, in addition to the same stretch in the L direction as in the L-T plane, in the L-S plane. Comparing to the L-T plane, the number density of Fe-containing particles in the L-S plane was consequently much higher. On the T-S plane, the total number of Fe-containing particles still remained unchanged, in despite of particle fragmentation, after rolling. If each Fe-containing particle was fragmented into three parts in the L direction on average, the particle density of the L-S plane became about 3 times that before rolling. Moreover, because of the pancake-shaped grain structure as shown in Fig. 1, the chance that particles intercepted with L-T surface is lower than that on the L-S plane and thus the particle density increasing induced by prior fracture was not that significant as that in the L-S plane. Therefore, the Fe-containing particles showed the highest density on the L-S plane and the lowest on the L-T plane. The difference in Fe-containing particle density between L-T and L-S planes was responsible for the higher weak-link density (15 mm^{-2}) measured on the L-S plane than that (11 mm^{-2}) on the L-T plane in the alloy,

as discussed earlier in the paper. Since fatigue cracks were preferably initiated at the Fe-containing particles, the more particles, the more crack initiation sites.

The number densities of the pre-fractured Fe-containing particles on the L-T and L-S planes were measured to be 19.5 and 32 mm⁻² respectively, much higher than that 0.18 mm⁻¹ on the T-S plane. The existence of the pre-fractured Fe-containing particles on the T-S plane was likely to be due to the micro-cracks formed during the prior rolling deformation in these Fe-containing particles not being parallel to the T-S plane. Some of these cracks could therefore still appear on the T-S plane. No pre-fractured Si-bearing particles were observed in the alloy, implying that the Si-bearing particles were tough enough to survive the large plastic deformation in the prior rolling deformation, while the Fe-containing particles were brittle, thereby could be fractured during rolling. Further work still needs to be conducted to verify if the Si-bearing particles are tough or brittle at both elevated and room temperatures, as compared to the Fe-containing particles in high strength Al alloys.

No pre-fractured Si-bearing particles were observed on all the L-T, L-S and T-S planes in the alloy. The pre-fracture rate of the Fe-containing particles on the L-S plane was 2.67%, slightly lower than that 3.16% on the L-T plane. This could be attributed to the fact that the Fe-containing particles were roughly pancake shaped, i.e., their sizes in the S direction were much smaller than those in L and T directions. When such a particle was fractured due to large deformation in rolling, on the L-T plane the micro-crack should be more likely to be identified, as it went all the way through the particle in the T direction on the surface. However, there might be a chance that the micro-crack could hardly be discerned on the L-S plane, when the sample surface intercepted with the crack at a location where the crack was tightly closed. As a result, the pre-fracture rate (i.e., the ratio of the number of the pre-fractured particles per area to the total number of particles per area including both Fe- and Si-bearing ones) of the particles measured on the L-S plane appeared to be smaller than on the L-T plane. As discussed in the next section, this was the main reason why fatigue cracks could be initiated from those Fe-containing particles that seemed to be non-pre-fractured in the L-T and L-S samples. These particles were likely to have been damaged by the prior forming deformation, though the damage might not be observed on the surface using optical microscopy.

4.3.4.2 After fatigue tests

Figures. 4.9(b,f,h,) show the fatigue cracks initiated from particles in the same areas as in Figures. 4.9(a,e,g), respectively, after fatigue tests. It is evident in Figures. 4.9(a,c) that not all the pre-fractured Fe-containing particle could lead to fatigue crack initiation on the L-T and L-S planes. And, some fatigue cracks were initiated from Fe-containing particles that were not pre-fractured on the L-T and L-S planes. All these fractured particles after fatigue tests, such as pre-fractured Fe-containing particles with and without fatigue cracks, and Si-bearing particles with fatigue cracks, were counted and statistically analyzed on L-T, L-S and T-S planes, respectively, as shown in Figure 4.11.

On the L-T and L-S planes, and the number density of the pre-fractured Fe-containing particles with and without fatigue cracks were 3.5 and 16 mm⁻², and 6.5 and 25.3 mm⁻², respectively (Figure 4.11). This indicated that fatigue initiation rates from the pre-fractured particles were about 25% on both the L-T and L-S planes. However, it appeared that there were also about 50% of the total fatigue cracks initiated from non-pre-fractured Fe-containing particles. The number densities of the fatigue cracks observed on L-T and L-S planes were 6.8 and 14.4 mm⁻², and number densities of the fatigue cracks formed at non-pre-fractured Fe-containing particles were 3.3 mm⁻² and 7.9 mm⁻² on the L-T and L-S planes, respectively. This phenomenon has been previously found in AA7075 high strength Al alloys [47]. With this result alone, it would be reasonable to believe that some of the Fe-containing particles could be fractured by the cyclic loading used in this work, so that the fatigue cracks could be initiated equally at pre-fractured and non-pre-fractured Fe-containing particles on the L-T and L-S planes. However, since no fatigue cracks were nucleated at Fe-containing particles on the T-S plane where the prior fracture of the Fe-containing particles had no effect on fatigue crack initiation, all the fatigue cracks observed on the L-T and L-S planes must be associated with the damage sustained by these particles due to the prior forming operations. In other words, the particles that did not appear to be pre-fractured but still resulted in fatigue crack initiation must have been damaged mechanically to certain degree, most likely beneath the surface, by the prior plastic deformation, though the damage was not visible on the surface. The damage could still serve as fatigue crack initiators during the fatigue tests.

On the T-S plane, almost all the cracks were initiated from Si-bearing particles shown in Figure 4.9(h). The crack number density was measured to be 1.1 mm⁻² on the T-S

plane, much smaller than those on the L-T and L-S planes. This could partially explain why the T-S sample had the highest fatigue limit, since it contained much less fatigue weak-links. Moreover, unlike Fe-containing particles, the Si-bearing particles were not fractured during the plastic deformation prior to the fatigue tests, thereby making it harder to initiate cracks at these particles, compared to crack initiation at the Fe-containing particles. Consequently, the T-S sample showed relatively higher fatigue limit than the L-T and L-S samples. Previously, the effect of the Si-bearing particles on fatigue crack initiation has not been sufficiently recognized in high strength Al alloys [48], as extensive work has been conducted mainly on the Fe-containing particles [14, 47, 165-169]. The result from the current study indicated that the Si-bearing particles could become the fatigue weak links if the Fe-containing particles were not mechanically damaged in the alloy.

The reason why the Fe-containing particles were the preferred crack initiation sites only on the L-T and L-S planes, but not on the T-S plane, was that they could be fractured roughly perpendicular to the L direction during the prior hot and cold rolling deformation in the alloy. As a result, the micro-cracks in these particles could serve as the fatigue crack initiators only on the L-T and L-S planes but not the T-S plane. On the T-S plane, the Si-bearing particles became the weaker links than the Fe-containing particles, indicating that the Fe-containing particles were harder than the Si-bearing ones. As a result, on the T-S plane, the cyclic loading used in this work could gradually generate enough stress concentration around a Si-bearing particle in the matrix to break the particle, but it was not sufficiently high to fracture a Fe-containing particle on the T-S plane, since the Fe-containing particle is much harder than the Si-bearing particle. These results profoundly verified that the prior fracture in the Fe-containing particles was the main reason for fatigue crack initiation at these particles in high strength Al alloys when loaded in the L direction.

The profound anisotropy of the crack initiation behavior found in the AA7075 Al alloy, as shown in Figures. 4.4 and 4.8, appeared to be different from that studied in an AA8090 Al-Li alloy plate [49]. This was primarily caused by the difference in crack initiation mechanism between the two alloys. In the Al-Li alloy, both L-T and L-S planes have a similar FWL density which is much lower than that on the S-L plane, because, when loaded in the L direction, crack initiation occurs predominantly on the {001} plane that

is perpendicular to the load axis in those grains that have an either cube or Goss orientation. These cube and Goss oriented grains are typical recrystallized grains, typically formed along large angle grain boundaries during hot rolling. Since the probabilities for these grains to form on both L-T and L-S planes should be the same, the weak-link densities on these planes is therefore similar in value in the alloy, unlike in the AA7075 Al alloy where the fatigue weak-link density on the L-T plane was about half of that on the L-S plane. When loaded in the S direction, cracks are formed preferably along the major grain boundaries, leading to a much greater weak-link density on the S-L plane in the Al-Li alloy, since the grain structure is a partially recrystallized and pancake-shaped.

Although pre-fractured or pre-damaged Fe-containing particles played an important role in fatigue crack initiation on the L-T and L-S planes, only a small fraction of them could become detrimental, as their fatigue crack initiation rates were only 17.9% and 20.3% on L-T and L-S, respectively. The majority of the pre-fractured Fe-containing particles appeared to be ineffective on fatigue crack initiation. Furthermore, as shown in Figures. 4.9(f, h), fatigue cracks were not necessarily initiated from the coarser particles. If the particle area on the surface is regarded as a measure for particle size, the area distributions of Fe-containing and Si-bearing particles, and the Fe-containing particles with fatigue cracks were measured, as shown in Figure 4.12. It can be seen in Figure 4.12 that more fatigue cracks were initiated from the Fe-containing particles with areas between 15 and 70 μm^2 , instead of the coarser ones. With a cross-sectioning technique on Focused Ion Beam (FIB), the authors of this paper have recently revealed that the thickness of a particle is a key factor controlling the growth behaviors of the micro-cracks in the Fe-containing particles in AA2024 Al alloys [25], in addition to the effects of texture, particle geometry, etc. studied in AA7075 Al alloys [14, 72]. It is still desirable to further understand quantitatively all the factors that control fatigue crack initiation at particles in high strength Al alloys, in order to quantify their fatigue crack initiation behaviors. In the following chapter, the 3-D effects of those constituent particle on the multiple fatigue crack nucleation behavior in different planes of AA7075 rolled plate will be studied in detail using FIB and other characterization methods.

4.4 Conclusions

- Fatigue weak-links (FWLs) were a Weibull function of applied maximum cyclic stress in the AA 7075-T651 aluminum alloy plate. There was a strong anisotropy of fatigue weak-links in the alloy with the highest weak-link density (15 mm^{-2}) on the L-S plane and lowest (4 mm^{-2}) on the T-S plane. The weak-link density on the L-T plane was 11 mm^{-2} .
- Fatigue cracks were predominantly initiated at Fe-containing particles on the L-T and L-S planes, but only at Si-bearing particles on the T-S plane in the AA 7075-T651 aluminum alloy. The pre-fractured or pre-damaged Fe-containing particles were responsible for fatigue crack initiation at Fe-containing particles on the L-T and L-S planes in the alloy.
- Fatigue limits of the L-T, L-S and T-S planes in the maximum cyclic stress by four-point bend were measured to be 243.6 MPa, 273.0 MPa and 280.6 MPa, respectively. Fewer fatigue weak-links present on the T-S plane attributed to the higher fatigue limit of the plane.

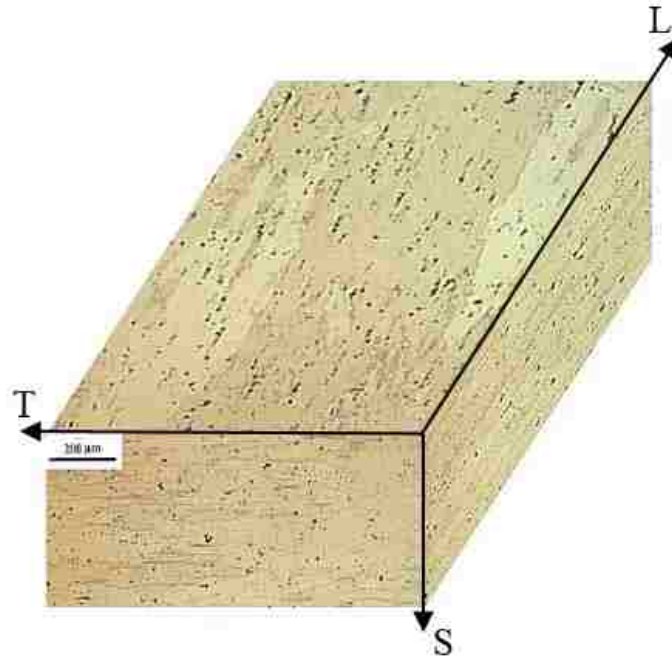


Figure 4.1 The Grain structure of the AA7075-T651 Al alloy.

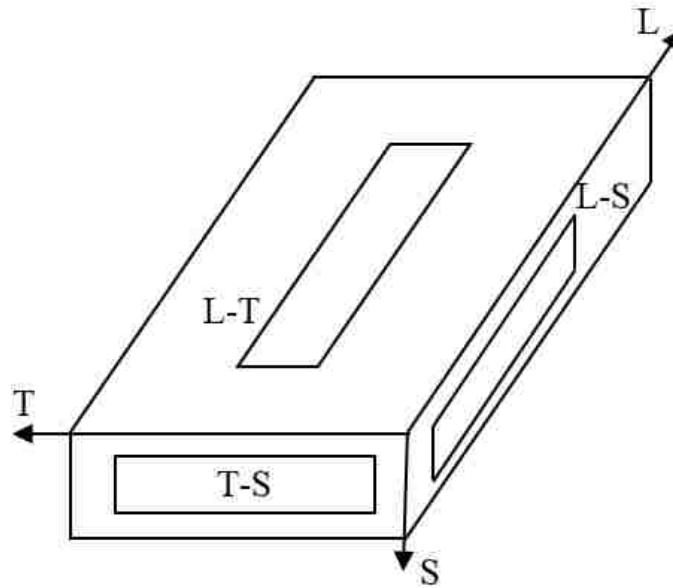


Figure 4.2 The geometry and orientation of the samples for four-point bend fatigue.

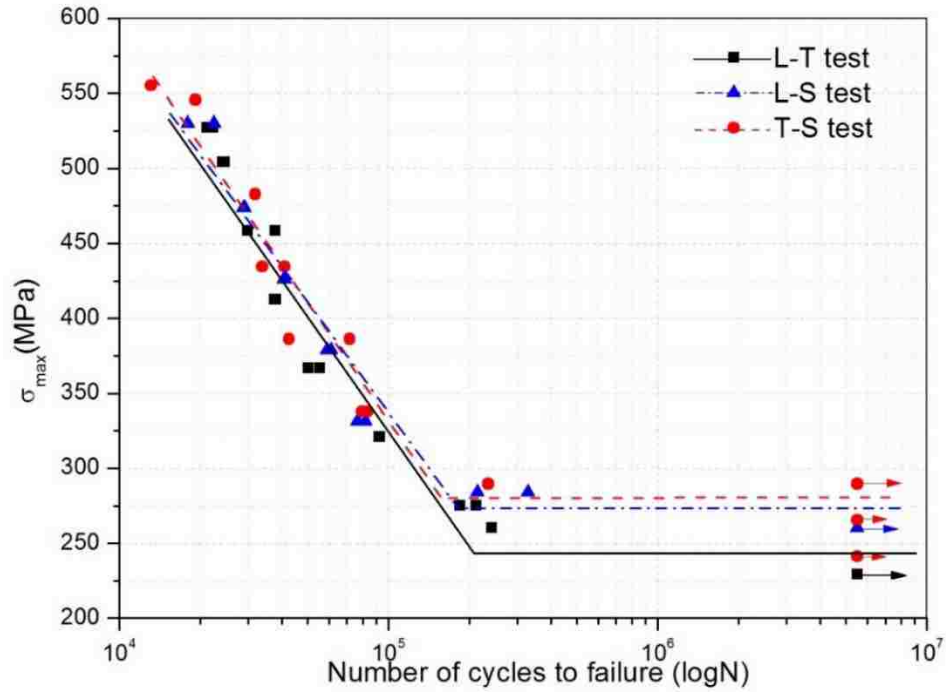


Figure 4.3 S-N curves of the samples on L-T, L-S and T-S planes of the AA7075-T651 Al alloy by four-point bend fatigue.

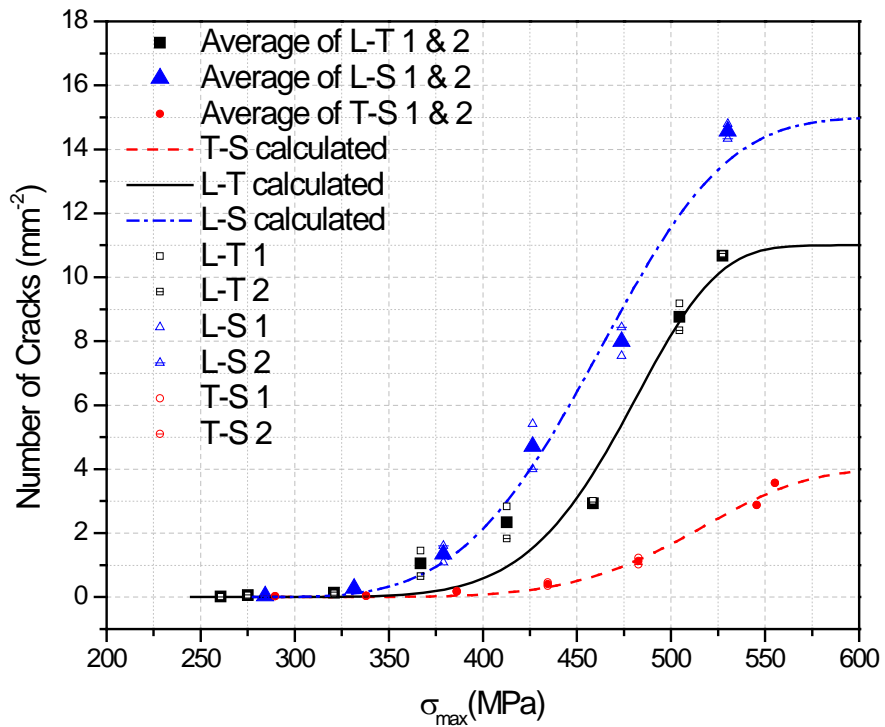


Figure 4.4 Plots of crack population vs. applied maximum cyclic stress in L-T, L-S and T-S samples of the AA7075-T651 Al alloy.

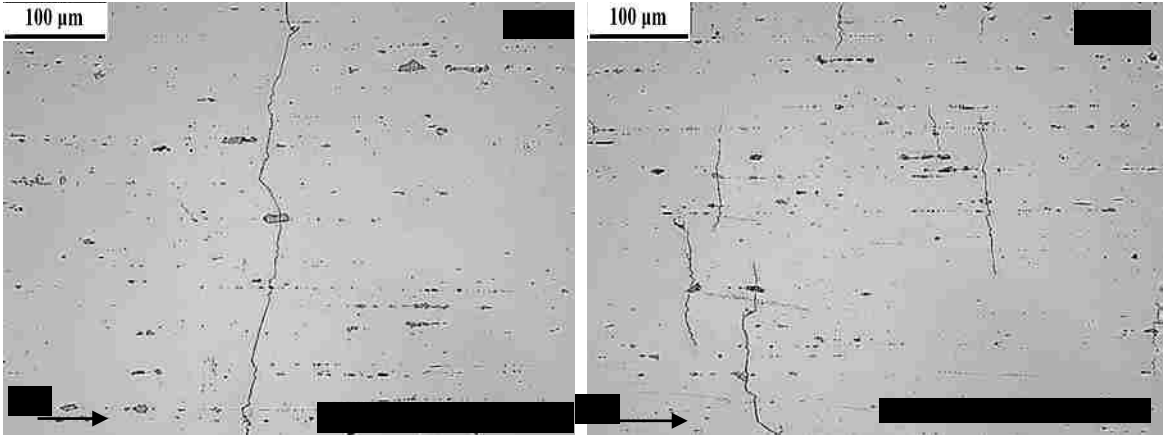


Figure 4.5 (a) Single fatigue crack initiation at a low stress level, the maximum cyclic stress = $70\% \sigma_y$; and (b) multiple crack nucleation at a higher stress level, the maximum cyclic stress = $100\% \sigma_y$, in L-S samples.

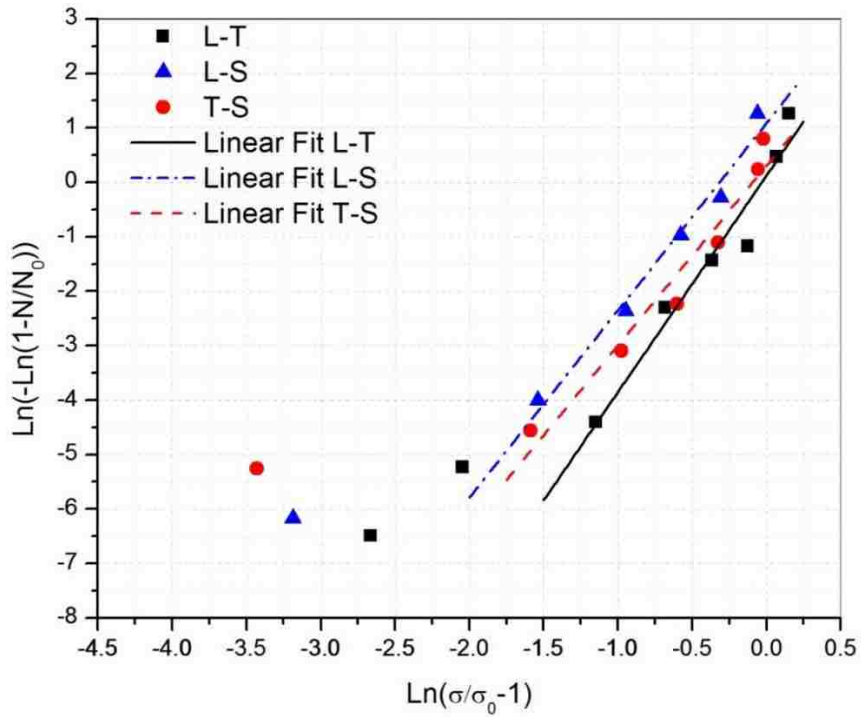


Figure 4.6 $\ln\left(-\ln\left(1-\frac{N}{N_0}\right)\right)$ vs $\ln\left(\frac{\sigma}{\sigma_0}-1\right)$ plots fitted by a Weibull function in L-T, L-S and T-S samples.

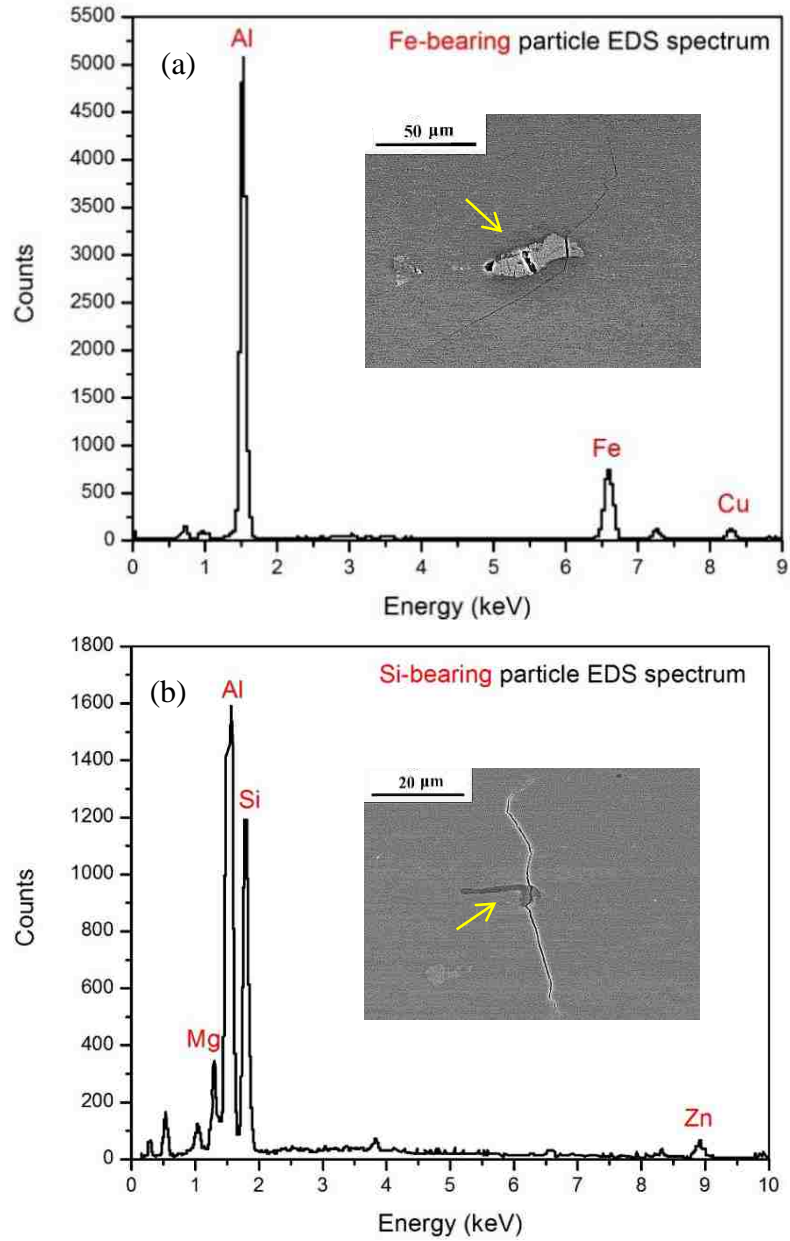


Figure 4.7 EDS spectra of the particles where fatigue cracks are initiated: (a) a pre-fractured Fe-containing particle on the L-T plane, and (b) a Si-bearing particle on the T-S plane in the AA7075 T651 Al alloy.

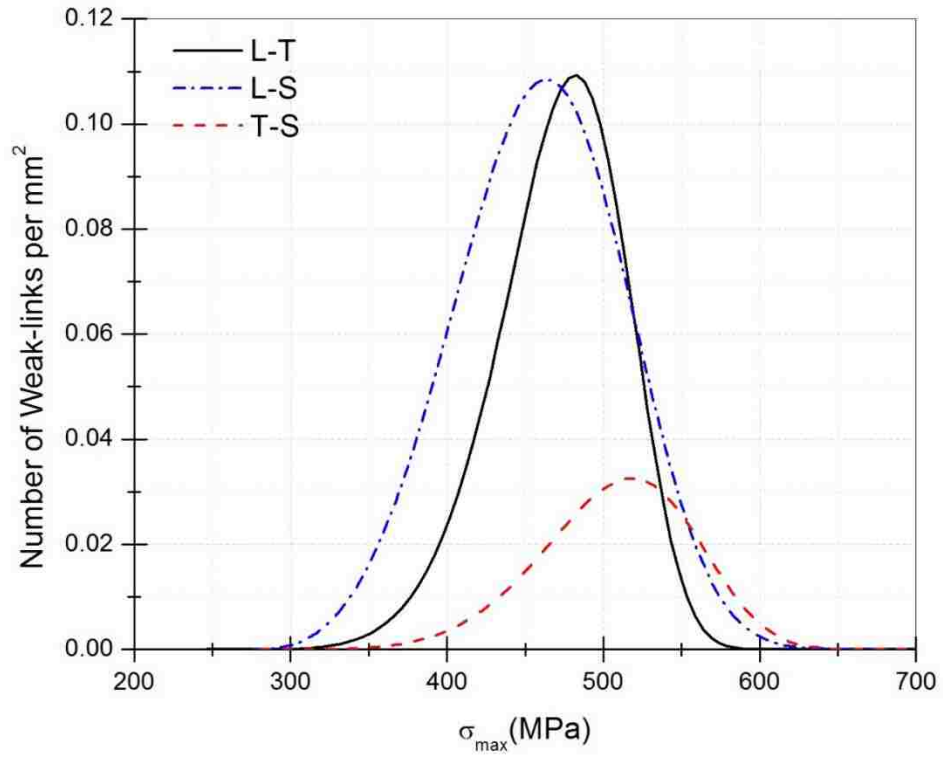


Figure 4.8 Strength distributions of fatigue weak-links in L-T, L-S and T-S samples of the AA 7075-T651 Al alloy.

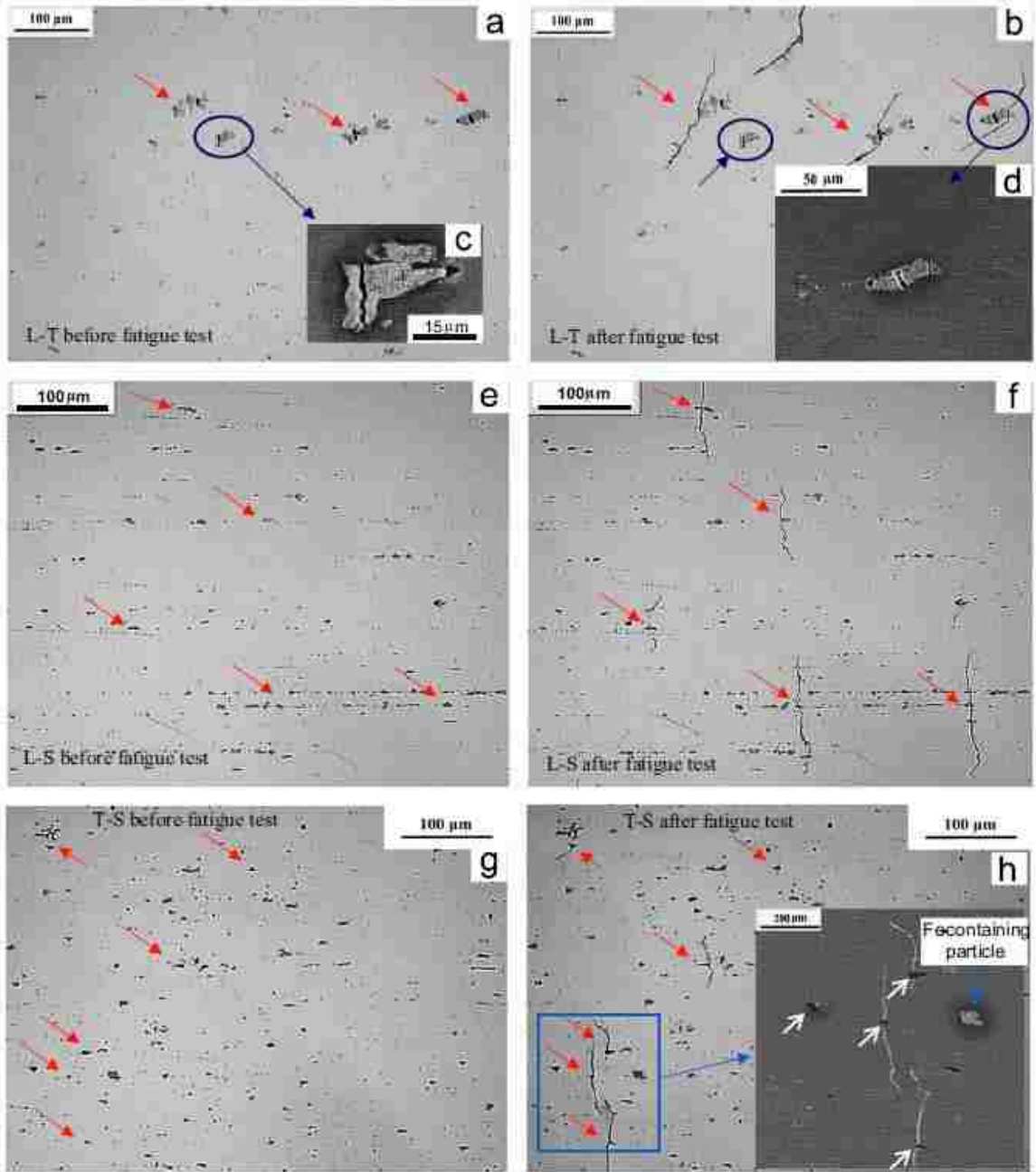


Figure 4.9 Constituent particles in a L-T sample: (a) before and (b) after fatigue tests; a L-S sample: (e) before and (f) after fatigue tests; and a T-S sample: (g) before and (h) after fatigue tests. (c) Pre-fractured Fe-containing particle which does not lead to fatigue crack initiation in L-T samples; (d) a fatigue crack initiated from a pre-fractured Fe-containing particle in the L-T sample; (i) fatigue cracks initiated at Si-bearing particles in the T-S sample, the cracks not necessarily initiated from coarser particles.

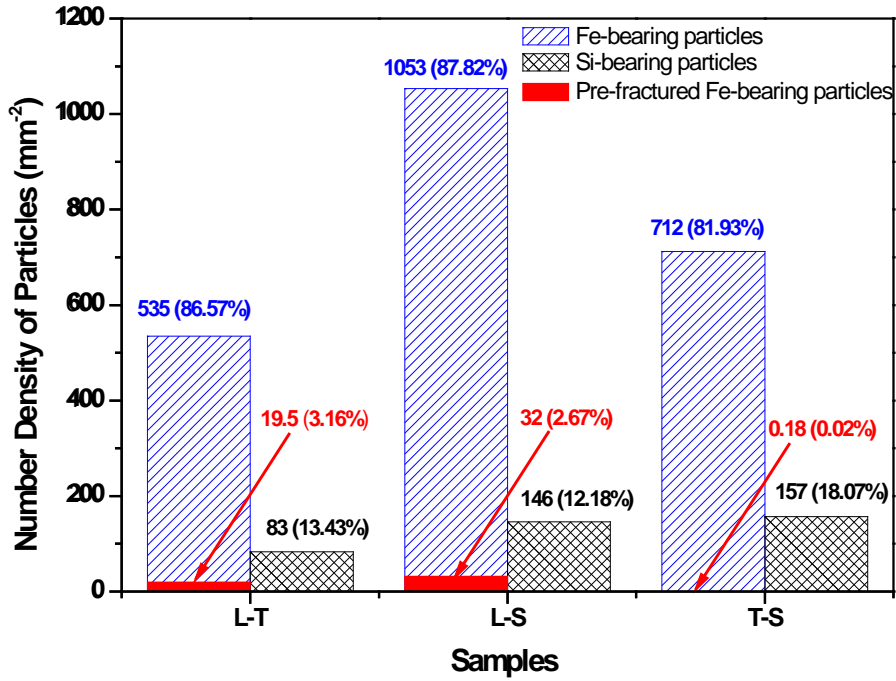


Figure 4.10 Number density (mm⁻²) and fraction of all types of constituent particles in L-T, L-S and T-S samples before fatigue tests.

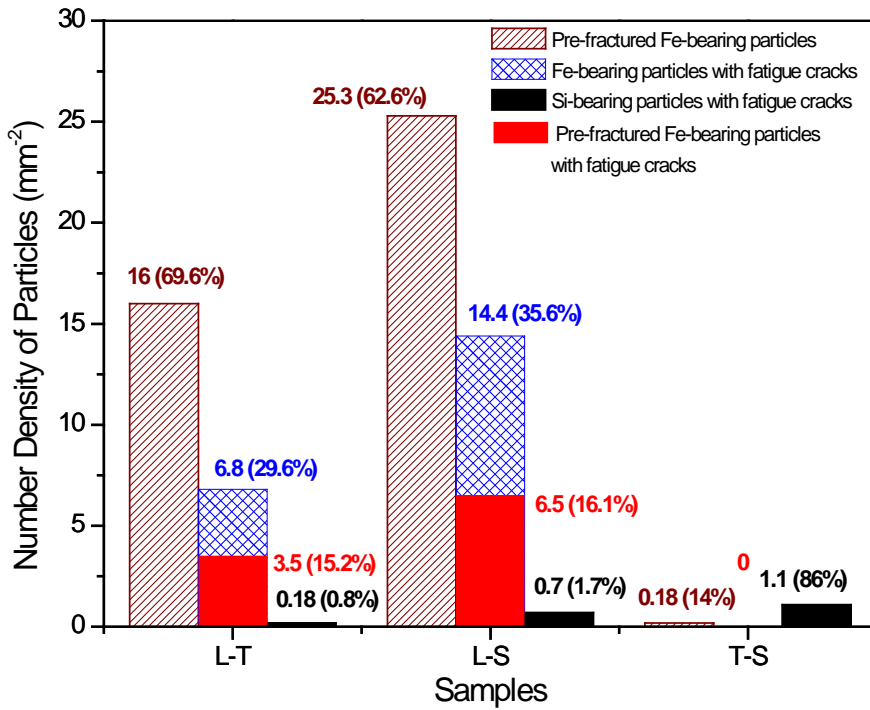


Figure 4.11 Number density (mm⁻²) and fraction of all types of the fractured constituent particles in L-T, L-S and T-S samples after fatigue failure.

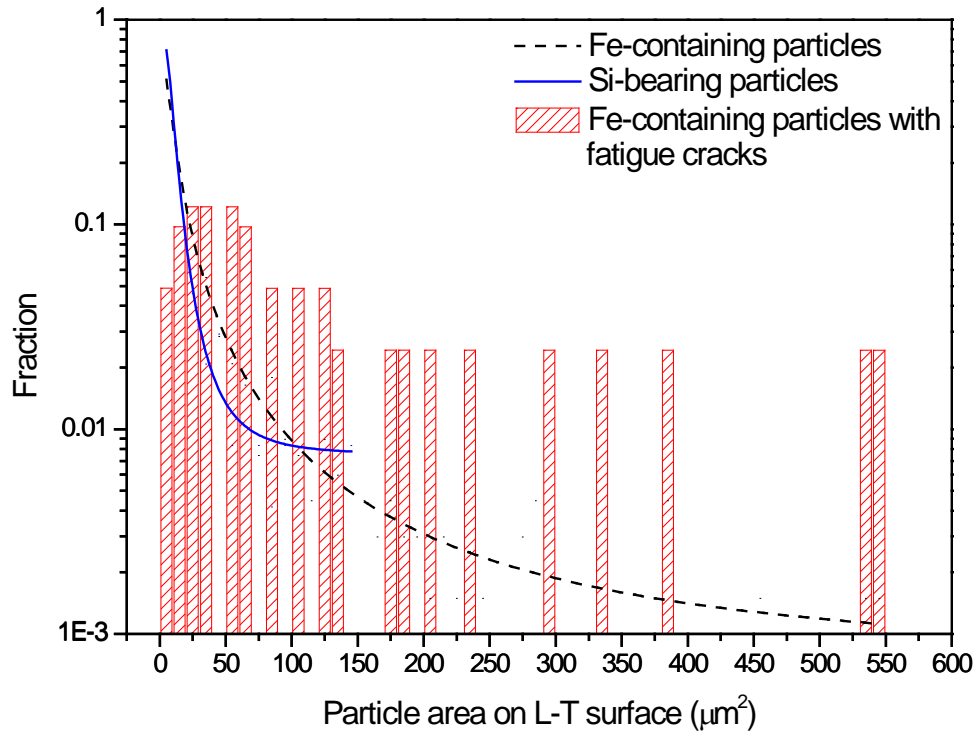


Figure 4.12 The area distribution of Fe-containing particle, Si-bearing particle and Fe-containing particle with fatigue cracks on L-T surface.

Chapter 5 3-D microstructural effects on anisotropic behaviors of fatigue crack initiation at constituent particles in an AA7075 T651 aluminum alloy using focused ion beam combined with EBSD, AFM and Nano-indentation

As described in previous chapters, four-point bend fatigue tests on an AA7075-T651 rolled plate were conducted along L-T, L-S and T-S planes, respectively, at room temperature, 20 Hz, R=0.1, in air. On L-T and L-S planes, pre-cracked Fe-containing particles were the predominant sites for fatigue crack initiation; whereas, on the T-S plane, Si-bearing particles became the preferred crack nucleation sites. In this chapter, in order to investigate the 3-D effects of these constituent particles on the anisotropic behaviors of fatigue crack nucleation in different planes of the AA7075 T651 thick plate, many fractured particles found on the samples after fatigue tests were cross-sectioned using Focused Ion Beam (FIB). It was found that thicker particles were more likely to lead to propagating fatigue cracks, and that those Si-bearing particles at which cracks were formed were all associated with micro-pores in the surface of sample. It was also found that fatigue cracks did not always follow the primary slip planes, i.e., $\{111\}$ planes, within a grain and sometimes may propagate in the direction approximately normal to loading direction. The detrimental Fe- and Si-particles initiating propagating fatigue cracks were not necessarily located in the grains with certain preferential orientations, as revealed with Electron Backscatter Diffraction (EBSD) measurement. Fe-containing particles appeared to be protruded on the mechanically polished surface, while Si-bearing particles were intruded, as observed in the 3-D topography by an Atomic Force Microscope (AFM). This was consistent with hardness measurements using Nano-indentation showing that Si-bearing particles were softer than Fe-containing ones in the alloy.

5.1 Introduction

AA7075 aluminum alloys are extensively used in load frame applications in aerospace industry, due to their high specific strength and fatigue resistance. In these applications, the structural components are often under high-cycle fatigue loading condition, in which a majority of the fatigue lives for these components is consumed in the nucleation period of the microstructurally small fatigue cracks [1, 43, 172]. In high strength aluminum alloys, especially 7xxx series, constituent particles, mainly Fe-bearing constituent particles (Al_7Cu_2Fe or $Al_{23}Fe_4Cu$ [53, 67, 170]), are known to be the preferred fatigue crack initiation sites, because of the pre-fracture or pre-damage in these particles during

thermo-mechanical processing such as rolling and extrusion. Si-bearing constituent particles (Mg_2Si [53, 67]) which are also a constituent phase in Al alloys are believed not to be the effective fatigue crack initiation sites [47, 48, 173, 174].

It has also been reported that multi-site fatigue crack nucleation could take place preferentially at those relatively coarse pre-cracked Fe-bearing particles on the surface in high strength aluminum alloys due to strong stress/strain concentration at these particles [52, 166, 168, 169]. However, based on statistical measurements on the constituent particles with fatigue cracks on the surface, it was found that fatigue cracks were not necessarily initiated at the coarser particles, but often at relatively smaller ones [45, 47]. Furthermore, only a very small percentage of Fe-bearing particles ($\leq 3.5\%$) could lead to fatigue crack nucleation, and most of the initiated crack are non-propagating [46, 47]. Both geometrical features (long and short dimensions, aspect ratio) and spatial location of the particles exhibited a substantial scatter, and were not appropriate to be the controlling factors for fatigue crack nucleation [47]. This might indicate that the 3-D geometrical features and micromechanical properties of these particles, and the local grain orientation, etc., need to be studied thoroughly, in order to identify the controlling factors that determine multi-site crack nucleation at the particles.

Hardness measurement on Fe- and Si-bearing particles were conducted using Nano-indentation in high strength aluminum alloys, showing that Fe-bearing particles are relatively brittle and harder than the matrix, while Si-bearing particles are believed to be relatively softer [52, 53, 71]. The micro-pillar compression technique was also used to evaluate the mechanical properties of those two types of particles, confirming that $\text{Al}_7\text{Cu}_2\text{Fe}$ phase was more brittle with the highest strength, while Si-bearing particles had yield strength that was lower than that of the Fe-bearing ones. This was consistent with some of the Nano-indentation measurement results, but it still remains a controversial subject [52, 53, 71, 175]. It has been further studied that cracks were preferentially initiated at the pre-fractured particles located in grains with an R-cube orientation in AA7010 aluminum alloys [52]. With the development of 3-D characterization techniques, such as Focused Ion Beam (FIB) and X-ray tomography, 3-D geometries of the constituent particles could be characterized to understand their effect on fatigue crack nucleation in high strength aluminum alloys [53, 72]. Although

FIB is a destructive and time-consuming technique, it is attractive to researchers in the field of metal fatigue due to its high-resolution. With FIB, Wei, et al. cross-sectioned a number of fractured particles in a 2xxx series aluminum alloy and found that the thickness of particles was the key factor controlling driving force for the fatigue crack nucleation at the particles. The advantage of X-ray tomography is non-destructive but its resolution is still limited by the voxel size, let alone the fact that high- and Nanosize-resolution tomography is still not widely accessible nowadays [176].

To investigate the multi-site fatigue crack nucleation phenomenon quantitatively, Zhai developed an experimental method to quantify this multi-site crack nucleation behavior in terms of fatigue weak-link (FWL) density and strength distribution in engineering alloys. It was firstly applied to an Al-Li alloy thick plate [49, 177]. It was revealed that the fatigue crack nucleation behaviors were strongly anisotropic on different planes of the hot cross rolled plate. When loaded in the S direction, the FWL density was much higher than that in the L direction in the plate, because fatigue cracks were preferentially initiated along the major boundaries of the pancake-shaped grains lying perpendicular to S direction. They were, however, nucleated along the $\{111\}$ plane perpendicular to the loading axis, when loaded in the L direction [49]. In the AA7075 T651 rolled plate, the multi-site fatigue crack nucleation behaviors on L-T, L-S and T-S planes were also significantly anisotropic, possibly due to the differences in the micro-texture, micro-mechanical properties and microstructure between these planes. It has been recognized that in L-T and L-S planes, the Fe-bearing particles were the preferred fatigue crack nucleation sites due to the pre-fracture of some of the particles occurring during prior thermo-mechanical processing. The fatigue performance in T-S samples (in which the load axis was along S direction) was superior to those on other two planes (i.e., L-T and L-S planes where the load axis was a long L direction) in terms of FWL density and strength distribution. On the T-S plane, almost all fatigue cracks were nucleated at Si-bearing rather than the Fe-bearing particles which were commonly regarded as the predominant crack nucleation sites in 7xxx series aluminum alloys [46].

In this study, to fully understand the effects of constituent particles on the anisotropic fatigue crack nucleation behaviors in a 7075 Al alloy plate, Focused Ion Beam (FIB) was employed to cross-section a number of those particles associated with fatigue crack initiation, including Fe- and Si-bearing particles, after fatigue tests. This allowed

revelation of the 3-D geometrical features and microstructure of those fractured particles beneath the sample surface. Three types of fractured Fe-bearing particles were observed: Type-1: crack in particles never extended into the matrix (thickness: $< 4.1 \mu\text{m}$); Type-2: cracks in particles extended into the matrix but stopped very soon (thickness: $4.1 \mu\text{m}$ - $8.3 \mu\text{m}$); and Type-3: cracks in particles can propagate in matrix (thickness: $> 8.3 \mu\text{m}$). Only two types of Si-bearing particles were found after fatigue tests: Type-1 (thickness: $< 6.5 \mu\text{m}$) and Type-3 (thickness: $> 8.3 \mu\text{m}$). It was found that the thicker particles were more likely to lead to the propagating fatigue cracks, and that those Si-bearing particles associated with fatigue crack initiation were combined with pores. Based on the EBSD measurement, it was also found that there was no explicit effect of microtexture of the grains containing the particles where the fatigue cracks were nucleated. The fatigue cracks did not always follow the primary slip planes, i.e. $\{111\}$ planes, in the grains where the particles were located. The topographic measurements by AFM revealed that Fe-containing particles were protruded on the mechanically polished surface, while Si-bearing particles were intruded on the surface, which was consistent with hardness measurements using Nano-indentation showing that Si-bearing particles were softer than Fe-containing ones in the alloy. This information with regard to the 3-D geometrical features and microstructures, micro-mechanical and micro-textural properties in the vicinity of fatigue crack nucleation sites, i.e. constituent particles, are being used in the development of a 3-D model for simulation of the fatigue crack nucleation behavior and quantification of FWL density and strength distribution in high strength aluminum alloys [178, 179].

5.2 Experimental details

5.2.1 Materials and samples

The AA 7075-T651 Aluminum alloy plate used in this study had been hot rolled to 8 mm in thickness and subsequently solution heat treated followed by artificial aging. Its chemical composition was 0.4%Si, 0.5%Fe, 1.61%Cu, 0.3%Mn, 2.5%Mg, 5.53%Zn, 0.2%Ti, 0.189%Cr in weight percentage, as shown in Table 3.1. In this alloy, there were generally two types of insoluble constituent particles that were formed by eutectic reaction during solidification, including Fe- and Si-bearing particles as shown in Figure 4.7. The alloy had a pancake-shaped grain structure with an average grain size of $4502.8 \times 376.6 \times 45.8 \mu\text{m}^3$ (L \times T \times S), as shown in Figure 4.1. Its yield and ultimate tensile strengths were measured to be 474 MPa and 530 MPa, 483 MPa and 548 MPa along the

L (rolling) and T (transverse) directions, as shown in Table 3.2, respectively. As shown in Figure 4.2, samples of $36.5 \times 10 \times 4.6 \text{ mm}^3$ for four point bend fatigue tests were cut parallel to three different planes, i.e., L-T (Rolling-Transverse), L-S (Rolling-Short transverse) and T-S planes, of the alloy plate. The sample surface in tension under four-point bend was ground using waterproof abrasive papers gradually from grit 240 to 1200, followed by mechanical polishing using alumina powders of 1 micron, 0.3 micron and 0.05 micron in size respectively, and final polishing using a silica colloidal suspension liquid.

5.2.2 Four-point bend fatigue testing

Four-point bend fatigue tests were conducted on the above-mentioned L-T, L-S and T-S samples at a stress ratio $R = 0.1$, frequency of 20 Hz, and room temperature, in a sinusoidal waveform, and ambient air. In order to observe the multi-site fatigue crack initiation on the sample surface conveniently, a fatigue test was terminated automatically when the sample deflection exceeded its maximum value, equivalent to the maximum cyclic stress, by 15%, to minimize growth of long cracks in the sample. As a result, the sample surface after the fatigue test could remain sufficiently flat for examining fatigue crack initiation sites on an optical microscope. Samples cut from different orientations in the alloy plate were tested at different maximum cyclic stresses to obtain S-N curves [46]. For all three planes of rolled plate, those samples fatigued at the maximum cyclic stress between 90% and 100% σ_y were selected for the study of fatigue crack initiation in this work, since, at these stress levels, a sufficiently large number of particles could generate fatigue cracks on the surface. The statistical behaviors of these particles could be investigated in crack initiation by studying their 3-D characteristics using FIB after fatigue tests.

5.2.3 Characterization of 3-D geometries and microstructures of fractured Fe- and Si-bearing constituent particles using SEM/FIB

Since in L-T and L-S planes of AA7075 rolled plate, the Fe-bearing particles were the predominant fatigue crack nucleation sites possibly due to the pre-fracture or pre-damage during the thermo-mechanical processing while Si-bearing particles were the major FWLs in T-S plane [46], the fractured Fe-bearing particles in L-T and L-S samples were referred to as a same subset and Si-bearing particles were the other subset in all the selected fractured particles. Among these fractured particles after fatigue loading, a number of fractured Fe-bearing particles in L-T and L-S samples as well as fractured Si-

bearing particles in T-S samples were cross-sectioned respectively in a dual beam SEM/FIB system, HITACHI NB5000 and FEI Quanta 200 3D, to reveal the 3-D geometries and microstructures of the particles beneath the sample surface. A tungsten film was deposited on the particle surfaces to protect cross-section of particle from damage by the high energy gallium ion beam. In addition to length, width and areas of those fractured particles on the sample surface, their thickness were also measured as the distance between the sample surface and the deepest point along the particle contour beneath the surface after cross-sectioning. An SEM micrograph was taken for cross-section of each of those fractured particles. FIB cross-sectioning was also used to verify the orientation of fatigue crack plane in 3-D by revealing the fatigue crack path beneath the sample surface.

5.2.4 Measurements of micro-texture, hardness and topography of constituent particles using EBSD, Nano-indentation and AFM

The EBSD measurements on the grains where those selected fractured constituent particles were located in were conducted with a HKL EBSD system associated with a Hitachi S4300 FE SEM, to investigate the effects of micro-texture in the vicinity of particles on the fatigue crack nucleation behavior. Based on EBSD measurements, the intersection lines between primary slip planes and surface planes or cross-section planes were determined to verify the crystallographic fatigue crack propagation behavior in AA7075 aluminum alloy. The topographies of the Fe- and Si-bearing particles on the mechanically polished surface were identified using AFM, Q-scope 250, to evaluate mechanical properties of the selected particles indirectly. Subsequently, the Nano-indentation, Nano Indenter G200 by Agilent Technologies, was used to accurately measure the Young's modulus and hardness of the constituent particles as well as the matrix in the AA7075 aluminum alloy. A intact L-T type of four-point bend sample was delicately mechanically polished following the procedure mentioned above, since the relatively large-surface area Fe- and Si-bearing particles on L-T plane could be selected to make each indent right in the center of each particle to avoid the effects from the surrounding matrix. Nano-indentation measurements were then conducted on selected approximately 10 Fe-bearing, Si-bearing particles and matrix sites, respectively. A continuous stiffness measurement (CSM) technique was used to obtain Modulus and Hardness vs. Displacement to the surface curves during indenting process. Young's modulus and hardness for each indentation were obtained by calculating the average

between 200 nm and 500 nm out of total displacement of indenter (1000 nm for Fe-bearing particle and matrix, 600 to 800 nm for Si-bearing particles due to small area). SEM was ultimately used to convince whether each indentation was located inside the particle and more importantly identify the deformation behavior around the indentation.

5.3 Results and discussions

5.3.1 3-D characterization of fractured Fe- and Si-bearing constituent particles after fatigue loading using FIB

Observations on the Fe- and Si-bearing particles with fatigue cracks after fatigue tests using optical microscope (OM) and SEM revealed that there were generally three typical types of fractured Fe-bearing particles and two types of fractured Si-bearing ones in the alloy, as shown in Figures 5.1 and 5.2. In Type-1 Fe-bearing particles on L-T or L-S planes (Figure 5.1(a)), micro-cracks due to fragmentation of the particles during the hot rolling in particles could not be extended into the matrix during fatigue tests. At Type-2 particles (Figure 5.1(b)), micro-cracks could be extended into the matrix but stopped very soon. The cracks at Type-3 particles (Figure 5.1(c)), could propagate into the matrix and became propagating cracks (Figure 5.3) that might lead to the final failure, or coalesced with other cracks (Figure 5.4) [52, 60, 72]. Type-1 Si-bearing particles on T-S plane (Figure 5.2(a)) could not initiate cracks in the matrix as well. In contrast, the Type-3 Si-bearing particles (Figure 5.2 (b)) were found to be always associated with relatively long fatigue cracks which were likely to cause the final failure. Therefore, both the type-3 Fe- and Si-bearing particles were the crack initiators most detrimental to the alloy under cyclic loading. Since all the fractured particles were selected from the samples at the same stress level which was one of the critical factors controlling crack initiation, the observed crack initiation behaviors were likely to be related to the geometrical features of these particles, such as cross-sectional area, length, width, thickness and aspect ratio. Conventionally, it has been believed that the particles with larger area or aspect ratio should be more likely to initiate fatigue cracks, thereby utilizing the probabilistic distribution of particle size to evaluate the fatigue crack initiation properties of materials [166, 172, 180, 181]. However, it could often be observed that fatigue cracks were not necessarily initiated from the coarser but smaller particles in the alloy, as shown in Figures 5.5 and 5.6. The analysis of the total surface area, length, width and aspect ratio of the three types of fractured Fe-bearing particles after fatigue tests revealed that there were no profound relationship between these

geometrical parameters and the crack initiation behaviors at these particles on the surface in the alloy. In other words, all these geometrical parameters could not be used to explain the observed three types of these Fe-bearing particles led to the three-types of cracks in the alloy. The same is true for the fractured Si-bearing particles, as shown in Figures 5.8 and 5.9. These 2-D geometrical parameters described above were invalid in describing the observed crack nucleation behaviors in the alloy [45, 47]. There must be the 3-D geometrical parameters that might dominate the crack initiation behaviors in the alloy.

It has previously been observed that multi-site fatigue cracks were initiated at mainly Fe-bearing particles, and the fatigue crack nucleation behaviors were strongly anisotropic on different planes of AA7075 T651 rolled plates [46-48, 72, 177]. In this work, it was found that fatigue cracks were preferably nucleated at Fe-bearing particles only on L-T and L-S planes, but predominantly at the Si-bearing particles on the T-S plane. This was likely to be caused by the effect of pre-fracture in the Fe-bearing particles during prior rolling deformation. The micro-cracks in the pre-fractured particles were parallel to the T-S plane, thereby presenting no detrimental effect on fatigue crack initiation at the Fe-bearing particles on the T-S plane. As a result, the Si-containing particles became the relatively weakest links for crack initiation on the T-S plane, as will be discussed in detail later in this chapter.

To further reveal the geometries and microstructures of those fractured particles in 3-D, different types of fractured particles, including Fe- and Si-bearing particles, were selected and cross-sectioned using FIB in this work. The cross-sections of the type-1, 2 and 3 Fe-bearing particles are shown in Figures 5.1 (d), (e) and (f), respectively. The thicknesses of all the particles cross-sectioned using the FIB technique were measured and plotted against their length/thickness aspect ratios, as shown in Figure 5.7. It is evident in Figure 5.7 that the aspect ratio cannot be used to categorize these particles into the three types, but they can be divided into three groups in thickness that are equivalent to the three types of the Fe-bearing particles, respectively. Type-1 particles were usually the smallest in thickness, less than 4.1 μm thick, while type-3 particles were the thickest, greater than 8.3 μm . Out of the six selected type-3 Fe-bearing particles, there was a particle forming relatively long crack but only 4 μm thick. The reason for this exception will be interpreted separately later in this chapter by considering

microstructural, micro-textural or micromechanical factors. The thickness of type-2 particles was typical between 4.1 and 8.3 μm . It is indicated that the thicker Fe-bearing particles were more likely to initiate propagating fatigue cracks in L-T and L-S plane. Although multiple factors should be considered for the determination of the driving force for fatigue crack nucleation at a particle, such as applied maximum cyclic stress, grain orientation and 3-D geometrical parameters, etc., the thickness of these particles played a paramount role in promoting fatigue crack nucleation at the particles, and could semi-quantify the driving force by introducing empirical fracture mechanics equations. It has been verified by Wen in AA2024 aluminum alloy that the thickness of the Fe-bearing particles was the key factor for fatigue crack initiation. The driving force, ΔK , of the micro-crack inside particles could be estimated using the equation for quantifying the driving force for a semi-circular surface crack in an infinite matrix [72, 182].

For the two types of fractured Si-bearing particles in T-S plane, the selected fractured particles were also cross-sectioned using FIB, and it can be seen from Figures 5.2 (c) and (d) that the type-3 Si-bearing particle was much thicker than type-1 particle. The plots of aspect ratio (length/thickness, i.e. T/L) vs. thickness showed that the type-1 Si-bearing particles were all thinner than 6.5 μm in thickness, while the thickness of type-3 Si-bearing particles were almost greater than 8.3 μm with one exception that one type-3 particle was located in the region of type-1 particles. Nevertheless, the thickness of fractured Si-bearing particles appeared to be a key factor controlling the fatigue crack nucleation behavior at Si-particles on T-S plane of the alloy. It should be further noticed that there was a pore inside the type-3 Si-bearing particle in Figure 5.2 (d). In this work, it was found that all the cross-sectioned type-3 Si-bearing particles contained a pore. That could profoundly reveal that the pores inside type-3 Si-bearing particles were the initial damage needed to nucleate fatigue cracks at the particles, since these particles could hardly be fractured during the prior deformation processing. The porosities acted as the predominant fatigue crack source in casting aluminum alloys. Because the strain or stress concentration increased significantly around pores especially when the pores were just buried beneath the sample surface [36, 44, 183]. In AA7075 aluminum alloy, the pores also remain from the solidification and thermo-mechanical processing, the majority of which were always associated with the constituent particle, including Fe- and Si-bearing particles [53, 176]. However, the type-3 Fe-bearing particles were hardly observed to be associated with pores from the cross-sections of Fe-bearing particles

using FIB (Figures 5.1 (d)-(f)) and the fracture surface of L-S sample (Figure 5.3). Based on the finite element simulation of fatigue crack initiation on inclusions and voids, only the pores and particles debonded with matrix were the critical crack nucleation sites. In other words, those particle well bonded with matrix may not become the active fatigue crack sites [36]. It can be observed from the cross-sections of those fractured Fe-bearing particles in Figures 5.1 (d) - (f) that all three types of Fe-bearing particle were all well bonded with matrix, indirectly verifying that the pre-crack or pre-damage in the Fe-bearing contributed to the fatigue crack nucleation when loading was parallel to L direction. Conversely, the type-3 Si-bearing particle was obviously debonded with matrix which can be observed from both the cross-section and sample surface as shown in Figure 5.2 (d). Therefore, in T-S samples, when under cyclic loading parallel to T direction, pre-cracks in Fe-bearing particles were not perpendicular to the loading direction, and thus the thicker or debonded type-3 Si-bearing particle associated with pores became the major fatigue crack nucleation sites.

There were two exceptions of thinner particles (Fe-containing, 4.1 μm thick, and Si-bearing, 3.6 μm thick, particles) causing type-3 cracks. It seems controversial with the conclusion that the thickness of particles was the key factor controlling the driving force of fatigue crack nucleation. In reality, it is not the case because the fatigue crack nucleation behavior is not attributed to only one factor but many other factors as well. It is shown in Figure 5.11 that the type-3 Fe-bearing particle with thickness around 4 μm still could form the relatively long fatigue crack. This Fe-bearing particle was actually mixed with Si-bearing particle pointed by the yellow arrows in Figure 5.11 (a), and thus the composite particle facilitated the fatigue crack formation by coupling with the softer Si-bearing particle which was readily broken and debonded with matrix during cyclic loading. The cross-section using FIB was the evidence for particle's debonding with matrix, and the hardness measurement will be conducted in the following chapter demonstrating that Si-bearing particle was softer compared to Fe-bearing particle [36, 52, 53]. The exceptional Si-bearing particle was still more detrimental to the final failure compared to type-1 particle, Even if the thickness of this particle was only 3.6 μm , because on the surface as shown in Figure 5.12 (a) the fatigue crack was propagating along the interface between particle and matrix implying that the interface was weakened by the debonding. More importantly, the 3-D geometry was identified that there was a pore that accounted for approximately 60% or more out of total volume of this type-3

Si-particle. The strain or stress concentration will significantly increase around this type of Si-bearing particle. Hence, even if relatively thin, this type-3 particle was coupled with internal pore just buried beneath the surface and debonded interface which both facilitated the formation of propagation of fatigue crack, i.e. to possess extremely high crack nucleation driving force [36, 44]. In overall, the thicker pre-fractured or pre-damaged Fe-bearing particles were the critical fatigue crack initiation sites in L-T or L-S plane. The thicker Si-bearing particles associated pores were more likely to nucleate propagating cracks in T-S plane. The debonded interface between particle and matrix could facilitate the fatigue crack nucleation as well.

5.3.2 The effects of micro-texture on fatigue crack nucleation at constituent particles using EBSD

In conjunction with electron backscattering diffraction (EBSD) technique could crystallographic orientations of the grains where all selected fractured particles initiating non-extended, extended and propagating fatigue cracks were located be obtained, such that the local micro-textural effects on the fatigue crack nucleation could be investigated. For fatigue crack nucleation events at Fe-bearing particles in L-T and L-S, the parent grain orientations of all the 3 types of fractured particles were represented in a $\{111\}$ pole figure as shown in Figure 5.13: four type-1 Fe-bearing particles, six type-2 Fe-bearing particles and seven type-3 Fe-bearing particles. Similarly, fourteen type-3 Si-bearing particles in T-S sample were presented in another $\{111\}$ pole figure (Figure 5.14), and typical texture components in aluminum alloy rolled plate were plotted in Figure 5.15 as a reference for determination of the preferential grain orientation initiating propagating fatigue cracks. It can be observed in Figure 5.13 that only #2 and #5 type-3 Fe-bearing particles were located in Brass texture represented by red crossings, while none of other fractured particles, including type-1, type-2 and remaining type-3, were preferentially located in a certain oriented grain. In the pole figure of type-3 Si-bearing particles (Figure 5.14), the distribution of crystallographic orientations of grain where fractured particles were located was even more stochastic. 11 particles out of 14 selected fractured type-3 Si-bearing particle were not located in any typical oriented grains, and remaining three Si-bearing particles were in Brass, S and R-cube oriented grains, respectively. It can be also noticed that among all the fractured particles the type-3 Fe- and Si-bearing particles should be more detrimental to the final fatigue failure, simply because both of them can nucleate

propagating fatigue cracks. Although the type-3 fractured particles as propagating fatigue crack initiation sites were not numerous enough to carry out a reliable statistical analysis, a qualitative trend could be obtained in the surrounding texture distribution of type-3 fractured particles showing that a majority of type-3 fractured particles (71.4% for Fe-bearing particles; 78.6% for Si-bearing particles) were more or less located in randomly oriented grains rather than any preferential typical texture in rolled plate as shown in Figure 5.16, no matter what types of particles (Fe- and Si-bearing ones) or which planes cyclic fatigue stress was applied on (L-T, L-S or T-S).

Furthermore, in order to provide reliable experimental data in our 3-D model to simulate fatigue crack initiation behavior and to quantify FWL density and strength distribution in AA7075 T651, the short fatigue crack early propagation behavior was investigated, i.e. to determine whether fatigue cracks propagated in planar slip or non-planar slip planes. The crystallographic orientation of the grains which the fractured particles were located in was measured using EBSD, and based on measured Euler angles of each grain, the intersection lines between sample surface and primary slip planes ($\{111\}$ planes for FCC structure) were calculated. Afterwards, the fatigue crack traces on the surface in selected grains were examined to exclude those cracks apparently not matching the intersection lines. It can be observed in Figures 5.17(a) and 5.18(a) that fatigue cracks were initiated at Fe-bearing particle in L-T sample and Si-bearing particle, respectively. For both of propagating fatigue cracks in the matrix, the crack paths on the surface were approximately perpendicular to cyclic loading direction and not following the primary slip plane surface traces as most of other fatigue cracks behaved in AA7075 aluminum alloy. There is an exception to this phenomenon for the upper crack initiated from the Si-bearing particle in Figure 5.18(a). This crack seems like matching the 11-1 plane surface trace but it is possible that the 11-1 plane trace is parallel to Mode I crack coincidentally. It can also be noted that their cracks growth paths were both wavy and the tip of crack initiated at Fe-bearing (Figure 5.17(a)) was relatively blunt, whereas fatigue crack path is straight and tip was very sharp as shown in Figure 5.19(a). It seems like following the planar slip planes well based on the observation of crack morphology on the surface. However, only surface trace analysis can not provide sufficient evidence to determine whether fatigue crack plane correspond to $\{111\}$ slip planes or not. Focused Ion Beam (FIB) was thereby utilized to reveal the fatigue crack plane orientation in 3-D, by sputtering matrix material in the path of crack propagation to fabricate a cross-

section perpendicular to the sample surface, as shown in Figure 5.19 (a). With similarity to verifying the matching situation of crack on the surface, the intersection lines between crack plane and the cross-section plane were identified as illustrated in the Figure 5.19(c). It can be clearly observed that the intersection line is close to -111 plane, however there was still several degrees off from the ideal -111 plane. That is because the coarse localized slip-bands that facilitated planar slip cracking were prone to form in the large recrystallized grains. However, in this work it can be easily observed that the unrecrystallized subgrains were distributed around those fractured particles, as shown in Figure 5.17(b), Figure 5.18(b) and Figure 5.19(b) the low angle grain boundaries (3-15 degrees) existed in targeted parent grain based on EBSD measurement [173, 184]. Accordingly, the fatigue crack in 7075 did not propagate along primary slip plane perfectly, which is consistent with the previous investigations by Gupta, Agnew and Gangloff et al. on the fatigue crack surface crystallography near the crack initiating constituent particle in AA7075 T651 aluminum alloy [120, 173, 185, 186]. They concluded that fatigue crack facets in the vicinity of initiating particles were observed to be parallel to a wide variety of crystallographic planes from {001} to {101} rather than always {111} slip planes. Although many experimental results described that fatigue cracks formed at slip-bands or grew along planar slip planes at early stage in pure metals or single crystals (Al, Cu and Fe) and some other alloys (2024, 8090 and stainless steel) [11, 56, 99, 160, 187, 188], this fatigue crack initiation and early growth behavior was not presented in 7xxx series aluminum alloys, especially in peak-aged T6 temper condition. It can be interpreted that in those planar slip alloys, the strain concentration around fatigue crack nucleation sites could readily lead to coarse planar slip that favored fatigue crack propagation in primary slip planes, i.e., {111} plane for FCC structure, due to non-existence of precipitates or presence of those shearable coherent Guinier-Preston (GP) zones and precipitates [56]. Nevertheless, the peak-aged hardened AA7075 T651 aluminum alloy contains strengthening precipitates or dispersoids (η' and η) wherein the basal planes of hexagonal η' are partially coherent with the {111} matrix planes and interface between the matrix and c direction of precipitate is incoherent [189]. Moreover, Cu content could not only increase the volume fraction of precipitates, but also increase the number of partially coherent and incoherent precipitates. Those distinct strengthening precipitates could be looped promoting more homogeneous slip to alter the crack growth path leading to non-crystallographic and

mode I crack lying in a plane normal to the load axis (as shown in Figures 5.17 and 5.18) [184, 190-192].

5.3.3 Examination of topography and mechanical properties of Fe- and Si-bearing constituent particles using AFM and Nano-indentation

The multi-site fatigue crack nucleation behavior was strongly anisotropic, due to distinct crack initiation mechanisms among L-T, L-S and T-S planes. When loaded along L direction (L-T and L-S), the fatigue cracks were preferentially initiated from stress or strain concentration sites around the pre-crack within Fe-bearing particles induced by prior thermo-mechanical processing. In this case, the pre-crack planes were normally perpendicular to loading direction (rolling direction), which was somehow mode-I fracture. Conversely, in the case of T-S sample, the pre-crack in Fe-bearing particle was not perpendicular to loading direction any more, and hence the Si-bearing particles associated with pores became dominant for the fatigue crack nucleation. In addition to the thickness of particle acting as the key factor controlling the crack initiation, the mechanical properties of those particles should play a role in the fatigue crack nucleation behavior and thus should be taken into consideration for development of 3-D microstructure-based short crack initiation and early growth model [179].

In this work, the four-point bend samples were ground gradually from grit 240 to 1200, followed by mechanical polishing using alumina powders of 1 micron, 0.3 micron and 0.05 micron in size respectively, and final polishing using a silica colloidal suspension liquid exclusively for evaluation of mechanical properties of both types of particles and matrix. It can be noted intuitively that the mechanically polished surfaces of matrix, Fe- and Si-bearing particle will differentiate from each other due to the variability of mechanical properties, such as Young's modulus and hardness. Therefore, atomic force microscope (AFM) was first introduced to characterize the topography of Fe- and Si-bearing particles. It can be observed in Figure 5.20 that the Fe-bearing particle (Figure (a)) was extruded compared to matrix surface and the apex was approximately 150 nm higher than matrix based on the Figure 5.20(c). In the contrary, Si-bearing particle (Figure 5.20(d)) was intruded and almost 1 μm lower than matrix, implying that Si-bearing particle was softer than matrix and Fe-bearing particle and more likely to be cracked during cyclic loading. To some degree, our AFM measurement results was not consistent with previous hardness measurement results using Nano-indentation by other

researchers: Fe-bearing particle was harder than Si-bearing ones, but both of them were harder than matrix with modulus of Fe-bearing particles ranging from 115 to 169 GPa and hardness ranging from 5 to 8.8 GPa, as well as modulus of Si-bearing particles ranging from 45 to 95 GPa and hardness ranging from 1.6 to 5.2 GPa [52, 53, 71, 175].

Given that there still remains a controversy regarding Nano-indentation measurement on Fe- and Si-bearing particles, hardness measurement was carried out using Nano-indentation on a series of selected matrix sites, Fe- and Si-bearing particles (approximately 10 for each set), respectively, to measure the Young's modulus and hardness statistically. Figure 5.21 shows the Nano-indentation measurement results that Fe-bearing particles possessed the highest Young's modulus (149.2 ± 11.9 GPa) and hardness (8.9 ± 0.87 GPa), while for Si-bearing particles, Young's modulus (82.2 ± 26.8 GPa) was almost the same as and a little lower than matrix (85.9 ± 3.5 GPa), however hardness value (4.03 ± 0.92 GPa) was much higher than matrix (2.01 ± 0.19 GPa). It can be readily noticed that all the average values of Young's modulus and hardness for matrix, Fe- and Si-bearing particle was locating in the range of results measured by other researchers [52, 53, 71]. However, as for the measurement error, Si-bearing particles results were scattered most severely, while results of matrix was consistent. It is possibly because of that pores associated with Si-bearing particles as described by FIB results. The SEM micrographs of Nano-indentation on matrix, Fe-bearing and Si-bearing particles is being shown in Figures 5.22 (a), (b) and (c). It can be seen in Figures 5.22 (a) and (b) the indents on either matrix or Fe-bearing particle were entire compared with Si-bearing particle. As shown in curves of modulus vs. displacement (Figure 5.23(a)) and hardness vs. displacement (Figure 5.23(b)), matrix curve could be stable as the displacement was deeper than 200 nm to surface, thus the average modulus and hardness were calculated according to the value between 200-500 nm. For Fe-bearing particle, the both curves started to decrease after 100 nm displacement, possibly due to low thickness of the Fe-bearing particle leading to measurement result coupled with matrix which was much softer than and not as stiff as Fe-bearing particle. For Si-bearing particle, it can be observed in Figure 5.22 (c) that the indent on Si-bearing particle was completely sink-in, consequently caused the micro-crack along the fringe of indent within Si-bearing particle and led to debonding at the interface between particle and matrix. It is possibly because there was a pore beneath Si-bearing particle surface to make surface sink during indentation process, which should be responsible for the scattered

measurement results in Figure 5.21. That can also explain double platforms and peaks in the CSM curves of Si-bearing particle in Figures 5.23 (a) and (b). At the early stage of indentation prior to 150 nm displacement, particle surface and pore was being compressed together to make measured modulus much lower than actual value and hardness decrease until the pore became completely flat. Afterwards, it was the real start point for indentation on a solid Si-bearing particle to make the subsequent curve behave normally and ultimately decrease due to the small size effects of particle [53]. This phenomenon verified the existence of pore within Si-bearing particle, and further illustrated why the hardness measurement on Si-bearing particle was not consistent as matrix and Fe-bearing particle. Accordingly, it is hard to conclude which modulus was larger between Si-bearing particle and matrix, however, based on limited number of measurements, Si-bearing particle (4.03 ± 0.92 GPa) was harder than matrix (2.01 ± 0.19 GPa), but still much softer than Fe-bearing particle which was stiffest (149.2 ± 11.9 GPa) and hardest (8.9 ± 0.87 GPa) among these measurement sites. This inferred that high stiffness made it easier to for Fe-bearing particle to fracture during the prior thermo-mechanical processing, which was responsible for fatigue crack nucleation in L-T and L-S samples. When loading direction was not perpendicular to the pre-formed cracks in Fe-bearing particle, i.e., T-S samples, the Si-bearing particle that were weaker than Fe-bearing particle in hardness could become the dominant fatigue crack nucleation sites, especially when Si-bearing particles were combined with pores.

5.4 Conclusions

- In L-T and L-S planes, the thicker and pre-cracked Fe-containing particles were the predominant sites for fatigue crack nucleation;
- In T-S plane, the thicker and debonded Si-bearing particles associated with pores were more likely to nucleate propagating cracks, which was verified by the Nano-indentation measurement.
- Fe-containing particles were protruded, while Si-bearing particles were intruded on the mechanically polished surface of the AA7075 T651 Al alloy, which was consistent with hardness measurements showing that Si-bearing particles were softer and more ductile than Fe-containing ones.

- Based on EBSD measurement, in the AA7075 T651 Al alloy, fatigue cracks did not perfectly follow the primary slip planes, i.e. one of {111} planes, and sometimes propagated approximately normal to loading direction; the more detrimental Fe- and Si-particles initiating Type-3 fatigue cracks were not preferentially located in a certain oriented grain.

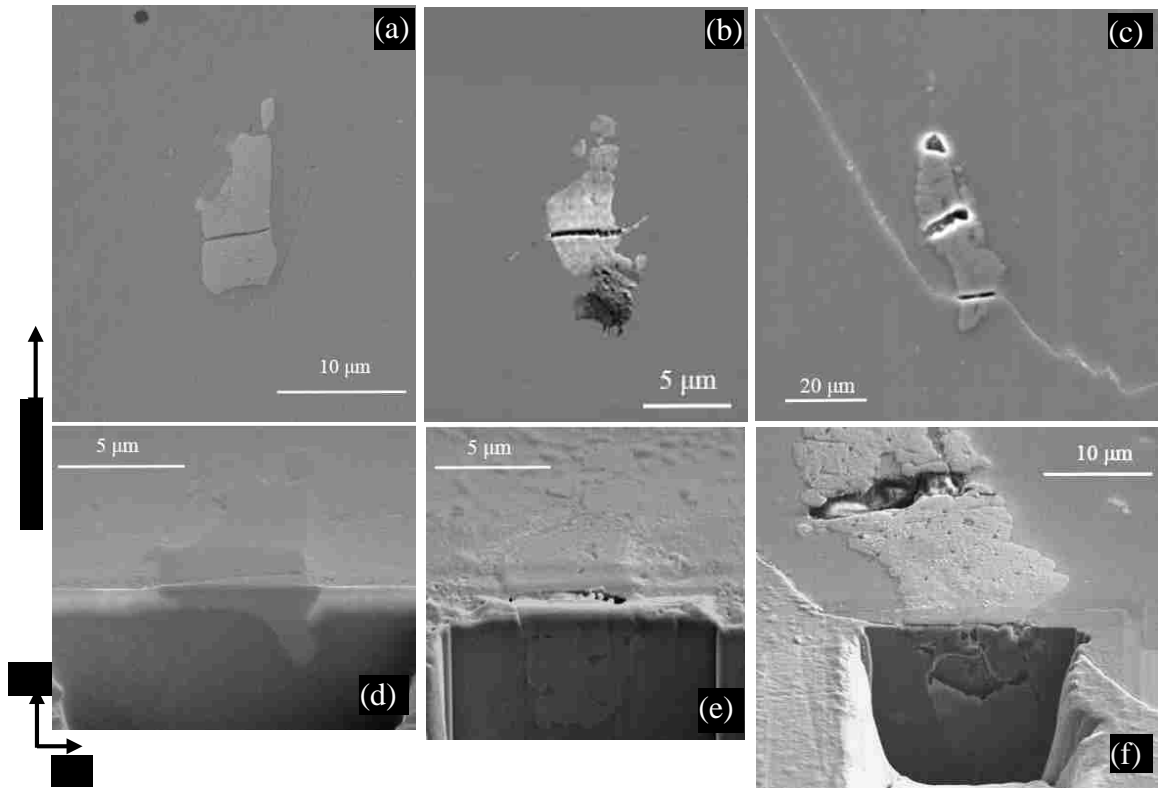


Figure 5.1 Three types of typical fractured Fe-bearing particles after fatigue loading and corresponding cross-sections using FIB in L-T or L-S planes: (a) a Type-1 particle, (b) a Type-2 particle, (c) a Type-3 particle, (d-f) Cross-sections of the Type-1, 2 and 3 particles, respectively.

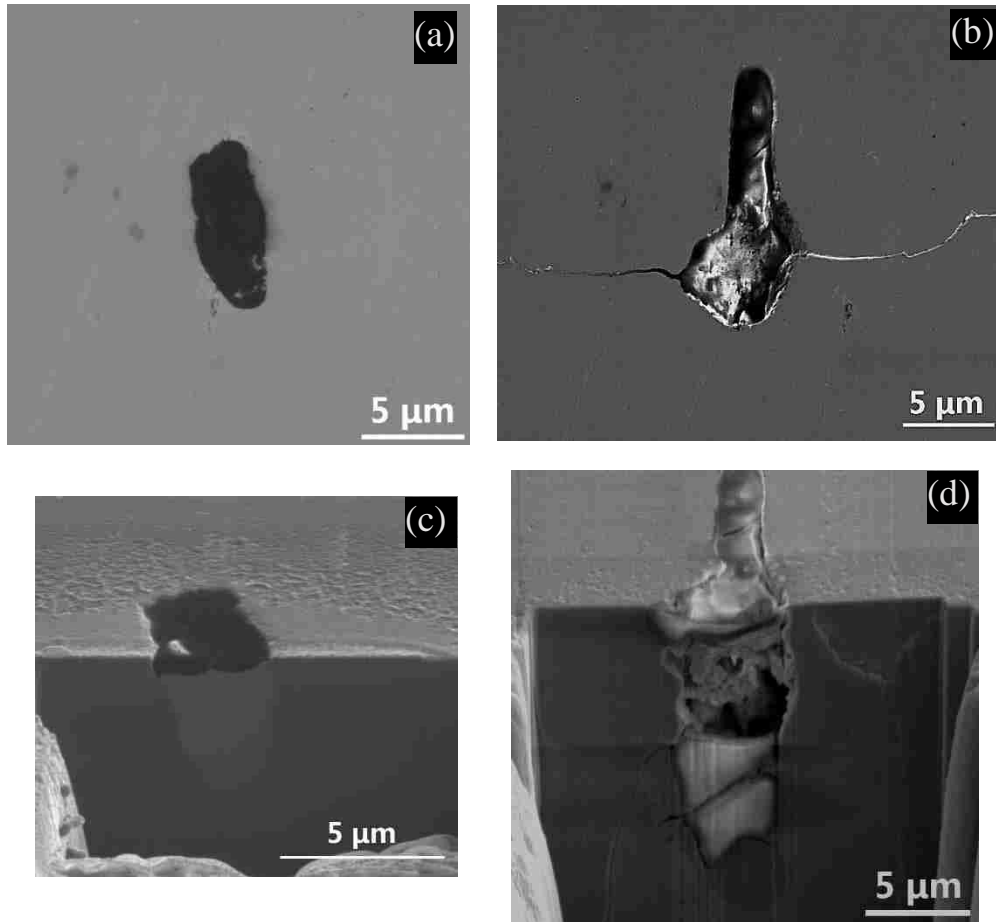


Figure 5.2 Two types of fractured Si-bearing particles after fatigue loading and corresponding cross-sections using FIB in T-S plane: (a) a Type-1 particle, (b) a Type-3 particle, (c) and (d) Cross-sections of the Type-1 and 3, respectively.

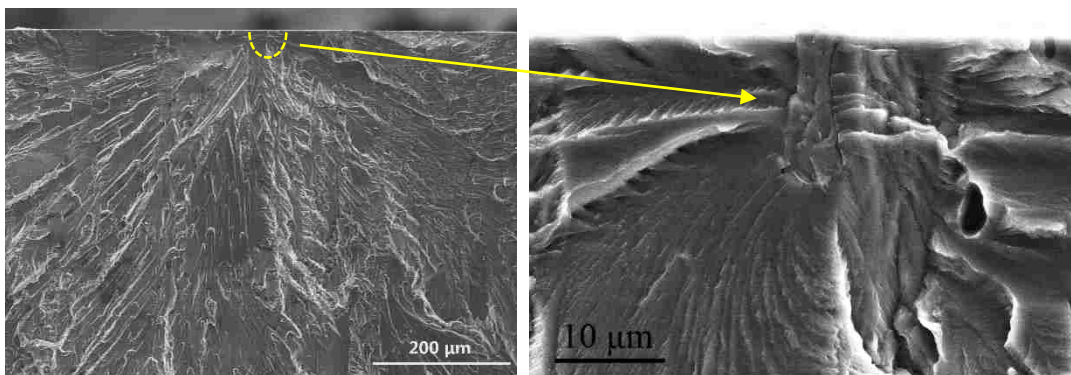


Figure 5.3 SEM observation of a fracture surface showing a main fatigue crack initiated at a single Type-3 Fe-bearing particle in a L-S sample.

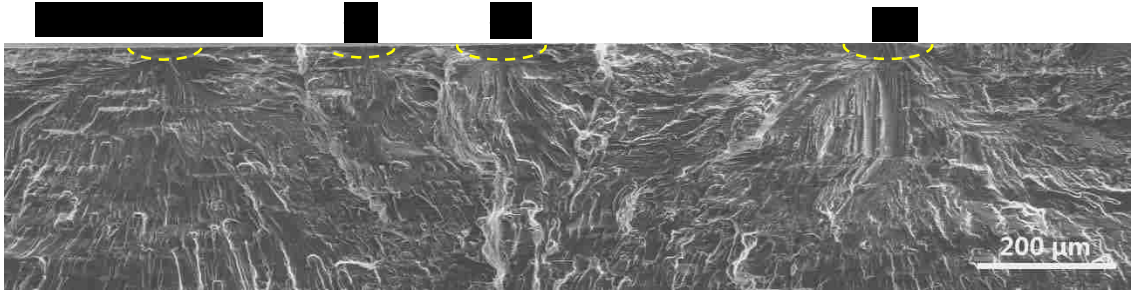


Figure 5.4 SEM observation of a fracture surface showing the coalescence of fatigue cracks initiated at Type-3 Fe-bearing particles in a L-T sample.

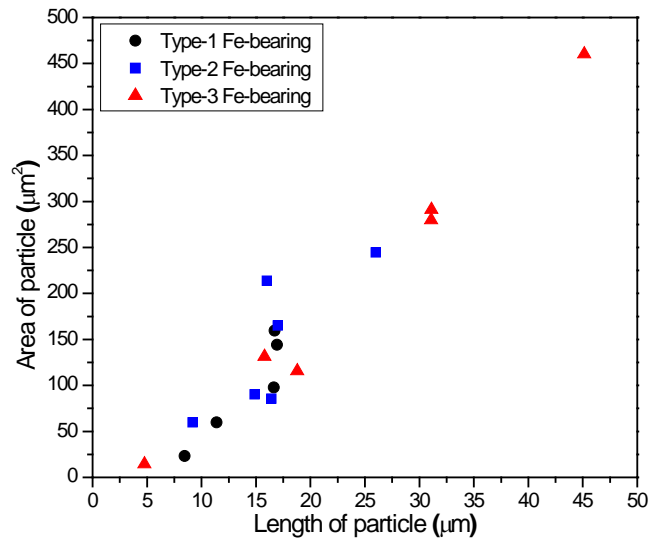


Figure 5.5 The plots of area vs. length of Fe-bearing particles on the L-T or L-S sample surface

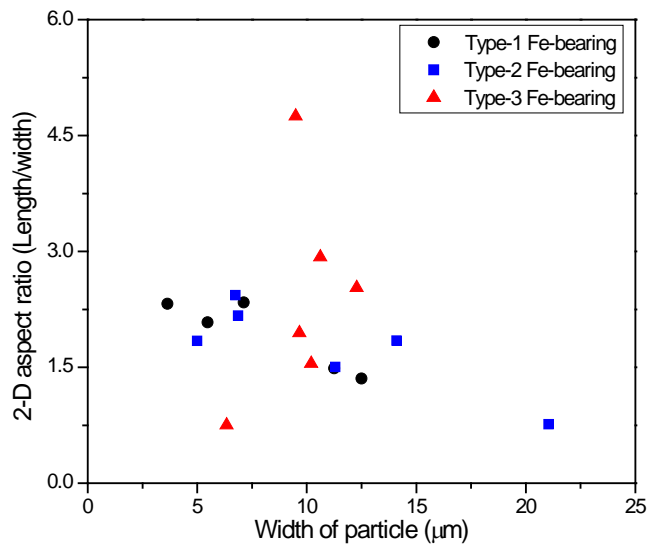


Figure 5.6 The plots of aspect ratio (length/width) vs. width of Fe-bearing particles on the L-T or L-S sample surface

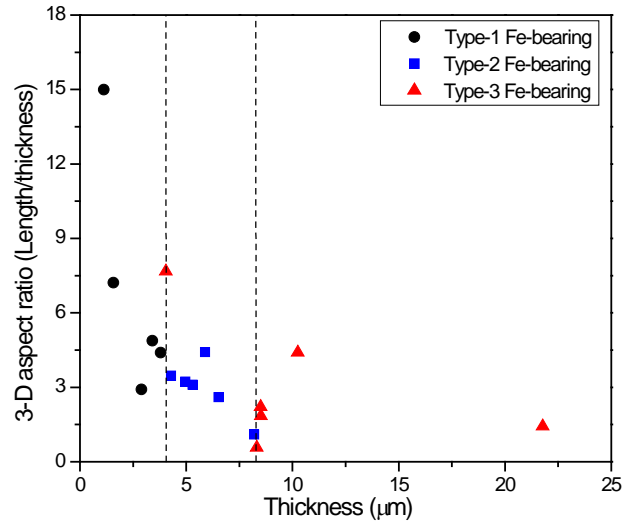


Figure 5.7 The plots of aspect ratio (length/thickness) vs. thickness of Fe-bearing particles on the L-T or L-S sample in 3-D

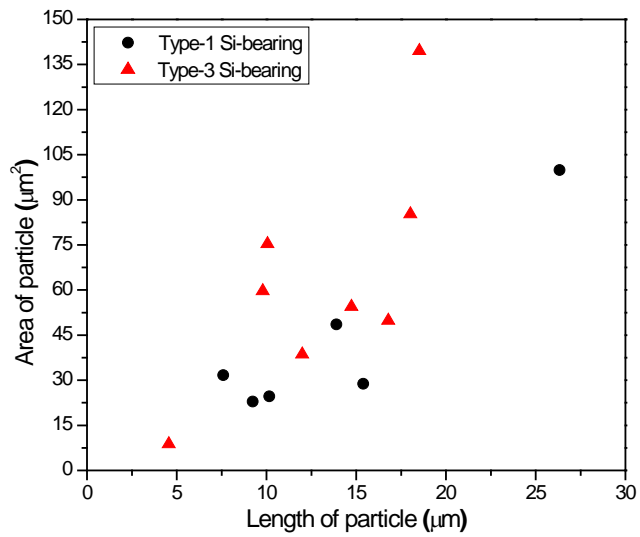


Figure 5.8 The plots of area vs. length of Si-bearing particles on the T-S sample surface

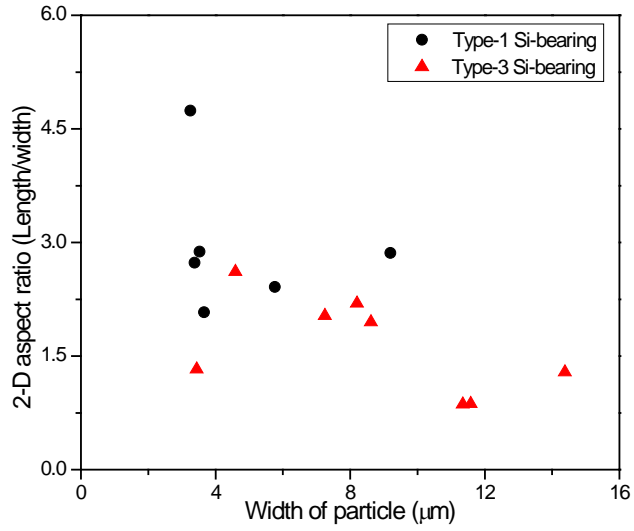


Figure 5.9 The plots of aspect ratio (length/width) vs. width of Si-bearing particles on the T-S sample surface

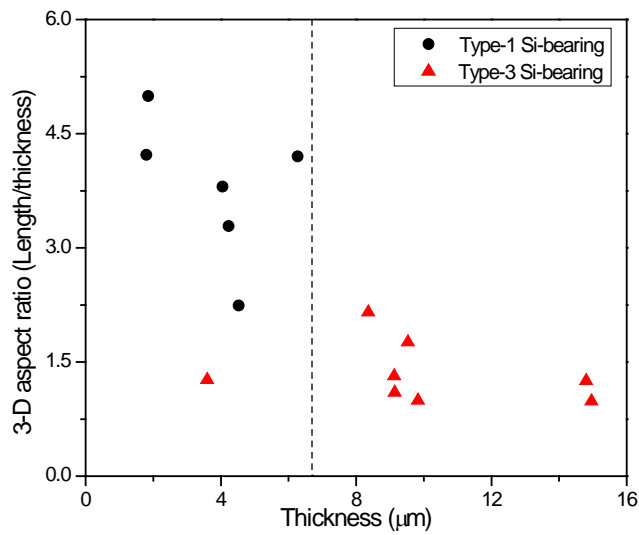


Figure 5.10 The plots of aspect ratio (length/thickness) vs. thickness of Si-bearing particles on the T-S sample in 3-D

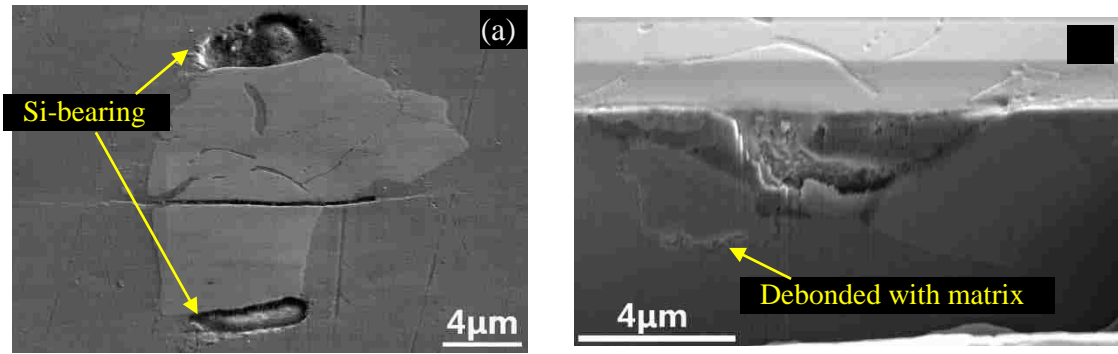


Figure 5.11 (a) the exceptional thin type-3 Fe-bearing in L-T plane and (b) the corresponding cross-section using FIB

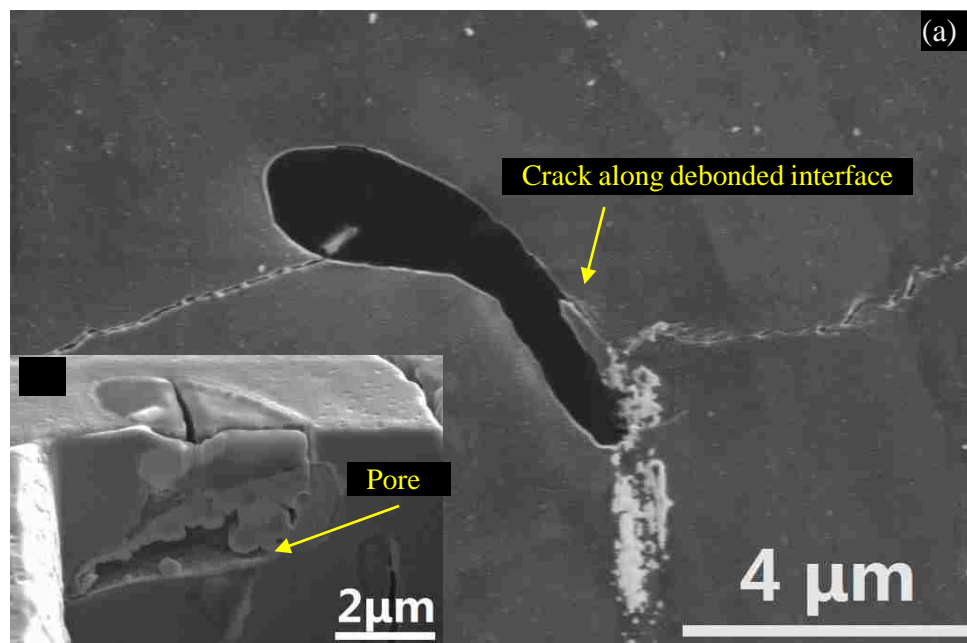


Figure 5.12 (a) the exceptional thin type-3 Si-bearing particle in T-S plane and (b) the cross-section of the corresponding particle using FIB

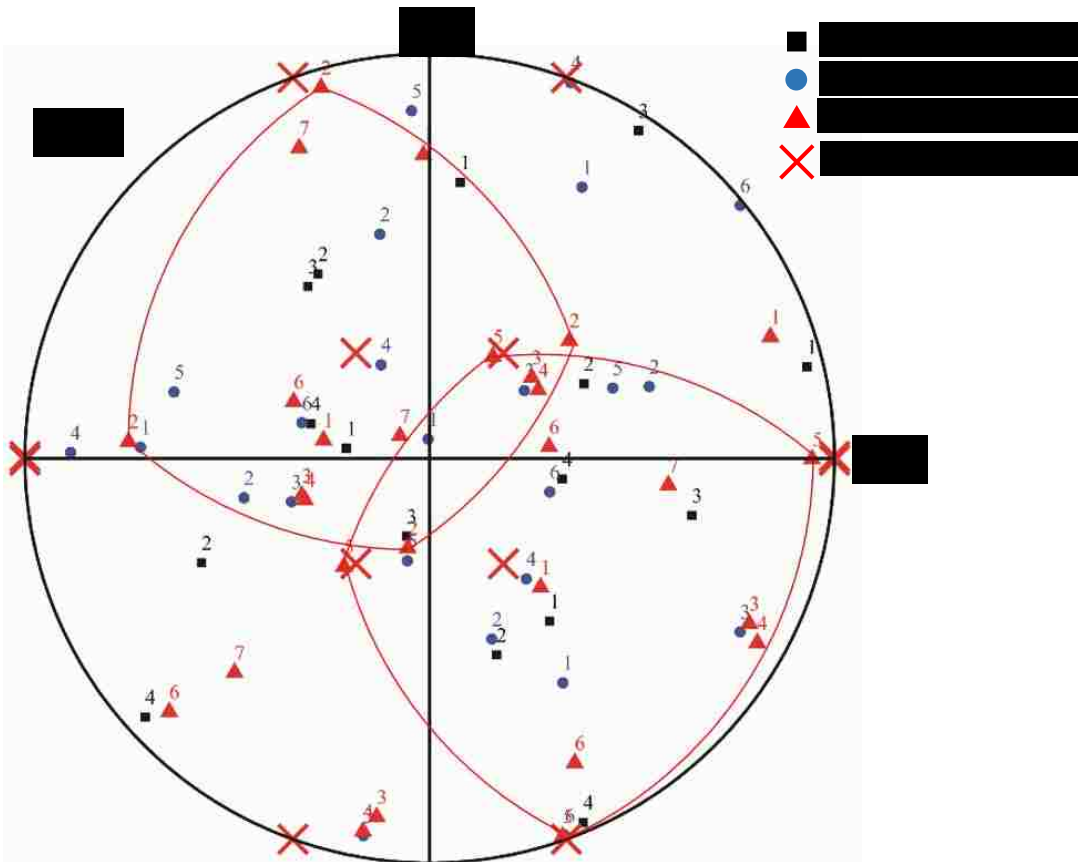


Figure 5.13 {111} pole figure of the grains where type-1, -2 and -3 fractured Fe-bearing particles were located in L-T or L-S samples in AA7075

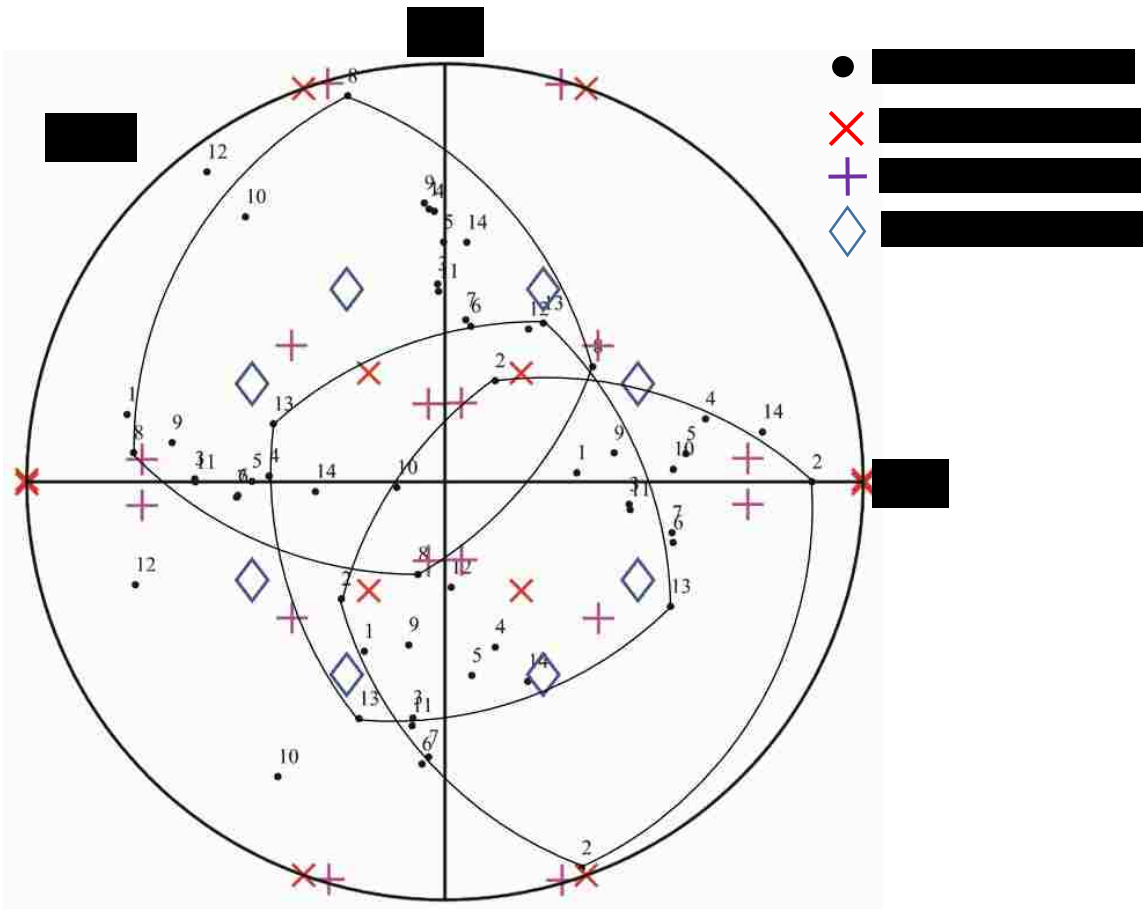


Figure 5.14 {111} pole figure of the grains where type-3 fractured Si-bearing particles were located in T-S samples in AA7075

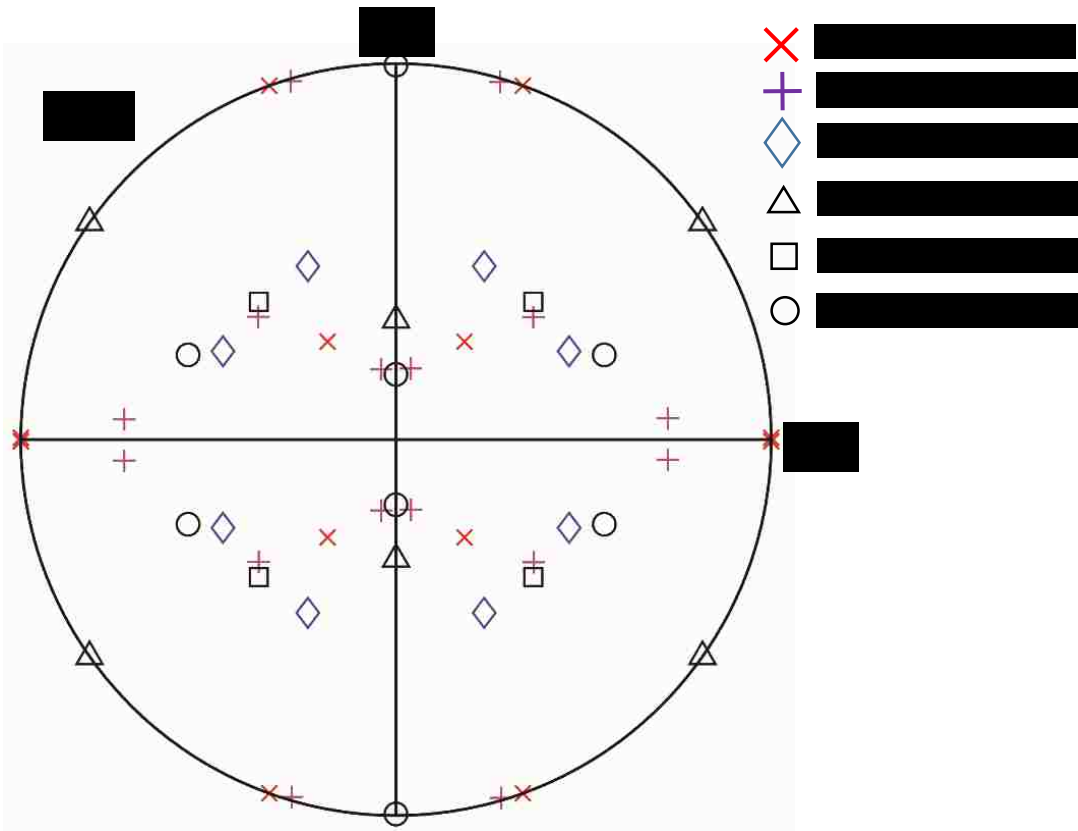


Figure 5.15 The typical textures in aluminum alloy rolled plate.

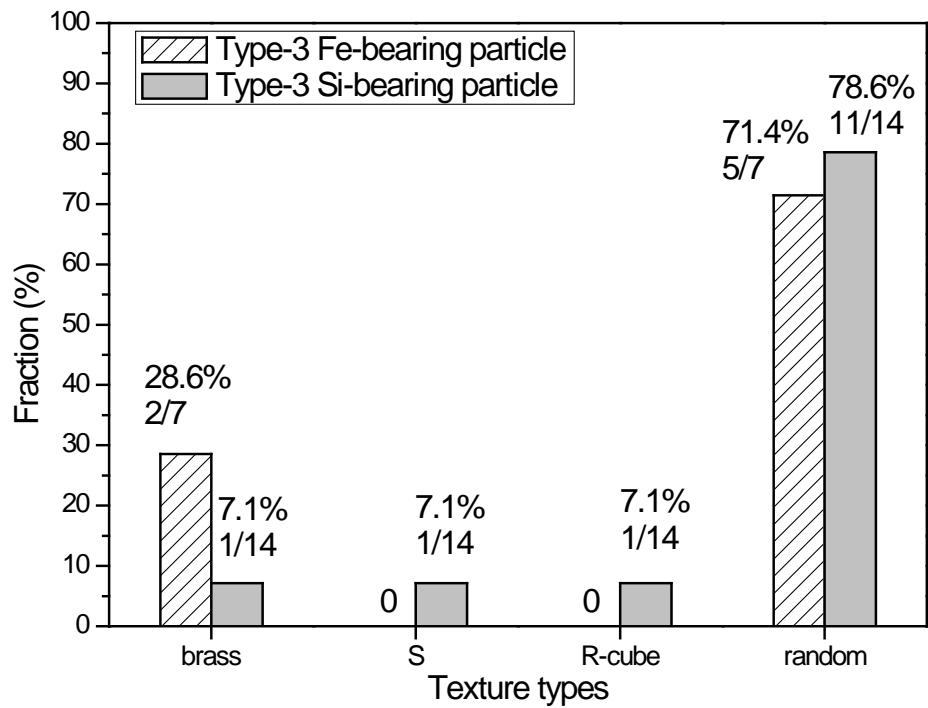


Figure 5.16 The distribution of parent grains of type-3 fractured Fe- and Si-bearing particles, respectively.

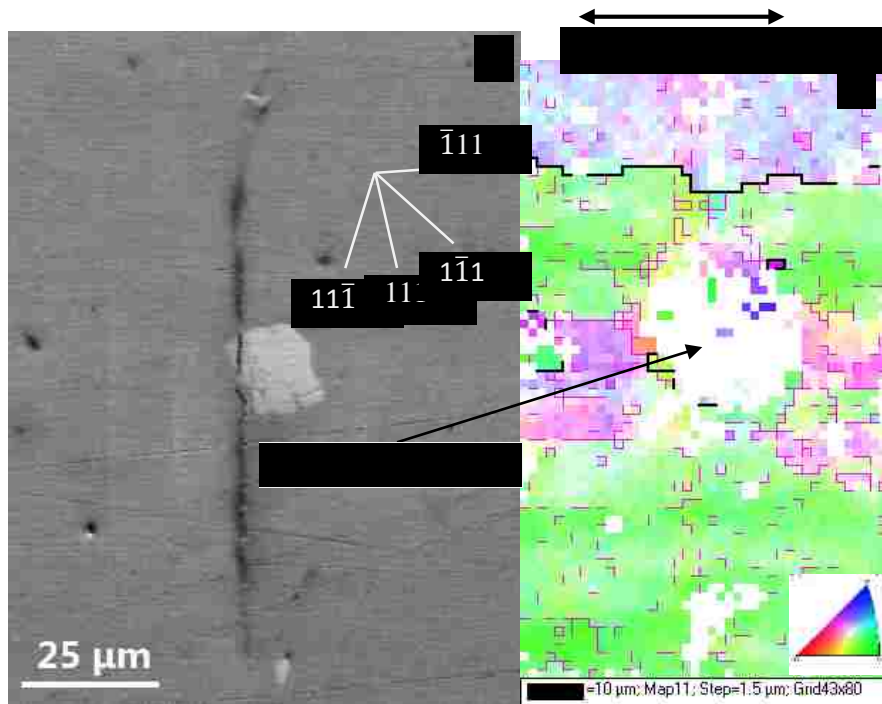


Figure 5.17 (a) a type-3 Fe-bearing particle with a crack normal to loading direction in L-T sample and $\{111\}$ plane surface trace; (b) orientation map of surrounding grain in terms of IPF using EBSD. Euler angle ($^{\circ}$): 234.5 34.9 68.7

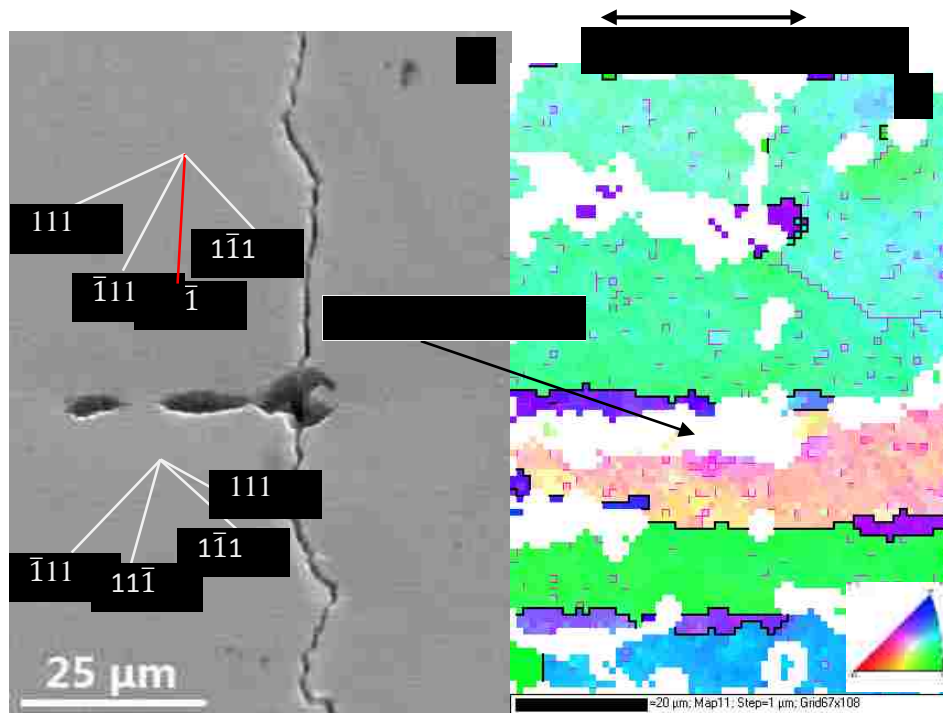


Figure 5.18 (a) a type-3 Si-bearing particle with a crack normal to loading direction in T-S sample and crack surface trace; (b) orientation map of surrounding grain in terms of IPF using EBSD. Euler angle ($^{\circ}$): 113.2 39.7 71.3; 55.5 27.4 22.4

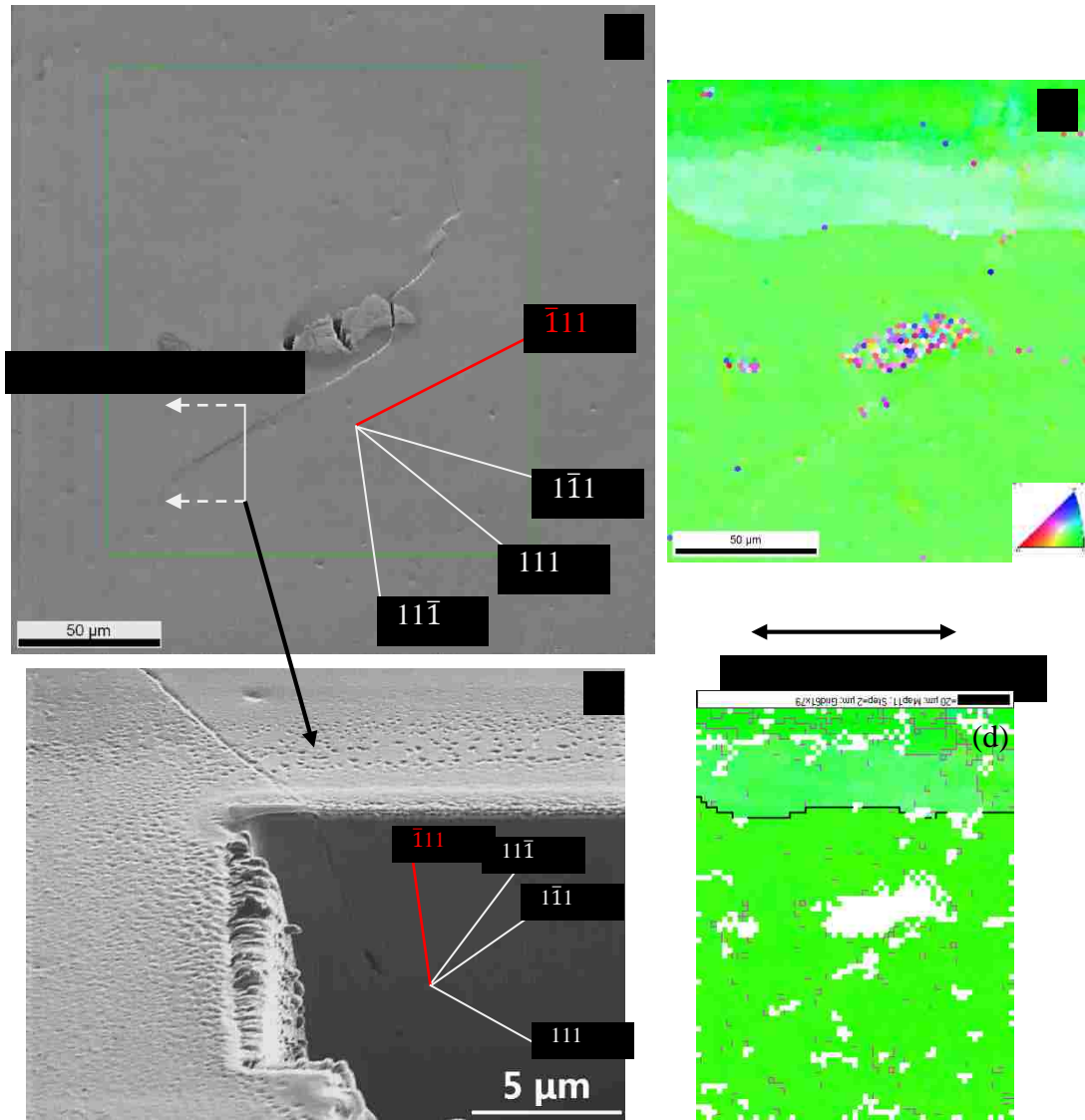


Figure 5.19 Short fatigue crack propagation behavior in an AA7075 T651 rolled plate: (a) a type-3 fractured Fe-bearing particles in L-T sample; (b) orientation map of surrounding grain in terms of IPF using EBSD (c) the cross-section of fatigue crack plane on the crack growth path using FIB. Euler angle (°): 63.3 37 89.4; (d) low-angle grain boundaries in grain in EBSD mapping.

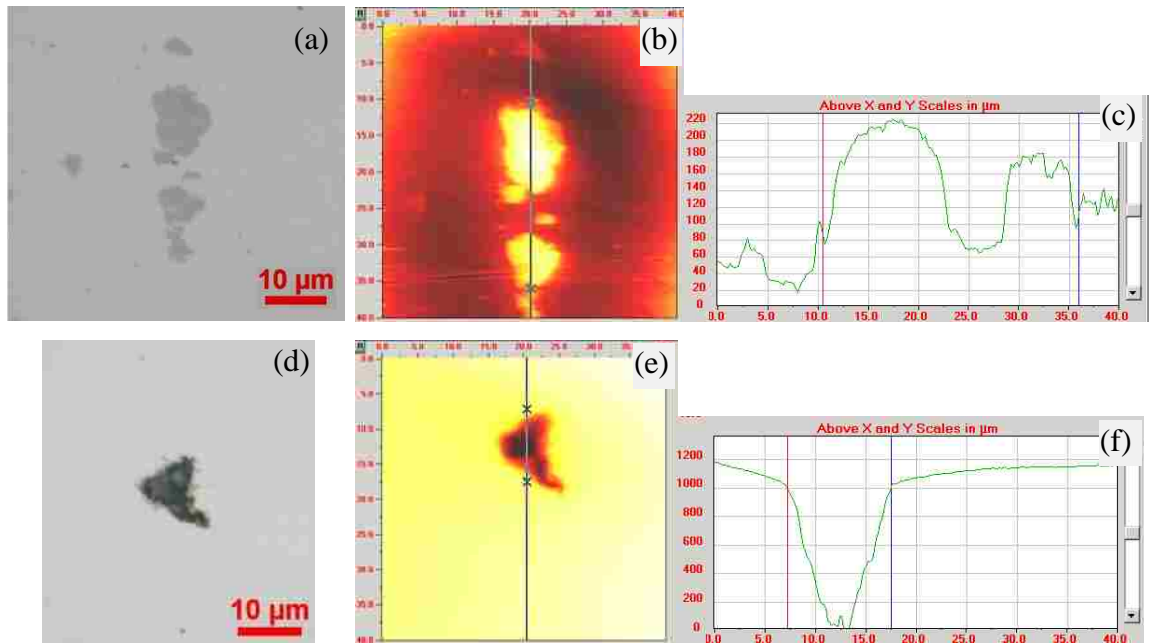


Figure 5.20 Topography of Fe- and Si-bearing particle on the mechanically polished surface using AFM: (a) optical micrograph, (b) extruded topography using AFM (c) depth profile compared to surface between two crossings along the selected linear path in (b) of Fe-bearing, (d) optical micrograph, (e) intruded topography using AFM, (f) depth profile compared to surface between two crossings along the selected linear path in (e) of Si-bearing particle. (Unit: nm)

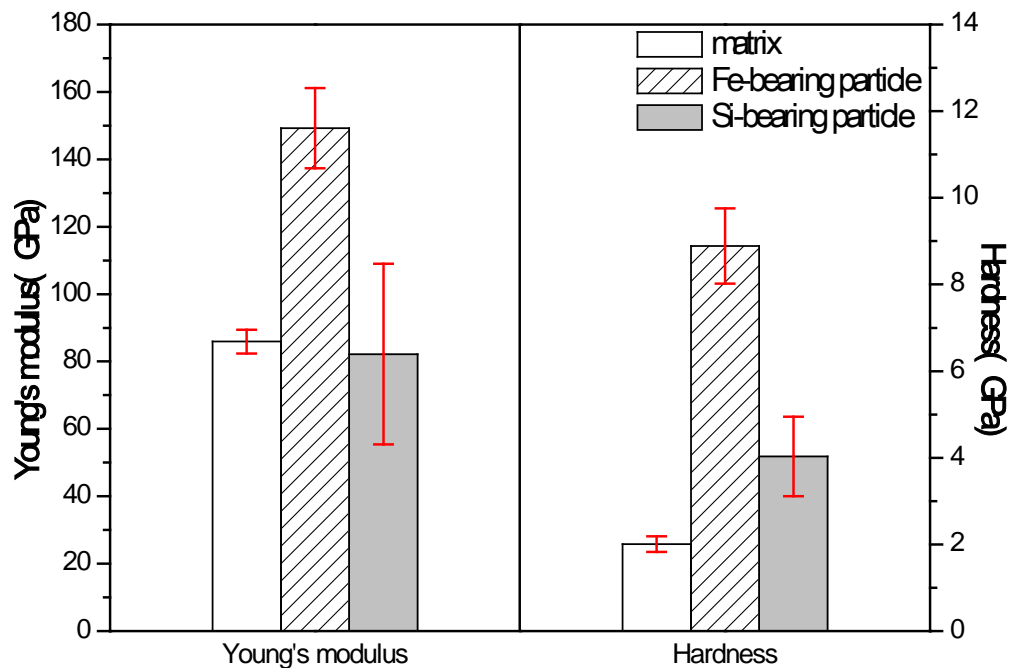


Figure 5.21 Comparison of Young's moduli and hardness of matrix, Fe- and Si-bearing particles in AA7075 T651 aluminum alloy

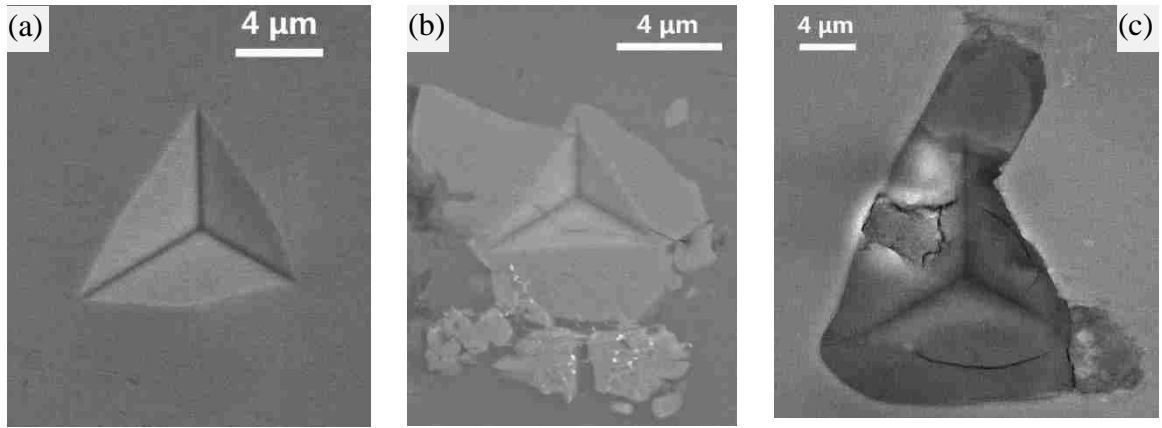


Figure 5.22 SEM micrographs of indentations in (a) sample matrix, (b) Fe-bearing particle, and (c) Si-bearing particle on mechanically polished surface.

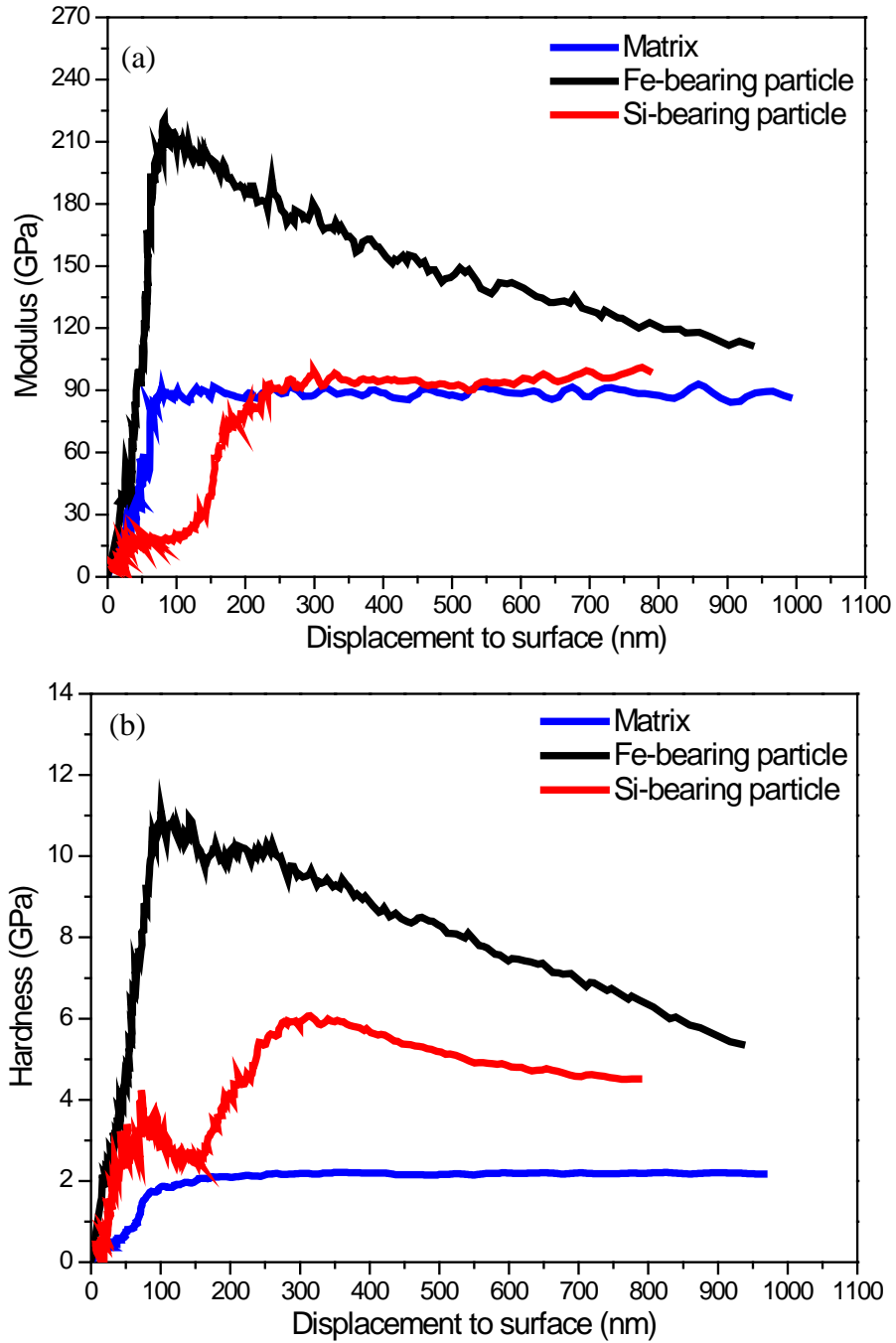


Figure 5.23 Nano-indentation measurements using CSM technique on AA7075 T651 matrix, Fe- and Si-bearing particles: (a) Young's modulus-displacement curve, and (b) hardness-displacement curve.

Chapter 6 Simulation of multi-site fatigue crack nucleation behaviors at pre-crack in constituent particles by using micro-notches fabricated with FIB in AA2024-T351 and AA7075-T651 Al alloys rolled plate

In fatigued four-point bend samples of both AA2024-T351 and AA7075-T651 Al alloys, three types of fractured Fe-containing constituent particles were categorized after high cycle fatigue loading: Type I, cracks in particles (thinnest) never extended into the matrix; Type II, cracks in particles (medium thickness) extended into the matrix but stopped very soon; Type III, cracks in particles (thickest) extended into matrix and had the chance to become propagating cracks leading to final failure. In this chapter, three series of rectangular micro-notches with different dimensions were fabricated using Focused Ion Beam (FIB) in selected grains using Electron Backscattered Diffraction (EBSD) on T-S plane of AA2024 T351 and AA7075 T651 Al alloys rolled plate, respectively, to mimic typical pre-crack in the those three types of Fe-bearing constituent particles nucleating fatigue cracks as summarized in previous chapters. The four-point bend fatigue tests have been carried out on those samples, and the multi-site fatigue cracks initiated at the fabricated micro-notches were monitored at a certain cycle interval using optical microscope. The effects of 3-D geometry, dimensions of micro-notches, local micro-texture on the observed fatigue crack nucleation behavior were characterized using SEM, FIB and EBSD. Specifically, after fatigue loading, the wider and deeper notches became the fatigue cracks initiation sites more easily. In AA2024-T351 samples, cracks preferred to propagate in the $\{111\}$ slip planes with smallest twist angle and relatively large Schmid factor. In AA7075-T651 samples, cracks did not follow the crystallographic slip planes perfectly. All the experimental information could be utilized in the microstructure-based 3-D model to simulate fatigue crack initiation and early growth in AA2024 (planar slip type) and AA7075 (non-planar slip type) aluminum alloys, respectively, by taking into consideration driving force and resistance to short crack growth.

6.1 Introduction

High strength aluminum alloys, such as 2000 and 7000 series aluminum alloys, have been extensively used in aerospace and automotive industries due to their high specific strength and fatigue resistance. In these applications, a majority of components were in service under high-cycle fatigue loading, in which the early stage of fatigue life, i.e. incubation, initiation and early growth of short fatigue crack is critical since up to 90%

of the total fatigue life could be consumed during this period [1, 14, 162]. The early stage is also strongly dependent on the local microstructures. For both 2000 [56, 57, 59, 60, 72] and 7000 [46-48, 172] series alloys, the fatigue cracks are predominantly initiated at Fe-bearing constituent particle (Al_7Cu_2Fe) possibly due to the pre-crack or pre-damage during the prior thermo-mechanical deformation, especially when the applied cyclic loading is parallel to the rolling direction [46] which is the most frequent application scenario. To better understand fatigue crack nucleation mechanism and predict the fatigue life of in-service component more reliably and precisely, a lot of efforts have been made by researchers to take into account many possible factors influencing fatigue crack initiation behavior, such as geometry and size of particle, local grain microstructure and orientation, stress/strain amplitude, aspect ratio and so forth. It has been reported that fatigue cracks are prone to be initiated at those relatively coarse pre-cracked Fe-bearing particles on the surface in high strength aluminum alloys due to stronger stress/strain concentration [52, 166, 168, 169]. Similarly, the higher internal stress could be generated inside constituent particle with a larger aspect ratio (L/S) on L-S plane in AA7075 T651 [172]. However, based on statistical analysis on multiple fatigue crack initiation at constituent particles on the surface, it showed that fatigue cracks are not necessarily initiated at the coarse particles but often at relatively small ones [45, 47]. Wei and author cross-sectioned a series of fractured particle in AA2024 and AA7075 high strength aluminum alloys to make analogous conclusions that the thickness of particles was the key factor controlling driving force for the fatigue crack nucleation [72]. In addition to the particle size or geometrical effects on fatigue crack nucleation, the local crystallographic orientation was also frequently regarded as the major factor influencing the crack initiation, e.g. the twist-cube orientation was observed to be more likely to induce crack nucleation in 7010 and 7075 aluminum alloy [14, 52]. The preferable local orientation facilitated formation of slip-band on low-index crystallographic planes or often along $\{111\}$ planes [52, 193, 194], wherein the effective shear stress dominated the driving force for fatigue crack nucleation [195], and consequently many 2D or 3D mechanics-based models were built to assess the driving force of crack nucleation in terms of maximum plastic shear strain amplitude or fatigue indicator parameter (FIP) [12, 37-40]. However, the prerequisite of this driving force definition was that fatigue crack propagated in the crystallographic slip planes, which commonly occurred in pure metals or single crystals (Al, Cu and Fe) and some other alloys (2024, 8090 and stainless steel) [11, 56, 99, 160, 187, 188]. Obviously, slip-band

based initiation criteria is not applicable in 7000 series aluminum alloys, since fatigue crack often propagated along non-crystallographic slip planes, and occasionally normal to the loading axis [173].

It could be noted that there are so many factors needing to be taken into consideration, such as size, geometry, local microstructure, crystallographic orientation, etc., if a comprehensive 3-D microstructure-based model would be built to simulate fatigue crack nucleation behavior. More importantly, almost all preliminary models only considered the driving force for crack nucleation, whereas resistance to short fatigue crack growth was ignored. Zhai et al. found that short fatigue crack growth was significantly influenced by local microstructures, especially grain boundary (GB). When fatigue crack propagated through GB, the tilting and twisting of crack plane contributed to the resistance to short crack growth, especially the twist component [99]. Wei subsequently quantify the short fatigue crack growth resistance as a Weibull function of twist angle of crack plane at GB in 2024 aluminum alloy, in which the particle/matrix interface was also prone to retard short fatigue crack nucleation from $\text{Al}_7\text{Cu}_2\text{Fe}$ constituent particle. Furthermore, the local grain orientation and particle 3-D geometry could significantly influenced fatigue crack nucleation [72]. Accordingly, to replicate a reliable 3-D model based on experimental data to simulate short fatigue crack nucleation is not only complex but also needs taking into account resistance to short crack growth which is sensitive to the particle geometry and surrounding microstructure. To simplify establishment of model and fill the gap between complexity of actual microstructure and hypothesis in the process of replicating 3-D microstructure-based model, a series of rectangular micro-notches with different dimensions were fabricated using FIB to simulate fractured particles inducing fatigue crack nucleation in selected grains which orientations have been identified using EBSD in AA2024-T351 and AA7075-T651 aluminum alloys, and fatigue cracks initiated at those micro-notches in these two representative alloys were observed during cyclic loading aiming at providing our model with more concrete and direct experimental information, i.e. the key factors contributing to driving force and resistance of fatigue crack nucleation, for two types of aluminum alloys, i.e., planar slip and non-planar slip alloys.

6.2 Experimental details

6.2.1 Materials and samples

Two precipitation-hardened high strength aluminum alloys, Al-Cu alloy AA2024-T351 and Al-Zn-Mg-Cu alloy AA7075-T651, were selected as research materials. Both of the alloys were hot rolled to 30 mm and 8 mm in thickness, respectively. The 2024 rolled plate was solution heat treated followed by natural aging and had a pancake-shaped grain structure, average grain size of $361 \times 97 \times 37 \mu\text{m}^3$ (L×T×S). Its chemical composition was 3.5% Cu, 1.3% Mg, 0.4% Fe, 0.4% Mn, 0.3% Si, 0.1% Cr, 0.15% Ti, <0.24% Zn in weight percentage and yield strength was measured to be 358 MPa along T (transverse) direction. The 7075 rolled plate was also solution heat treated followed by artificial aging and had a similar pancake-shaped grain structure with coarser average grain size of $4502.8 \times 376.6 \times 45.8 \mu\text{m}^3$ (L×T×S). Its chemical composition was 0.4% Si, 0.5% Fe, 1.61% Cu, 0.3% Mn, 2.5% Mg, 5.53% Zn, 0.2% Ti, 0.19% Cr in weight percentage. Its yield strength was measured to be 483 MPa along T (transverse) direction. For both alloys, samples ($36 \times 8 \times 4.6 \text{ mm}^3$) for subsequent four-point bend fatigue test were cut with the plane under the tension-tension loading being parallel to the T-S plane (T-transverse direction and S-short transverse direction) and the loading axis being along the T direction (Figure 6.1(a)), since the critical fatigue crack nucleation sites on T-S plane were Si-bearing particle associated pores as discussed in Chapter 5 and therefore crack nucleation behavior at micro-notches simulating pre-crack in Fe-bearing particles could avoid the interference from the pre-crack in the Fe-bearing particle on L-T or L-S planes. Another reason to choose T-S sample in the experiment is that the thickness of grain along L direction (thickness direction on T-S sample) is the largest which can guarantee microstructures beneath fabricated micro-notches do not influence the initiated short fatigue crack growth at the early stage. The sample surface in tension under four-point bend was ground using waterproof abrasive papers gradually from grit 240 to 1200, followed by mechanical polishing using alumina powders of 1 micron, 0.3 micron, 0.05 micron in size and a silica colloidal suspension liquid, and ultimately etched with Keller's etchant to reveal grain structure (Figure 6.1(a)) prior to subsequent experimental procedures.

6.2.2 Fabrication of micro-notches in selected grains using EBSD and FIB

As the multi-site fatigue crack nucleation in 2024 and 7075 was primarily attributed to Fe-bearing particles which may be pre-fractured or pre-damaged during the prior

thermo-mechanical deformation, especially on L-T and L-S plane where the crack plane was perpendicular to rolling direction (L), a series of micro-notches have been fabricated to simulate the possible fatigue crack nucleation sites, i.e. Fe-bearing particles using FIB in selected grains. The selection of appropriate grain was following the three criteria: firstly, the area of selected grain should be large enough to contain the fabricated micro-notches with different dimensions; secondly, the distance between selected grains should be far enough to avoid the shielding effects between plastic deformation zones induced by propagating fatigue cracks at multiple sites. Third, the orientations of selected grains were as close as possible by choosing the same texture components within 15° misorientation in EBSD mapping, to reduce the effects of local grain orientation. Subsequently, EBSD was furthermore introduced to select the targets grains by distinguishing low and large grain boundaries and gaining the corresponding grain orientation information. As shown in Figure 6.1(b), 5 to 7 EBSD mapping measurements were carried out to make them distribute as uniform as possible on the tensile surface in each four-point bend sample. In each EBSD mapping (Figure 6.1(c), one or two micro-notches were fabricated dependent on the area of mapping itself and the size of designed micro-notches (Figure 6.1(d)). In 2024 and 7075, the thickness of constituent particles was the key factor controlling the driving force for crack nucleation [72], and categorized those particles into three groups: Type-1, cracks in particles (thinnest in particle thickness, for specific dimensions, please refer to chapter 5 and [72]) never extended into the matrix; Type-2, cracks in particles (in the medium range of particle thickness) extended into the matrix but stopped very soon; Type-3, cracks in particles (thickest in particle thickness) extended into matrix and had the chance to become propagating cracks leading to final failure. Accordingly, in order to further investigate the effects on the geometrical parameters (width, depth and aspect ratio L/S in 3-D) on crack nucleation, three batches of rectangular micro-notches were therefore designed in terms of distinct pairing of width and depth to simulate three types of fractured particles initiating fatigue cracks. First batch was keeping the width the same and the depth different; second batch was keeping the depth same and width different; third batch was keeping the cross-section area same with different combination of width and depth, i.e. aspect ratio. The geometry and dimensions of three batches of micro-notches are shown schematically in Figure 6.2 and 6.3 in 3-D and on S-L projection plane. Since the actual depth of micro-notch was hard to be gained as the designed dimension, fabrication of micro-notch was started at relatively low milling current using FIB, and subsequently

the depth would be measured by identifying the narrow cross-section on L-T plane using SEM which was 32° tilted to horizontal plane at tilting compensation mode until the final depth was close to the designed dimension. The detailed designed and actual dimensions of those micro-notches were represented in the Tables 6.1 and 6.2.

6.2.3 Four-point bend fatigue testing for observation of fatigue crack nucleation behavior and FIB cross-sectioning

The notched samples of 2024 and 7075 were fatigued using a self-aligning four-point bend rig (Figure 3.2) under a constant maximum stress, at a frequency of 20 Hz, stress ratio $R=0.1$ and room temperature in air. The applied stress levels were both chosen as 95% out of the yield strength with accordance of the S-N curve measurement so as to track the fatigue crack within reasonable fatigue cycles. The fatigue tests were periodically interrupted to check the fatigue crack nucleation situation at each micro-notch on the sample surface using an optical microscope at different magnification from $50\times$ to $500\times$. An interval between 1000 to 3000 cycles was chosen, so that the crack tip propagation in both grains and near-GB regions could be monitored as continuously as possible. The fatigue testing was terminated until there were obviously one or more type-3 fatigue cracks initiated which were prone to be the main crack leading to final failure. After the fatigue testing, all crack nucleation behavior at all micro-notches were recorded and summarized. Based on crystal orientations of the parent grains obtained by prior EBSD measurement (Oxford HKL system), the effects of crystallographic orientation, twist angles of initiated crack at notch root, Schmid factor combined the geometry factor of micro-notches have been analyzed in details in 2024 and 7075, respectively. Finally, the fatigue crack traces on surface (T-S plane) and cross-section (S-L plane) were revealed using a Hitachi NB5000 dual beam SEM/FIB system. Subsequently, compared with the traces of primary slip planes on corresponding planes calculated based on orientation information using EBSD, the short fatigue crack crystallographic slip behavior could be examined in both aluminum alloys, which would be discussed in more details later.

6.3 Results and discussions

6.3.1 Multi-site fatigue crack nucleation at micro-notches in AA2024-T351 and AA7075-T651 Al alloys

The four-point bend fatigue tests were conducted on each of those samples with a variety of micro-notches fabricated using FIB. Because the micro-notches were designed to simulate the pre-fractured Fe-bearing particles and the thickness of the particles was the key factor controlling the driving force of fatigue crack nucleation, for each batch of micro-notches, three types of micro-notches were thus designed dependent on different depth of notch, i.e. the deeper micro-notch should be more likely to nucleate propagating crack (Type-3 crack). The proper definition for each notch is essential to distinguish and track fatigue nucleation among many micro-notches with various combinations of width and depth. The method of naming each notch could be illustrated as the following and referred to Tables 6.1 and 6.2 in detail: the #1, 2 and 3 represent the batch number for 2024 and 7075, respectively; T1, 2 and 3 represent the designed type of notch; the last digit of the notch name is just the sequence number of the same type notch which is used to identify each notch, for example, in 7075, #1-T3-2 represents the second designed Type-3 notch in Batch-1 in 7075. For now, the similar multiple crack nucleation behavior as described in previous chapters could be investigated explicitly.

As shown in Figure 6.4 in 2024 aluminum alloy, it is shown that three batches of micro-notches with different combination of notch width and depth were distributed in the dimensions diagram of width vs. depth: the solid signs (black circles, blue squares and red triangles) marked the designed ideal dimensions of notches in three batches, respectively. The hollow sign of corresponding geometries represented the actual dimensions of micro-notches fabricated by FIB. The dot lines with an arrow at the end pointed out the trend of becoming ideal type-3 notch (Type-3) which is more detrimental. Based on observation of the multiple crack nucleation after fatigue loading, It can be concluded that the wider and deeper notch is more detrimental, as in the red highlighted area in the upper right corner of Figure 6.4, all the micro-notches pointed by red arrows nucleated the propagating Type-3 fatigue cracks among all three batches of notches. In the middle of Figure 6.4, the area highlighted by blue represented the Type-2 crack zone which meant that the crack initiated from these notches stop propagating after extending into the matrix.

The similar crack nucleation behaviors were also observed that the wider and deeper micro-notches nucleated the propagating fatigue cracks as shown in Figure 6.5 all actual Type-3 notches were located in the area highlighted by red, whereas the real Type-2 notches were distributed in the area highlighted by blue where both width and depth was in the medium ranges of dimensions (15-30 μm and 6-9 μm). Accordingly, for both 2024 and 7075, the wider and deeper notches were the more detrimental for fatigue crack nucleation, i.e. width and depth should be both the key factors controlling the driving force for crack nucleation. However, it seems not consistent with the conclusion drawn from real constituent particles that thickness of particle is the only key factor controlling the driving force of crack nucleation, especially, the two exceptions of the notches #3-T1-2 in 2024 (Figure 6.4) and #3-T1-1 in 7075 (Figure 6.5) that were very shallow (6.2 and 4.8 μm) but extremely wide (40 μm for both) leading to the Type-3 cracks. If the depth is the only factor contributing to the driving force of nucleation as constituent particles, the two notches with such dimensions should not become the nucleation sites for the propagating cracks. However, in reality the phenomena is not controversial with the conclusion from the particle case and conversely could be explained scientifically with accordance to the fracture mechanics to quantify the driving force for a semi-circular surface crack in an infinite matrix [182], simply because in the case of crack nucleation from constituent, no such wide particles existed in the alloys leading to propagating cracks which might cover the contribution from width of particles to the crack nucleation. Based on the statistical analysis on width of particle on L-T plane in 7075 wherein relatively wide particles existed most likely (Figure 6.6), it could be observed that almost all the particle width were smaller than 25 μm and occasionally some 30 or 40 μm wide particles were only account for less than 0.1% of total number of particles. In conclusion, the width and depth of micro-notches actually should contribute to the driving force of crack nucleation.

6.3.2 Comparison of fatigue crack nucleation behaviors at micro-notches to mimic fractured particles between AA2024 and AA7075

After cyclic fatigue loading, it could be observed that multiple cracks were initiated from different micro-notches and the nucleation behavior has been summarized in Figure 6.4 for 2024 and Figure 6.5 for 7075. Those non-initiated notches was naturally regarded as Type-1 crack, while the initiated cracks, including Type-2 and 3, would be the objects

of research in the section. The factors that might influence Type-2 and 3 crack nucleation behaviors in these two alloys will be analyzed and explained in details, respectively.

As shown in Figure 6.7, a Type-2 fatigue crack was initiated from #3-T3-4 micro-notch in 2024, wherein two parts straight short cracks parallel to each other was observed to be nucleated from upper and lower notch root simultaneously. Based on the EBSD measurement in the vicinity of the notch, the four traces of primary slip planes $\{111\}$ on the sample surface were calculated and represented in Figure 6.7(a), demonstrating that the crack path was parallel to the trace of $(1\bar{1}1)$ highlighted by red on the surface. To verify the deduction that crack plane propagated along crystallographic slip plane, the FIB was introduced to cross-section in the path of upper crack in Figure 6.7(a), indicating that intersection lines of crack plane and cross-section (L-T) was parallel to trace of $(1\bar{1}1)$ on the cross-section by FIB again. Thus, it could be concluded safely that the fatigue crack propagated along $(1\bar{1}1)$ plane. The twist angle of the crack plane at micro-notch root could be obtained and equal to 10.5° , the definition of twist angle was schematically illustrated in Figure 6.7(d). Similarly, the relatively long fatigue crack initiated from the #1-T3-1 notch in 2024 induced final failure of this sample. From the morphology of crack, it could be observed that the crack path was also fairly straight and parallel to the trace of $(1\bar{1}1)$ plane on the surface calculated based on the EBSD measurement in Figure 6.8(b). The phenomenon has not been convinced by observing the cross-section by FIB because the crack became the main crack. In the future, the fractography would be carried out to investigate the fracture surface furtherly, and hereby the long crack was assumed to be parallel to primary slip plane which could be supported by other further scientific explanations. In overall, the conclusion can be draw the fatigue crack prefer to be propagating in the crystallographic slip planes, i.e. $\{111\}$ plane. The phenomenon could also be supported by the parallel slip bands observed along long crack tip where the severe plastic deformation occurred as shown in Figure 6.9(a), which was consistent with the observation in the austenitic steel [160].

Accordingly, the shear stress components should be the main contributor to the driving force of crack nucleation in 2024. As shown in Table 6.3, the maximum Schmid factor in all four $\{111\}$ planes were given, and it was demonstrated that for Type-2 crack, the crack followed the $(1\bar{1}1)$ plane with the maximum Schmid factor equal to 0.4896. However, for Type-3 crack, if the crack followed the $(1\bar{1}1)$ plane as indicated in Figure

6.8(a), the Schmid factor of $(1\bar{1}1)$ in this case was only 0.2273 which was not the highest one compared with other slip planes. This results are therefore needed to be investigated continuously. In reality, at the very early stage of total fatigue life, microstructurally small fatigue crack was extremely sensitive to the local microstructures and might be readily retarded when just initiated. Thus, for investigation of the crack nucleation behavior, besides of the driving force, the local resistance to crack growth at the early stage should be essentially taken into consideration as well. The twist angle of short crack plane at grain boundary (GB) influence crack propagation significantly [99]. Wei subsequently quantify the short fatigue crack growth resistance as a Weibull function of twist angle of crack plane at GB in 2024 aluminum alloy, in which the particle/matrix interface was also prone to retard short fatigue crack nucleation from Al_7Cu_2Fe constituent particle [72, 196]. Now that in this work all the micro-notches was fabricated using FIB to mimic the fractured Fe-bearing particle aiming at simulating the fatigue crack nucleation from particle. The twist of crack plane at notch root also should be the key factor for the resistance. It can be seen in Table 6.3 the Type-2 crack indeed followed the path with minimum twist angle equal to 10.5° , which makes it crack propagating along crystallographic slip planes reasonable combined with maximum Schmid factor contributing to the driving force. As shown in Figure 6.10(a), the normalized the Schmid factor deducted by minimum normalized twist angle was obviously the largest demonstrating that crack should follow the $(1\bar{1}1)$ plane highlighted by the red rectangular. In Type-3 case, although the Schmid factor was not the largest, the twist angle of $(1\bar{1}1)$ plane was only 3.7° which was much smaller than others. If the driving force and resistance were considered at the same time, it could be more reasonable to follow the $(1\bar{1}1)$ plane as well since the driving force deduced by resistance attributed to the twist angle was relatively high among all planes as shown in Figure 6.10(b).

In the contrary, fatigue cracks in 7075 did not appear similar nucleation behavior as that in 2024. As shown in Figure 6.11(a), the Type-2 crack was initiated at micro-notch. The path of upper and lower part of this crack was firstly not straight as behaved in 2024. The Type-2 crack in Figure 6.11(a) was roughly normal to the loading direction (T-Transverse direction) and more important did not follow any traces of $\{111\}$ planes on surface. In Figure 6.11(b), the relatively long Type-3 crack seemed like following crystallographic slip plane although the path of crack on the surface was a little wavy and curved. Based on the EBSD measurement, the Euler angles in the parent grain were

obtained and the traces of corresponding $\{111\}$ planes were calculated. It was shown that no one $\{111\}$ plane was perfectly matching the crack path on the surface. Also, when the crack became a long crack, no slip bands were observed along the fatigue crack as shown in Figure 6.9(b), while only severely plastic deformed zone formed around the long crack tip possibly induced by the dislocation pile-up. In conclusion, 7075 was not crystallographic planar-slip alloys as 2024, i.e. the fatigue cracks did not follow the $\{111\}$ planes, which was consistent with the experimental results in 7000 series aluminum alloys [173].

6.4 Conclusions

Three batches of micro-notches were fabricated in selected grains of T-S samples in AA2024-T351 and AA7075-T651 aluminum alloys using FIB to mimic fractured particles. After fatigue loading, the wider and deeper micro-notches became the fatigue cracks initiation sites more easily. In AA2024-T351 samples, cracks preferred to propagate in the $\{111\}$ slip planes with smallest twist angle and relatively large Schmid factor. In AA7075-T651 samples, cracks did not follow the crystallographic slip planes perfectly. Based on these experimental data, a 3-D quantitative model could be eventually developed to simulate fatigue crack initiation by taking into consideration driving force and resistance to short crack growth.

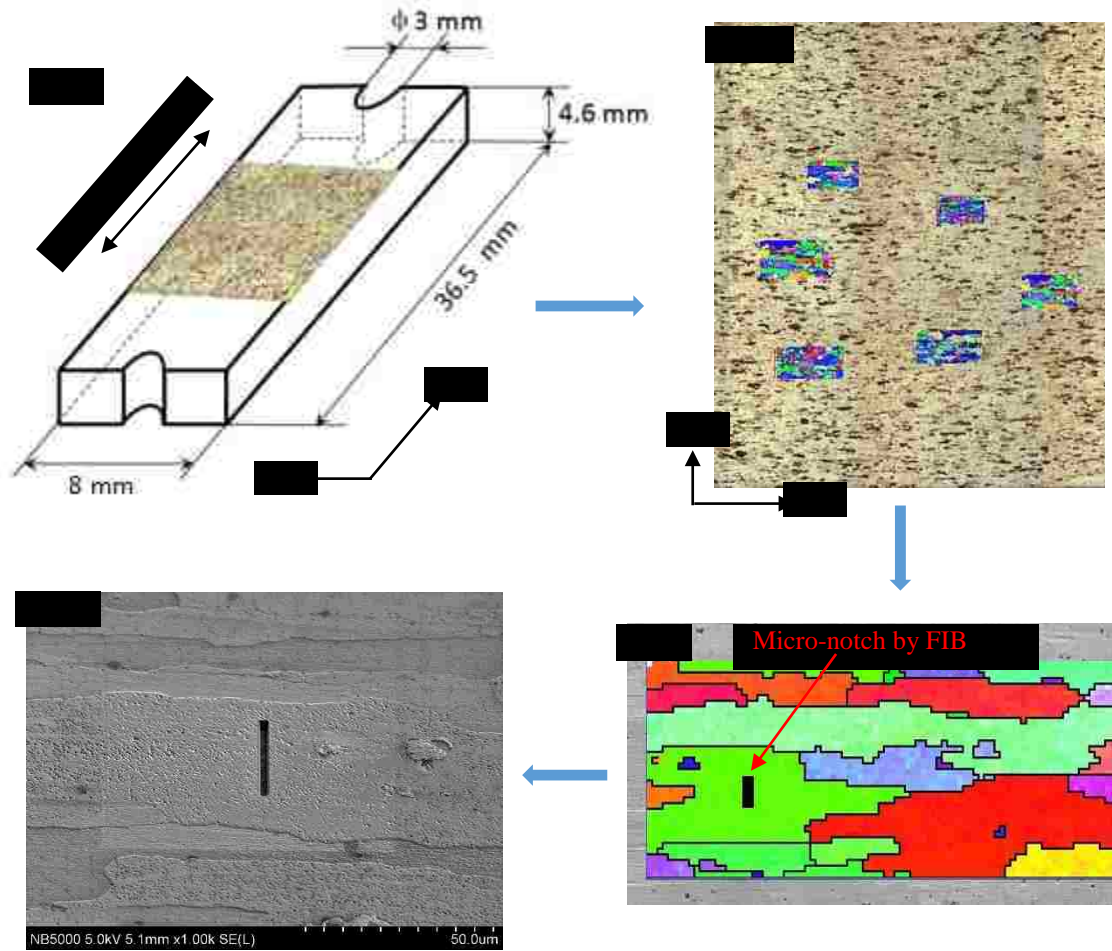


Figure 6.1 The schematic working procedure of fabricating micro-notches in selected grains using EBSD and FIB on T-S plane of AA2024 and AA7075: (a) the geometry and dimension of T-S four-point bend samples and grain microstructure on the tensile surface; (b) EBSD mapping distributed uniformly on tensile surface of T-S sample; (c) selection of grain for fabrication of micro-notch using FIB in EBSD mapping; (d) a SEM micrograph of a micro-notch fabricated by FIB. (note: for only illustrating the working procedure, the arbitrary microstructure, EBSD mapping and scale were chosen from 2024 and 7075, respectively.)

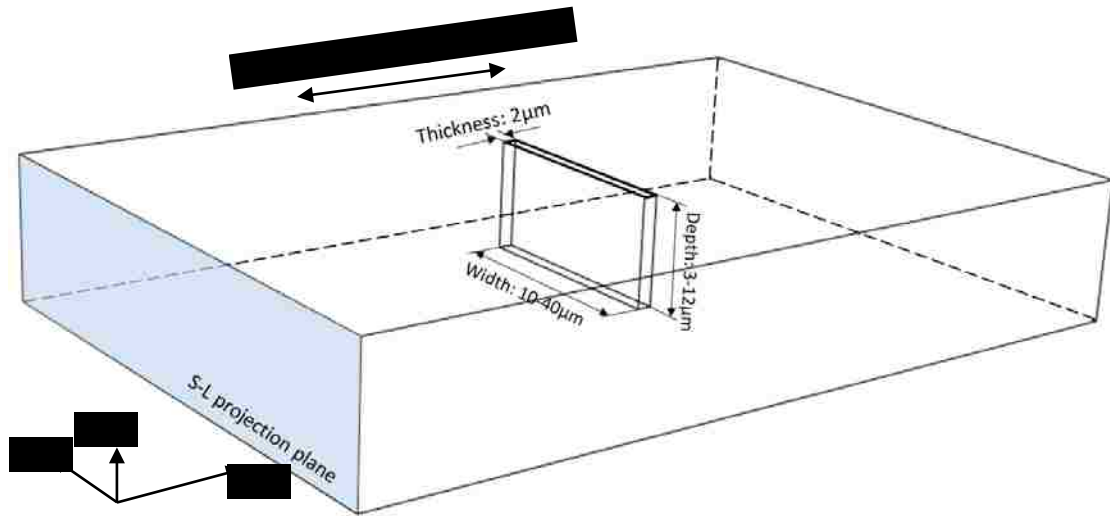


Figure 6.2 The designed rectangular geometry and the definitions of width, depth and thickness of micro-notches fabricated by FIB in 3-D in T-S samples.

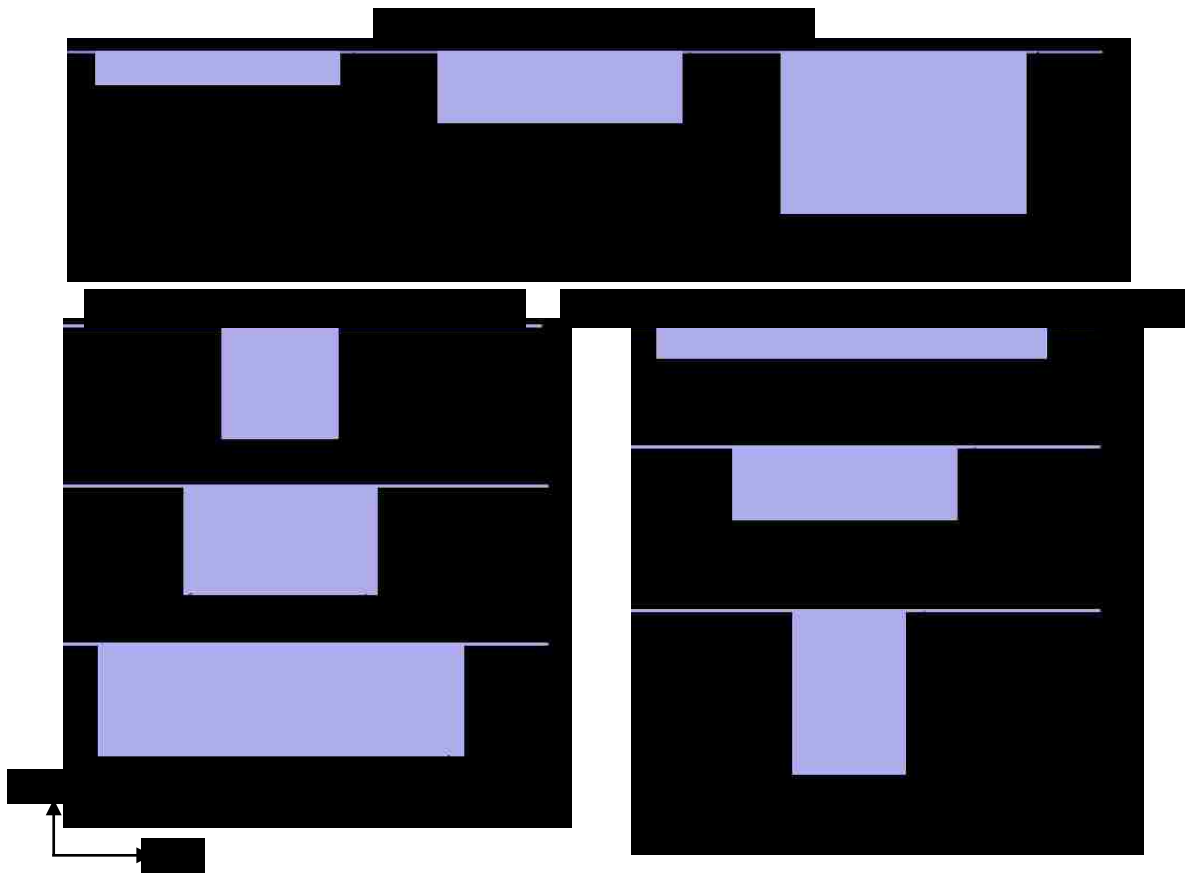


Figure 6.3 The detailed dimensions of three batches of micro-notches fabricated by FIB on S-L projection plane highlighted by light blue in Figure 6.2 in T-S samples.

Table 6.1 The designed and actual dimensions and fatigue crack initiation status of three batches of micro-notches fabricated by FIB in 2024.

#1 batch-same width, different depth(2024)				
sample name	micro-notch size (μm)			initiation status
	width	depth	actual depth	
#1-T1-1	30	3	2.3	no
#1-T1-2	30	3	2.7	no
#1-T2-1	30	6	7.4	no
#1-T2-2	30	6	8.1	no
#1-T3-1	30	12	12.2	Type-3
#1-T3-2	30	12	12.5	Type-3
#2 batch-same depth, different width(2024)				
sample name	micro-notch size (μm)			initiation status
	width	depth	actual depth	
#2-T1-1	10	10	8.1	no
#2-T1-2	10	10	9.1	no
#2-T2-1	20	10	10.4	no
#2-T2-2	20	10	11	no
#2-T3-1	40	10	12.6	no
#2-T3-2	40	10	9.9	Type-3
#3 batch-same cross-section, different aspect ratio L/S(2024)				
sample name	micro-notch size (μm)			initiation status
	width	depth	actual depth	
#3-T1-1	40	3	4.8	no
#3-T1-2	40	3	6.2	Type-3
#3-T1-3	40	3	3.8	no
#3-T2-1	20	6	7.3	no
#3-T2-2	20	6	7.1	no
#3-T2-3	20	6	10.4	Type-2
#3-T2-4	20	6	9.11	no
#3-T3-1	10	12	16	no
#3-T3-2	10	12	15	no
#3-T3-3	10	12	13	no
#3-T3-4	10	12	11.1	Type-2

Table 6.2 The designed and actual dimensions and fatigue crack initiation status of three batches of micro-notches fabricated by FIB in 7075.

#1 batch-same width, different depth(7075)				
sample name	micro-notch size (μm)			initiation status
	width	depth	actual depth	
#1-T1-1	30	3	3.2	no
#1-T1-2	30	3	3.7	no
#1-T1-3	30	3	2	no
#1-T2-1	30	6	7.7	Type-2
#1-T2-2	30	6	7.5	no
#1-T3-1	30	12	12.9	Type-3
#1-T3-2	30	12	14	Type-3
#2 batch-same depth, different width(7075)				
sample name	micro-notch size (μm)			initiation status
	width	depth	actual depth	
#2-T1-1	10	10	9.5	no
#2-T1-2	10	10	7.8	no
#2-T2-1	20	10	10.6	no
#2-T2-2	20	10	9.7	Type-3
#2-T3-1	40	10	9.5	no
#2-T3-2	40	10	16.9	Type-3
#3 batch-same cross-section, different aspect ratio L/S(7075)				
sample name	micro-notch size (μm)			initiation status
	width	depth	actual depth	
#3-T1-1	40	3	4.8	Type-3
#3-T1-2	40	3	3.2	no
#3-T2-1	20	6	8.2	Type-2
#3-T2-2	20	6	8.9	Type-3
#3-T3-1	10	12	12	no
#3-T3-2	10	12	11	no

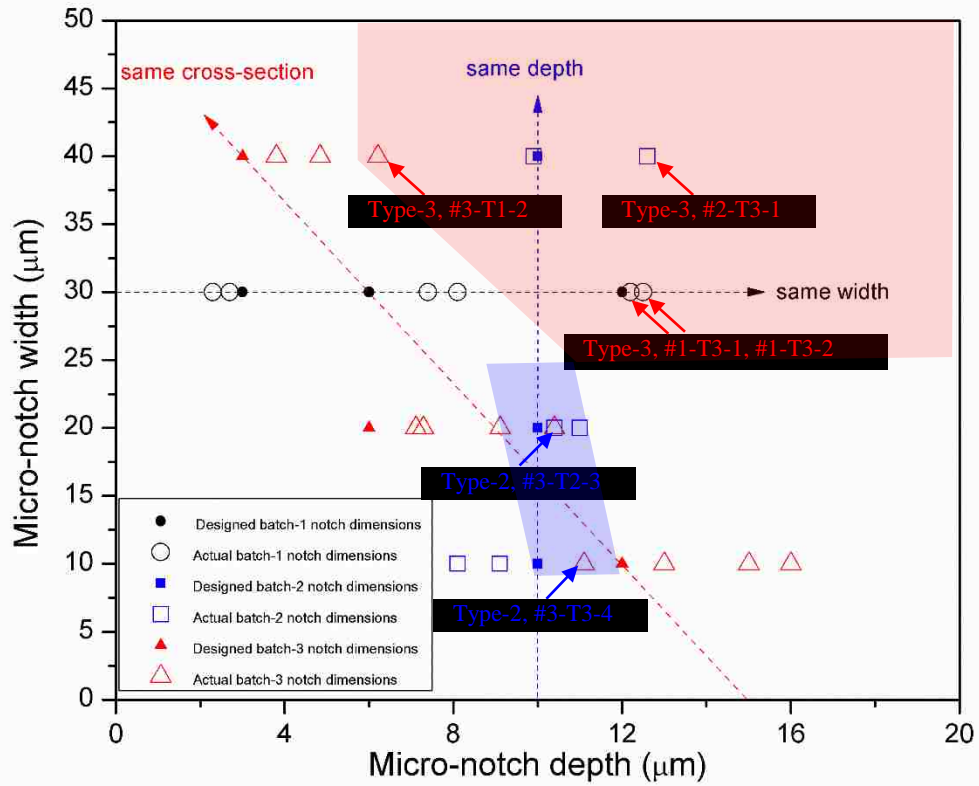


Figure 6.4 The schematic diagram to illustrate the designed and actual dimensions of three batches of micro-notches fabricated by FIB in AA2024 T351 Al alloy, fatigue crack nucleation status from notches after fatigue loading: notches pointed by red arrows nucleated type-3 fatigue cracks, and those pointed by blue arrows nucleated type-2 fatigue cracks, remaining notches did not nucleated any cracks representing type-1 situation (red highlighted area: type-3 cracks; blue highlighted area: type-2 cracks; other area might represent the type-1 crack.)

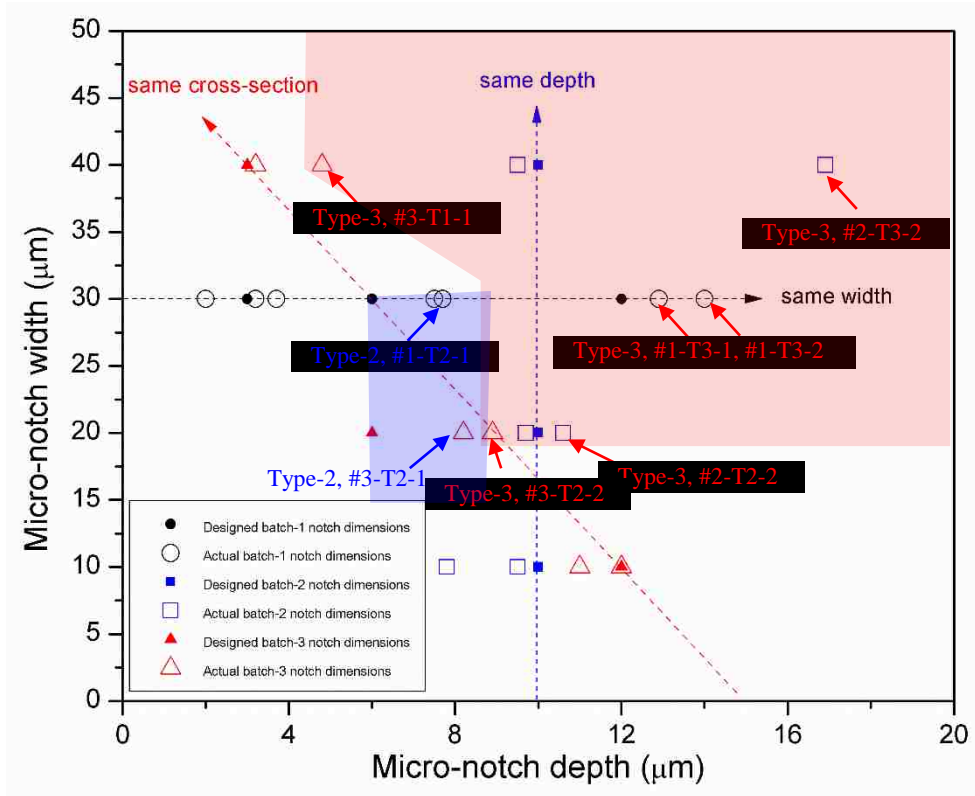


Figure 6.5 The schematic diagram to illustrate the designed and actual dimensions of three batches of micro-notches fabricated by FIB in AA7075 T651 Al alloy, fatigue crack nucleation status from notches after fatigue loading: notches pointed by red arrows nucleated type-3 fatigue cracks, and those pointed by blue arrows nucleated type-2 fatigue cracks, remaining notches did not nucleated any cracks representing type-1 situation (red highlighted area: type-3 cracks; blue highlighted area: type-2 cracks; other area might represent the type-1 crack.)

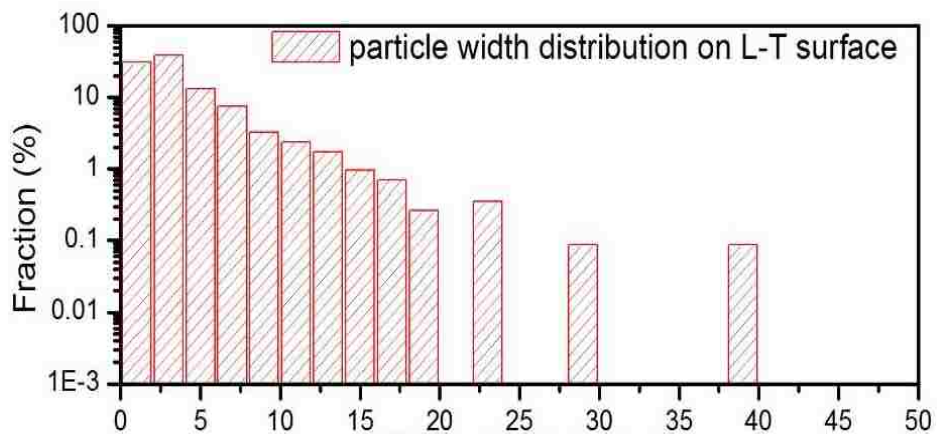


Figure 6.6 constituent particle width distribution on L-T plane of AA7075.

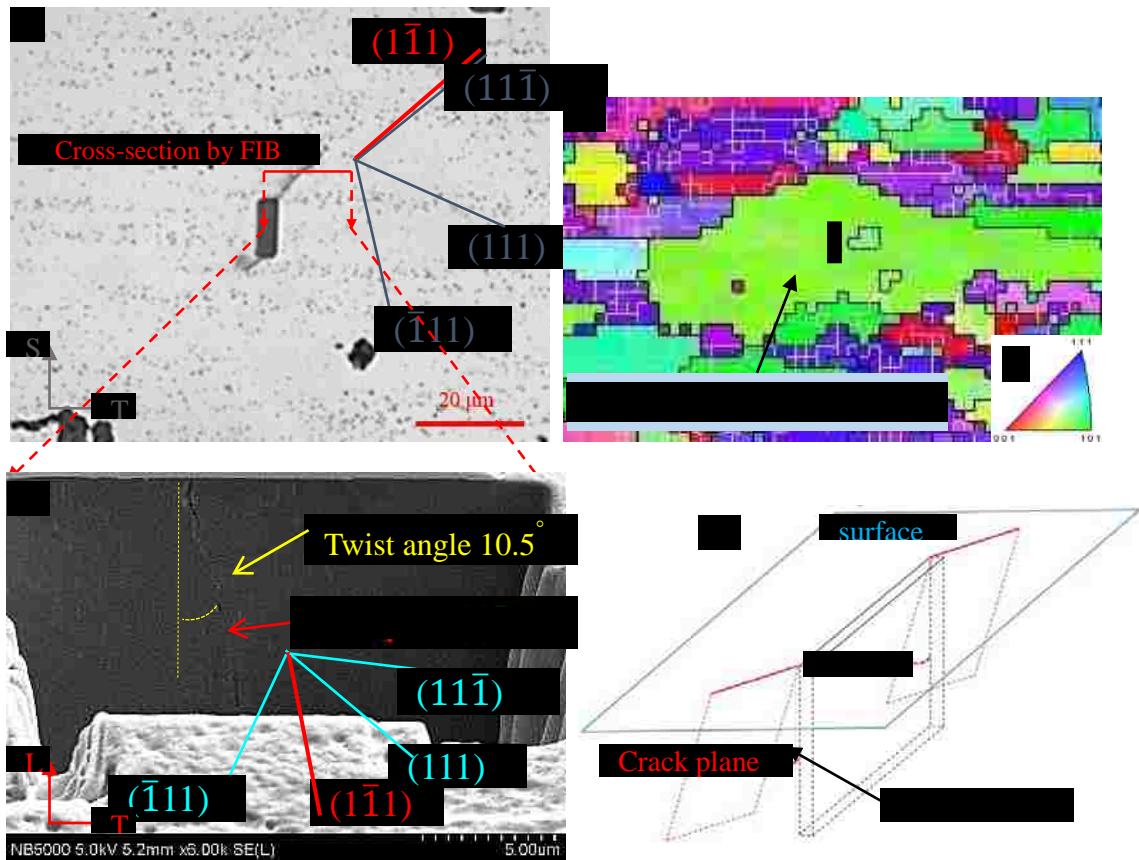


Figure 6.7 a Type-2 fatigue crack initiated at #3-T3-4 micro-notch in AA2024: (a) a short crack extended into matrix and crack path was parallel to $(1\bar{1}1)$ trace on the surface; (b) the EBSD mapping of surrounding grains and the Euler angles of parent grain; (c) the cross-section by using FIB on the crack path as shown in (a) and the intersection between crack plane and cross-section surface (L-T) parallel to $(1\bar{1}1)$ trace indicating the twist angle at notch root is equal to 10.5° ; (d) a 3-D schematic to illustrate the twist angle at notch root.

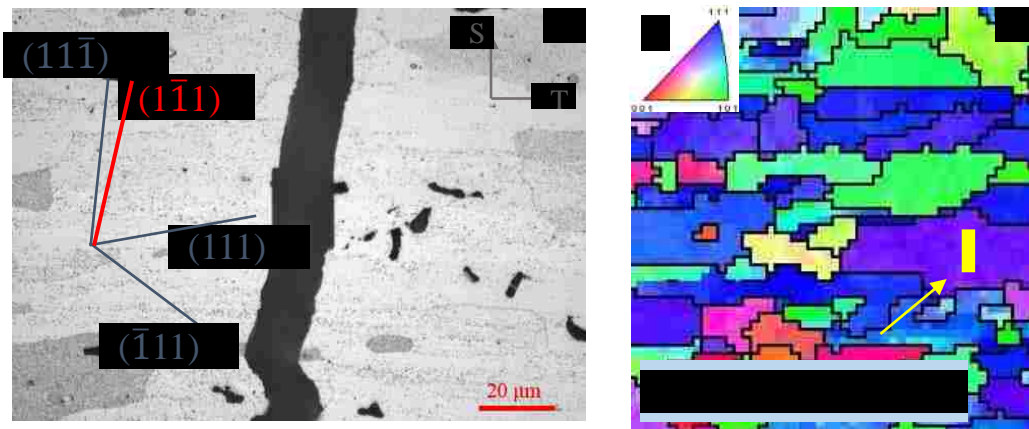


Figure 6.8 a Type-3 fatigue crack initiated at #1-T3-1 micro-notch in AA2024: (a) a relatively long crack extended into matrix and was propagating in the matrix leading to the final failure, and all traces of $\{111\}$ planes on the surface; (b) the EBSD mapping of surrounding grains and the Euler angles of parent grain.

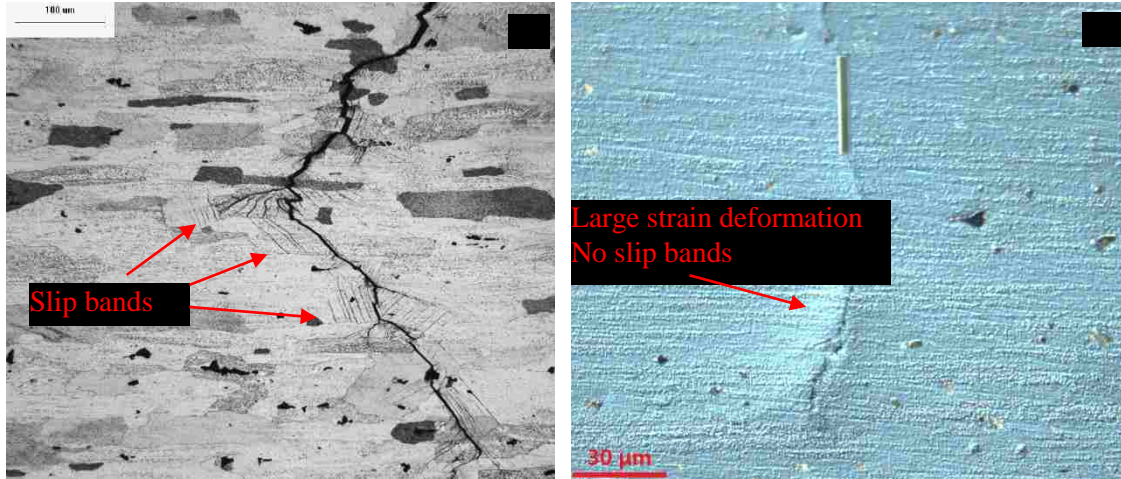


Figure 6.9 (a) The slip bands locating along the relatively long fatigue crack in 2024; (b) no slip bands were observed along long crack in 7075, conversely large strain deformed topography could be observed on polarized light mode using optical microscope.

Table 6.3 Twist angles α ($^\circ$) at notch root and maximum Schmid factor (SF) of the corresponding $\{111\}$ of Type-2 crack initiated from #3-T3-4 and Type-3 crack initiated from #1-T3-1 in 2024.

Slip planes	Type-2: #3-T3-4 in 2024				Type-3: #1-T3-1 in 2024			
	α ($^\circ$)	α normalized by max. α	SF	SF normalized by max. SF	α ($^\circ$)	α normalized by max. α	SF	SF normalized by max. SF
111	49.9	0.6078	0.3408	0.6961	69.4	0.9378	0.1451	0.3528
$\bar{1}\bar{1}\bar{1}$	25.7	0.3130	0.4174	0.8525	41.7	0.5635	0.4113	1
$\bar{1}\bar{1}\bar{1}$	10.5	0.1279	0.4896	1	3.7	0.05	0.2273	0.5526
$11\bar{1}$	82.1	1	0.1254	0.2561	74	1	0.254	0.6176

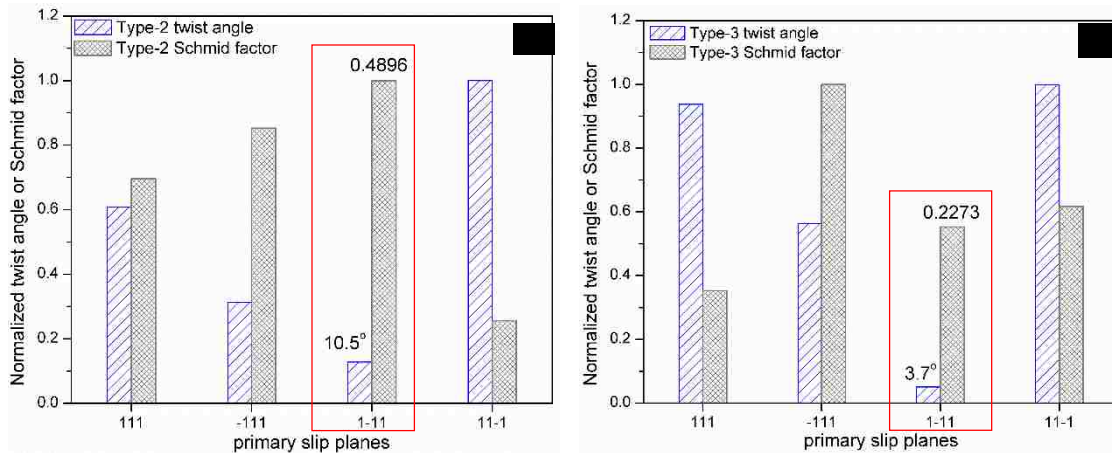


Figure 6.10 The twist angles and Schmid factors of four $\{111\}$ planes normalized by the corresponding the maximum values in (a) Type-2 and (b) Type-3 cases in 2024, respectively.

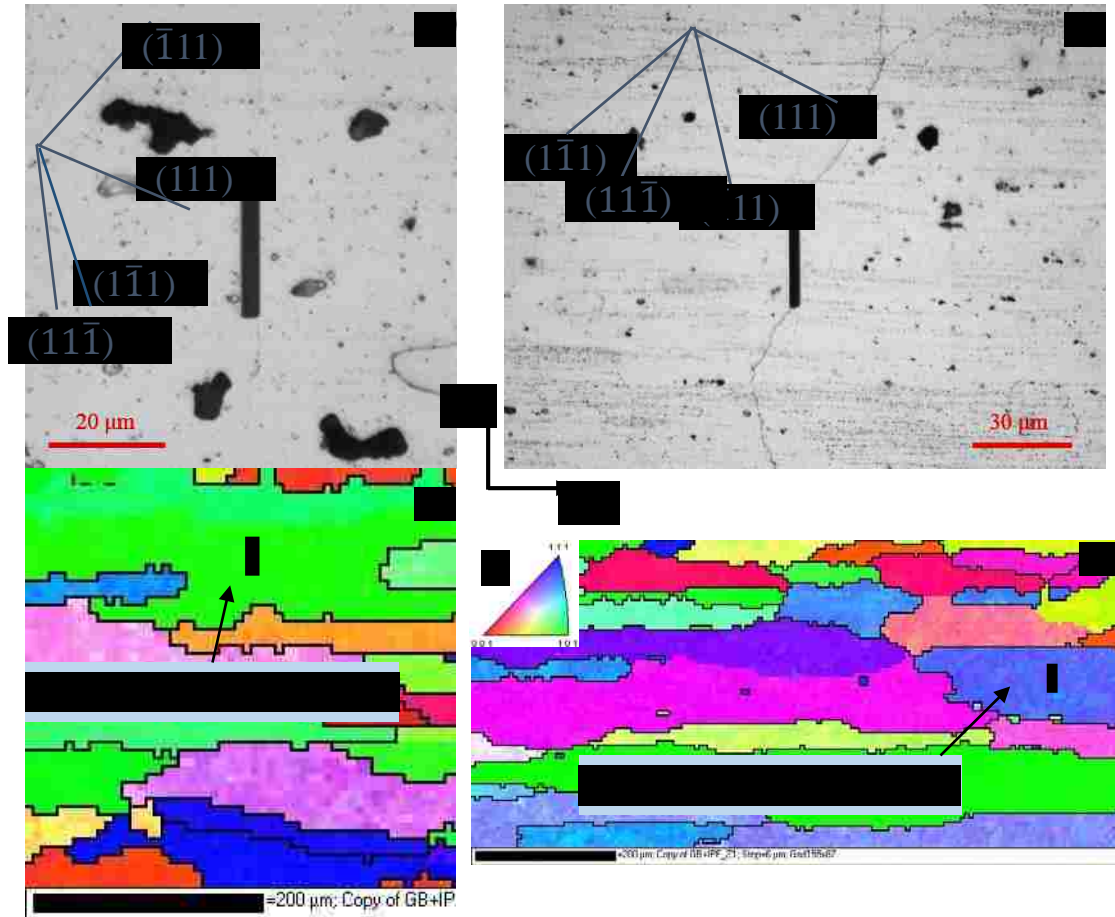


Figure 6.11 (a) a Type-2 fatigue crack initiated at #3-T2-1 micro-notch and $\{111\}$ plane traces on the surface in 7075; (b) a Type-3 fatigue crack initiated at #1-T3-2 micro-notch and the $\{111\}$ plane traces in 7075; (c) the EBSD mapping around #3-T2-1 and the Euler angles of parent grain where #3-T2-1 was located; (d) the EBSD mapping around #1-T3-2 and the Euler angles of parent grain where #1-T3-2 was located.

Chapter 7 Conclusions

An experimental method was further developed to quantify the multi-site fatigue crack nucleation behaviors in terms of FWL density and strength distribution which can be regarded as fatigue properties of materials. By utilizing this experimental method, the anisotropy of multi-site fatigue crack nucleation was investigated in an AA7075-T651 rolled plate with FIB, EBSD, AFM and Nano-indentation. The 3-D characteristics of Fe- and Si-bearing constituent particles showed a key effect on the multi-site fatigue crack nucleation behaviors on L-T, L-S and T-S planes in this alloy. Rectangular micro-notches with three different dimensions were fabricated using FIB in selected grains on the T-S planes in AA2024-T351 and AA7075-T651 aluminum alloys which had respectively a strong and weak tendency for planar slip, to verify the 3-D effect of the pre-fractured particles on fatigue crack initiation in these alloys. All these experimental data could pave the way to building a 3-D microstructural-based model to quantify the fatigue crack initiation behaviors by taking into consideration both the driving force and resistance to short crack growth. The following main conclusions can be drawn from the current research work:

- 1) Among all the sigmodal functions, the three parameter Weibull-type function was found to be the more appropriate one to describe the relation of FWLs with the applied maximum cyclic stress or strain in engineering alloys.
- 2) Non-uniform distribution of the porosities that were potential FWLs in an A713 alloy could affect the FWL density observed on the sample surface. Therefore, the crack initiation rate density instead of FWL density should be used in the Weibull function to quantify the relation between FWLs and the applied stress more accurately and reliably.
- 3) The applied maximum cyclic strain should be used in the Weibull function to describe the relationship between FWL population and maximum cyclic strain in an alloy, when the maximum cyclic stress exceeded the yield stress of an alloy.

- 4) Relative humidity profoundly increased FWLs in Al alloys. FWL density was 1 mm⁻² at 0% relative humidity, in contrast to 1.3 mm⁻² at 50% relative humidity in AA2026 Al alloy.
- 5) The experimental technique developed in this work to characterize FWLs possesses advantages over the traditional S-N curve method to evaluate the fatigue crack initiation behaviors of engineering alloys. It could quantitatively characterize the FWL density and strength distribution of an alloy which shows multi-site fatigue crack nucleation. It allows quantitative evaluation of the crack nucleation sites in engineering alloys for alloy design, quality control and improvement.
- 6) Fatigue weak-links (FWLs) were a Weibull function of applied maximum cyclic stress in the AA 7075-T651 aluminum alloy plate. There was a strong anisotropy of fatigue weak-links in the alloy with the highest weak-link density (15 mm⁻²) being on the L-S plane and the lowest (4 mm⁻²) on the T-S plane. The weak-link density on the L-T plane was 11 mm⁻².
- 7) Fatigue cracks were predominantly initiated at the pre-fractured Fe-containing particles on the L-T and L-S planes, but only at Si-bearing particles on the T-S plane in the AA 7075-T651 aluminum alloy. The pre-fractured or pre-damaged Fe-containing particles (3.16% on L-T and 2.67% on L-S plane) were the precursors for fatigue crack initiation on the L-T and L-S planes in the alloy.
- 8) Fatigue limits of the L-T, L-S and T-S planes in maximum cyclic stress by four-point bend were measured to be 243.6 MPa, 273.0 MPa and 280.6 MPa, respectively. Fewer fatigue weak-links presented on the T-S plane, which was attributed to the fact that the pre-fractured Fe-containing particles had no effect on crack initiation on this plane since the micro-cracks in the particles were roughly parallel to the T-S plane.
- 9) On the T-S plane, those thick (> 8.3 μm) Si-bearing particles that were combined with gas pores were more likely to nucleate propagating cracks, which was verified by cross-sectioning the particles using FIB.

- 10) Fe-containing particles on the mechanically polished surface were protruded in high strength Al alloys, while Si-bearing particles were intruded, which was consistent with the nano-hardness measurements showing that Si-bearing particles were softer and more ductile than the Fe-containing ones.
- 11) Based on EBSD measurements on the fatigued AA7075 T651 Al alloy, fatigue cracks did not exclusively follow the primary slip planes, i.e. $\{111\}$ planes, and sometimes propagated approximately normal to the loading direction. No specific grain orientations were found that were associated with those Fe- and Si-particles at which Type-III fatigue cracks were initiated in the AA7075 alloy.
- 12) Rectangular micro-notches with three typical dimensions were fabricated in the selected grains on the T-S planes in AA2024-T351 and AA7075-T651 aluminum alloys using FIB, to verify the 3-D geometrical effects of the pre-fractured particles. The fatigue tests on these samples revealed that the wider and deeper a micro-notch, the easier a fatigue crack could be initiated from the notch. A map of fatigue crack initiation was obtained in terms of micro-notch depth and width, showing the regions (in the depth vs. width plot) of forming types-I, II and III, respectively.
- 13) In AA2024-T351 samples, cracks preferred to propagate along the $\{111\}$ slip plane with smallest twist angle and relatively large Schmidt factor. In AA7075-T651 samples, cracks did not follow a specific crystallographic slip plane.
- 14) The experimental data obtained from this research work could pave a way to building a 3-D quantitative model for simulation of the fatigue crack initiation behaviors by taking into account both the driving force and resistance to short crack growth in high strength Al alloys.

References

- [1] S. Suresh, *Fatigue of Materials*, 2nd ed., Cambridge University Press, 1998.
- [2] J. SCHIJVE, *Fatigue of Structures and Materials*, Kluwer Academic Publishers, 2001.
- [3] R.C. Alderliesten, J. Schijve, S. van der Zwaag, *Eng Fract Mech*, 73 (2006) 697-709.
- [4] J.A. Collins, *Failure of Materials in Mechanical Design*, 2nd ed., A Wiley-Interscience Publication, 1993.
- [5] J.A. Ewing, J.C.W. Humfrey, *Philosophical Transactions of the Royal Society of London Series a-Containing Papers of a Mathematical or Physical Character*, 200 (1903) 241-U228.
- [6] W. Baxter, P.-C. Wang, *MTA*, 21 (1990) 1151-1159.
- [7] S. S, *International Metal Reviews*, 29 (1984) 445-475.
- [8] W. Cassada, J. Liu, J. Staley, *Advanced Materials & Processes*, 160 (2002) 27-29.
- [9] V.V. Bolotin, *Mechanics of fatigue*, CRC Press, Boca Raton, 1999.
- [10] D.L. McDowell, *Mat Sci Eng a-Struct*, 468 (2007) 4-14.
- [11] D.L. McDowell, F.P.E. Dunne, *International Journal of Fatigue*, 32 (2010) 1521-1542.
- [12] D.L. McDowell, K. Gall, M.F. Horstemeyer, J. Fan, *Eng Fract Mech*, 70 (2003) 49-80.
- [13] J.H. Fan, D.L. McDowell, M.F. Horstemeyer, K. Gall, *Eng Fract Mech*, 68 (2001) 1687-1706.
- [14] J.D. Hochhalter, D.J. Littlewood, R.J. Christ, M.G. Veilleux, J.E. Bozek, A.R. Ingraffea, A.M. Maniatty, *Model Simul Mater Sc*, 18 (2010).
- [15] U. Krupp, *Fatigue Crack Propagation in Metals and Alloys*, 2007.
- [16] T.C. Lindley, K.J. Nix, *Proc. Fatigue Crack Growth*, (1986).
- [17] C.S. Barrett, *Structure of Metals (crystallographic method, principles and data)*, McGRAW-Hill book company, 1952.
- [18] H. Mughrabi, R. Wang, K. Differt, U. Essmann, *Fatigue Mechanisms*, ASTM, Philadelphia, 1983.
- [19] U. Essmann, U. Gosele, H. Mughrabi, *Philos Mag A*, 44 (1981) 405-426.
- [20] C. Scheerder, *Delft University of Technology*, 1992.
- [21] K.K. Sankaran, R. Perez, K.V. Jata, *Advanced Materials & Processes*, 158 (2000) 53-54.
- [22] A. Hunsche, P. Neumann, *Acta Metallurgica*, 34 (1986) 207-217.
- [23] W.A. Wood, *Philos Mag*, 3 (1958) 692-699.
- [24] P.J.E. Forsyth, *Nature*, 171 (1953) 172-173.
- [25] A.S. Cheng, C. Laird, *Materials Science and Engineering*, 51 (1981) 111-121.
- [26] D. Sigler, M.C. Montpetit, W.L. Haworth, *Metallurgical Transactions a-Physical Metallurgy and Materials Science*, 14 (1983) 931-938.

- [27] W.L. Haworth, A.F. Hieber, R.K. Mueller, *Metallurgical Transactions a-Physical Metallurgy and Materials Science*, 8 (1977) 1597-1604.
- [28] B.L. Boyce, J.R. Michael, P.G. Kotula, *Acta Materialia*, 52 (2004) 1609-1619.
- [29] C. Laird, J.M. Finney, D. Kuhlmannwilsdorf, *Materials Science and Engineering*, 50 (1981) 127-136.
- [30] R. Chang, W.L. Morris, O. Buck, *Scripta Metallurgica*, 13 (1979) 191-194.
- [31] W.L. Morris, M.R. James, *Metallurgical Transactions a-Physical Metallurgy and Materials Science*, 11 (1980) 850-851.
- [32] K. Tanaka, *Metallurgical Transactions a-Physical Metallurgy and Materials Science*, 13 (1982) 117-123.
- [33] K. Tanaka, T. Mura, *J. Appl. Mech.-Trans. ASME*, 48 (1981) 97-103.
- [34] K. Tanaka, T. Mura, *Mech Mater*, 1 (1982) 63-73.
- [35] K. Tanaka, T. Mura, *Acta Metallurgica*, 32 (1984) 1731-1740.
- [36] K. Gall, M.F. Horstemeyer, B.W. Degner, D.L. McDowell, J.H. Fan, *International Journal of Fracture*, 108 (2001) 207-233.
- [37] Y. Xue, D.L. McDowell, M.F. Horstemeyer, M.H. Dale, J.B. Jordon, *Eng Fract Mech*, 74 (2007) 2810-2823.
- [38] H. Zhang, H. Toda, P.C. Qu, Y. Sakaguchi, M. Kobayashi, K. Uesugi, Y. Suzuki, *Acta Materialia*, 57 (2009) 3287-3300.
- [39] M.M. Shenoy, R.S. Kumar, D.L. McDowell, *International Journal of Fatigue*, 27 (2005) 113-127.
- [40] C. Przybyla, R. Prasannavenkatesan, N. Salajegheh, D.L. McDowell, *International Journal of Fatigue*, 32 (2010) 512-525.
- [41] A. Fatemi, D.F. Socie, *Fatigue & Fracture of Engineering Materials & Structures*, 11 (1988) 149-165.
- [42] A. Fatemi, L. Yang, *International Journal of Fatigue*, 20 (1998) 9-34.
- [43] J.D. Hochhalter, D.J. Littlewood, M.G. Veilleux, J.E. Bozek, A.M. Maniatty, A.D. Rollett, A.R. Ingraffea, *Model Simul Mater Sc*, 19 (2011).
- [44] Z.Q. Xu, W. Wen, T.G. Zhai, *Metall Mater Trans A*, 43A (2012) 2763-2770.
- [45] *Mat Sci Eng a-Struct*, 3639-3644.
- [46] Y. Jin, P. Cai, W. Wen, H. Nagaumi, B. Xu, Y. Zhang, T. Zhai, *Materials Science and Engineering: A*, 622 (2015) 7-15.
- [47] D.G. Harlow, J. Nardiello, J. Payne, *International Journal of Fatigue*, 32 (2010) 505-511.

- [48] J. Payne, G. Welsh, R.J. Christ, Jr., J. Nardiello, J.M. Papazian, *International Journal of Fatigue*, 32 (2010) 247-255.
- [49] T. Zhai, *Metall Mater Trans A*, 37A (2006) 3139-3147.
- [50] W. Weibull, *Proc. Roy.Swedish Inst. Eng. Res.*, 151:1 (1939).
- [51] G.E. Totten, D.S. MacKenzie, *Handbook of Aluminum: Vol. 1: Physical Metallurgy and Processes*, Marcel Dekker, the United States of America, 2003.
- [52] G. Patton, C. Rinaldi, Y. Brechet, G. Lormand, R. Fougères, *Mat Sci Eng a-Struct*, 254 (1998) 207-218.
- [53] S.S. Singh, C. Schwartzstein, J.J. Williams, X. Xiao, F. De Carlo, N. Chawla, *J Alloy Compd*, 602 (2014) 163-174.
- [54] W.L. Morris, *MTA*, 11 (1980) 1117-1123.
- [55] W.L. Morris, *MTA*, 10 (1979) 5-11.
- [56] C.Y. Kung, M.E. Fine, *Metallurgical Transactions a-Physical Metallurgy and Materials Science*, 10 (1979) 603-610.
- [57] W.L. Morris, *MTA*, 9 (1978) 1345-1348.
- [58] W.L. Morris, *MTA*, 8 (1977) 1087-1093.
- [59] A. Zabett, A. Plumtree, *Fatigue & Fracture of Engineering Materials & Structures*, 18 (1995) 801-809.
- [60] E.A. DeBartolo, B.M. Hillberry, *International Journal of Fatigue*, 20 (1998) 727-735.
- [61] C.B. Fuller, A.R. Krause, D.C. Dunand, D.N. Seidman, *Mat Sci Eng a-Struct*, 338 (2002) 8-16.
- [62] J. Boselli, P.D. Pitcher, P.J. Gregson, I. Sinclair, *Scripta Materialia*, 38 (1998) 839-844.
- [63] T.S. Srivatsan, D. Kolar, P. Magnusen, *Mater Design*, 23 (2002) 129-139.
- [64] J.C.W. Vandekastele, D. Broek, *Eng Fract Mech*, 9 (1977) 625-&.
- [65] J.N. Goodier, *Journal of the American Ceramic Society*, 16 (1933) 220-228.
- [66] P. Lamagnere, D. Girodin, P. Meynaud, F. Vergne, A. Vincent, *Mat Sci Eng a-Struct*, 215 (1996) 134-142.
- [67] R. Gurbuz, S.P. Alpay, *Scripta Metallurgica Et Materialia*, 30 (1994) 1373-1376.
- [68] V.B. Dutta, S. Suresh, R.O. Ritchie, *Metallurgical Transactions a-Physical Metallurgy and Materials Science*, 15 (1984) 1193-1207.
- [69] A. Zabett, A. Plumtree, *Fatigue & Fracture of Engineering Materials & Structures*, 18 (1995) 801-809.
- [70] W.L. Morris, O. Buck, H.L. Marcus, *Metallurgical Transactions a-Physical Metallurgy and Materials Science*, 7 (1976) 1161-1165.

- [71] O. LE, University of pittsburgh, PA, 2003.
- [72] W. Wen, A.H.W. Ngan, Y. Zhang, B. Xu, T. Zhai, *Materials Science and Engineering: A*, 564 (2013) 97-101.
- [73] K.S. Chan, *International Journal of Fatigue*, 32 (2010) 1428-1447.
- [74] J.M. Hyzak, I.M. Bernstein, *Metallurgical Transactions a-Physical Metallurgy and Materials Science*, 13 (1982) 33-43.
- [75] C.Q. Bowles, J. Schijve, *International Journal of Fracture*, 9 (1973) 171-179.
- [76] S.G. Grosskreutz J, *proceedings of second international conference on fracture*, Chapman and Hall, Brighton(UK), 1969, pp. p.620-629.
- [77] S. Pearson, *Eng Fract Mech*, 7 (1975) 235-247.
- [78] Y. Xue, H. El Kadiri, M.F. Horstmeyer, J.B. Jordon, H. Weiland, *Acta Materialia*, 55 (2007) 1975-1984.
- [79] S. Nishijima, K. Kanazawa, *Fatigue & Fracture of Engineering Materials & Structures*, 22 (1999) 601-607.
- [80] Y. Murakami, T. Nomoto, T. Ueda, *Fatigue & Fracture of Engineering Materials & Structures*, 22 (1999) 581-590.
- [81] C. Bathias, *Fatigue & Fracture of Engineering Materials & Structures*, 22 (1999) 559-565.
- [82] Q.Y. Wang, J.Y. Berard, A. Dubarre, G. Baudry, S. Rathery, C. Bathias, *Fatigue & Fracture of Engineering Materials & Structures*, 22 (1999) 667-672.
- [83] Q.Y. Wang, C. Bathias, N. Kawagoishi, Q. Chen, *International Journal of Fatigue*, 24 (2002) 1269-1274.
- [84] Brooksba.D, K.W. Andrews, *Journal of the Iron and Steel Institute*, 207 (1969) 474-&.
- [85] C. DR, K. D, S. RA, In: *Superalloys* (1984) P. 245-273.
- [86] H. ES, R. PG, (1996) p. 359–368.
- [87] D.A. Jablonski, *Materials Science and Engineering*, 48 (1981) 189-198.
- [88] F. Alexandre, S. Deyber, A. Pineau, *Scripta Materialia*, 50 (2004) 25-30.
- [89] L. Kunz, P. Lukas, R. Konecna, *International Journal of Fatigue*, 32 (2010) 908-913.
- [90] C. Bathias, P.C. Paris, *International Journal of Fatigue*, 32 (2010) 894-897.
- [91] H.C. Burghard, *Metallurgical Transactions*, 5 (1974) 2083-2094.
- [92] F. Sarioglu, F.O. Orhaner, *Mat Sci Eng a-Struct*, 248 (1998) 115-119.
- [93] A.K. Vasudevan, R.D. Doherty, *Acta Metallurgica*, 35 (1987) 1193-1219.
- [94] Z.Q. Zheng, B. Cai, T. Zhai, S.C. Li, *Mat Sci Eng a-Struct*, 528 (2011) 2017-2022.
- [95] M. Kikuchi, K. Shiozawa, J.R. Weertman, *Acta Metallurgica*, 29 (1981) 1747-1758.

- [96] D.L. Davidson, R.G. Tryon, M. Oja, R. Matthews, K.S.R. Chandran, *Metall Mater Trans A*, 38A (2007) 2214-2225.
- [97] W.L. Morris, M.R. James, O. Buck, *Eng Fract Mech*, 18 (1983) 871-877.
- [98] J. Lankford, *Fatigue of Engineering Materials and Structures*, 5 (1982) 233-248.
- [99] T. Zhai, A.J. Wilkinson, J.W. Martin, *Acta Materialia*, 48 (2000) 4917-4927.
- [100] T. Zhai, X.P. Jiang, J.X. Li, M.D. Garratt, G.H. Bray, *International Journal of Fatigue*, 27 (2005) 1202-1209.
- [101] J.P. Anson, J.E. Gruzleski, *Materials Characterization*, 43 (1999) 319-335.
- [102] X. Zhu, J.W. Jones, J.E. Allison, *Metall Mater Trans A*, 39A (2008) 2681-2688.
- [103] K.S. Chan, P. Jones, Q.G. Wang, *Mat Sci Eng a-Struct*, 341 (2003) 18-34.
- [104] Q.G. Wang, D. Apelian, D.A. Lados, *Journal of Light Metals*, 1 (2001) 73-84.
- [105] J.H. Fan, D.L. McDowell, M.F. Horstemeyer, K. Gall, *Eng Fract Mech*, 70 (2003) 1281-1302.
- [106] Y.X. Gao, J.Z. Yi, P.D. Lee, T.C. Lindley, *Fatigue & Fracture of Engineering Materials & Structures*, 27 (2004) 559-570.
- [107] P. Li, P.D. Lee, D.M. Maijer, T.C. Lindley, *Acta Materialia*, 57 (2009) 3539-3548.
- [108] D.L. McDowell, K. Gall, M.F. Horstemeyer, J. Fan, *Eng Fract Mech*, 70 (2003) 49-80.
- [109] W. Wen, A.A. Luo, T. Zhai, Y. Jin, Y.-T. Cheng, I. Hoffmann, *Scripta Materialia*.
- [110] U. Krupp, *Fatigue Crack Propagation in Metals and Alloys*, WILEY-VCH Verlag GmbH & Co. KGaA, 2007.
- [111] S.E. Stanzltschegg, H.R. Mayer, A. Beste, S. Kroll, *International Journal of Fatigue*, 17 (1995) 149-155.
- [112] H.T. Pang, P.A.S. Reed, *International Journal of Fatigue*, 25 (2003) 1089-1099.
- [113] R. Sunder, W.J. Porter, N.E. Ashbaugh, *Fatigue & Fracture of Engineering Materials & Structures*, 25 (2002) 1015-1024.
- [114] J. Kang, D.S. Wilkinson, J.D. Embury, K. Hussain, Investigation on mechanism of ductile fracture of AA5754 sheet, in: W.J. Poole, M.A. Wells, D.J. Lloyd (Eds.) *Aluminium Alloys 2006*, Pts 1 and 2: Research through Innovation and Technology, 2006, pp. 985-990.
- [115] J. Polak, P. Liskutin, V. Ocenasek, K. Sperlink, Short crack growth in 1441 and 1450 Al-Li alloys, in: J.H. Driver, B. Dubost, F. Durand, R. Fougères, P. Guyot, P. Sainfort, M. Suery (Eds.) *Mater Sci Forum*, 1996, pp. 1429-1434.
- [116] H. Abdelraouf, T.H. Topper, A. Plumtree, *Fatigue & Fracture of Engineering Materials & Structures*, 15 (1992) 895-909.
- [117] W.X. Feng, F.S. Lin, E.A. Starke, *Metallurgical Transactions a-Physical Metallurgy and Materials Science*, 15 (1984) 1209-1220.

- [118] M. Mineur, P. Villechaise, J. Mendez, *Mat Sci Eng a-Struct*, 286 (2000) 257-268.
- [119] C.J. Taylor, T. Zhai, A.J. Wilkinson, J.W. Martin, *J Microsc-Oxford*, 195 (1999) 239-247.
- [120] D.C. Slavik, R.P. Gangloff, *Acta Materialia*, 44 (1996) 3515-3534.
- [121] D.C. Slavik, J.A. Wert, R.P. Gangloff, *J Mater Res*, 8 (1993) 2482-2491.
- [122] X.J. Wu, W. Wallace, M.D. Raizenne, A.K. Koul, *Metall Mater Trans A*, 25 (1994) 575-588.
- [123] M. Peters, A. Gysler, G. Lutjering, *Metallurgical Transactions a-Physical Metallurgy and Materials Science*, 15 (1984) 1597-1605.
- [124] D.L. Chen, M.C. Chaturvedi, N. Goel, N.L. Richards, *International Journal of Fatigue*, 21 (1999) 1079-1086.
- [125] Annual book of ASTM standards, 2000.
- [126] T. Zhai, Y.G. Xu, J.W. Martin, A.J. Wilkinson, G.A.D. Briggs, *International Journal of Fatigue*, 21 (1999) 889-894.
- [127] D. Newey, M.A. Wilkins, H.M. Pollock, *Journal of Physics E-Scientific Instruments*, 15 (1982) 119-122.
- [128] Y.C. Lu, D.C. Jones, G.P. Tandon, S. Putthanasarat, G.A. Schoeppner, *Exp. Mech.*, 50 (2010) 491-499.
- [129] W.C. Oliver, G.M. Pharr, *J Mater Res*, 7 (1992) 1564-1583.
- [130] G.M. Pharr, W.C. Oliver, F.R. Brotzen, *J Mater Res*, 7 (1992) 613-617.
- [131] W.C. Oliver, G.M. Pharr, *J Mater Res*, 19 (2004) 3-20.
- [132] D. McMullan, *Scanning*, 17 (1995) 175-185.
- [133] C.A. Volkert, A.M. Minor, *Mrs Bulletin*, 32 (2007) 389-395.
- [134] L.A. Giannuzzi, F.A. Stevie, *Micron*, 30 (1999) 197-204.
- [135] L. Bischoff, W. Pilz, T. Ganetsos, R.G. Forbes, C. Akhmadaliev, *Ultramicroscopy*, 107 (2007) 865-868.
- [136] S. Reyntjens, R. Puers, *Journal of Micromechanics and Microengineering*, 11 (2001) 287-300.
- [137] J. Gierak, *Semiconductor Science and Technology*, 24 (2009).
- [138] R.A. Wilson, H.A. Bullen, Northern Kentucky university.
- [139] H.J. Bunge, *Texture Analysis in Material Science*, Butterworths, London, 1982.
- [140] U.F. Kocks, C.N. Tome, H.R. Wenk, *Texture and Anisotropy: Preferred Orientations in Polycrystals and Their Effect on Materials Properties*, Cambridge University Press, London, 2000.
- [141] H.J. Bunge, *Texture Analysis in Materials Science: Mathematical Methods*, Butterworths, London, 1982.

- [142] O. Engler, V. Randle, Introduction to Texture Analysis Macrotexture, Microtexture, and Orientation Mapping, CRC Press, 2010.
- [143] J. Hansen, J. Pospiech, K. Lucke, Tables for Texture Analysis of Cubic Crystals, Springer-Verlag, Berlin, 1978.
- [144] B.F. Decker, E.T. Asp, D. Harker, Journal of Applied Physics, 19 (1948) 388-392.
- [145] S. Kikuchi, J. Appl. Phys., 5 (1928).
- [146] D.J. Dingley, K. Baba-Kishi, V. Randle, An Atlas of Backscatter Kikuchi Diffraction Patterns, Institute of Physics Publishing, Bristol, 1994.
- [147] G. Gottstein, O. Engler, Journal De Physique Iv, 3 (1993) 2137-2142.
- [148] M. Oja, K.S.R. Chandran, R.G. Tryon, International Journal of Fatigue, 32 (2010) 551-556.
- [149] W.O. Soboyejo, W. Shen, T.S. Srivatsan, Mech Mater, 36 (2004) 141-159.
- [150] J.X. Li, T. Zhai, M.D. Garratt, G.H. Bray, Metall Mater Trans A, 36A (2005) 2529-2539.
- [151] R.E. Ricker, D.J. Duquette, Metallurgical Transactions a-Physical Metallurgy and Materials Science, 19 (1988) 1775-1783.
- [152] S.E. Stanzl-Tschegg, H. Mayer, International Journal of Fatigue, 23 (2001) S231-S237.
- [153] W. Weibull, J. Appl. Mech.-Trans. ASME, 18 (1951) 293-297.
- [154] D. Casellas, R. Perez, J.M. Prado, Mat Sci Eng a-Struct, 398 (2005) 171-179.
- [155] Y.X. Zhao, Mat Sci Eng a-Struct, 344 (2003) 229-239.
- [156] S.J. Kim, Y.S. Kim, S.W. Kwon, On characteristics of Weibull distribution parameters of fatigue crack growth lives, in: K. Kishimoto, M. Kikuchi, T. Shoji, M. Saka (Eds.) Advances in Fracture and Failure Prevention, Pts 1 and 2, 2004, pp. 1275-1280.
- [157] T. Delahay, T. Palin-Luc, International Journal of Fatigue, 28 (2006) 474-484.
- [158] H.J. Sutherland, P.S. Veers, Wind Energy, ASME, 16 (1995) 83-90.
- [159] J. Li, University of Kentucky, 2006, pp. 131.
- [160] Z. Lv, P. Cai, Y. Jin, T. Zhai, J Alloy Compd, (Submitted).
- [161] P. Cai, Y. Jin, Q. Tian, T. Zhai, Scripta Materialia, (To be submitted).
- [162] J. Schijve, Fatigue of Structures and Materials 2nd Edition, 2009.
- [163] H. Qing, W. Yang, J. Lu, International Journal of Damage Mechanics, 19 (2010) 767-785.
- [164] A. Merati, International Journal of Fatigue, 27 (2005) 33-44.
- [165] M.A. Przystupa, R.J. Bucci, P.E. Magnusen, A.J. Hinkle, International Journal of Fatigue, 19 (1997) 285-288.
- [166] P.J. Laz, B.M. Hillberry, International Journal of Fatigue, 20 (1998) 263-270.
- [167] P.S. Pao, C.R. Feng, S.J. Gill, Corrosion, 56 (2000) 1022-1031.

- [168] J.Z. Yi, Y.X. Gao, P.D. Lee, T.C. Lindley, *Materials Science and Engineering: A*, 386 (2004) 396-407.
- [169] D.G. Harlow, M.Z. Wang, R.P. Wei, *Metall Mater Trans A*, 37A (2006) 3367-3373.
- [170] M. Gao, C.R. Feng, R.P. Wei, *Metall Mater Trans A*, 29 (1998) 1145-1151.
- [171] T.H.S. Sanders Jr., J.T., Review of fatigue strength and fracture research on high-strength aluminium alloys, *Fatigue and Microstructure*, Proc. of ASM Materials Science Seminar, American Society of Metal, 1979, pp. 467-522.
- [172] J.E. Bozek, J.D. Hochhalter, M.G. Veilleux, M. Liu, G. Heber, S.D. Sintay, A.D. Rollett, D.J. Littlewood, A.M. Maniatty, H. Weiland, R.J. Christ, Jr., J. Payne, G. Welsh, D.G. Harlow, P.A. Wawrzynek, A.R. Ingraffea, *Model Simul Mater Sc*, 16 (2008).
- [173] V.K. Gupta, S.R. Agnew, *International Journal of Fatigue*, 33 (2011) 1159-1174.
- [174] E.A. Starke Jr, J.T. Staley, *Progress in Aerospace Sciences*, 32 (1996) 131-172.
- [175] S.S. Singh, E.Y. Guo, H.X. Xie, N. Chawla, *Intermetallics*, 62 (2015) 69-75.
- [176] E. Nizery, H. Proudhon, J.Y. Buffiere, P. Cloetens, T.F. Morgeneyer, S. Forest, *Philos Mag*, 95 (2015) 2731-2746.
- [177] Y. Jin, P. Cai, Q.B. Tian, C.Y. Liang, D.J. Ke, G. Wang, T. Zhai, *Fatigue & Fracture of Engineering Materials & Structures*, (2016) n/a-n/a.
- [178] L. Yang, Y. Jin, P. Cai, T. Zhai, *Proceedings of the 15th International Conference on Aluminum Alloys*, Chongqing, China, 2016.
- [179] P. Cai, Y. Jin, T. Zhai, (to be submitted).
- [180] E.A. DeBartolo, B.M. Hillberry, *International Journal of Fatigue*, 23 (2001) S79-S86.
- [181] M. Liao, *Eng Fract Mech*, 76 (2009) 668-680.
- [182] D. Gross, T. Seelig, *Fracture Mechanics with an Introduction to Micromechanics*, Springer Verlag, Berlin, Heidelberg, 2006.
- [183] Y. Shen, T.F. Morgeneyer, J. Garnier, L. Allais, L. Helfen, J. Crépin, *Acta Materialia*, 61 (2013) 2571-2582.
- [184] F.S. Lin, E.A. Starke, *Materials Science and Engineering*, 39 (1979) 27-41.
- [185] Y. Ro, S.R. Agnew, R.P. Gangloff, *Metall Mater Trans A*, 38A (2007) 3042-3062.
- [186] Y. Ro, S.R. Agnew, R.P. Gangloff, *Metall Mater Trans A*, 39A (2008) 1449-1465.
- [187] D.L. McDowell, *International Journal of Fracture*, 80 (1996) 103-145.
- [188] U. Krupp, W. Floer, J.F. Lei, Y.M. Hu, H.J. Christ, A. Schick, C.P. Fritzen, *Philos Mag A*, 82 (2002) 3321-3332.
- [189] J.E. Hatch, *Aluminum: Properties and Physical Metallurgy*, Technology & Engineering, 1984.
- [190] F.S. Lin, E.A. Starke, *Materials Science and Engineering*, 45 (1980) 153-165.

- [191] H.C. Heikkinen, F.-S. Lin, E.A. Starke, *Materials Science and Engineering*, 51 (1981) 17-23.
- [192] B. Sarkar, M. Marek, E.A. Starke, *Metallurgical Transactions a-Physical Metallurgy and Materials Science*, 12 (1981) 1939-1943.
- [193] G.G. Garrett, J.F. Knott, *Acta Metallurgica*, 23 (1975) 841-848.
- [194] J.S. Santner, D. Eylon, *Metallurgical Transactions a-Physical Metallurgy and Materials Science*, 10 (1979) 841-848.
- [195] A.J. McEvily, T.L. Johnston, *International Journal of Fracture Mechanics*, 3 (1967) 45-74.
- [196] W. Wen, P. Cai, A.H.W. Ngan, T. Zhai, *Materials Science and Engineering: A*, (under review).

VITA

Place of Birth: Shenyang, Liaoning, China

Education:

- University of Kentucky, Lexington, Kentucky
2011 - present Ph.D. candidate (Materials Science and Engineering)
- University of Science and Technology Beijing, Beijing, China
2008 - 2011 M.E. (Disaster Prevention & Mitigation Engineering & Protective Engineering)
- China University of Mining and Technology Beijing, Beijing, China
2003 - 2007 B.E. (Materials Science and Engineering)

Honors and Awards:

- Outstanding Graduate Student, Chemical & Materials Engineering Department, University of Kentucky, 2016
- Best Student Poster Finalist Award, CNMS (Center for Nanophase Materials Sciences) User Meeting, Center of Nanophase Materials Sciences, Oak Ridge National Laboratory, 2014
- Visiting Scientist Grant, the University of Hong Kong, 2013

Publications:

- Y. Jin and T. Zhai, Simulation of multi-site fatigue crack nucleation at pre-crack in constituent particles by using micro-notches fabricated with FIB in AA2024 T351 and AA7075 T651 Al alloys rolled plate, to be submitted
- Y. Jin, L. Yang and T. Zhai, etc., 3-D microstructural effects on anisotropic fatigue crack initiation at constituent particle in an AA7075 T651 Al alloy rolled plate using focused ion beam combined with EBSD, AFM and Nano-indentation, to be submitted
- Y. Jin, P. Cai, Q. Tian and T. Zhai, An experimental methodology for quantitative characterization of multi-site fatigue crack nucleation in high strength aluminum alloys, *Fatigue & Fracture of Engineering Materials & Structures*, 39(6) (2016), pp. 696-711
- Y. Jin, P. Cai, W. Wen and T. Zhai, etc., The anisotropy of fatigue crack nucleation in an AA7075 T651 Al alloy plate, *Materials Science and Engineering: A* 622(2015), pp. 7-15
- P. Cai, Y. Jin and T. Zhai, Simulation of fatigue crack initiation behaviors from micro-notches in high strength Al alloys, *to be submitted*
- L. Yang, Y. Jin, P. Cai and T. Zhai, etc., Quantitative characterization of fatigue weak-links in high strength Al alloys, *Proceedings of the 15th International Conference on Aluminum Alloys*, June 12-16, 2016, Chongqing, China, submitted
- L. Yang, Y. Jin and T. Zhai, A numerical simulation for fatigue crack branching in AA7050 T7651 Al thick plate, to be submitted

- L. Yang, Y. Jin and T. Zhai, etc., A 3-D model for quantification of fatigue weak-link density and strength in an A713 cast aluminum alloy, to be submitted
- Z. Lv, P. Cai, Y. Jin and T. Zhai, etc., Fatigue behaviors and damage mechanism of Cr-Mn-N austenitic steel, *Journal of Alloys and Compounds*, under review
- C. Cui, T. Xue, Y. Jin, etc., Tensile and fatigue behavior of Ni-Ni₃Si eutectic in situ composites, *Materials Science and Technology*, 02(2016), pp. 1-6
- W. Wen, A. Luo, T. Zhai, Y. Jin, etc., Improved bending fatigue and corrosion properties of a Mg-Al-Mn alloy by super vacuum die casting, *Scripta Materialia*, Vol. 67 (2012), pp. 879-882
- H. Ji, Y. Zhang, Y. Jin, Experimental study of confining pressure effect on acoustic emission characteristics of monzonite granite, *Chinese Journal of Rock Mechanics and Engineering*, Vol. 31 (2012), pp. 1162-1168
- H. Ji, H. Wang, Y. Jin, Experimental research on frequency characteristics of acoustic emission signals under uniaxial compression of granite, *Chinese Journal of Rock Mechanics and Engineering*, Vol. 31 (2012), pp. 2900-2905
- H. Ji, Z. Hou, Y. Jin, Comparative analysis of acoustic emission signal frequency characteristics between packsand and granite, *2nd ISRM International Young Scholars' Symposium on Rock Mechanics*, Beijing, China, Oct. 14-16, 2011

Technical presentations (*presenter)

- Y. Jin*, L. Yang, P. Cai and T. Zhai, etc. A 3-D understanding of the anisotropy in fatigue crack nucleation in an AA7075 T651 Al alloy plate, *2016 TMS meeting*, Nashville, Tennessee, US (invited)
- P. Cai*, T. Zhai, Y. Jin, etc. Quantitative effects of texture and grain size on short fatigue crack growth in high strength Al alloys by a 3D microstructural-based model, *2016 TMS meeting*, Nashville, Tennessee, US
- L. Yang*, Z. Xu, Y. Jin, etc. A 3-D Model for quantification of fatigue weak-link strength in an A713 cast aluminum alloy, *2016 TMS meeting*, Nashville, Tennessee, US
- Y. Jin* and T. Zhai, Fatigue weak-links in high strength Al alloys, *ASM Chapter meeting*, Lexington, Kentucky, US (invited)
- Y. Jin*, P. Cai and T. Zhai, etc. 3-D effects of constituent particles on fatigue crack initiation in high strength aluminum alloys by FIB, *2015 TMS meeting*, Orlando, Florida, US
- Y. Jin, L. Yang, T. Zhai* and T. Leonhardt. Textures in pure Mo processed by different thermo-mechanical processes, *2015 TMS meeting*, Orlando, Florida, US
- L. Yang*, Y. Jin, etc. Simulation of fatigue crack deviation in AA7050 T7651 Al alloy thick plates, *2015 TMS meeting*, Orlando, Florida, US
- P. Cai*, Y. Jin, etc. Modeling of the 3-D effects of particles on fatigue crack initiation in high strength Al alloys, *2015 TMS meeting*, Orlando, Florida, US
- Y. Jin*, P. Cai, W. Wen and T. Zhai, Quantitative understanding 3-D effects of constituent particles on fatigue crack initiation in high strength aluminum alloys by FIB, *2014 CNMS User Meeting*, Oak Ridge National Laboratory, Oak Ridge, Tennessee, US (poster)
- Y. Jin*, The anisotropy of fatigue crack nucleation in an AA7075 T651 Al Alloy plates, *2014*

MACE spring symposium, Lexington, Kentucky, US (poster)

- Y. Jin* and T. Zhai, The anisotropy of fatigue crack nucleation in an AA7075 T651 Al Alloy plates, *2014 TMS meeting*, San Diego, California, US
- Y. Jin and T. Zhai*, The anisotropy of fatigue weak-link density and strength distribution in an AA7075 T651 Plate, *2013 AeroMat conference and exposition*, Bellevue, Washington, US
- W. Wen, Y. Jin*, A. Luo and T. Zhai, Improved environmental bending fatigue strength of Mg-Al-Mn Alloy by Super Vacuum Die Cast, *2013 TMS meeting*, San Antonio, Texas, US